



THE UNIVERSITY *of* EDINBURGH

This thesis has been submitted in fulfilment of the requirements for a postgraduate degree (e.g. PhD, MPhil, DClinPsychol) at the University of Edinburgh. Please note the following terms and conditions of use:

This work is protected by copyright and other intellectual property rights, which are retained by the thesis author, unless otherwise stated.

A copy can be downloaded for personal non-commercial research or study, without prior permission or charge.

This thesis cannot be reproduced or quoted extensively from without first obtaining permission in writing from the author.

The content must not be changed in any way or sold commercially in any format or medium without the formal permission of the author.

When referring to this work, full bibliographic details including the author, title, awarding institution and date of the thesis must be given.

Modelling Brugada Syndrome using induced pluripotent stem cells

Franziska Sendfeld

M.Sc



This dissertation is submitted for the degree
of
Doctor of Philosophy

The University of Edinburgh

2015

DECLARATION

This thesis is the result of my own work and includes nothing which is the outcome of work done in collaboration, except where indicated in the text.

This thesis includes material that has been the outcome of work done in collaboration. The portions of the thesis that were done in collaboration have been explicitly designated within the acknowledgements. The names of the collaborators and the nature of their contribution have been stated.

The work in this thesis has not been submitted for any other degree or professional qualification.

Franziska Sendfeld

“Nothing in the world can take the place of persistence. Talent will not; nothing is more common than unsuccessful men with talent. Genius will not; unrewarded genius is almost a proverb. Education will not; the world is full of educated derelicts. Persistence and determination alone are omnipotent. The slogan Press On! has solved and always will solve the problems of the human race.”

– Calvin Coolidge

ABSTRACT

Objective: Brugada Syndrome is an autosomal dominant congenital heart disease that is responsible for 20% of sudden deaths of patients with structurally normal hearts. The majority of mutations involve the cardiac sodium channel gene *SCN5A* and give rise to classical symptoms, which include an abnormal electrocardiogram with ST segment elevation and a predisposition to ventricular fibrillation. To date, the implantation of a cardioverter defibrillator is the only proven effective treatment of the disease. The ability to reprogram dermal fibroblasts to induced pluripotent stem (iPS) cells and to differentiate these into cardiomyocytes with the same genetic background provides a novel approach to studying inherited cardiac channelopathies with advantages over existing model systems. Whilst this technique has enormous potential to model inherited channelopathies, such as Brugada Syndrome, the derived cells have not been fully characterised and compared to foetal and adult cardiomyocytes.

Methods: Dermal fibroblasts from a patient with Brugada syndrome (*SCN5A*; c.1100G>A - pARG367HIS) and an age- and sex-matched control were reprogrammed using episomal vectors. All newly derived iPS cell lines were fully characterised using immunocytochemistry, flow cytometry, real-time quantitative reverse transcription PCR and single nucleotide polymorphism analysis and were compared to established human embryonic stem (hES) cell and in-house derived healthy control iPS cell lines. The same control cell lines were used to compare the efficiencies of several cardiac differentiation media. Spontaneously contracting areas, derived from control as well as patient iPS cell lines, were disaggregated and single cardiomyocytes were compared to foetal and adult cardiomyocytes isolated from primary human tissue using immunocytochemistry, transmission electron microscopy, membrane visualisation, calcium imaging and electrophysiology.

Results: Comparison of cardiac differentiation protocols using healthy control hES and iPS cell lines found that despite significant inter-line variability with regard to efficiency of cardiac formation guided differentiation protocols could be used to reliably and efficiently generate beating bodies. Spontaneous contraction was observed in stem cell-derived cardiomyocytes and human foetal cardiomyocytes. Pluripotent stem cell-derived cardiomyocytes stained for markers of the cardiac contractile apparatus such as α -actinin, cardiac troponin I and cardiac troponin T. They also expressed functional voltage-activated sodium channels and exhibited action potential triggered calcium-induced calcium release. Stem cell-derived cardiomyocytes showed organisation of myofibrils, ultrastructure and calcium handling more similar to foetal than adult cardiomyocytes. Brugada Syndrome patient-specific cardiomyocytes were structurally indistinguishable from healthy control iPS cell line-derived cardiomyocytes. Electrophysiological analysis of sodium current density confirmed a ~50% reduction in patient-derived compared to healthy control-derived cardiomyocytes.

Conclusion: Although iPS cells give rise to a mixture of immature and more mature cardiomyocytes, they all express typical cardiac proteins and have functional cardiac sodium channels. Results illustrate the ability of patient-specific iPS cell technology to model the abnormal functional phenotype of an inherited channelopathy that is independent of structural abnormalities and that the relative immaturity of iPS cell-derived cardiomyocytes does not prevent their use as an accurate model system for channelopathies affecting the cardiac sodium channel $Na_v1.5$. This iPS cell based model system for classical Brugada Syndrome allows for the first time to study the mutation in its native environment and holds promise for further studies to investigate disease mechanisms of known and unknown mutations and to develop new therapies.

ACKNOWLEDGEMENTS

I am indebted to Dr Nicholas Mills for not only giving me the opportunity to pursue a PhD in his group but especially for letting me experience some of the clinical aspect to our scientific research. Our stimulating discussions and his constant faith in my work allowed me to work independently and to grow as a scientist and I am proud of what we have achieved together. I would also like to thank Professor Sir Ian Wilmut and Dr Olga Tura-Ceide for their guidance and advice.

Thank you to the other members of our group; I have enjoyed the opportunity to watch and learn from their knowledge and experience. A heartfelt thank you to Dr Claire Medine who has gone above and beyond in providing advice when asked, encouragement when needed and laughs that were much appreciated. I'm grateful to Dr Amanda Hunter and Dr Mairi Brittan for providing the patient's biopsy and Dr Gareth Sullivan for providing control iPS cell lines. I am grateful to our collaborator Prof Ramon Brugada and his research group at the Universitat de Girona for lending their considerable electrophysiology expertise. Dr Fabiana Scornik and Dr Guillermo Pérez have been instrumental in optimising the setting for recording sodium currents (Figure 12 and Figure 38) while Dr Elisabet Selga provided sequencing results (Figure 41) as well as current recordings of the patient-derived cells (Figure 56).

Einen besonderen Dank an meine Familie, insbesondere meine Eltern, die mir nicht nur immer mit Rat und Tat zur Seite stehen, sondern mir auch mit Ermutigungen und Unterstützung Vertrauen in meine eigenen Fähigkeiten geben. Schwesterherz, die einzige die mich zur Weißglut treiben kann und zum lachen bringt bis die Tränen kullern, du bist mir ewig Vorbild und Inspiration. Weil bei einer Doktorarbeit der Wahnsinn nicht lange auf sich warten lässt, sind gute Freunde unabdinglich und ich hatte das besondere Glück mit der Besten von ihnen zusammenzuwohnen. "All work and no play makes Jack a dull boy", isiliye kadi mehnat ko meetha banaya coffee breaks ne. Sharmin, tumne mujhe sirf jhela hi nahi, balki meri saari bewkoofiyo mein mujhe protsahit bhi kiya, jiske karan yeh kathin raasta itna mazedaar raha. Toh behshak main yeh thesis tumhe bade pyaar se samarpit karti hoon. Meine endlose Dankbarkeit gilt dir Dave, für Unterstützung mit weit mehr als schnödem Mammon, für das Ertragen von Frustrationen und Teilen von Erfolgen und für das Licht am Ende vom Tunnel.

TABLE OF CONTENTS

DECLARATION	II
ABSTRACT	IV
ACKNOWLEDGEMENTS	VI
TABLE OF CONTENTS	VII
LIST OF FIGURES	XIII
LIST OF TABLES	XV
LIST OF ABBREVIATIONS	XVI

CHAPTER 1

GENERAL INTRODUCTION

1.1	Brugada Syndrome	2
1.1.1	SCN5A	4
1.1.2	Murine model of Brugada Syndrome	7
1.1.2.1	Scn5a heterozygous knock-out mice	7
1.1.2.2	Scn5a-1798insD knock-in mice	10
1.1.2.3	Scn1b knock-out mice	11
1.1.2.4	Strengths and limitations of the murine model	11
1.1.3	Porcine model	12
1.1.4	Canine Model of Brugada Syndrome	12
1.1.4.1	J-wave/Osborne wave	12
1.1.4.2	ST segment elevation	13
1.1.4.3	T-Wave alternans and VF/VT	14
1.1.4.4	Sex differences	15
1.1.4.5	Prediction of high risk patients and treatment	15
1.1.4.6	Strengths and limitations of the canine model	16
1.1.5	Expression systems modelling Brugada Syndrome	17
1.1.5.1	Altered $Na_v1.5$ properties	17
1.1.5.2	Complete loss of I_{Na}	19
1.1.5.3	Induced Brugada Syndrome	20
1.1.5.4	Other genes associated with Brugada Syndrome	21
1.1.5.5	Strengths and limitations of expression systems	24

1.2	Induced pluripotent stem cell-derived cardiomyocytes	25
1.2.1	Induced pluripotent stem cells	25
1.2.2	Improvements of retroviral reprogramming efficiency	26
1.2.3	Alternative reprogramming techniques	26
1.2.4	iPS cell-based model systems	28
1.2.5	Cardiac differentiation of iPS cells	30
1.2.5.1	Unguided differentiation	30
1.2.5.2	Co-culture differentiation	32
1.2.5.3	Guided differentiation	35
1.3	Cardiomyocyte Biology	40
1.3.1	Physiology and structure	40
1.3.1.1	Myofibrils and sarcomeres	41
1.3.1.2	Sarcoplasmic reticulum	43
1.3.1.3	Intercalated discs	43
1.3.2	Function	44
1.3.2.1	Action potential	44
1.3.2.2	Calcium-induced calcium release	46
1.3.2.3	Contraction and relaxation	47
	HYPOTHESES	50
	AIMS	51

CHAPTER 2

MATERIALS AND METHODS

2.1	Solutions and media	53
2.1.1	Solutions and reagents	53
2.1.2	Media and supplements	55
2.2	Cell lines	57
2.3	Isolation of human primary cardiomyocytes	58
2.3.1	Isolation of foetal cardiomyocytes	58
2.3.2	Isolation of adult cardiomyocytes	59
2.4	Derivation and maintenance of iPS cells	60
2.4.1	Skin biopsy and isolation of fibroblasts	60
2.4.2	Reprogramming of fibroblasts to induced pluripotent stem cells using	

episomal vectors _____	61
2.4.3 Maintenance of pluripotent stem cell lines _____	62
2.4.3.1 Preparation of mouse embryonic fibroblasts (MEFs) as feeder cells and production of MEF conditioned medium (MEF CM) _____	62
2.4.3.2 Feeder-layer system _____	62
2.4.3.3 Feeder-free system _____	63
2.5 Differentiation of pluripotent stem cells to cardiomyocytes _____	63
2.5.1 Three germ layer differentiation _____	63
2.5.2 Directed hepatic differentiation _____	63
2.5.3 END-2 co-culture _____	64
2.5.3.1 Maintenance of END-2 cells _____	64
2.5.3.2 Growth arrest of END-2 cells _____	64
2.5.3.3 Production of END-2 conditioned medium _____	64
2.5.4 Cardiac Differentiation _____	65
2.5.5 Disaggregation of beating bodies _____	66
2.6 Characterisation of iPS cells and cardiomyocytes _____	67
2.6.1 Single Nucleotide Polymorphism (SNP) analysis _____	67
2.6.1.1 Sample preparation _____	67
2.6.1.2 Analysis _____	67
2.6.2 Sequencing _____	69
2.6.3 Histology _____	70
2.6.3.1 Cell fixation _____	70
2.6.3.2 Immunocytochemistry _____	70
2.6.3.3 Tissue sectioning _____	72
2.6.3.4 Immunohistochemistry _____	72
2.6.3.5 Flow cytometry _____	73
2.6.4 Reverse transcriptase polymerase chain reaction (RT-PCR) _____	74
2.6.4.1 RNA extraction and purification _____	74
2.6.4.2 Complementary DNA synthesis _____	75
2.6.4.3 Polymerase chain reaction (PCR) _____	76
2.6.4.4 Real-time quantitative reverse transcription PCR (qPCR) _____	78
2.6.5 Transmission electron microscopy (TEM) _____	81
2.6.5.1 Sample preparation _____	81
2.6.5.2 Sectioning and analysis _____	82
2.6.6 Intracellular Ca ²⁺ handling _____	82
2.6.6.1 Sample preparation _____	82
2.6.6.2 Image acquisition and analysis _____	83
2.6.7 Membrane visualisation _____	83

2.6.7.1	Sample preparation	83
2.6.7.2	Image acquisition and analysis	84
2.6.8	Electrophysiology	84
2.7	Statistical Analysis	87

CHAPTER 3

CHARACTERISATION OF PLURIPOTENT STEM CELLS AND THEIR DIFFERENTIATION TO CARDIOMYOCYTES

3.1	Abstract	89
3.2	Introduction	90
3.3	Aims	93
3.4	Results	94
3.4.1	Morphology	94
3.4.2	Chromosomal integrity	95
3.4.3	Expression of pluripotency markers - Reverse transcription polymerase chain reaction	96
3.4.4	Expression of pluripotency markers - Quantitative RT-PCR	98
3.4.5	Expression of pluripotency markers - Immunocytochemistry	99
3.4.6	Expression of pluripotency markers - Flow cytometry	100
3.4.7	Three germ layer formation	102
3.4.8	Comparison of cardiac differentiation protocols	103
3.5	Discussion and Conclusion	110

CHAPTER 4

CHARACTERISATION OF HUMAN CARDIAC TISSUE AND PLURIPOTENT STEM CELL-DERIVED CARDIOMYOCYTES

4.1	Abstract	114
4.2	Introduction	115
4.3	Aims	118
4.4	Results	119
4.4.1	Morphology	119

4.4.1.1	Primary cardiac tissue _____	119
4.4.1.2	Pluripotent stem cell-derived beating bodies and cardiomyocytes ____	121
4.4.2	Expression of cardiac markers _____	122
4.4.2.1	Primary human cardiac tissue _____	122
4.4.2.2	Pluripotent stem cell-derived cardiomyocytes _____	126
4.4.3	Ultrastructure _____	128
4.4.3.1	Primary tissue _____	128
4.4.3.2	Pluripotent stem cell-derived cardiomyocytes _____	130
4.4.4	Membrane visualisation _____	132
4.4.5	Intracellular calcium imaging _____	133
4.4.6	Electrophysiology _____	139
4.5	Discussion and Conclusion _____	141

CHAPTER 5

GENERATION AND CHARACTERISATION OF BRUGADA SYNDROME IPS CELL-DERIVED CARDIOMYOCYTES

5.1	Abstract _____	148
5.2	Introduction _____	149
5.3	Aims _____	151
5.4	Results _____	152
5.4.1	Generation and characterisation of iPS cells _____	153
5.4.1.1	Morphology _____	154
5.4.1.2	Mutation in SCN5A _____	155
5.4.1.3	Expression of pluripotency markers - Quantitative RT-PCR _____	155
5.4.1.4	Expression of pluripotency markers - Immunocytochemistry _____	156
5.4.1.5	Expression of pluripotency markers - Flow cytometry _____	158
5.4.1.6	Three germ layer formation _____	159
5.4.1.7	Chromosomal integrity _____	161
5.4.2	Generation and characterisation of cardiomyocytes _____	164
5.4.2.1	BP-derived cardiomyocytes - Morphology _____	164
5.4.2.2	BP-derived cardiomyocytes - Cardiac markers _____	165
5.4.2.3	BP-derived cardiomyocytes - Ultrastructure _____	168
5.4.2.4	BP-derived cardiomyocytes - Membrane visualisation _____	169
5.4.2.5	BP-derived cardiomyocytes - Intracellular calcium imaging _____	170
5.4.2.6	Electrophysiology _____	173

5.5	Discussion and Conclusion	175
-----	---------------------------	-----

CHAPTER 6

GENERAL DISCUSSION

6.1	Limitations of this study	183
-----	---------------------------	-----

6.2	Future directions	186
-----	-------------------	-----

REFERENCES		188
------------	--	-----

LIST OF FIGURES

Figure 1: Normal vs Brugada Syndrome ECG _____	2
Figure 2: Na _v 1.5 channel scheme showing the location of mutations in SCN5A identified in patients with the Brugada Syndrome _____	5
Figure 3: Overview of model systems of Brugada Syndrome _____	8
Figure 4: Schematic of an iPS cell based model system to model an inherited cardiac disease _____	29
Figure 5: Schematic of cardiac muscle cell _____	41
Figure 6: Schematic of a single relaxed sarcomere _____	43
Figure 7: Schematic of a ventricular action potential _____	45
Figure 8: Schematic of SNP array analysis _____	68
Figure 9: Representative gating strategy for flow cytometry analysis _____	74
Figure 10: PCR optimisation of primers for pluripotency markers _____	77
Figure 11: Optimisation of qPCR conditions _____	79
Figure 12: Sodium current recordings in High Na ⁺ and Low Na ⁺ bath solution _____	87
Figure 13: Overview of protocols employed to generate cardiomyocytes from iPS and hES cells _____	92
Figure 14: Morphology of hES and iPS cells in culture _____	95
Figure 15: Microduplications identified through SNP analysis _____	96
Figure 16: RT-PCR analysis of pluripotency markers _____	97
Figure 17: Pluripotency transcription factor expression _____	99
Figure 18: Immunocytochemistry for pluripotency markers Nanog, Oct-4 and Tra-1-60 _____	100
Figure 19: Flow cytometry analysis of pluripotency markers SSEA-3 and SSEA-4 _____	101
Figure 20: Immunocytochemistry for the three germ layers _____	102
Figure 21: Initial comparison of different EB formation media and cardiac differentiation media _____	104
Figure 22: Comparison of unguided and guided cardiac differentiation protocols in three pluripotent stem cell lines _____	107
Figure 23: Morphology of adult and foetal cardiomyocytes _____	120
Figure 24: hES and iPS cell-derived beating bodies and single cardiomyocytes _____	121
Figure 25: Immunocytochemistry for cardiac marker alpha actinin in adult cardiomyocytes in culture _____	123
Figure 26: Immunocytochemistry for cardiac markers in foetal cardiomyocytes in culture _____	124
Figure 27: Immunohistochemistry for cardiac markers in sections of adult cardiac tissue _____	125
Figure 28: Immunohistochemistry for cardiac markers in sections of foetal cardiac tissue _____	126

Figure 29: Immunocytochemistry for cardiac markers in pluripotent stem cell-derived cardiomyocytes _____	127
Figure 30: TEM images of primary human cardiomyocytes _____	128
Figure 31: TEM images of primary human cardiomyocytes _____	130
Figure 32: TEM images of pluripotent stem cell-derived cardiomyocytes _____	131
Figure 33: Visualisation of cell membrane _____	133
Figure 34: Effect of Tetrodotoxin on calcium-induced calcium release in a beating body	134
Figure 35: Calcium transients in foetal and stem cell-derived cardiomyocytes _____	136
Figure 36: Single calcium transient in spontaneously contracting cardiomyocytes _____	137
Figure 37: Decay kinetics of calcium transients in foetal and stem cell-derived cardiomyocytes _____	138
Figure 38: I-V curve of H9-derived cardiomyocytes _____	140
Figure 39: Clinical and genetic characterization of the patient and his family. _____	153
Figure 40: Morphology of BP and HV3 iPS cell lines in culture _____	154
Figure 41: Sequencing analysis of SCN5A in BP and HV3 cell lines _____	155
Figure 42: Pluripotency transcription factor expression _____	156
Figure 43: Immunocytochemistry for pluripotency markers Nanog, Oct-4 and Tra-1-60 in BP iPS cell clones _____	157
Figure 44: Immunocytochemistry for pluripotency markers Nanog, Oct-4 and Tra-1-60 in HV3 iPS cell clones _____	158
Figure 45: Immunocytochemistry for the three germ layers formed by BP iPS cell clones	160
Figure 46: Immunocytochemistry for the three germ layers formed by HV3 iPS cell clones _____	161
Figure 47: Microduplications identified through SNP analysis _____	162
Figure 48: Beating bodies and single cardiomyocytes derived from BP-C5 and BP-C26 ____	165
Figure 49: Immunocytochemistry for cardiac markers in cardiomyocytes derived from BP-C26 _____	166
Figure 50: Immunocytochemistry for cardiac markers in cardiomyocytes derived from BP-C5 _____	167
Figure 51: TEM of BP iPS cell-derived cardiomyocytes _____	169
Figure 52: Visualisation of cell membrane of BP iPS cell-derived cardiomyocytes _____	170
Figure 53: Calcium transients in BP iPS cell-derived cardiomyocytes _____	171
Figure 54: Single calcium transient in spontaneously contracting cardiomyocytes _____	172
Figure 55: Decay kinetics of calcium transients in foetal and BP iPS cell-derived cardiomyocytes _____	173
Figure 56: Sodium current densities of cardiomyocytes derived from Brugada Syndrome patient and healthy control iPS cells _____	174

LIST OF TABLES

Table 1: Known Na _v 1.5 binding partners _____	6
Table 2: Genes other than SCN5A associated with Brugada Syndrome _____	23
Table 3: Composition of growth and differentiation media _____	56
Table 4: List of commercially obtained and in-house derived cell lines _____	57
Table 5: Composition of buffers used to isolate human foetal cardiomyocytes _____	58
Table 6: Composition of buffers used to disaggregate beating bodies _____	66
Table 7: Antibodies used for immunostaining _____	70
Table 8: Detailed staining protocols for immunocytochemistry _____	71
Table 9: Antibodies used for flow cytometry _____	73
Table 10: Primers used for RT-PCR with optimised conditions _____	77
Table 11: Primers used for qPCR with optimised final concentration _____	80
Table 12: Buffers for electrophysiology _____	85
Table 13: Percentage of cells expressing SSEA-3 and SSEA-4 _____	101
Table 14: Statistical comparison of total numbers of beating bodies generated during cardiac differentiation _____	108
Table 15: Statistical comparison of percentage of beating bodies generated during cardiac differentiation _____	109
Table 16: Percentage of cells expressing SSEA-3 and SSEA-4 _____	159
Table 18: Microduplications identified through SNP analysis and the genes affected _____	163

LIST OF ABBREVIATIONS

a.u.	– Arbitrary units
AFP	– Alpha-fetoprotein
ANOVA	– Analysis of variance
AV	– Atrial ventricular
BAF	– β -Allele Frequency
BDMA	– Benzyl dimethylamine
bFGF	– Human basic fibroblast growth factor
BMP	– Bone morphogenetic protein
BSA	– Bovine serum albumin
bSF	– Basic serum-free medium
cDNA	– Complementary DNA
CICR	– Calcium-induced calcium release
cTnI	– Cardiac troponin I
cTnT	– Cardiac troponin T
DAPI	– 4',6-diamidino-2-phenylindole
DDSA	– Dodecenyl succinic anhydride
DKK1	– Dickkopf-related protein 1
DMEM	– Dulbecco's modified eagle medium
DMSO	– Dimethyl sulfoxide
EB	– Embryoid body
ECG	– Electrocardiogram
EDTA	– Ethylenediaminetetraacetic acid
END-2	– Mouse visceral endoderm-like cell line
END-2 CM	– Mouse visceral endoderm-like cell line conditioned medium
FANS	– Familial Arrhythmia Network for Scotland
FCS	– Foetal calf serum
FGF	– Fibroblast growth factor
GMP	– Good manufacturing practice
GOI	– Gene of interest
GSK-3	– Glycogen synthase kinase 3
HAND	– Heart- and neural crest derivatives-expressed protein
HEK293	– Human embryonic kidney cells 293
hES cell	– Human embryonic stem cell
HRC	– Histidine-rich calcium-binding protein
I_{Na}	– Sodium inward current
iPS cell	– Induced pluripotent stem cell
I_{to}	– Transient potassium outward current
Klf4	– Krüppel-like factor 4
KO-DMEM	– Knock-out dulbecco's modified eagle medium

KOSR	– Knock-out serum replacement
L-Glut	– L-glutamine
LN ₂	– Liquid nitrogen
LOH	– Loss of heterozygosity
LQT	– Long QT Syndrome
MEF	– Myocyte-specific enhancer factor
MEF CM	– Mouse embryonic fibroblast conditioned medium
MEFs	– Mouse embryonic fibroblasts
mRNA	– Messenger RNA
NCX1	– Sodium-calcium exchanger
NEAA	– Non-essential amino acids
Oct-4	– Octamer-binding transcription factor 4
PBS	– Phosphate buffered saline
PCR	– Polymerase chain reaction
PenStrep	– Penicillin, streptomycin
PFA	– Paraformaldehyde
PGI ₂	– Prostaglandin I ₂
PO buffer	– Phosphate buffer
qPCR	– Real-time quantitative reverse transcription PCR
RAA	– Right atrial appendage
RT-PCR	– Reverse transcriptase PCR
SEM	– Standard error of the mean
SERCA	– Sarcoplasmic endoplasmic reticulum calcium ATPase
SNBTS	– Scottish National Blood Transfusion Service
SNP	– Single nucleotide polymorphism
Sox2	– Sex determining region Y-box 2
SR	– Sarcoplasmic reticulum
SSEA	– Stage-specific embryonic antigen
T _A	– Annealing temperature
TEM	– Transmission electron microscopy
TGF-β	– Transforming growth factor β
t-tubules	– Transverse tubules
TTX	– Tetrodotoxin
UTF1	– Undifferentiated embryonic cell transcription factor 1
VEGF	– Vascular endothelial growth factor
VF	– Ventricular fibrillation
VT	– Ventricular tachycardia
β-Merc	– β-Mercaptoethanol

CHAPTER 1

General introduction

1.1 Brugada Syndrome

Brugada Syndrome is an autosomal dominant congenital heart disorder that is responsible for 20% of sudden deaths of patients with structurally normal hearts¹. First described by the Brugada brothers in 1992² it is characterised by an abnormal electrocardiogram (ECG) with ST segment elevation in the right precordial leads V₁-V₃ (Figure 1) and right bundle-branch block frequently leading to ventricular fibrillation (VF) and sudden cardiac death in patients with structurally normal hearts. Patients often present with symptoms of ventricular tachycardia (VT), bradycardia, and atrial ventricular (AV) node conduction disorder, and more males than females present with symptoms of Brugada Syndrome. The most important criterion for diagnosis of Brugada Syndrome is a spontaneous or drug inducible ST segment elevation in the 12-lead ECG. Patient ECGs are subject to fluctuations are more likely to exhibit spontaneous classical Brugada Syndrome patterns between 12 am and 6 am³. This has important implications since spontaneous ST segment elevation is considered a risk factor. For the definitive diagnosis one of five possible clinical characteristics has to be met¹: a family history of sudden cardiac death, a family history of ST segment elevation, agonal respiration during sleep, a history of VT/VF or inducibility of VT/VF during electrophysiological study. To date, the implantation of a cardioverter defibrillator is the only proven effective treatment of the disorder^{4, 5}.

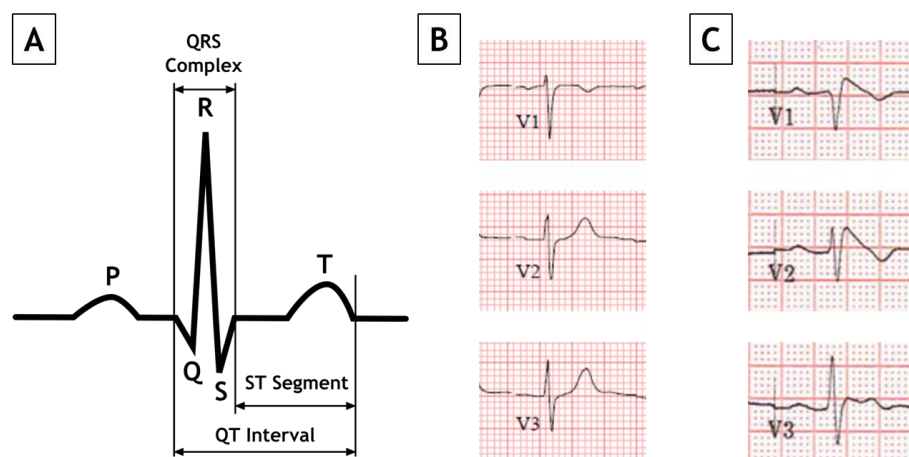


Figure 1: Normal vs Brugada Syndrome ECG

A – Schematic diagram of a normal sinus rhythm, B – normal ECG, C – ECG of a patient with Brugada Syndrome

Some patients can be asymptomatic for life, some present with syncope and some suffer from sudden cardiac death caused by ventricular fibrillation without prior symptoms. Men are not only more likely than women to develop Brugada Syndrome but also carry a 5.5-fold increased risk of sudden cardiac death. While the mean age of patients with VF episodes is 41 ± 15 years¹, arrhythmic events may occur from the age of 2 causing sudden cardiac death in infants and young children^{6, 7}. The prevalence of Brugada Syndrome is low in the general population but higher in Asia than in the United States and Europe which has been thoroughly reviewed elsewhere⁸. Fever frequently induces ECG changes and VF in both adults and children^{1, 6, 10}. Generally, frequency of abnormal ECGs with a classical Brugada Syndrome phenotype is also much higher in adults compared to children⁹. Patients are more likely to suffer an arrhythmic event at night¹¹, which might be attributed to activity of the vagus nerve^{12, 13}, and atrial fibrillation is commonly observed in 11-14% of Brugada Syndrome patients¹⁴.

Even though Brugada Syndrome has been associated with mutations in 17 genes¹⁵, its main identified genetic cause is a mutation in *SCN5A*¹⁶. This gene encodes the alpha-subunit of the cardiac sodium channel $Na_v1.5$ responsible for sodium inward current (I_{Na}) and is located in the membrane of cardiomyocytes. In order to understand the underlying mechanisms of the Brugada phenotype, different model systems have been utilized. These models include transgenic mice¹⁷, canine heart preparations¹⁸ and expression of mutant *SCN5A* in different expression systems¹⁶. This literature review aims to analyse the most commonly used systems to model Brugada Syndrome to show their major accomplishments as well as their advantages and disadvantages. In addition to model systems, Brugada Syndrome patients have been studied extensively both to understand the underlying mechanism as well as to improve treatment¹⁹⁻²¹. These clinical studies combined with experimental models have led to the proposal of several mechanisms. The two most prominent hypotheses propose conduction delay in the right ventricle (depolarisation hypothesis) and transmural dispersion of repolarisation between the endo- and epicardium of the right ventricular outflow tract (repolarization hypothesis) as the mechanism underlying

Brugada Syndrome. Arguments for and against either hypothesis have been extensively reviewed and discussed^{22, 23}.

1.1.1 SCN5A

SCN5A, located on chromosome 3p21, is the gene that encodes the alpha-subunit of cardiac sodium channel $\text{Na}_v1.5$ (Figure 2). It is made up of four homologues transmembrane domains (DI-DIV) each consisting of 6 transmembrane segments (1-6) and neighbouring homologues domains are connected through linker loops. The positively charged transmembrane segment 4 has been associated with voltage-dependent activation of $\text{Na}_v1.5$ ^{24, 25}, while inactivation of the channel has been attributed to intracellular loops III and IV. The transmembrane segments 6 and the loops between 5 and 6 in each domain form the Na^+ -conducting channel pore²⁶. Although the alpha-subunit of $\text{Na}_v1.5$ by itself is sufficient to act as a voltage-dependent sodium channel, it is part of a large multi-protein complex. The alpha-subunit interacts with four beta-subunits that are encoded by *SCN1B*, *SCN2B*, *SCN3B* and *SCN4B*^{27, 24}. Each 30-35 kDa protein contains a transmembrane alpha-helix with an extracellular N-terminus and an intracellular C-terminus and while beta-subunits 1 and 3 bind to the alpha-subunit through non-covalent bonds, subunits 2 and 4 bind through disulphide bonds.

Beta-subunits play a potential role in $\text{Na}_v1.5$ cell surface expression and have been shown to modulate I_{Na} density and /or gating characteristics²⁷. Other binding partners include cytoskeletal, regulatory, trafficking, cell adhesion and gap junction proteins (Table 1) that have recently been reviewed in detail by Willis et al.²⁸. Not all $\text{Na}_v1.5$ -protein interaction sites have been identified but it has been shown that some binding partners interact with $\text{Na}_v1.5$ between loops II and III or at its C-terminus which contains a PDZ domain. The PDZ domain consists of postsynaptic density protein, *Drosophila* disc large tumour suppressor and zonula occludens-1 protein.

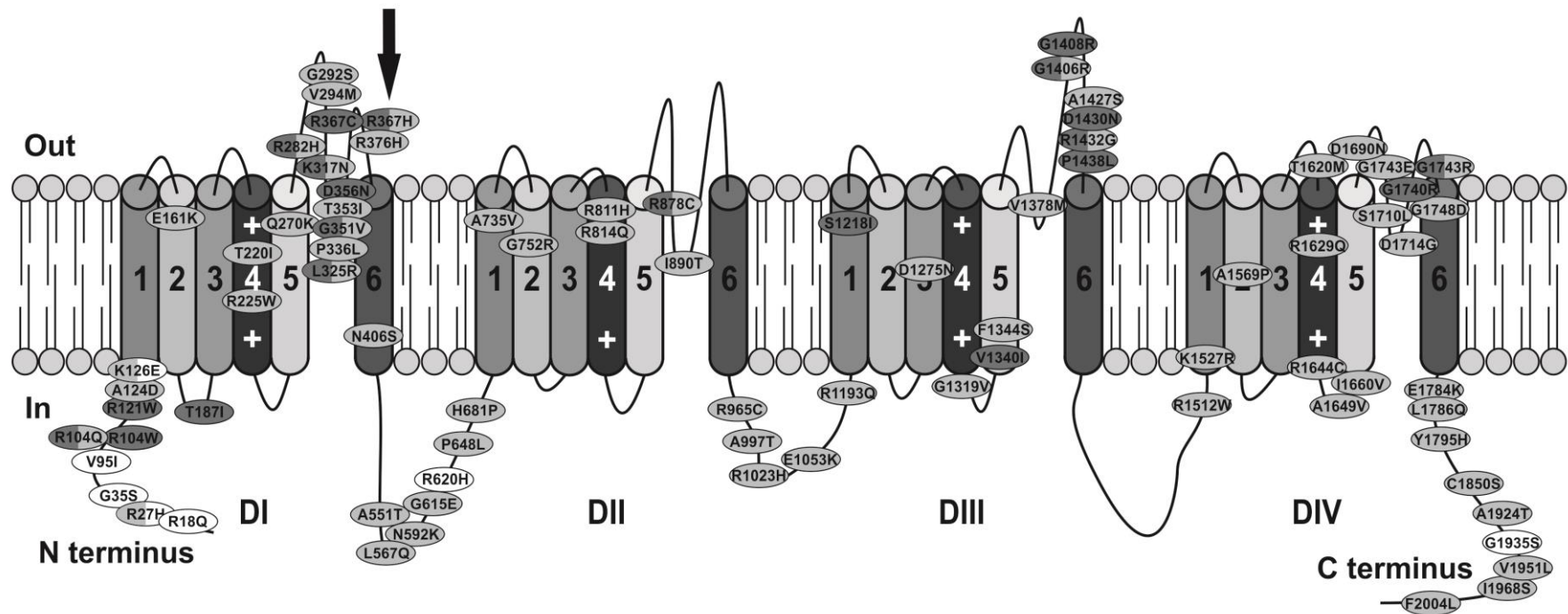


Figure 2: Na_v1.5 channel scheme showing the location of mutations in SCN5A identified in patients with the Brugada Syndrome

Of the >400 *SCN5A* mutations linked to Brugada Syndrome only missense mutations that have been functionally characterized using expression systems are displayed. Nonsense and insertion or deletion mutations are not shown. Mutations described to cause a complete loss of I_{Na} are dark grey, those reported to alter Na_v1.5 properties are light grey, and white indicates no changes in channel properties. Mutations for which 2 different types of alterations have been reported are displayed in both colors. The mutation investigated in this study is indicated by a black arrow.

Table 1: Known Nav1.5 binding partners

Protein	Protein function	Nav1.5 Interaction Site	Ref.
AnkyrinG	Anchoring, transport	Domain II and III loop	29
Caveolin-3	Anchoring, caveolae formation	?	30
Desmoglein-2	Desmosome structure	?	31
Dystrophin	Cytoskeletal, anchoring	COOH-terminus PDZ-binding domain	32
FHF	Growth factor	COOH-terminus	33
GPD1-L	Enzyme, modulator	?	34
MOG-1	Intranuclear traffic	Domain II and III loop	35
Plakophilin-2	Desmosome structure	?	36
SAP97	Scaffolding	COOH-terminus PDZ-binding domain	37
Syntrophin	Cytoskeletal, adaptor	COOH-terminus PDZ-binding domain	38

FHF – fibroblast growth factor homologous factors; GPD1-L – glycerol-3-phosphate dehydrogenase-like protein; MOG1 – multicopy suppressor of *gsp-1*; SAP97 – synapse-associated protein 97

Mutations in *SCN5A* can lead to a number of clinical phenotypes depending on whether they cause a gain or loss of function. A mutation that causes a gain of function can result in increased late I_{Na} , leading to Long QT Syndrome type 3 (LQT3). A loss-of-function mutation on the other hand can lead to decreased peak I_{Na} , which is associated with Brugada syndrome, sick sinus syndrome and cardiac conduction diseases. In cases where a mutation causes both a gain in late I_{Na} and a loss of peak I_{Na} can lead to overlap syndromes (e.g. Brugada syndrome/LQT3). Additionally, familial lone atrial fibrillation has been linked to both gain- and loss-of-function mutations³⁹.

1.1.2 Murine model of Brugada Syndrome

Two approaches are conceivable, one knocking out the mouse equivalent of the human *SCN5A* (*Scn5a*) to simulate a generic Brugada Syndrome phenotype, the other one introducing a specific mutation found in Brugada Syndrome patients and replicating its associated phenotype.

1.1.2.1 *Scn5a* heterozygous knock-out mice

In 2002 Papadatos et al.¹⁷ generated a mouse model for arrhythmias through targeted disruption of *Scn5a* (Figure 3). Homozygous knock-out mice exhibited embryonic lethality caused by their structurally abnormal hearts. Heterozygous knock-out mice (*Scn5a*^{+/-}) were indistinguishable from their wild type (WT) littermates regarding weight, heart/body weight ratio, heart morphology and mortality. ECGs of *Scn5a*^{+/-} mice revealed a slow conduction compared to WT mice but a normal QT interval. These findings were affirmed with whole cell patch-clamp recordings showing a ~50% reduction in sodium conductance causing impaired action potential propagation, conduction block, re-entrant arrhythmias and ventricular tachycardia. *Scn5a*^{+/-} mice exhibited several cardiac phenotypes however not one strictly representative of the Brugada Syndrome. Phenotypic heterogeneity, even resulting in some symptom-free mutation carriers, in *Scn5a*^{+/-} mice as well as in patients carrying a *SCN5A* mutation, could at least in part be explained by varying levels of Na_v1.5 protein expression, with severity of the phenotype correlating with the expression levels of WT Na_v1.5⁴⁰.

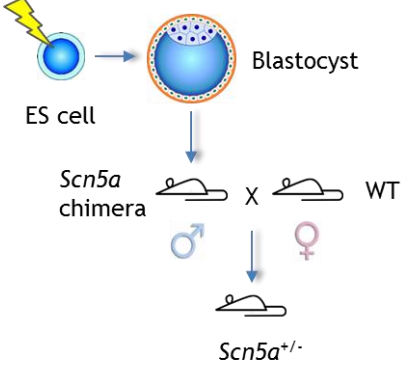
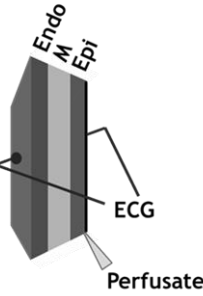
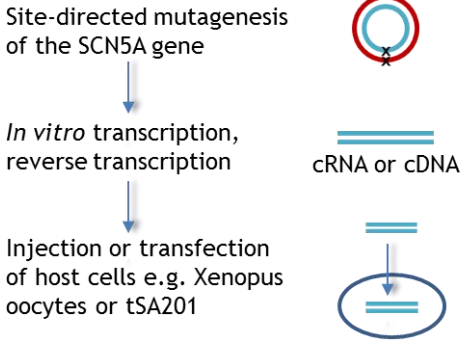
Mouse Model	Canine Model	Expression System
 <p>ES cell → Blastocyst → <i>Scn5a</i> chimera × WT → <i>Scn5a</i>^{+/-}</p>	 <p>Brugada Syndrome is induced by:</p> <ul style="list-style-type: none"> • Na⁺-channel blockers e.g. flecainide • Ca²⁺-channel blockers e.g. verapamil • K⁺-channel openers e.g. pinacidil <p>ECG, Perfusate</p>	 <p>Site-directed mutagenesis of the SCN5A gene → <i>In vitro</i> transcription, reverse transcription → cRNA or cDNA → Injection or transfection of host cells e.g. Xenopus oocytes or tSA201</p>
<p>Analysed parameters: surface ECGs, morphology of heart, disease progression</p> <p>Strengths:</p> <ul style="list-style-type: none"> • Right physiological environment • Effects during different developmental stages <p>Limitations:</p> <ul style="list-style-type: none"> • Cardiac electrophysiological characteristics of mice and humans are markedly different • Expensive • investigation at the molecular level limited restricted to known mutations 	<p>Analysed parameters: transmembrane action potential</p> <p>Strengths:</p> <ul style="list-style-type: none"> • Right physiological environment • cells in epi- and endocardium can be investigated <p>Limitations:</p> <ul style="list-style-type: none"> • Brugada Syndrome phenotype is drug induced • Combinations of channel blockers and/or openers not representative of conditions in patients • Possibilities for drug screening limited • Not representative of atypical Brugada Syndrome patients 	<p>Analysed parameters: action potentials, cellular localisation of mutant channels</p> <p>Strengths:</p> <ul style="list-style-type: none"> • Investigates molecular mechanisms of specific mutation found in patients • Inexpensive, easy to maintain and manipulate <p>Limitations:</p> <ul style="list-style-type: none"> • Limited to known mutations • no insight into atypical patients or heterogeneity of phenotypes with same mutation • contradictory results from expression of mutant channels in different cell lines • morphologically and functionally very different from cardiomyocytes

Figure 3: Overview of model systems of Brugada Syndrome

The mouse model described in this initial report was subsequently used by different groups to investigate in how far it recapitulates phenotypes observed in Brugada Syndrome patients, drug response and to examine the underlying causes of those phenotypes observed. Age- and sex-related factors in disease progression such as an increased risk of cardiac related mortality, and developing AV node conduction disorder and bradycardia in old males have successfully been replicated^{41, 42, 43}. All these studies verified the *Scn5a* heterozygous knock out mouse as a suitable system to model Brugada Syndrome.

Studies looking to recapitulate the response of Brugada Syndrome patients to pro- and anti-arrhythmic drugs showed that, compared to WT, flecainide-treated *Scn5a*^{+/-} Langendorff perfused hearts indeed reiterated the pro-arrhythmic effects of this Na_v1.5 blocker on Brugada patients⁴⁴. ECGs from anesthetized WT and *Scn5a*^{+/-} mice, recorded by Martin and co-workers⁴⁵, showed that the ventricular arrhythmias, ST segment elevation, increased transmural repolarisation gradients and abnormal conduction was accentuated in *Scn5a*^{+/-} mice by treatment with flecainide but not quinidine, a class Ia anti-arrhythmic agent. Surprisingly both flecainide and quinidine suppressed spontaneous and induced atrial arrhythmias, suggesting a different mechanism for ventricular and atrial arrhythmias⁴⁶. These studies verified the *Scn5a*^{+/-} mouse as a suitable model system for Brugada Syndrome by replicating the effects of flecainide and quinidine on Brugada Syndrome patients.

So far only one aspect of the advantages provided by a model system has been considered, namely the ability to replicate the disease phenotypes observed in patients. Another possible application of model systems is the in-depth analysis of the underlying physiological mechanisms of individual symptoms. Attempts to find the physiological basis of ventricular tachycardia, one of the main symptoms leading to sudden cardiac death, have led to two hypotheses, namely altered conduction times and repolarisation gradients.

To test these hypotheses, monophasic action potentials (MAP) were recorded from Langendorff-perfused WT and *Scn5a*^{+/-} hearts before and after administration of flecainide and quinidine^{47, 48}. MAP recordings of neighbouring epi- and endocardium from the right and left ventricle and activation latencies suggested a key role of transmural gradients rather than altered conduction times in arrhythmogenicity associated with Brugada Syndrome. Transmural gradients were accentuated in the right but not left ventricle.

The *Scn5a*^{+/-} mouse models Brugada Syndrome quite accurately concerning the impact of age and sex on the progression of the disease and drug response. *Scn5a*^{+/-} mice show an increased risk of AV node conduction disorder, bradycardia and cardiac related death in old males as well as an accentuation of the Brugada Syndrome phenotype after administration of flecainide. Using this model system, researchers have also been able to link atrial arrhythmias to Brugada Syndrome and to determine transmural gradients as the major contributor to development of VT.

1.1.2.2 *Scn5a-1798insD knock-in mice*

In addition to knocking out *Scn5a*, creating a system that models a generic Brugada Syndrome phenotype, investigators also generated a mouse strain carrying the murine equivalent of the human *SCN5A-1795insD* mutation, enabling them to investigate the effects of a specific mutation and compare them to observations made in patients. Members of a Dutch family carrying a *SCN5A-1795insD* mutation display overlap symptoms of LQT3, Brugada Syndrome and progressive cardiac conduction defects. LQT3 and Brugada Syndrome are usually associated with gain and loss-of-function mutations in *SCN5A* respectively⁴⁹. Mice carrying a *Scn5a-1798insD* mutation indeed show a similar phenotype demonstrating bradycardia, right ventricular conduction slowing and QT prolongation, confirming that a single mutation is sufficient to cause the overlap syndrome⁵⁰.

1.1.2.3 *Scn1b* knock-out mice

It is important not to forget that every model system has its restrictions. Phenotypes observed in models do not necessarily reflect those examined in patients as the example of the *Scn1b* knock-out mouse illustrated⁵¹. The knock-out of *Scn1b*, the gene encoding the beta subunit of the cardiac sodium channel $Na_v1.5$, triggered ventricular repolarisation which is not present in Brugada Syndrome patients with a *SCN1B* loss-of-function mutation. The inconsistency could either be due to differences between loss-of-function mutation and knock-out or fundamental differences in physiology relating to the species.

The heterozygous knock-out of *Scn5a* in mice generated a mouse model that accurately replicates most of the phenotypes associated with the Brugada Syndrome including sex-dependent disease progression and drug response. It also proved valuable as a tool for exploring transmural gradients as the underlying cause of VT in patients. Mice carrying the equivalent of the human *SCN5A*-1795insD mutation exhibited a phenotype similar to the human phenotype, confirming that a single mutation is sufficient to cause an overlap of Brugada Syndrome and LQT3.

1.1.2.4 *Strengths and limitations of the murine model*

The advantage of using a model organism rather than a single cell expression system is that a mutation of interest can be investigated in its physiological environment and during different developmental stages. The effect of $Na_v1.5$ depletion on the morphology of ventricles for example would not have become apparent in an expression system. However, despite giving valuable insight into the Brugada phenotype, the cardiac electrophysiological characteristics of mice and humans are markedly different as exemplified by studies using the *Scn1b* knock-out mice. In addition to being expensive, two major limitations of this model system remain. Firstly, research at the molecular level is restricted by the limited life-span of isolated cardiomyocytes in culture. Secondly, the murine model only allows for

investigations of known genetic causes and has this far been restricted to *SCN5A* mutations which make up for only 11-28% of all Brugada Syndrome cases⁵².

1.1.3 Porcine model

Recently, a large-animal porcine model was developed to model *SCN5A* mutations. Pigs carrying the porcine equivalent of the human nonsense mutation *SCN5A-E555X*, previously identified in a patient with Brugada Syndrome, were generated and their hearts Langendorff perfused and investigated⁵³. Their hearts are similar to those of humans in terms of structure and function, and in this model showed no structural abnormalities, but conduction slowing and an increased susceptibility to ventricular arrhythmias accurately modelling aspects of the human disease phenotype.

1.1.4 Canine Model of Brugada Syndrome

Almost all experiments utilizing the canine model for Brugada Syndrome are based on arterially perfused wedges of canine left or right ventricles rather than a whole heart. These are then treated with drugs to induce the Brugada phenotype¹⁸. Over the years and depending on the group different drugs have been used to cause the Brugada phenotype, all of which are either sodium channel blockers (e.g. pilsicainide⁵⁴), calcium channel blockers (e.g. verapamil⁵⁵) or potassium channel openers (e.g. pinacidil⁵⁶) and are administered either alone or in combination (Figure 3). These induced systems are then exploited in order to investigate the underlying electrophysiological cause of the abnormalities observed on the electrocardiogram in Brugada Syndrome.

1.1.4.1 J-wave/Osborne wave

The J-wave, also called Osborne wave, is a positive deflection located between the QRS and ST segment in an ECG (Figure 1) and is, among others, found in patients at

risk of developing ventricular fibrillation, such as Brugada Syndrome patients. The drug induced canine heart preparation was first suggested as a suitable model system for the Brugada Syndrome in 1996, when Yan and Antzelevitch investigated the underlying cause of the J-wave¹⁸. Transmembrane action potential (AP) recordings suggested a voltage gradient across the ventricular wall as the underlying cause of the J-wave. Similar results could be achieved by cooling of the right ventricular outflow tract (RVOT) in test-subjects⁵⁷, providing a possible *in vivo* model.

1.1.4.2 ST segment elevation

In an ECG of a Brugada patient the ST segment elevation is the most striking feature and is one of the criteria used for diagnosis of Brugada Syndrome (Figure 1). Several groups have pursued investigations to find the electrophysiological alterations that lead to ST segment elevation. The ST segment of an ECG represents the time between depolarisation and repolarisation of the ventricles.

Yan and Antzelevitch used flecainide and acetylcholine to induce Brugada Syndrome in a canine model, proposing that ST segment elevations are caused by the same transmural voltage gradient across the epicardial RV wall that causes the J-wave^{18, 58}. The transmural voltage gradient across the epicardial RV wall is caused by a depression of the AP dome. Their results also indicated that phase 2 re-entry (P2R) could cause extrasystolic activity in the RV wall which could serve as a substrate for VF/VT. ST segment elevation had previously been linked to electrical heterogeneity in the recovery phase, a substrate for P2R⁵⁴. Further experiments have shown that repolarisation abnormalities associated with ST segment elevation are more precisely located in the RVOT in both patients and model system^{59, 60}.

In conclusion, while transmural dispersion of repolarisation leads to ST segment elevation in the ECG, dispersion of repolarisation in the epicardium of the RV causes P2R with extrasystoles that can degenerate to VF/VT, the main cause of sudden cardiac death in Brugada Syndrome patients.

1.1.4.3 T-Wave alternans and VF/VT

Another feature of the Brugada phenotype associated with loss of the action potential dome, besides J-waves and ST segment elevation, is T-wave alternans (TWA). TWA is a beat to beat variation in amplitude, polarity and morphology of the T-wave in an ECG which in patients has been associated with an increased risk of ventricular arrhythmias. Morita et al. were the first to describe its electrophysiological foundation and showed that it is at least in part caused by the same increased dispersion of repolarisation that causes ST segment elevation⁶¹. Recently Fish and Antzelevitch showed that TWA shares another feature with ST segment elevation. The results from an arterially perfused RV wedge preparation induced with verapamil, a sodium and calcium channel blocker, indicate that TWA could be caused not only by an AP dome loss but also a concealed P2R which both lead to transmural dispersion of repolarisation which could trigger VF/VT⁶². This study used verapamil to induce Brugada Syndrome by blocking calcium and sodium channels, but this drug is only recognized for its calcium channel blocking properties. Even though both the heterozygous loss of either the cardiac sodium or calcium channel causes Brugada Syndrome, there are phenotypic differences between them⁶³. This questions the applicability of the data gathered from model systems using a combined sodium/calcium channel block approach.

To sum up, T-wave alternans is a feature of the Brugada Syndrome that appears to have the same electrophysiological basis as ST segment elevation, namely P2R and loss of AP dome, leading to an increased risk of VF/VT. In addition, the probability of developing ventricular arrhythmias at certain heart rates is not only influenced by mutations in different channels but there is also a notable temperature component. Following the observation that ventricular arrhythmias are promoted by fever in BrS patients Morita and co-workers conducted experiments looking at the effects of hyperthermia and hypothermia on functional dynamics and spatial heterogeneity of RV electrophysiological activity. AP recordings of the hypothermia model showed spontaneous activation triggered by prolongation and increased dispersion of AP duration. Recordings of the hyperthermic system, modelling fever, exhibited shorter AP durations causing premature ventricular activations and reentrant VT⁶⁴.

1.1.4.4 Sex differences

One curious aspect about Brugada Syndrome is that even though mutations causing the disorder are equally inherited by males and females, males are 8-10 times more likely to develop symptoms⁶⁵. Canine epicardium preparations have shown a smaller transient outward potassium current (I_{to}) density in females compared to males, which could protect them from developing Brugada Syndrome but make them more prone to progressive conduction problems when inward currents like I_{Na} are compromised⁶⁶. Another study showed that I_{Na} amplitude in the LV epicardium of females is smaller compared to males and that testosterone modulates this amplitude⁶⁷. This could put females at a higher risk of developing arrhythmias in the LV, a feature found in LQTS, and explain why the incidence of arrhythmias related to LQTS is lower in males than females.

1.1.4.5 Prediction of high risk patients and treatment

Even though discovering the mechanisms which lead to ventricular arrhythmias is important, the ultimate goal remains to apply the gathered knowledge to improve methods for diagnosis, prediction of high risk patients and treatment.

Investigations of conduction abnormalities, such as right bundle branch block, led to the discovery of fragmented QRS (f-QRS) as a new marker for Brugada patients with a high risk of syncope and developing spontaneous VF⁶⁸. Fragmented QRS are conduction abnormalities within the QRS complex and can manifest as multiple spikes in the QRS complex of an ECG. In terms of treatment, most strategies aim at preventing sudden death caused by ventricular arrhythmias rather than treating the underlying cause, loss of sodium channel function. Recently, using the canine model, researchers were able to show that a more focused application of radiofrequency catheter ablation (RFCA) to the epicardium might be more efficient in eradicating VTs in Brugada Syndrome patients⁶⁹.

These examples illustrate how the canine model system could help not only to find new, easy to measure, markers for high risk patients, but also suggest possible improvements for established treatments.

Canine preparations have proven to be a useful system for modelling Brugada Syndrome. Not only have they linked J-waves, ST segment elevation and T-wave alternans to a depression of the action potential dome, they were also instrumental in determining that a lower I_{to} density in females compared to males, could protect them from developing Brugada Syndrome. In addition, the canine model helped reveal f-QRS as a new marker for high risk patients and suggested an improved method of using RFCA to treat VT in Brugada Syndrome patients.

1.1.4.6 Strengths and limitations of the canine model

The main advantages of having a heart preparation are that cells in epi- and endocardium can be investigated, and that they remain in their natural environment.

The most obvious limitation of this system is that the Brugada Syndrome phenotype is drug induced. Combinations of sodium and calcium channel blockers and/or potassium channel openers have been used, even though the majority of patients only carry one mutation and experiments have shown subtle differences in phenotypes depending on which channel is bearing the mutation. Because the Brugada Syndrome phenotype is drug induced, drug screening is limited not only due to possible interactions with the channel blocking agent but also because mutations underlying Brugada Syndrome may be more complex than simple loss-of-function modelled by a drug induced Brugada Syndrome phenotype. Unfortunately, it also does not allow for investigations of either atypical Brugada Syndrome patients with no mutation but a Brugada phenotype, or vice versa.

1.1.5 Expression systems modelling Brugada Syndrome

Experiments using expression systems aim at deciphering the biophysical properties of single cells, which can give clues to understand the underlying molecular mechanisms of Brugada Syndrome. Plasmids carrying mutations identified in Brugada Syndrome patients are mainly transfected into either tsA201 cells or *Xenopus* oocytes. *Xenopus laevis* (frog) oocytes are rather large, about 1mm, and cheap to maintain and manipulate; both of which make them a desirable tool for electrophysiological experiments. tsA201 cells are immortalised Human Embryonic Kidney (HEK) 293 cells. Comparative experiments quickly showed that results from both expression systems were, depending on the mutation, contradictory. Employing expression systems, investigators have been able to study biophysical consequences of Brugada Syndrome associated mutations, which generally lead to reduced net sodium current, due to altered $Na_v1.5$ properties or complete loss of I_{Na} . Expression systems have also been used to study double mutants and mutations in genes other than *SCN5A* that have been associated with the Brugada Syndrome phenotype. Since the focus of this literature review is to discuss the strengths and limitations of model systems, only a few selected studies will be used to highlight the main identified mechanisms through which mutations can cause Brugada Syndrome.

1.1.5.1 Altered $Na_v1.5$ properties

Three mechanisms have been proposed to explain how the channel's altered function can lead to the cardiac dysfunction. The first mechanism, a shift in steady-state activation and/or inactivation curve, was suggested after studying 1795insD. The insertion of an aspartic acid after position 1795 (1795insD) was discovered after screening a large family with members exhibiting symptoms of both Brugada and LQT3 syndrome. Indeed, altered $Na_v1.5$ function can lead to other cardiovascular disorders besides Brugada Syndrome, as well as overlap syndromes⁷⁰. Expression of 1795insD in *Xenopus* oocytes and tsA201 cells revealed a negative shift of the steady-state inactivation curve and positive shift of the steady-state activation curve^{71, 72}. Studies on other mutations revealed that the shift of activation and

inactivation curves can be towards more negative or positive voltages, and can occur together or separately. These alterations in channel properties would result in a reduction of action potential amplitude, which is in accordance with the heterogeneity of repolarisation across the ventricular wall observed in the canine model of Brugada Syndrome. A residual sodium current, only detected in tsA201 cells but not *Xenopus* oocytes, was hypothesised to cause long QT intervals and explain symptoms of LQTS in individuals carrying this insertion⁷². Examination of other mutations found to cause both LQT3 and Brugada Syndrome in carriers revealed the same biophysical mechanism⁷³. Observing that two mutations, A735V and R1192Q⁷⁴, found in families with sudden unexplained nocturnal death syndrome (SUNDS) resulted in the same shift in activation and inactivation curve led to the conclusion that Brugada Syndrome and SUNDS are the same disorder⁷⁴.

After studying 1795insD in tsA201 cells, Veldkamp et al. proposed a second mechanism⁷⁵ in addition to the change of voltage dependence of activation and inactivation described above. They suggested that some mutant channels enter an intermediate state of inactivation from which they recover relatively slower than WT channels. Prolonged recovery from inactivation that could lead to arrhythmias in Brugada patients⁷⁶ was also described as the underlying mechanism for Na_v1.5 carrying the T1620M mutation. These results were however restricted to expression in tsA201 cells whereas *Xenopus* oocytes transfected with the same mutation showed the opposite phenotype⁷⁷.

Lastly, mutations can alter the time-dependence of steady-state inactivation resulting in accelerated or decelerated inactivation^{78, 79}. Whereas a faster current decay reduces the net sodium current, a feature linked to Brugada Syndrome, slower current decay is generally associated with LQT3 and appears in Brugada Syndrome patients in combination with reduced peak current or current window due to shifts in activation and/or inactivation curves^{78, 80}.

In summary, these investigations showed that there are three mechanisms by which altered properties of mutant Na_v1.5 cause Brugada Syndrome. The first mechanism, a

shift of the activation and/or inactivation curves, is consistent with reduced action potential durations. This generates transmural heterogeneity of repolarisation between the epicardium and endocardium across the ventricular wall causing ST segment elevations in the ECG. The second mechanism, enhanced intermediate/slow inactivation, results in reduced I_{Na} . The third mechanism, accelerated inactivation, reduces the net sodium current.

1.1.5.2 Complete loss of I_{Na}

Rather than altering channel properties, mutations can also result in a complete loss of current. Both trafficking defects and truncated proteins have been linked to loss of function of $Na_v1.5$ in Brugada Syndrome patients, and again, depending on the mutation, expression in *Xenopus* oocytes and tsA201 cells gives rise to contradictory observations.

One such example is R1432G, which lead to completely abolished functional expression in tsA201 cells while producing reduced sodium current when expressed in *Xenopus* oocytes. Mutant channels in tsA201 cells were shown to be localised in the endoplasmic reticulum⁸¹ exposing disrupted cell-surface localisation of $Na_v1.5$ as one of the mechanisms underlying Brugada Syndrome.

Besides disruption of protein transport to the cell membrane, Brugada Syndrome has also been linked to expression defects. Some mutations found in Brugada patients, such as E473X and N1774+12X, produce truncated proteins and hence no detectable sodium current⁸². When these mutant channels were heterozygously expressed with WT channels, a 50% reduction of sodium current was detected. However, unlike channels whose function has been altered by a mutation, no effects on activation or inactivation curves or on their kinetics were reported⁸³.

1.1.5.3 Induced Brugada Syndrome

Expression systems have been also used to study the effects of external factors on the behaviour of mutant $\text{Na}_v1.5$. For example, functional expression of $\text{Na}_v1.5$ carrying the G1740R mutation appears to depend on the temperature at which the currents are recorded. Expression in tsA201 generated no currents at 37°C, whereas at 22°C macroscopic sodium currents could be detected⁸².

Beside temperature sensitivity, mutations in *SCN5A* have also been shown to cause drug induced Brugada Syndrome. In rare cases, a mutation in *SCN5A* can cause a Type 1 Brugada Syndrome phenotype with ST segment elevation after administration of lidocaine. A double mutation, V232I+L1308F, was identified in a patient exhibiting lidocaine induced Brugada Syndrome⁸⁴. WT and mutant channels expressed in tsA201 exhibited similar current-voltage relationships but the maximum current was reduced in cells expressing the double mutation after lidocaine administration. A slower recovery from inactivation and a shift of steady-state inactivation towards more negative voltages after lidocaine treatment was also observed, resulting in manifestation of the Brugada phenotype⁸⁴. The additive effects of both mutations appear to sensitize the sodium channel to lidocaine. This study therefore suggests that caution should be exerted when treating patients carrying said mutation with Class I anti-arrhythmic drugs.

Certain drugs can also not only trigger symptoms in people with an unidentified mutation but cause a non-genetic form of Brugada Syndrome. These drugs include medication used to treat some forms of arrhythmia, angina, high blood pressure, depression, and other mental illnesses. Hypercalcemia, hyperkalaemia as well as hypokalaemia have also been associated with acquired Brugada syndrome.

1.1.5.4 Other genes associated with Brugada Syndrome

Mutations in *SCN5A* account for the majority (11-28%) of Brugada Syndrome cases with a defined genetic cause⁵². Nonetheless, mutations in other channels, or channel regulatory proteins, have also been linked to the Brugada Syndrome albeit at smaller percentages. Thus far, mutations in 16 other genes have been found through screenings of patients¹⁵. These include genes encoding for the L-type calcium channels $Ca_v1.2$ (*CACNA1c*) and $Ca_v\beta2b$ (*CACNB2b*)^{85, 86}, glycerol-3-phosphate dehydrogenase 1-like enzyme (*GPD1L*)⁸⁷, beta-subunits of the sodium channel (*SCN1B*⁸⁸, *SCN2B*⁸⁹, *SCN3B*⁹⁰) and MiRP2 (*KCNE3*)⁹¹, among others. However, only a few have been functionally studied. Mutations in *SCN2B*, *SCN3B*, *SCN1B* and *GPD1L* have been shown to cause a reduction in sodium current, in some cases due to disruption in trafficking of $Na_v1.5$ to the cells surface⁹². Also, a mutated MiRP2 has been reported to trigger an increased I_{to} intensity⁹¹. Two mechanisms have been associated with mutated *CACNA1c* or *CACNB2b* found in Brugada patients, and while both result in loss of function, one is caused by reduction of L-type calcium current, the other one triggers accelerated inactivation of calcium current⁸⁵. Table 2 gives an overview of some of the mutations in genes other than *SCN5A* that have been found in patients with Brugada Syndrome. A more detailed description of the various Brugada Syndrome subtypes can be found in the Nielsen et al. review¹⁵.

Mutations associated with Brugada Syndrome are found in ion channels and proteins that regulate ion channel function. Gain- or loss-of-function mutations in these genes can affect the resting membrane potential, or can directly or indirectly lead to changes in depolarisation or repolarisation dynamics during action potential propagation. Like loss-of-function mutations in *SCN5A* these alterations lead to decreased action potential domes or action potential durations resulting in the characteristic electrophysiological Brugada Syndrome phenotype. In affected people without an identified gene mutation, the cause of Brugada syndrome is often unknown but could include mutations in as of yet unidentified regulatory proteins or promotor regions.

To sum up, investigators found four mechanisms by which mutations in *SCN5A* cause Brugada Syndrome. They can alter biophysical properties of $\text{Na}_v1.5$ by firstly causing shifts of steady-state activation and/or inactivation curves, secondly enhancing intermediate/slow inactivation or thirdly accelerate inactivation. Lastly, mutations can result in a complete loss of function by producing truncated proteins or disrupting trafficking to the cell surface. Expression systems have also been utilized to examine the functional effects of a double mutant that puts its carriers at risk of developing VF if treated with lidocaine due to altered $\text{Na}_v1.5$ -lidocaine binding, as well as to study mutations in other genes and their possible role in Brugada Syndrome.

Table 2: Genes other than *SCN5A* associated with Brugada Syndrome

Subtype	Affected gene	Affected protein	Ionic current	AA substitution	Functional effect	Ref.
2	<i>GPD1-L</i>	G3PD1L	I_{Na}	A280V	↓	34
3	<i>CACNA1C</i>	$Ca_v1.2$	I_{Ca-L}	A39V	↓	86
				G490R	↓	
				E1115K	↓	
				R1880Q	↓	
				V2014I	↓	
4	<i>CACNB2</i>	$Ca_v\beta2$	I_{Ca-L}	D2130N	↓	86
				S481L	↓	
				T11I	↓	
				S143F	↓	
				L399F	↓	
				T450I	↓	
				D538E	↓	
V340I	N/A					
E499D	N/A					
5	<i>SCN1B</i>	$Na_v\beta1$	I_{Na}	W179X	↓	88
				R214Q	↓	
				H162P	N/A	
				Q204R	N/A	
6	<i>KCNE3</i>	MiRP2	I_{to}/I_{Ks}	R99H	↑	91
7	<i>SCN3B</i>	$Na_v\beta3$	I_{Na}	L10P	↓	90
				V110I	↓	
8	<i>KCNH2</i>	hERG1	I_{Kr}	G873S	↑	93
				N985S	↑	
				R1135H	↑	
9	<i>KCNJ8</i>	Kir6.1	I_{KATP}	S422L	↑	94
10	<i>CACNA2D1</i>	$Ca_v\alpha_2\delta-1$	I_{Ca-L}	D550Y	N/A	95
				S709N	N/A	
				Q917H	N/A	
11	<i>RANGRF</i>	MOG1	I_{Na}	E83D	↓	35
12	<i>KCNE5</i>	MiRP4	I_{to}/I_{Ks}	Y81H	↑	96
				D92E; E93X	↑	
13	<i>KCND3</i>	$K_v4.3$	I_{to}	L450F	↑	97
				G600R	↑	
14	<i>HCN4</i>	HCN4	I_f	S841L	N/A	98
15	<i>SLMAP</i>	SLMAP	I_{Na}	V269I	↓	99
				E710A	↓	
16	<i>TRPM4</i>	TRPM4	NSC _{Ca}	R144W	N/A	100
				A432T	↑	
				G555R	N/A	
				G582S	N/A	
				F773I	N/A	
				P779R	↓	
17	<i>SCN2B</i>	$Na_v\beta2$	I_{Na}	T873I	↑	101
				D211G	↓	

↓ – Loss-of-function; ↑ – Gain-of-function; N/A – not available

1.1.5.5 Strengths and limitations of expression systems

Of all three presented model systems, expression systems are the only ones investigating the molecular mechanism of mutations found in patients rather than looking at manifestations of generic *SCN5A* knock-out or drug induced $\text{Na}_v1.5$ block. Cell-based model systems are inexpensive and relatively easy to maintain and manipulate. Although 17 genes have been associated with Brugada Syndrome, the genetic cause for two thirds of all patients remains unidentified. That limits this model system to examination of known genetic causes and it also gives no insight into the heterogeneity of phenotypes between family members carrying the same mutation, some developing Brugada Syndrome and others not. One major issue remaining is the contradictory results from expression of mutant channels in different cell lines. Even though tsa201 cells expressing $\text{Na}_v1.5$ generate sodium currents, these cells are morphologically and functionally very different from cardiomyocytes.

Despite the fact that all three model systems have helped understand the molecular basis for certain features they have obvious limitations. The main restriction for all model systems so far remains, that they can only model cases in which the underlying genetic alteration is identified. However, only approximately one third of all Brugada patients carry a known mutation¹⁰². These model systems also fail to deliver explanations for or a way to investigate mutation carriers who show no symptoms.

A new model system based on the generation of induced pluripotent stem cell-derived cardiomyocytes offers a unique chance to overcome the above stated limitations and allow investigations none of the other systems would.

1.2 Induced pluripotent stem cell-derived cardiomyocytes

1.2.1 Induced pluripotent stem cells

The ground breaking work that led to the discovery of iPS cells was based on decades of research into ES cells, nuclear fusion and cloning. When in 1958 the transplantation of a somatic *Xenopus* nucleus into an unfertilised *Xenopus* oocyte led to the development of a sexually mature individual¹⁰³ it provided the first evidence that fully differentiated nuclei contained the same genetic information as ES cells and that if exposed to appropriate stimuli it can be reprogrammed to an undifferentiated ES-like state. Based on this and according observations in mammalian cells¹⁰⁴ Takahashi and Yamanaka hypothesised that the reprogramming effects of oocyte and ES cell cytoplasm could be mimicked by the expression of a small number of ES cell-specific genes. The initial experiments identified 24 candidate genes that, when delivered using retroviral vectors, were able to reprogramme mouse fibroblasts to induced pluripotent stem (iPS) cells¹⁰⁵. Further investigations limited the number of factors essential for reprogramming to the so called 4 Yamanaka factors: Oct-4, Klf4, Sox2 and c-Myc. The resulting iPS cells expressed pluripotency markers and gave rise to teratomas containing all three germ layers when transplanted into immunodeficient mice. Even after loss of transgene expression through gene silencing the reprogrammed cells maintained their pluripotency, indicating that transient over-expression of exogenous factors was sufficient to activate endogenous expression of pluripotency genes. Although retroviral vectors are an efficient delivery system for the reprogramming factors concerns were raised about the long-term effects of random genetic integration and possible re-activation of transgenes. Genetic alteration could influence differentiation into specific cell lineages¹⁰⁶ and re-activation in particular of oncogenes Klf4 and c-Myc led to tumour formation in 20% of the offspring of adult chimeras¹⁰⁷. Only a year after the first reported generation of murine iPS cells it was demonstrated that human fibroblasts could be reprogrammed to iPS cells at a relatively high efficiency (0.1%) using retroviral vectors carrying the original 4 factors^{108, 109}. Like murine iPS cells human iPS cells expressed markers of pluripotency and were able to form all three germ layers *in vitro* as well as *in vivo*.

1.2.2 Improvements of retroviral reprogramming efficiency

Having demonstrated that human somatic cells can be reprogrammed to iPS cells, investigators quickly began researching non-integrating delivery systems and non-oncogenic transcription factors to not only make iPS cell lines more stable but eventually clinically relevant. It was shown that mouse and human fibroblast could be reprogrammed using only three of the original four factors (Oct-4, Sox2 and Klf4) although the process took longer in the absence of c-Myc¹¹⁰. Alternatively, transcription factors for oncogenes Klf4 and c-Myc could be completely replaced by transcription factors for non-oncogenic Lin28 and Nanog with no negative impact on reprogramming efficiency or outcome¹⁰⁶.

One approach to increase reprogramming efficiency was to combine the original 4 Yamanaka factors with additional factors such as human telomerase (hTERT) and SV40 large T antigen¹¹¹ or p53 siRNA and Undifferentiated embryonic cell transcription factor 1 (UTF1)¹¹². The addition of the latter two increased efficiency 100-fold even in absence of c-Myc. Another approach was the use of small molecules that could not only improve efficiency but also replace certain transcription factors¹¹³. Indeed, recent reports showed that small molecules alone are sufficient to generate murine iPS cells¹¹⁴ and only require addition of Oct-4 to successfully reprogramme human fibroblasts to iPS cells¹¹⁵. Although the mechanisms by which small molecules such as valproic acid¹¹⁶ support reprogramming are not always understood it appears that most are associated with chromatin remodelling.

1.2.3 Alternative reprogramming techniques

To overcome the obstacle of potentially gene-disrupting integration of transgenes into the host genome associated with retroviruses several other reprogramming methods were explored including non-integrating viruses, excisable transposons and DNA-free techniques.

An example of a non-integrating viral reprogramming system is the adenovirus which has been used to derive both murine¹¹⁷ and human¹¹⁸ iPS cells. In spite of having the advantage of targeting dividing as well as non-dividing cells the adenoviral delivery system was associated with very low reprogramming efficiency. Similarly inefficient was a completely virus-free reprogramming technique employing transient transfection with non-integrating plasmids derived from the Epstein-Barr virus and was originally only able to generate murine iPS cells¹¹⁹. It became a tool for reprogramming of human fibroblasts after changing the delivery system to non-integrating episomal vectors encoding for Lin28, Nanog and SV40 large T antigen in addition to the Yamanaka factors¹²⁰ but even after these modifications efficiency remained very low.

Instead of preventing integration of transgenes altogether they can be transiently integrated for the duration of reprogramming. Excisable transposons are delivered with the PiggyBac technique, a gene delivery system that allows for temporary integration into the host genome with subsequent excision^{121, 122}. The PiggyBac transposon vector encodes for a cassette of all 4 Yamanaka factors linked by 2A peptides and is flanked by inverted terminal repeat sequences. PiggyBac transposase, co-transfected with the transposon vector, recognises these sequences and mediates the relatively random integration of the transposon into the host genome. Once target cells have been reprogrammed transposons can be excised by simply re-transfecting generated iPS cells with the transposase expression vector.

In 2009 an entirely transgene-free technique was developed wherein human fibroblasts were reprogrammed using recombinant proteins¹²³. Cell extracts from 4 HEK293 cell lines, each expressing one of the 4 Yamanaka factors fused to a cell-penetrating peptide, were applied to target cells once a week for 6 weeks. Although a promising transgene alternative, the very low reprogramming efficiency and technical challenges suggested that further optimisation might be necessary.

A different and more efficient transgene-free technique was developed a short time later wherein human fibroblasts were reprogrammed using synthetic mRNAs¹²⁴.

Oct-4, Sox2, Klf4, c-Myc and Lin28 mRNAs were synthesised and modified *in vitro* to counteract their relative instability and susceptibility to degradation. Successful reprogramming still required daily transfections for up to 17 days with colonies usually appearing around day 20 with an efficiency of 0.0001%.

1.2.4 iPS cell-based model systems

Cutting edge research by Yamanaka and colleagues provided an alternative for ethically difficult hES cell work and has already proven its utility in disease modelling. The great advantage of this technique is that skin cells carrying the desired genetic profile can be obtained directly from the patient, reprogrammed and differentiated to the specific tissue that is affected by the disease. This technique allows investigators to study the mutant proteins in their native environment including all modifier proteins independent of whether the genetic alteration is known or not. The earliest proof of principle generation of patient-specific iPS cell lines, including Duchenne muscular dystrophy, Parkinson disease and Huntington disease, was reported by Park et al. in 2008¹²⁵. This study did however not include any disease modelling characterisation of specific cell lineages involved in disease progression. To date several cardiac disorders including LQT1¹²⁶, LQT2¹²⁷ and Timothy syndrome¹²⁸ have been modelled using the iPS cell approach (Figure 4). Although there are no studies looking at classical Brugada Syndrome phenotypes, Davis et al. recently derived cardiomyocytes from patients carrying the *SCN5A*-1795insD mutation¹²⁹. *SCN5A*-1795insD causes Brugada Syndrome/LQT3 overlap symptoms and, as described above, had previously been studied in both mouse model and expression systems. The patient-specific iPS cell-derived cardiomyocytes recapitulated the decreased I_{Na} peak and persistent I_{Na} associated with Brugada Syndrome and LQT3 respectively.

iPS cells based cardiac disease model system

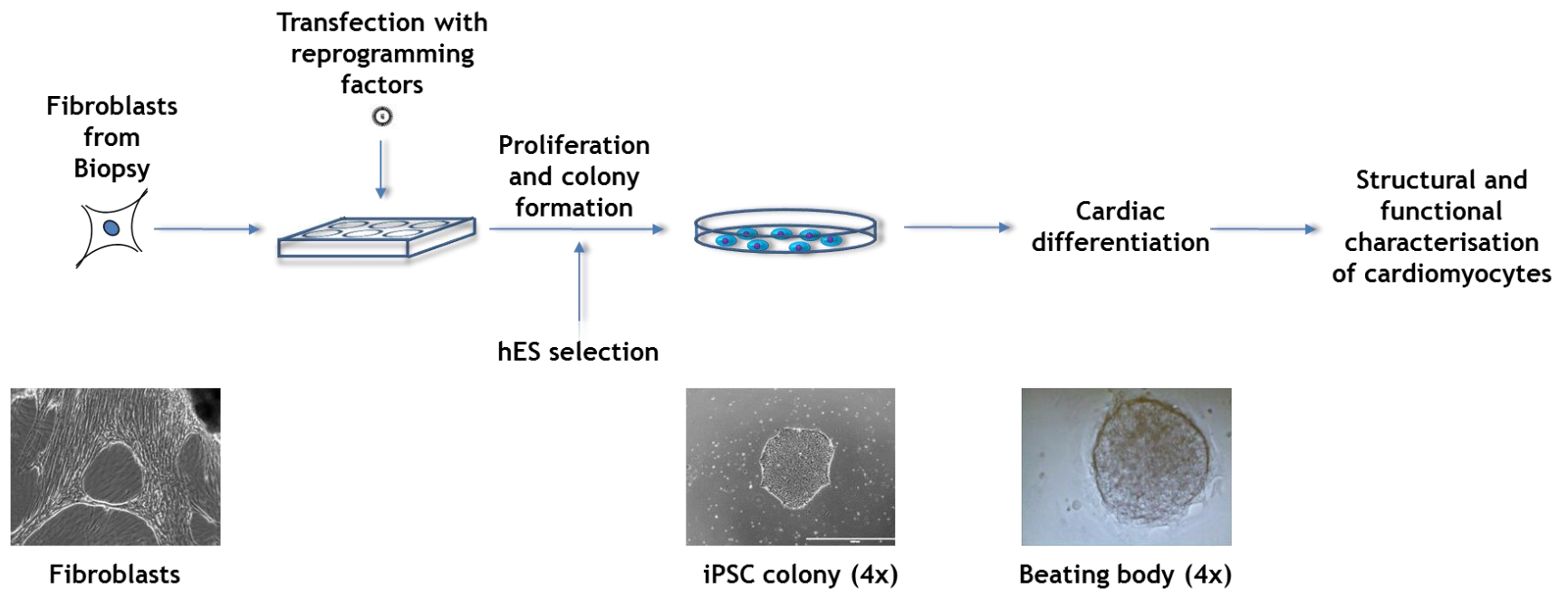


Figure 4: Schematic of an iPS cell based model system to model an inherited cardiac disease

1.2.5 Cardiac differentiation of iPS cells

Before the development of reliable *in vitro* cardiac differentiation protocols, researchers transplanted undifferentiated mouse ES cells directly into the myocardium of infarcted and healthy control mice to test their regenerative capabilities. Their hypothesis was that the cardiac environment such as the extracellular matrix and factors released by cardiomyocytes would be sufficient for cardiac differentiation and maturation of those ES cells. What they found however was that transplanted ES cells quickly and consistently formed cardiac teratomas that contained no more cardiomyocytes than teratomas formed in the hind-limb control¹³⁰. These findings suggested that transplantation of *in vitro* differentiated cardiomyocytes might be required to prevent teratoma formation and for cardiac repair to be successful. Other important aspects to consider, if attempting to make pluripotent stem cell-derived cardiomyocytes clinically relevant, were developing a differentiation protocol that was not only scalable but also modifiable to be Good manufacturing practice (GMP) compliant.

Over the years a variety of cardiac differentiation protocols have been published using first hES cells and later also iPS cells. All protocols can be clustered into three categories: unguided differentiation, co-culture with END-2 cells and guided differentiation.

1.2.5.1 Unguided differentiation

Unguided cardiac differentiation is the technically easiest and most inexpensive of the three protocols requiring no additional supplements in form of growth factors or small molecules to be added to the culture medium. Undifferentiated pluripotent stem cells are simply lifted and transferred into ultra-low attachment plates with differentiation medium containing serum. Ultra-low attachment plates prevent adherence in response to which hES and iPS cells form three dimensional aggregates called embryoid bodies (EBs) and this aggregation process itself initiates differentiation. After several days in suspension, EBs are plated onto a matrix such as

gelatine or poly-L-lysine that promotes attachment and further differentiation. Spontaneous differentiation of EBs into contractile cardiac muscle was first observed during investigations into the general differentiation potential of hES cells *in vitro*¹³¹ and was subsequently shown to also occur in EBs derived from iPS cells¹³². Cells within these contracting clusters exhibited structural and functional properties of cardiomyocytes¹³³. Like in embryogenesis cardiac cells are among the first cells to be formed and contracting EBs or beating bodies appear as early as a few days after plating. Cells within an embryoid body spontaneously differentiate into cells from all three germ layers and cell-to-cell interactions with cells differentiating towards endoderm appear to be sufficient to drive differentiation of adjacent cells towards mesoderm and further towards a cardiac commitment¹³⁴. In the original protocol, EBs were generated by simple mechanical disruption of undifferentiated pluripotent stem cells, resulting in beating bodies that differed in size as well as the percentage of cardiomyocytes they contained. Because in this setting the composition of cells within an EB is not externally guided differentiation is random and therefore the number of beating bodies generated is subject to great variability. In addition to relatively low efficiency of overall <10% beating bodies and <1% cardiomyocytes¹³³, unguided differentiation shows great inter-line variability. Efforts to make EB formation more consistent with regard to size and morphology were successful using hanging-drop¹³⁵, forced aggregation^{136, 137} or micro-contact printing¹³⁸ methods but had only limited effect on differentiation efficiency or variability¹³⁷. Some of the initial difficulties with these techniques are likely attributable to the fact that the size of forced aggregates was originally optimised for haematopoietic rather than cardiac differentiation which might differ with respect to optimal aggregation size. Comparison of EBs from 4 hES cell lines generated through forced aggregation showed inter-line variability not only with respect to cardiac differentiation potential (1%-10%) but also EB growth. The idea of forced aggregation as a means to limit variability and increase efficiency was taken up again years later in connection with a guided cardiac differentiation protocol¹³⁹. Over time, media supplements as well as external culture conditions were altered to improve efficiency. Regular foetal calf serum (FCS) was substituted for HyClone FCS and 5-azacytidine, a known cardiogenic factor in differentiation of murine cell lines¹⁴⁰, was added in a

time-dependent manner¹⁴¹. These changes increased efficiency to up to 70% in hES cells but did not succeed in reducing variability¹⁴¹. Culturing EBs under dynamic conditions (stirred suspension) was shown to almost double beating body formation efficiency to 50% when comparing EBs generated through mechanical disruption to micro-contact printing¹³⁸. Hypoxia (4% compared to 20% oxygen tension) tested in the same study had no significant effect on efficiency. Electrical stimulation resulting in an increase in reactive oxygen species has also been hypothesised to play a role in cardiac differentiation of hES cells¹⁴². Despite its great inter-line variability and relatively low efficiency, unguided differentiation is still widely used owing to its simplicity and low costs.

1.2.5.2 Co-culture differentiation

As established above, spontaneous cardiac differentiation is not very efficient as well as highly cell line-dependent. In order to reduce variability and to induce cardiac differentiation in cell lines seemingly incapable of spontaneously differentiating towards cardiac lineages, a protocol inspired by embryogenesis was developed. During embryogenesis, proximity of visceral endoderm is sufficient to induce cardiac lineage specification of adjacent mesoderm^{143, 144}. Simulating these conditions *in vitro*, both mouse embryonic carcinoma and mouse ES cells formed spontaneously contracting cardiac muscle when co-cultured with a mouse visceral-endoderm-like cell line (END-2)¹⁴⁵. Later, END-2 cells were shown to have similar cardiogenic effects on both hES and iPS cells^{146, 147}. Undifferentiated pluripotent stem cells were plated onto growth-arrested END-2 cell replacing mouse embryonic fibroblasts (MEFs) as feeders and cultured for up to 6 weeks in medium containing serum. Under these conditions beating areas formed even from cell lines that did not spontaneously undergo cardiac differentiation using the unguided protocols. Efficiency however was difficult to compare to previous protocols since it was presented as the percentage of wells of a 12-well plate containing beating areas. The total number of cardiomyocytes in a 12-well plate on day 12 of differentiation was increased almost 40-fold when hES and END-2 cells were co-cultured in serum-free conditions with 10^{-4} M ascorbic acid added to differentiation medium¹⁴⁸. The

inhibitory effect of serum was shown to be concentration dependent and similar using either serum or serum-replacement.

Further improvement of the protocol was driven by efforts to make it easier scalable as well as more efficient. Graichen et al. showed that the cardiogenic potential of END-2 cells was co-culture independent and likely stemmed from a soluble factor released by the cells into the medium¹⁴⁹. EBs were generated from three hES cell lines in serum-free medium overnight and subsequently cultured in suspension in serum-free END-2 conditioned medium (END-2 CM). When assessed on day 12 of differentiation suspension culture in END-2 CM resulted in 50% beating bodies. Analysis of gene expression of EBs throughout differentiation showed rapid up-regulation of mesodermal genes normally expressed in the primitive streak. A small molecule screen identified two p38 MAPK inhibitors (SB203580, SB202190) that significantly increased differentiation efficiency when added at concentrations <10 μ M from the beginning of differentiation. The mechanism by which they act is not well understood but p38 MAPK signalling has been shown to be activated during neuroectoderm formation¹⁴⁹. It appears as if SB203580 enhances mesoderm induction but it has no inhibitory effects even if present for the entire period of differentiation. Addition of SB203580 to END-2 CM increased beating body formation from ~50% to ~71% and total cardiomyocyte numbers from 10% to 20%. Although on average more efficient, the protocol still showed considerable variability in efficiency between cell lines and technical replicates.

The final change to the co-culture protocol was made with the aim of developing a xeno-free alternative, thereby making it compatible with the GMP and possibly clinically relevant. Comparative gene expression analysis of END-2 and a related but non-cardiogenic cell line showed up-regulation of two key enzymes of the prostaglandin I₂ (PGI₂) synthesis pathway in END-2 cells¹⁵⁰. In accordance with that, END-2 CM contained PGI₂ at levels 6-10 fold higher than control CM. EBs from two hES cell lines were formed in serum-free medium overnight and transferred into serum-free medium supplemented with PGI₂ the next day. After 12 days of suspension culture ~20% of EBs were contracting. Addition of SB203580

led to a further slight increase of efficiency yielding >10% cardiomyocytes. Another parameter tested at the same time was whether insulin had inhibitory effects on cardiac differentiation. Insulin supports long-term cell growth by facilitating uptake of glucose and amino acids from the medium and is a common additive in cell culture¹⁵¹. Removal of insulin from medium had no evident negative effects on cell survival but presence of insulin, especially during the early stages of differentiation, significantly inhibited formation of endoderm and mesoderm while at the same time promoting neuroectoderm development. Although the exact mechanisms are not understood it was hypothesised that insulin removal and addition of PGI₂ and SB203580 might, at least in part, be inducing cardiac differentiation indirectly through endoderm formation. This was suggested based on the up-regulation of endoderm markers, especially those of visceral endoderm, preceding cardiac development in this system. It was further suggested that inhibitory effects of insulin were mediated through activation of the PI3K/Akt pathway.

Overall, serum-free medium supplemented with PGI₂ and SB203580 induced cardiac differentiation at levels similar to END-2 CM alone but less than END-2 CM supplemented with SB203580. Unlike END-2 CM however, the newly developed chemically defined differentiation medium was compatible with GMP and offered opportunities to act as a platform for additional screens for cardiogenic small molecules. While subsequently this co-culture protocol was not further improved with regards to differentiation efficiency, it was slightly altered with respect to maintenance of derived cardiomyocytes. After initial differentiation cardiomyocytes were re-plated onto new END-2 cells followed by short-term culture in three dimensional aggregates¹⁵². Cardiomyocytes maintained under these conditions for up to one year showed enhanced electrophysiological maturation, an aspect particularly of interest for disease modelling and drug toxicity screens.

1.2.5.3 Guided differentiation

Co-culture with endoderm-like END-2 cells had shown that even *in vitro*, cues from endodermal cells can be sufficient to direct undifferentiated cells towards cardiac commitment, suggesting that developmental cues might be recapitulated in a dish to initiate cardiomyocyte differentiation via mesoderm and subsequently cardiac mesoderm development. Employing members of the three major families of growth factors associated with cardiac induction (BMP, activin, Wnt)¹⁵³, guided cardiac differentiation was developed as an *in vitro* adaptation of *in vivo* cardiogenesis during embryonic development. Both EB and monolayer based protocols were developed independently by two groups and although the composition of differentiation media changed over time, the principal of stepwise induction of mesoderm followed by cardiac mesoderm and finally cardiomyocyte commitment remained. Initially, induction of mesoderm was achieved through media supplemented with growth factors of the transforming growth factor beta (TGF- β) family before the role of canonical Wnt signalling was fully appreciated and while in the beginning protocols were developed using hES cells and recombinant proteins, in time they were complimented or replaced by iPS cells and small molecules.

Mesoderm induction through growth factors

The first published guided differentiation protocols employed factors that had been shown in species like *Xenopus*¹⁵⁴, chicken¹⁵⁵ and mice¹⁵⁶ to induce mesoderm formation and cardiac lineage commitment. In 2007 Laflamme et al. showed that a high density monolayer of H7 hES cells could be differentiated to spontaneously contracting cells using activin A and bone morphogenetic protein 4 (BMP4)¹⁵⁷. 1×10^5 undifferentiated single hES cells were seeded per cm^2 and were culture feeder-free in MEF-conditioned medium for 6 days. Differentiation was initiated with RPMI/B27 medium supplemented with 100 ng/mL human recombinant activin A for 24 hours, followed by 10 ng/mL human recombinant BMP4 for 4 days. Spontaneous contractions were observed after 7 additional days in RPMI/B27 medium supplemented with knockout serum replacement (KOSR) with yields

consistently >30% cardiomyocytes. A serum-free version of this protocol achieved similar efficiencies¹⁵⁸.

At the same time a similar protocol was developed focusing not only on mesoderm induction through activin A and BMP4 media supplements but also investigated the role of canonical Wnt signalling in human cardiac differentiation¹⁵⁹. Stage-specific inhibition of the canonical Wnt pathway had previously been shown to be a requirement for cardiac development in other species¹⁶⁰⁻¹⁶². The 3-stage protocol they developed used vascular endothelial growth factor (VEGF), human basic fibroblast growth factor (bFGF) and Dickkopf-related protein 1 (DKK1), a canonical Wnt inhibitor, in addition to BMP4 and activin A. During the first stage, formation of a primitive-streak-like population and mesoderm is induced in EBs with 0.5 ng/mL BMP4 for 24 hours and 10 ng/mL BMP4, 5 ng/mL bFGF and 3 ng/mL activin A for 4 days. Stage 2, cardiac mesoderm induction through 150 ng/mL DKK1 and 10 ng/mL VEGF for 4 days, is followed by stage 3, expansion of cardiovascular lineages, during which EBs are treated with 10 ng/mL VEGF, 150 ng/mL DKK1 and 5 ng/mL bFGF for 6 days. For the first 10-12 days EBs are cultured under hypoxic (5% O₂) conditions, which was then followed by normoxia. In their hands activating A and BMP4 alone were sufficient to induce mesoderm and cardiac lineage formation but addition of FGF increased differentiation efficiency from 20% to 40% cardiomyocytes. Although supplementation of differentiation medium with Wnt inhibitor DKK1 increased overall efficiency only slightly (~45% cardiomyocytes), experiments indicated that stage-specific inhibition of canonical Wnt signalling is crucial for cardiac differentiation. While Wnt3a increased cardiac differentiation when added during mesoderm specification (day 0-4), it completely inhibited it when added afterwards (day 4). Conversely, DKK1 had the opposite effect by completely inhibiting cardiac lineage formation when added during day 0-4, but promoting it when added around day 4 of differentiation.

The role of canonical Wnt signalling in cardiac differentiation

A subsequent study further investigated the mechanisms by which this biphasic stage-specific activation and inhibition of canonical Wnt signalling regulates cardiac differentiation¹³⁴. EBs derived from 3 hES cell lines were treated with Wnt3a for 48 hours in serum-supplemented medium, followed by a further 4 days in suspension without Wnt3a before being plated onto gelatine coated dishes in serum-reduced medium. Finally, on day 8 after EB formation medium was changed to serum-free medium. This protocol was optimised by varying serum concentrations at every stage and supplementing medium with several compounds including different Wnt isoforms for the first 48 hours. Alternatively, instead of EBs undifferentiated monolayers were used but showed drastically reduced expression of cardiac markers. Lack of serum at the beginning decreased EB size and although it resulted in the highest expression of mesoderm markers, EBs showed low expression of cardiac genes. High serum and insulin levels throughout differentiation on the other hand, drastically reduced cardiac formation. As observed previously by other groups, EB size had a significant influence on differentiation efficiency¹³⁷. Comparison of the different compounds showed that cardiogenic effects were restricted to Wnt3a. Wnt3a alone was sufficient to induce mesoderm and cardiac lineage formation by activating β -catenin through stabilisation and nuclear translocation.

In hES cell differentiation, activin A and BMP4 were shown to induce endogenous canonical Wnt expression and low expression in some cell lines was linked to reduced cardiogenic potential¹⁶³ which could explain some of the variability seen between cell lines. Cardiac differentiation efficacy of these cell lines could be increased by addition of exogenous Wnt3a throughout early stages of differentiation. Alternatively, efficient cardiac differentiation (>60% cardiomyocytes) was achieved in a number of hES and iPS cell lines through optimisation of exogenous activin A and BMP4 concentrations, activin and/or BMP antagonists and differentiation kinetics for each line individually, likely reflecting differences in endogenously produced factors¹⁶⁴.

Moving forward after better understanding the mechanisms controlling mesoderm induction, efforts were made to further reduce inter-line variability of differentiation efficiency and finding small molecules to compliment or replace recombinant proteins.

Addressing the former, BurrIDGE et al. developed a protocol that combined knowledge of chemically defined medium to induce mesoderm with that of the impact of EB size on successful cardiac differentiation¹³⁹. It was developed through step-by-step optimisation of >45 parameters grouped in 4 phases that included pluripotent stem cell culture prior to differentiation, mesoderm induction, cardiac specification and finally cardiomyocyte development. For the final protocol, undifferentiated cells were grown feeder-free in monolayers for a minimum of 3 passages before differentiation, creating a uniform pluripotent stem cell population. Forced aggregates, each containing 5000 of these cells, were formed with RPMI and polyvinyl alcohol in uncoated 96 well V-bottom plates and mesoderm formation was induced with 25 ng/mL of BMP4 and 5 ng/mL of FGF2 for the first 48 hours. For cardiac specification, medium was replaced with RPMI supplemented with 20% serum on day 2. Maturation and final cardiomyocyte development was achieved through attachment of forced aggregates to a tissue culture surface when transferred to coated 96 well U-bottom plates in serum-free medium on day 4. This protocol, derived using one hES cell line and subsequently tested with a further 3 hES and 7 iPS cell lines, consistently yielded 95% beating bodies, making it faster, more efficient and more reliable than previous guided differentiation protocols. On the other hand continued culture of pluripotent stem cells as single cells and forced aggregation make it also technically more challenging.

Growth factor-free cardiac differentiation

Concerning the identification of cardiogenic small molecules, two approaches have been taken: unbiased screens that might reveal new previously unknown pathways by which cardiomyogenesis is controlled, and biased screening, with a clear function and target pathway in mind. The first approach identified several compounds

including but not limited to DMSO¹⁶⁵, ascorbic acid¹⁶⁶, cardiogenols¹⁶⁷ and sulfonyl-hydrazones¹⁶⁸ and while some have a wide range of effects on cells (DMSO, ascorbic acid), others are specific to pathways involved in cardiogenesis (sulfonyl-hydrazones). However, not every compound identified this way can be linked to a definitive pathway and the mechanisms by which they promote cardiac differentiation remain poorly understood (SB203580)¹⁴⁹.

The second approach usually employs molecules previously identified to act on a certain pathway and are used to replace recombinant proteins making protocols cheaper, more easily scalable and bringing them closer to GMP standards for possible future clinical applications. One such example is the completely growth factor-free protocol developed by Lian et al. guiding cardiac differentiation solely by manipulating canonical Wnt signalling¹⁶⁹. Using genetically engineered cell lines with dox-inducible knock-down of β -catenin they confirmed that knock-down of β -catenin during the first days of differentiation completely inhibits cardiac differentiation while doing the same after mesoderm induction increases differentiation efficiency. Unlike other protocols described thus far, mesoderm induction was achieved through use of glycogen synthase kinase 3 (GSK-3) inhibitors in place of activin A or BMP4. GSK-3 is a serine/threonine protein kinase that, among many other things, phosphorylates β -catenin thereby marking it for degradation. By inhibiting GSK-3, phosphorylation and degradation of β -catenin are prevented and activation of the canonical Wnt pathway leads to mesoderm induction. GSK-3 inhibition increased cardiac differentiation efficiencies drastically in both EB and monolayer systems. In their final protocol feeder-free pluripotent stem cells were seeded in a high-density monolayer and cultured for 5 days. Differentiation was initiated with RPMI/B27-insulin supplemented with a small molecule GSK-3 inhibitor (BIO or CHIR99021) for 24 hours followed by 2 days in RPMI/B27-insulin. After mesoderm induction, the canonical Wnt pathway was inhibited for 2 days with RPMI/B27-insulin supplemented with a small molecule Wnt inhibitor (IWP2 or IWP4). On day 5 medium was changed to RPMI/B27-insulin to be replaced by RPMI/B27 on day 7. This serum- and growth factor-free protocol consistently yielded more than 82% cardiomyocytes with three hES and three iPS

cell lines showing that manipulation of endogenous Wnt signalling is sufficient to drive undifferentiated stem cells towards a cardiac fate and while addition of exogenous activin A and BMP4 in that scenario is not necessary, inhibition of their endogenous counterparts at the same time drastically reduces cardiac differentiation efficiency.

Taken together, hES and iPS cells differentiated *in vitro* not only represent a continuous supply of desired cell types such as cardiomyocytes but also provide a tool with which to study development. Investigations into Wnt signalling were driven by a desire to improve *in vitro* cardiac differentiation and not only provided the field with far more reliable, robust and efficient differentiation protocols with reduced inter-line variability, but also delivered new insight into the mechanisms involved in the control of mesoderm formation.

1.3 Cardiomyocyte Biology

All of the information on cardiomyocyte physiology and function provided in this segment, unless otherwise denoted, was gathered from “Berne & Levy Physiology”¹⁷⁰.

1.3.1 Physiology and structure

The heart muscle, or myocardium, is located between layers of simple squamous epithelium called endocardium and epicardium, and is mostly made up of cardiomyocytes. There are a number of cardiomyocyte subtypes that differ in physiological aspects relating to their electrophysiological properties. Pacemaker cells, located in the sinoatrial node, spontaneously depolarise and initiate contraction, thereby controlling the heart-rate. Atrial cells are generally smaller than ventricular cells with fewer myofibrils, fewer transverse tubules (t-tubules) and a slightly different action potential pattern. Both contract in response to stimulation of pacemaker cells in a coordinated manner. Other subtypes include cells of the AV

node, conducting the pacemaker stimulation from atrium to ventricle, and cells of the Purkinje fibres conducting the stimulation signal throughout the ventricles. The following description will mainly be focusing on ventricular cardiomyocytes, the subtype causing fatal arrhythmias in patients with Brugada Syndrome.

A typical cardiomyocyte, rod-shaped and branched, measures 100 μm in length and 10 μm in width, contains one nucleus, mitochondria that take up 25-30% of the cell's volume, several myofibrils, an extensive sarcoplasmic reticulum network and invaginations of the cell membrane called t-tubules (Figure 5). Cardiomyocytes are connected through intercalated discs allowing them to act as an electrical and mechanical syncytium, resulting in the synchronised contraction of the heart.

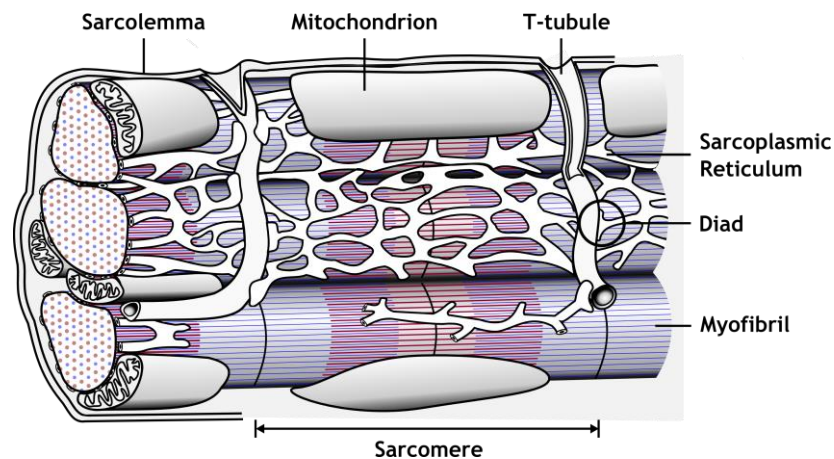


Figure 5: Schematic of cardiac muscle cell

1.3.1.1 Myofibrils and sarcomeres

Myofibrils are bundles of fibres that run along the length of every cardiomyocyte and form their contractile apparatus. Thin filaments, mainly composed of actin molecules, and thick filaments, primarily composed of myosin molecules, are organised in sarcomeres, the repeating functional units of myofibrils. Each sarcomere is bordered by Z-lines and while thin filaments anchored at those Z-lines extend towards the middle (M-line), thick filaments are anchored at the M-line and extend towards the Z-lines (Figure 6). The binding of myosin to actin is what leads to

contraction and is described in more detail later on. The area surrounding the Z-line, where in a relaxed state thin filaments are not overlapping with thick filaments, are called I-bands. The area between two I-bands covering the entire length of a thick filament is labelled A-band, while the area surrounding the M-line where thick filaments are not overlapping with thin filaments is called H-band.

Thin filaments are formed by monomeric (globular) actin molecules that polymerise into filamentous actin, a two-stranded helix, stretching along the cytoskeletal protein nebulin. Filamentous actin strands are anchored to Z-lines by α -actinin and capZ protein while tropomodulin, located at the other end of a thin filament, is thought to help regulate a filaments length. Actin filaments have myosin binding sites which in a relaxed muscle are covered by tropomyosin dimers. The binding of each tropomyosin dimer to the actin filament is facilitated by a troponin complex consisting of troponin C, troponin I and troponin T.

Thick filaments are formed by polymerisation of myosin molecules. Each myosin molecule consists of one pair of heavy chains and two pairs of light chains. The C-terminus of each of the two heavy chains is called the tail region and together they form an α -helix. The N-terminus of each heavy chain, termed the head region, is associated with a pair of light chains and extends away from the thick and towards the thin filament. The head region is the part that during contraction interacts with the actin filament. It also has an ATPase activity essential during contraction which is modulated by one of the light chains. Thick filaments are connected to Z-lines through large elastic proteins called titin, which extend from Z-lines to M-lines. In the A-band, where thin and thick filaments overlap, each thin filament is surrounded by three thick filaments, while each thick filament is surrounded by 6 thin filaments. Along a thick filament myosin molecules are oriented in a helical array such that myosin heads connect to each of these 6 surrounding thin filaments.

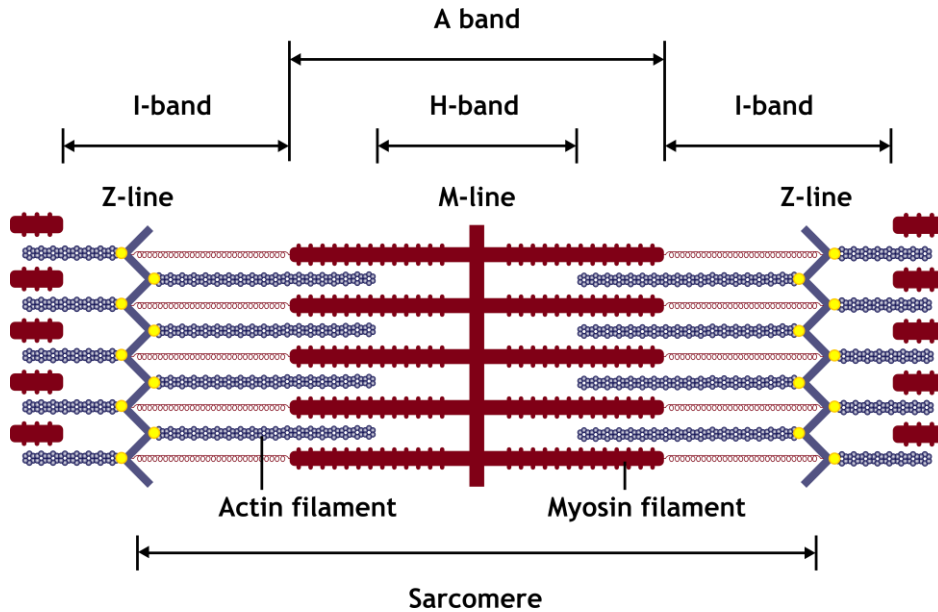


Figure 6: Schematic of a single relaxed sarcomere

1.3.1.2 Sarcoplasmic reticulum

The sarcoplasmic reticulum (SR) is an extensive membrane network, equivalent to smooth endoplasmic reticulum in non-muscle cells, enveloping each myofibril in the area between two Z-lines. It functions as a calcium storage which releases calcium into the sarcoplasm during contraction and again removes it from the sarcoplasm for muscle relaxation. In cardiac muscle cells the terminal cisterna of an SR and a t-tubule in close proximity form a diad. This structure, located at the Z-lines of sarcomeres, plays an important role in excitation-contraction coupling, a process described in detail below.

1.3.1.3 Intercalated discs

Once a cardiomyocyte has been excited, the contraction spreads like a wave through the heart because neighbouring cardiomyocytes are connected through intercalated discs at their bipolar ends. Intercalated discs, always coinciding with Z-lines, are an

assembly of fascia adherens, desmosomes and gap junctions. Fascia adherens and desmosomes form a physical connection between two adjacent cardiomyocytes preventing damage during contractions. Fascia adherens establish intercellular contact through N-cadherin and anchor actin filaments of the nearest sarcomere through catenin and plakoglobin. At desmosomes, cadherins establish intercellular contact while desmoplakin, plakophilin, and plakoglobin anchor intermediate filaments¹⁷¹. Gap junctions form a direct electrical connection between the sarcoplasm of neighbouring cardiomyocytes. Hemichannels (connexons) shaped by six connexin molecules in each of the adjacent cell membranes connect to form a gap junction that is non-discriminately permeable to small ions. The connexin isoform predominantly present in adult ventricular cardiomyocytes is connexin-43.

1.3.2 Function

Contraction of the heart is initiated by pacemaker cells in the sinoatrial node that spontaneously depolarise, generating an action potential. This initial action potential propagates through gap junctions from the sinoatrial node to atria, atrioventricular node and finally ventricles. In each cardiomyocyte action potentials trigger calcium-induced calcium release which results in contraction. This mechanism is called excitation-contraction coupling.

1.3.2.1 Action potential

Basis for any action potential is a concentration gradient of ions across the cell membrane. While extracellular concentration of sodium and calcium ions far supersedes their intracellular concentration, the opposite is true for potassium ions. Electrical and concentration gradients are defined by the electrochemical equilibrium for each ion. The normal membrane or resting potential of -90 mV is mostly determined by the equilibrium potential for potassium due to the relatively higher permeability of the membrane for potassium compared to other ions. Through the influx of ions from an excited neighbouring cardiomyocyte (through gap junctions)

the membrane potential becomes less negative. Should this increase pass the threshold of around -65 mV an action potential is initiated. An action potential travels as a wave of depolarisation along the length of a cell, the wave of depolarisation propagating in form of local circuit currents. Reaching the end of the cardiomyocyte the action potential propagates to the next cardiomyocyte through gap junctions.

Action potentials in ventricular cardiomyocytes are characterised by 5 phases. In an action potential recording (Figure 7) the initial fast upstroke (depolarisation) is followed by a notch (early repolarisation), plateau and return to baseline (repolarisation).

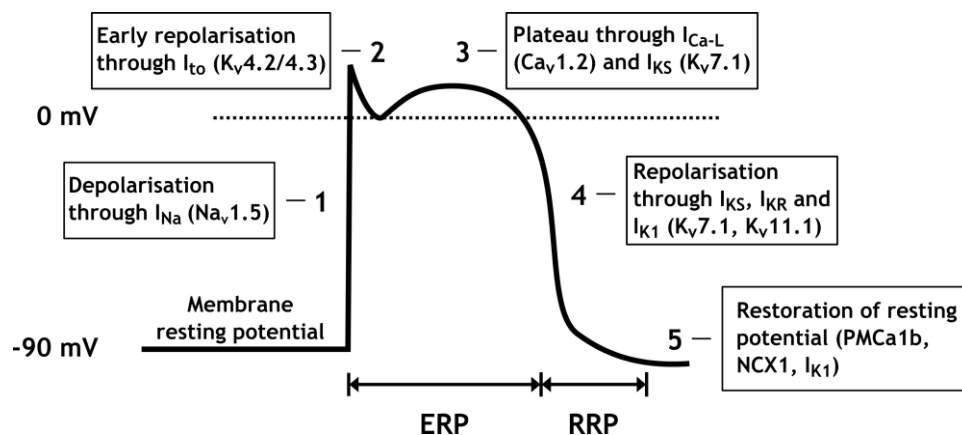


Figure 7: Schematic of a ventricular action potential

ERP – effective refractory period, RRP – relative refractory period

During the first phase, a sudden change in membrane potential causes voltage-gated sodium channels to increase their open probability for a very short time. The electrochemical gradient causes a drastic influx of sodium ions (I_{Na}) through the open channels resulting in fast depolarisation. Almost immediately after activation, a conformation change occurs in sodium channels shifting them into an inactive state. As long as they are in this inactive state (effective refractory period) they cannot be activated again. During the relative refractory period, channels gradually change

their conformation once more to the closed state, in which activation is again possible. This mechanism contributes to prevent sustained contraction and allows complete relaxation. The second phase begins with the opening of voltage-gated potassium channels triggered by the sudden decrease of membrane potential. The resulting transient outward current (I_{to}) starts to counteract sodium influx and the membrane potential begins to become more negative. The size of the notch in this early repolarisation phase is dependent on I_{to} density, which in the left ventricle is higher in epicardium and mid-myocardium compared to endocardium. In the third phase, the slight repolarisation caused by potassium efflux (I_{to}) opens voltage-gated L-type and T-type calcium channels as well as delayed rectifier potassium channels. The simultaneous continued efflux of potassium as I_{to} , I_K and I_{K1} and influx of calcium balance each other out creating an action potential plateau. The fourth phase is marked by the closing of calcium channels while continued potassium efflux in form of I_{to} , I_K , and I_{K1} drives final repolarisation. During the fifth and last phase, the resting state, electrochemical equilibria are restored to their pre-action potential state. The sodium-potassium-ATPase is utilised to transport potassium in while simultaneously transporting sodium out of the cell; with the energy gained through hydrolysis of one ATP molecule, three sodium and two potassium ions are transported. Calcium in turn is transported out of the cell through a calcium-ATPase pump (PMCa1b) and through the sodium-calcium exchanger (NCX1), an antiporter that carries three sodium ions into the cell in exchange for transporting one calcium ion out of the cell.

1.3.2.2 Calcium-induced calcium release

Calcium influx through L-type calcium channels during the third phase of an action potential causes calcium-induced calcium release (CICR) and is crucial for contraction in cardiomyocytes. Terminal cisternae of the SR, located near t-tubules above Z-lines, are enriched in ryanodine receptors. Ryanodine receptors are homotetrameric calcium-gated calcium channels that open in response to calcium entering the cell. RyR2, the cardiac ryanodine receptor isoform, forms a complex with junctin, triadin, and calsequestrin. Junctin and triadin are located in the SR

membrane near RyR2 and bind to both RyR2 channels and calsequestrin. Calsequestrin, a protein with low affinity for calcium, is located in the lumen of the SR particularly at the terminal cisternae. Its low-affinity binding of calcium not only helps establish the high concentration gradient of calcium across the SR membrane but also a quick release into the cytoplasm upon opening of RyR2. Another protein with a low affinity for calcium, histidine-rich calcium-binding protein (HRC), is also present in the lumen of the SR albeit at a lower concentration. Opening of RyR2 leads to a massive calcium release from the SR causing a dramatic increase in intracellular calcium concentration. Calcium released into the cytoplasm this way binds to the troponin complexes exposing the myosin binding sites which results in contraction. The onset of contraction coincides with the peak of intracellular calcium concentration and maximum contraction corresponds approximately with calcium concentration half returned to baseline.

In cardiomyocytes, even in the absence of extracellular calcium an action potential can be initiated. Without the influx of calcium however no calcium release from the SR is triggered and no contraction occurs.

1.3.2.3 Contraction and relaxation

During contraction, myosin molecules of thick filaments bind to actin molecules of thin filaments resulting in a sliding of the two filaments along each other. In the relaxed state, however, the myosin binding sites on the actin filaments are blocked by tropomyosin. Each tropomyosin dimer lies in the cleft of the actin double helix spanning 7 globular actin monomers and adjacent tropomyosin molecules are arranged head-to-tail. Inhibition of myosin binding through tropomyosin is facilitated by a complex of three troponins. Tropomyosin overlaps with the N-terminus of troponin T while the C-terminus of troponin T binds to troponin C and troponin I, which in turn interacts with actin. Troponin C has 4 calcium binding sites, two with high and two with low affinity for calcium. The two high-affinity sites bind calcium even in the relaxed state and appear to regulate interaction of troponin I and troponin T. Low-affinity sites in contrast only bind calcium after CICR when

intracellular calcium concentration crosses a threshold. Binding of calcium causes a conformational change that increases binding of troponin C and troponin I, which causes the latter to be released from the actin filament. This conformational shift increases tropomyosin movement exposing myosin binding sites. Because contraction is controlled by inhibition and exposure of myosin binding sites on actin filaments, it is said to be thin filament dependent.

The binding and release of myosin is collectively termed the cross-bridge cycle, during which chemical energy stored as ATP is transformed into mechanical energy of contraction. In its relaxed state, myosin has partially hydrolysed ATP bound. Upon exposure of myosin binding sites due to increase in intracellular calcium concentration, a myosin head binds to an actin molecule creating a cross-bridge. Complete hydrolysis, resulting in the release of ADP and inorganic phosphate (P_i), causes a conformational change of the myosin head, pulling the actin filament towards the centre of the sarcomere. This change in conformation, also called ratchet action, is what causes the sliding of filaments. Binding of a new ATP molecule causes myosin to be released from actin and partial hydrolysis causes the myosin head to change its conformation back to the original state. As long as myosin binding sites on actin filaments are exposed, this cross-bridge cycle continues, progressively shortening the sarcomere until calcium is sequestered back into the SR. The shortening of a sarcomere during contraction is a consequence of the bipolar orientation of myosin molecules at the M-line. While at the M-line myosin molecules are arranged tail-to-tail, thick filaments polymerise away from the midline in a head-to-tail association resulting in Z-lines being drawn together towards the centre of the sarcomere during contraction.

Relaxation after contraction occurs when intracellular calcium is extruded from the cytoplasm. Approximately 30% of intracellular calcium present during contraction will have entered the cell through voltage-gated calcium channels to trigger release of the remaining 70% from the SR. Were all intracellular calcium to be taken up by the SR at the end of contraction, the amount of calcium stored in the SR would continuously increase and result in calcium overload. Restoring cytosolic calcium

concentration to base-level therefore requires mechanisms by which calcium can be extruded from the cell as well as re-sequestered into the SR. As described above the sodium-calcium exchanger in the cell membrane transports one calcium ion out by using the electro-chemically favourable transport of three sodium ions into the cell. Up-take by the SR takes place through a calcium pump called sarcoplasmic endoplasmic reticulum calcium ATPase (SERCA) found in the SR membrane. For each ATP molecule SERCA hydrolyses it transports two calcium ions into the SR lumen. Although SERCA is less abundant than the sodium-calcium exchanger it has a greater affinity for calcium and therefore accounts for a greater percentage of calcium extrusion. With the removal of intracellular calcium the troponin-tropomyosin complex returns to its previous position at myosin binding sites once more inhibiting myosin-actin cross-bridge formation.

HYPOTHESES

- I) Brugada Syndrome can be modelled *in vitro* using cardiomyocytes derived from induced pluripotent stem cells.

- II) Human stem cell-derived cardiomyocytes are structurally and functionally similar to human foetal cardiomyocytes.

AIMS

- I) To establish comprehensive tests to assess pluripotency and differentiation potential of pluripotent stem cells and to systematically compare and optimise cardiac differentiation protocols to establish a reliable, efficient and robust protocol. (Chapter3)

- II) To assess the maturity and functionality of pluripotent stem cell-derived cardiomyocytes by comparing them to isolated primary human adult and foetal cardiomyocytes. (Chapter 4)

- III) To generate iPS cells from a Brugada Syndrome patient and controls, to assess their pluripotency and differentiation potential, and to characterise cardiomyocytes derived from these cell lines. (Chapter 5)

CHAPTER 2

Materials and Methods

2.1 Solutions and media

2.1.1 Solutions and reagents

Reagent	Supplier	Catalogue number
Boric acid	Sigma-Aldrich	6768
Collagenase IV	LifeTechnologies	17104019
Ethylenediaminetetraacetic acid (EDTA)	Sigma-Aldrich	E5134
Phosphate buffered saline (PBS)	LifeTechnologies	003002
Paraformaldehyde (PFA)	Sigma-Aldrich	158127
Sodium phosphate dibasic anhydrous	Sigma-Aldrich	RES20908-A7
Sodium phosphate monobasic dihydrate	Sigma-Aldrich	71505
Trizma base	Sigma-Aldrich	T1503
Tween 20	Sigma-Aldrich	P2287
Matrigel	BDBiosciences	354230
0.25% Trypsin/EDTA	Sigma-Aldrich	T4049

Collagenase IV

A 200 U/mL collagenase IV solution was prepared in KO-DMEM, filter sterilised, aliquoted and stored at -20°.

M buffer

PBS was supplemented with 1% (v/v) FCS and 1% (v/v) 200 mM EDTA and filter sterilised.

4% PFA

4% (w/v) PFA powder was added to PBS, heated to 60°C, and cleared by the addition of 1 M NaOH. Paraformaldehyde is an insoluble polymer. NaOH catalyses the hydrolysis to methylene hydrate, while addition of heat accelerates the reaction.

PBS 1 PBS tablet dissolved in 500 mL MilliQ water

PBST PBS supplemented with 0.1% (v/v) Tween 20

0.2 M Phosphate buffer (PO buffer)

20.44 g Sodium phosphate dibasic anhydrous

7.79 g Sodium phosphate monobasic dihydrate

MilliQ water ad 1 L, pH 7.2

10x TBE Electrophoresis Buffer

108 g of Trizma base

55 g of Boric acid

7.5 g of EDTA

MilliQ water ad 1 L

2.1.2 Media and supplements

Medium component	Abbreviation	Supplier	Catalogue number
B-27 supplement	-	LifeTechnologies	17504-044
Bovine Serum Albumin	BSA	Sigma-Aldrich	A7906
Creatine	-	Sigma-Aldrich	C0780
Dimethyl sulfoxide	DMSO	Sigma-Aldrich	D2650
Dulbecco's Modified Eagle Medium	DMEM	LifeTechnologies	11995065
Dulbecco's Modified Eagle Medium + GlutaMaxII	DMEM + GlutaMaxII	LifeTechnologies	10566016
Foetal calf serum	FCS	LifeTechnologies	10082-139
Gentamicin, AmphotericinB	-	LifeTechnologies	R01510
Human basic fibroblast growth factor	bFGF	Peprotech	100-18B
HyClone foetal calf serum	HyClone FCS	Fisher Scientific UK Ltd	HZSH3007103H
Knock-Out DMEM	KO-DMEM	LifeTechnologies	10829018
Knock-Out Serum Replacement	KOSR	LifeTechnologies	10828028
L-carnitine	-	Sigma-Aldrich	C0283
L-Glutamine	L-Glut	LifeTechnologies	25030024
Medium 199	-	LifeTechnologies	11150-059
MEM Non-Essential Amino Acids	NEAA	LifeTechnologies	11140-035
Penicillin, Streptomycin	PenStrep	LifeTechnologies	15070063
RPMI	-	LifeTechnologies	11875-093
Taurine	-	Sigma-Aldrich	T8691
TeSR-E8	-	Stem Cell Technologies	05940
β -Mercaptoethanol	β -Merc	LifeTechnologies	31350010

Table 3: Composition of growth and differentiation media

Medium	Base medium	Serum (v/v)	PenStrep	NEAA	L-Glut	β-Merc	Additives
20% HyClone	KO-DMEM	20% HyClone	+	+	+	+	-
basic serum-free medium (bSF)	DMEM	-	-	+	+	+	-
EB medium	DMEM	10% FCS	+	+	+	+	-
END-2 differentiation medium	DMEM	-	+	+	+	+	-
END-2 medium	DMEM	20% FCS	+	+	+	+	-
Fibroblast growth medium	DMEM+ GlutaMaxII	10% HyClone	+	-	-	-	50 µg/mL Gentamicin, 1.25 µg/mL Amphotericin B
iPS medium	KO-DMEM	20% KOSR	+	+	+	+	10 ng/mL bFGF
M199 medium	Medium 199	2% FCS	+	-	-	-	20 mM taurine, 2 mM L-carnitine, 5 mM creatine, 2 mg/mL BSA
MEF medium/ 10% FCS	DMEM	10% FCS	+	-	+	-	-
SR-DMSO	KO-DMEM	20% KOSR	+	+	+(1 mM)	+(0.2 mM)	1% (v/v) DMSO

Unless otherwise stated: PenStrep – 50 U/mL Penicillin, 50 µg/mL Streptomycin; L-Glut – 2 mM; β-Merc – 0.1 mM; NEAA – 1x

2.2 Cell lines

Table 4: List of commercially obtained and in-house derived cell lines

	Cell line	Sex	Age of donor	Type of donor tissue	Method for reprogramming	Provider
hES cells	WA09 (H9)	Female	N/A	Inner cell mass	N/A	University of Wisconsin
	33-D9	Male	56	Fibroblast (CRL-2465)	Retroviruses	Dr Gareth J. Sullivan ¹⁷²
	34-D6	Female	40	Fibroblast (CRL-2524)	Retroviruses	Dr Gareth J. Sullivan ¹⁷²
Human iPS cells	BP-C5	Male	69	Fibroblast	Episomal vectors	Franziska Sendfeld
	BP-C6	Male	69	Fibroblast	Episomal vectors	Franziska Sendfeld
	BP-C11	Male	69	Fibroblast	Episomal vectors	Franziska Sendfeld
	BP-C15	Male	69	Fibroblast	Episomal vectors	Franziska Sendfeld
	BP-C26	Male	69	Fibroblast	Episomal vectors	Franziska Sendfeld
	HV3-C11	Male	65	Fibroblast	Episomal vectors	Franziska Sendfeld
	HV3-C19	Male	65	Fibroblast	Episomal vectors	Franziska Sendfeld
	HV3-C23	Male	65	Fibroblast	Episomal vectors	Franziska Sendfeld
	HV3-C24	Male	65	Fibroblast	Episomal vectors	Franziska Sendfeld
	HV3-C28	Male	65	Fibroblast	Episomal vectors	Franziska Sendfeld
	Fibroblasts	CRL-2097	Male	Neonatal	Skin biopsy	N/A
BP		Male	69	Skin biopsy	N/A	Franziska Sendfeld
HV3		Male	65	Skin biopsy	N/A	Franziska Sendfeld

BP – Brugada Syndrome patient, *SCN5A* (c.1100G>A - pARG367HIS); HV3 – Healthy volunteer 3

2.3 Isolation of human primary cardiomyocytes

2.3.1 Isolation of foetal cardiomyocytes

Table 5: Composition of buffers used to isolate human foetal cardiomyocytes

Component	Supplier	Catalogue number	Buffer 1	Buffer 2	Buffer 3	Buffer 4
HEPES	Sigma-Aldrich	H3375	10 mM	10 mM	10 mM	10 mM
NaCl	Sigma-Aldrich	S5886	129 mM	129 mM	129 mM	129 mM
KCl	Sigma-Aldrich	P5405	4.7 mM	4.7 mM	4.7 mM	4.7 mM
KH ₂ PO ₄	Sigma-Aldrich	P0662	1.2 mM	1.2 mM	1.2 mM	1.2 mM
MgSO ₄	Sigma-Aldrich	M2643	1.2 mM	1.2 mM	1.2 mM	1.2 mM
NaHCO ₃	Sigma-Aldrich	S5761	5 mM	5 mM	5 mM	5 mM
BSA	Sigma-Aldrich	A7906	2 mg/mL	2 mg/mL	2 mg/mL	2 mg/mL
Taurine	Sigma-Aldrich	T8691	20 mM	20 mM	20 mM	20 mM
L-carnitine	Sigma-Aldrich	C0283	2 mM	2 mM	2 mM	2 mM
Creatine	Sigma-Aldrich	C0780	5 mM	5 mM	5 mM	5 mM
BDM	Sigma-Aldrich	B0753	30 mM	30 mM	30 mM	30 mM
Protease XXIV	Sigma-Aldrich	P8038	-	4 U/mL	-	-
Collagenase A	Roche	10103578001	-	-	1 mg/mL	1 mg/mL
Hyaluronidase	Sigma-Aldrich	H3506	-	-	0.5 mg/mL	-
pH (NaOH)			7.4	7.4	7.4	7.4
Glucose	Sigma-Aldrich	G0350500	5.5 mM	5.5 mM	5.5 mM	5.5 mM

Based on the method published by Mummery et al.¹⁷³.

This study was approved by the South East Scotland Research Ethics Committee (REC reference 08/S1101/1) and written informed consent was obtained from all subjects. Buffers were prepared as detailed in Table 5, filter-sterilised and stored at -20°C in 5 and 10 mL aliquots. Glucose was added to each aliquot after thawing. Human foetal cardiac tissue from 11-16 week-old fetuses was obtained from patients undergoing elective termination of pregnancy. Cardiac samples were stored in PBS on ice immediately after dissection and processed within 30 min. Tissue was transferred to Buffer 1 and connective and adipose tissue was removed using scalpels, keeping shear stress to a minimum. After carefully mincing the tissue into $\sim 1\text{ mm}^3$ big pieces, they were washed with Buffer 1 for 3 x 3 min at room temperature. A 15 min incubation in Buffer 2 at room temperature was followed by 3 x 20 min incubations in Buffer 3 and 1 x 20 min incubation in Buffer 4 in a shaking water bath at 37°C . Following each incubation in Buffer 3 or 4, supernatants were collected, centrifuged at 600 rpm for 4 min at room temperature and pellets resuspended in 1 mL of Buffer 1. All resuspended pellets were pooled and Ca^{2+} reintroduced by adding 1 M CaCl_2 at 4 min intervals up to a final concentration of 1.79 mM. Finally the cell suspension was centrifuged at 600 rpm for 4 min at room temperature and the pellet resuspended in 10% FCS and plated onto 1% gelatine. Alternatively cells were resuspended and plated in M199 medium.

2.3.2 Isolation of adult cardiomyocytes

Based on the method published by Smits et al.¹⁷⁴ adult human cardiac ventricular and atrial tissue received from the Scottish National Blood Transfusion Service (SNBTS) was stored in PBS on ice and processed immediately upon arrival in the laboratory. Right atrial appendages from routine cardiac surgery were collected according to procedures approved by the South East Scotland SAHSC BioResource committee under existing ethical approvals. Written informed consent was obtained from all subjects. Cardiac tissue was collected and stored in 10% FCS and processed within 30 min. Residual blood was washed off of cardiac samples with ice-cold M-buffer, adipose and scar tissue was removed with sterile scissors and the remaining tissue dissected into $\sim 1\text{ mm}^3$ pieces using sterile scalpels. Mincing tissue was transferred to

a conical tube, allowed to settle in M-buffer and washed twice with cold PBS, removing all serum before the enzymatic digestion. After estimating the volume of the tissue, a 1 mg/mL Collagenase A solution was added at a ratio of 1:2.5 and the mix was incubated in a 37°C shaking water bath. After 30 min the digested tissue was dissociated by pipetting and passed through a 40 µm cell strainer. Cells were collected on ice, the cell strainer washed 5 times with cold M-buffer and the flow-through collected and pooled on ice. The cell suspension was pelleted at 300 g for 5 min at room temperature, washed in cold M-buffer, pelleted again, resuspended in 10% FCS or M199 medium and plated onto 1% gelatine coated plastic-ware.

2.4 Derivation and maintenance of iPS cells

2.4.1 Skin biopsy and isolation of fibroblasts

This study was approved by the South East Scotland Research Ethics Committee (REC reference 11-SS-0095) and written informed consent was obtained from all subjects. Dermal biopsies were collected in 10% FCS on ice and processed within an hour of collection. Tissue was transferred into minimal volume of fibroblast growth medium before dissecting off the epidermis and fat with sterile scalpels. The remaining tissue was dissected into 1 mm³ pieces. Four tissue pieces were transferred to each well of a tissue culture treated 6 well plate, covered by a sterile coverslip, leaving room for cell expansion, and slowly submerged in fibroblast growth medium. The tissue pieces were cultured at 37°C with 5% CO₂ with the first medium change carried out after 7 days and subsequently every 4-5 days. Once fibroblasts had grown out from the tissue and expanded they were harvested and subsequently passaged using enzymatic treatment as follows. After medium had been removed with PBS, cells were incubated with 0.25% Trypsin/EDTA for 5 min at 37°C. Trypsin was deactivated through addition of medium containing serum. Cells were then harvested with minimal agitation to prevent cell damage, pelleted at 1000 rpm for 5 min, resuspended in medium and cultured in tissue culture treated flasks with media changes every other day.

2.4.2 Reprogramming of fibroblasts to induced pluripotent stem cells using episomal vectors

The following Addgene Y4 combination episomal vectors were used:

pCXLE-hOCT3/4-shp53-F (Addgene 27077; Oct4 & shp53), pCXLE-hSK (Addgene 27078; Sox2 & Klf), pCXLE-hUL (Addgene 27080; LMyc & Lin28)

Fibroblasts were expanded, harvested as described above and counted using a haemocytometer. 0.5×10^6 cells per electroporation were resuspended in 100 μL Amaxa NHDF buffer (Amaxa NHDF Nucleofector Kit, Lonza, VPD 1001) and 5 μg DNA (1.7 μg hOct3/4-shp53, 1.6 μg hSK and 1.7 μg hUL vectors). The mixture was transferred into an Amaxa Nucleofector 2b (Lonza, AAB 1001) cuvette and cells were electroporated using program U023. During transfer, care was taken that no bubbles were introduced, as these would interfere with transfer of electricity resulting in an electric arc. Electroporated cells were resuspended in pre-warmed antibiotic-free fibroblast growth medium with an Amaxa pipette and plated in one well of a 6 well plate. After 24 hours and then again 4 days post-electroporation medium was replaced with 10% FCS. Seven days after electroporation cells were lifted with Trypsin/EDTA as described above and re-plated into a 0.1% gelatine coated tissue culture treated 10 cm culture dish in 10% FCS. After 24 hours, medium was aspirated and replaced with hES cell selection medium TeSR-E8. Media changes were subsequently carried out every two days and cell morphology was assessed using a Nikon Eclipse TE300 light microscope. Genuine induced pluripotent stem cell colonies appeared between 20-25 days after electroporation and were manually picked into separate wells of Matrigel coated 4 well plates in TeSR-E8. Colonies were treated as individual clones and expanded to give rise to independent cell lines. Since episomal vectors do not integrate into the host genome and are not co-replicated during cell proliferation, they are lost over time and therefore, clones that failed to express pluripotency genes endogenously would not give rise to stable pluripotent stem cell lines.

2.4.3 Maintenance of pluripotent stem cell lines

2.4.3.1 Preparation of mouse embryonic fibroblasts (MEFs) as feeder cells and production of MEF conditioned medium (MEF CM)

P0 MEFs were expanded in MEF medium on tissue culture treated flasks at 37°C and 5% CO₂. After reaching confluency, MEFs were harvested, using 0.25% Trypsin-EDTA as described for fibroblasts, resuspended in MEF medium and irradiated at 40 Gy. The right amount of radiation causes DNA damage leading to senescence-like growth arrest. Afterwards MEFs were counted, using a haemocytometer, pelleted at 1000 rpm for 5 min, resuspended in FCS containing 10% (v/v) DMSO (Sigma-Aldrich, D2650) and stored in aliquots at -80°C for a week before being transferred to liquid nitrogen (LN₂). To limit cell death and improve recovery after thawing, MEFs were kept on ice whenever possible and were transferred to -80°C immediately after resuspension in a minimal volume of freezing mix. Alternatively MEFs were bought in from VHBio (07GSC6001G) in aliquots of 4-5 x 10⁶ cells.

For MEF CM 12.5 x 10⁶ irradiated MEFs were seeded per T225 tissue culture treated flask in MEF medium. The medium was replaced with 100 mL iPS medium supplemented with 4 ng/mL bFGF the next day and subsequently collected and replaced with new media every 24 hours for 7 days. All collected MEF conditioned media was pooled, filter sterilised and stored in aliquots at -20°C or -80°C for short or long-term storage.

2.4.3.2 Feeder-layer system

Pluripotent stem cells were maintained in iPS medium on Matrigel coated plates containing irradiated MEFs (10⁶ cells per 6 well plate) and were cultured at 37°C and 5% CO₂. Media changes were carried out daily and cells were passaged enzymatically and mechanically using Collagenase IV and cell scrapers upon reaching 70-90% confluency.

2.4.3.3 Feeder-free system

Pluripotent stem cells were maintained on Matrigel coated plates in MEF conditioned medium or TeSR-E8 at 37°C and 5% CO₂. Media changes were carried out daily and cells were passaged chemically and mechanically using sterile cell scrapers and 0.5 mM EDTA (LifeTechnologies, AM9260G) for 4 min at room temperature.

2.5 Differentiation of pluripotent stem cells to cardiomyocytes

2.5.1 Three germ layer differentiation

Embryoid bodies (EBs) were formed from confluent undifferentiated pluripotent stem cell colonies. After a 30 s incubation with Collagenase IV at 37°C, colonies were washed with PBS and mechanically disrupted with a sterile pipette to yield evenly sized clumps. These clumps were harvested, transferred onto non-treated tissue culture dishes and cultured in suspension in EB medium at 37°C and 5% CO₂. Medium was changed every other day by letting EBs settle in a conical tube, carefully aspirating supernatant and resuspending in new medium. On day 7 EBs were plated onto 0.1% gelatine coated tissue culture treated plates and cultured for a further 10 days, continuing media changes every other day. EBs were fixed and stained for the three germ layers endoderm, ectoderm and mesoderm as described in section 2.6.3.2.

2.5.2 Directed hepatic differentiation

Protocol based on Sullivan et al.¹⁷² Undifferentiated pluripotent stem cells were cultured feeder-free before direct hepatic differentiation. Upon reaching 40-50% confluency the medium was changed to RMPI supplemented with B-27 supplement, PenStrep and Wnt3a (50 ng/mL) for 3 days, and with activin A (100 ng/mL) for 2 days. Media changes were carried out daily for 3 days before changing medium to SR-DMSO continuing media changes every other day for 5 days. Hepatocyte

morphology was confirmed with a light microscope before fixation and staining for hepatic markers (2.6.3.2).

2.5.3 END-2 co-culture

2.5.3.1 Maintenance of END-2 cells

END-2 (mouse visceral endoderm-like cell line) cells were grown on tissue culture treated flasks in END-2 medium at 37°C with 5% CO₂. Cells were passaged enzymatically with 0.25% Trypsin/EDTA as described previously upon reaching 80% confluency.

2.5.3.2 Growth arrest of END-2 cells

For growth arrest through radiation treatment END-2 cells were harvested, counted and irradiated as described for MEFs. Gamma radiation doses of 30, 35, 37 and 40 Gy were tested in order to ensure cells survival and growth arrest.

Alternatively, 100% confluent END-2 cells in a T175 flask were growth arrested with mitomycin C (Sigma-Aldrich, M4287). Mitomycin C was added to media at a final concentration of 10 µg/mL and incubated with the cells for 2 hours and 45 min. It was subsequently washed off with medium once and PBS twice.

2.5.3.3 Production of END-2 conditioned medium

To each T175 flask, 100% confluent with growth arrested END-2 cells, 55 mL of END-2 differentiation medium was added immediately after mitomycin C treatment. END-2 differentiation medium was conditioned at 37°C and 5% CO₂ for 4 days before being harvested, filter sterilised, aliquoted and stored at -80°C.

2.5.4 Cardiac Differentiation

Cardiac differentiation protocols previously published by Mummery¹⁴⁶, Xu^{141, 150} and Graichen et al.¹⁴⁹ were used as the basis for a systematic comparison and optimisation to find the most reliable, efficient and robust protocol for the cell lines studied in this project. EBs were formed as described above, cultured in suspension for up to 20 days without plating or for 4 days before being plated onto 0.1% gelatine coated tissue culture treated 6 well plates. Different media for EB formation as well as differentiation media with and without 5 μ M SB203580 (Tocris, 1202) and 2 μ M PGI₂ (Sigma-Aldrich, 18220-1) were tested. Three protocols were then tested on three cell lines (33-D9, 34-D6, H9) in biological as well as technical triplicate. The comparison is illustrated and discussed in further detail in Chapter 3. Efficiency was analysed with regard to the number of beating bodies derived from each well of undifferentiated stem cells as well as the percentage of EBs that formed beating bodies.

Analysis

Each of the three protocols was performed for each cell line in technical triplicate as well as biological triplicate. Technical triplicates for each experiment were averaged and used to calculate the mean and standard error of the mean for biological triplicates. Results were expressed as the number of beating bodies as well as the percentage of EBs that formed beating bodies per well of undifferentiated stem cells. Using GraphPad Prism 5.00 graphs were plotted and statistical analysis was carried out. After confirming normal distribution with the D'Agostino and Pearson omnibus K2 normality test data was analysed with regard to differences between protocols within the same cell line, differences between cell lines using the same protocol and differences between days 14 and 17 after EB formation. Differences between cell lines using the same protocol were analysed using a one-way analysis of variance (ANOVA) with a Tukey post-test. Differences between protocols within the same cell line and differences between days 14 and 17 after EB formation were analysed using a two-way ANOVA with a Bonferroni post-test. Both post-tests involved correction for multiple comparisons giving multiplicity adjusted p values.

2.5.5 Disaggregation of beating bodies

Table 6: Composition of buffers used to disaggregate beating bodies

Component	Supplier	Catalogue number	Buffer 1	Buffer 2	Buffer 3
NaCl	Sigma-Aldrich	S5886	120 mM	120 mM	-
KCl	Sigma-Aldrich	P5405	5.4 mM	5.4 mM	85 mM
MgSO ₄	Sigma-Aldrich	M2643	5 mM	5 mM	5 mM
Na pyruvate	Sigma-Aldrich	P5280	5 mM	5 mM	5 mM
Taurine	Sigma-Aldrich	T8691	20 mM	20 mM	20 mM
HEPES	Sigma-Aldrich	H3784	10 mM	10 mM	-
EGTA	Sigma-Aldrich	E0396	-	-	1 mM
Creatine	Sigma-Aldrich	27890	-	-	5 mM
CaCl ₂	Sigma-Aldrich	C5080	-	30µM	-
K ₂ HPO ₄	Sigma-Aldrich	P3786	-	-	30 mM
Na ₂ ATP	Sigma-Aldrich	A6419	-	-	2 mM
Collagenase B	Roche	1088807	-	1 mg/mL	-
pH (NaOH)		-	6.9	6.9	7.2
Glucose	Sigma-Aldrich	G8270	20 mM	20 mM	20 mM

Based on the methods published by Maltsev et al.¹⁷⁵ and Mummery et al.¹⁷⁶.

Buffers were prepared as listed in Table 6, filter-sterilised and stored at -20°C in 1 mL aliquots. Glucose was added to each aliquot after thawing. Beating areas were dissected, transferred into Buffer 1 and incubated at room temperature for 30 min. Bodies were then incubated in Buffer 2 at 37°C for 25-45 min, depending on their size, before being transferred to Buffer 3 and incubated at 37°C for 1 hour. Finally, beating bodies were transferred to 10% FCS, carefully broken up by pipetting 8-12 times using a P1000 pipette and plated onto 1% gelatine. Plating disaggregated bodies in a minimal amount of medium in droplets enhanced attachment and recovery. After 24 hours the medium was topped up and cardiomyocytes started to spontaneously contract 24-48 hours post disaggregation.

2.6 Characterisation of iPS cells and cardiomyocytes

2.6.1 Single Nucleotide Polymorphism (SNP) analysis

2.6.1.1 Sample preparation

Confluent wells of undifferentiated pluripotent stem cells were harvested with EDTA and pelleted at 200 g for 5 min. Cells were washed with PBS, centrifuged again and dry pellets were stored at -20°C. Genomic DNA was isolated from cell pellets using the MasterPure™ Complete DNA & RNA Purification Kit (Cambio, MC85200) according to manufacturer's specifications. Purified genomic DNA (500 ng) was sent to AROS Applied Biotechnology A/S (Aarhus, Denmark) for single nucleotide polymorphism (SNP) analysis. The employed SNP array, Illumina CytoSNP-12, incorporates 294,975 markers.

2.6.1.2 Analysis

The SNP array data was visualised and analysed using the Illumina Genome Viewer 1.9.0 of the Illumina GenomeStudio V2011.1 software. The Log R ratio and β -Allele Frequency (BAF) as indicators for genomic content were plotted and analysed for presence of microduplications and deletions. The Log R ratio was calculated as the

$\log_2(\text{sample/reference})$. The BAF was calculated as $(B/(A + B))$ with A and B representing the signals for each SNP. Figure 8 shows each SNP plotted according to its genotype with most SNPs clustering in the middle indicating heterozygosity. A duplication results in a sample value higher than the reference value and a shift of the Log R ratio away from zero towards more positive values. In the BAF plot duplications appear as a double band, representing genotypes of AAB or ABB. Loss of heterozygosity (LOH) as well as deletions lead to a loss of the heterozygous clusters in BAF. Deletions, but not LOH, result in a Log R ratio shift towards more negative values. Log R ratio and BAF were analysed for each chromosome for each cell line and results are attached as Appendix 1.

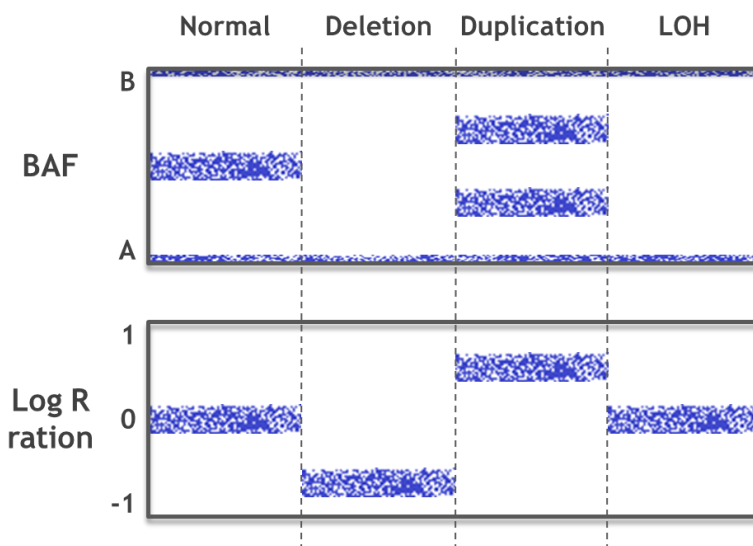


Figure 8: Schematic of SNP array analysis

The Log R ratio is calculated as the $\log_2(\text{sample/reference})$. The BAF is calculated as $(B/(A + B))$ with A and B representing the signals for each SNP. Analysed together BAF and Log R ratio can reveal the presence of deletions, duplications or loss of heterozygosity.

BAF – β -Allele Frequency, LOH – loss of heterozygosity

2.6.2 Sequencing

The patient chosen for this study had previously undergone genetic testing which identified the *SCN5A*_c.1100G>A variation as the likely cause for his condition. To confirm the presence of this variation in the iPS cell lines derived from the Brugada Syndrome patient and its absence from the iPS cell lines derived from the healthy volunteer, *SCN5A* was amplified (Verities PCR, Applied Biosystems, Austin, TX, USA), the PCR products were purified (ExoSAP-IT, Affymetrix, Inc. USB® Products, Cleveland, OH, USA) and they were directly sequenced in both directions (Big Dye Terminator v3.1 cycle sequencing kit and 3130XL Genetic Analyzer, both from Applied Biosystems). DNA sequences obtained were compared with *SCN5A* reference sequence NM_198056.2 using SeqScape v2.6 (Applied Biosystems). DNA sequencing was carried out by Dr Elisabet Selga.

2.6.3 Histology

2.6.3.1 Cell fixation

Cultured cells were PBS washed and subsequently fixed in 4% PFA for 10 min on ice or in 100% ice-cold methanol for 10 min at room temperature. The fixative was removed and cells were PBS washed and stored in PBS at 4°C until staining. PFA fixes cells by cross-linking proteins whereas methanol denatures them. Denaturation of proteins can cause epitopes to be either exposed or hidden; optimal fixation conditions may therefore vary for different antibodies and were optimised accordingly.

2.6.3.2 Immunocytochemistry

Cells fixed in 4% PFA were permeabilised with Triton X-100 (Sigma-Aldrich, T9284) in PBS for 10 min at room temperature. Unspecific antibody binding was limited by blocking with serum for 30-45 min and preparing primary antibody solutions in PBS supplemented with serum. Dilutions and staining conditions were optimised for each primary antibody and are summarised in Table 7 and Table 8.

Table 7: Antibodies used for immunostaining

Antibody Specificity	Cat #	Source	Isotype	Dilution
Nanog ^a	AF1997	Goat	IgG	1/100
Tra-1-60 ^b	sc-21705	Mouse	IgM	1/200
Oct-4 ^b	sc-101534	Mouse	IgG ₁	1/400
α -fetoprotein ^c	A8452	Mouse	IgG _{2a}	1/500
β -tubulin III ^c	T8660	Mouse	IgG _{2b}	1/1000
Muscle actin ^d	M0635	Mouse	IgG ₁	1/50
Cardiac troponin T ^e	ab8295	Mouse	IgG ₁	1/100
Cardiac troponin I ^e	ab47003	Rabbit	IgG	1/100
Alpha actinin ^e	ab50599	Rat	IgG _{2a}	1/300
Alpha actinin ^c	A5044	Mouse	IgM	1/500

^aR&D Systems, ^bSantaCruz Biotechnology, ^cSigma-Aldrich, ^dDako, ^eAbcam

Table 8: Detailed staining protocols for immunocytochemistry

	Fixation	Permeabilisation and block	Primary antibody	Secondary antibody
Nanog	4% PFA	0.1% Triton X-100 in PBS, 10 min 3% horse serum in PBS, 30 min	in 3% horse serum in PBS, 1 hour	Rabbit anti goat Alexa Fluor 568 1/400 in PBS, 1 hour
Tra-1-60	4% PFA	0.1% Triton X-100 in PBS, 10 min 3% goat serum in PBS, 30 min	in 3% goat serum in PBS, 1 hour	Goat anti mouse Alexa Fluor 488 1/400 in PBS, 1 hour
Oct-4	4% PFA	0.1% Triton X-100 in PBS, 10 min 3% goat serum, 30 min	in 3% goat serum in PBS, 1 hour	Goat anti mouse Alexa Fluor 488 1/400 in PBS, 1 hour
α-fetoprotein	100% Methanol	10% goat serum in PBST, 45 min	in 1% goat serum in PBST, 1 hour	Goat anti mouse Alexa Fluor 488 1/400 in PBS, 1 hour
β-tubulin III	100% Methanol	10% goat serum in PBST, 45 min	in 1% goat serum in PBST, 1 hour	Goat anti mouse Alexa Fluor 488 1/400 in PBS, 1 hour
Muscle actin	100% Methanol	10% goat serum in PBST, 45 min	in 1% goat serum in PBST, 1 hour	Goat anti mouse Alexa Fluor 488 1/400 in PBS, 1 hour
Cardiac troponin T	4% PFA	0.5% Triton X-100 in PBS, 10 min 3% goat serum, 30 min	in 3% goat serum in PBS, 1 hour	Goat anti mouse Alexa Fluor 488 1/400 in PBS, 1 hour
Cardiac troponin I	4% PFA	0.5% Triton X-100 in PBS, 10 min 3% goat serum, 30 min	in 3% goat serum in PBS, 1 hour	Goat anti rabbit Alexa Fluor 568 1/400 in PBS, 1 hour
Alpha actinin (mouse)	4% PFA	0.5% Triton X-100 in PBS, 10 min 3% goat serum, 30 min	in 3% goat serum in PBS, 1 hour	Goat anti mouse Alexa Fluor 488 1/400 in PBS, 1 hour
Alpha actinin (rat)	4% PFA	0.5% Triton X-100 in PBS, 10 min 3% goat serum, 30 min	in 3% goat serum in PBS, 1 hour	Chicken anti rat Alexa Fluor 488 1/400 in PBS, 1 hour

Cells were washed with PBS twice in between steps. After the last wash, cells were counterstained and mounted with ProLong Gold Antifade Reagent with DAPI (LifeTechnologies, P36935). DAPI (4',6-diamidino-2-phenylindole) is a fluorescent dye that visualises nuclei by binding strongly to A-T rich regions of the DNA. Cells grown on plastic were subsequently covered with coverslips. If cells had been grown on coverslips, these were transferred onto glass slides, cells facing down.

2.6.3.3 Tissue sectioning

Human cardiac tissue samples were processed within 30 min of arrival in the laboratory. Samples were washed with PBS and dissected into pieces $<1\text{ cm}^3$. Tissue pieces were snap frozen for 10 s in an isopentane (Sigma-Aldrich, M32631) bath in LN_2 before being stored in a small volume of isopentane at -80°C . Frozen tissue pieces were mounted onto a metal base with Tissue-Tek O.C.T. Compound (VWR International, 25608-930) and sectioned on a Vibratome UltraPro 5000 Cryostat. Each $6\text{ }\mu\text{m}$ thick section was transferred onto adhesion slides (VWR International, 631-0446) and allowed to dry at room temperature overnight.

2.6.3.4 Immunohistochemistry

Tissue sections were fixed in 4% PFA as before or in ice-cold methanol for 2 min, followed by 7 min in ice-cold acetone. After permeabilisation with 1 or 2% Triton X-100, sections were washed with PBS for 3 x 5 min. Slides were incubated with primary antibodies (Table 7) diluted in PBS or PBST for 1 hour at room temperature in a moist chamber. After 3 x 5 min washes with PBS, sections were incubated with secondary antibodies as described above (Table 8) in a moist chamber. Surplus antibodies were removed with 3 x 5 min PBS washes before briefly submerging slides in MilliQ water followed by 100% ethanol. Finally, stained tissue sections were mounted with DAPI Fluoromount-G (SouthernBiotech, 0100-20) and sealed under a coverslip. Slides were left to dry at room temperature in the dark for 24 hours before imaging. Fluorescent images were acquired at room temperature on a Zeiss Axio Observer Z1 motorised microscope using the AxioVision Software or Leica TCS SP8 using the Leica Application Suite Advanced Fluorescence Software (LAS AF 3.3.0.10134).

2.6.3.5 Flow cytometry

For each cell line three independent wells were analysed for expression of pluripotency markers SSEA-3 and SSEA-4. Pluripotent stem cells at ~80% confluency were incubated with TrypLE Select (LifeTechnologies, 12563-011) at 37°C, harvested in TeSR-E8 medium, counted and resuspended at 10⁶ cells/mL. Two FACS tubes with cell strainer caps were set up with 10⁵ cells each, one for staining, and the other one to be used as an unstained control. Cells were double stained according to specification given in Table 9 and both stained and unstained cells were incubated for 30 min at room temperature in the dark. Cells were then washed with PBS and pelleted at 900 rpm (Sigma-Aldrich, 4-16K) for 5 min at room temperature. The supernatant was decanted and cells were resuspended in 300 µL of 10% BD FACS Lysing solution (BD Biosciences, 349202) and stored at 4°C for up to 7 days before flow cytometry analysis.

Table 9: Antibodies used for flow cytometry

Antibody Specificity	Supplier	Catalogue number	Conjugate	Dilution	Isotype
SSEA-3	BioLegend	330306	Alexa Fluor 488	1/50	Rat IgM, κ
SSEA-4	BD Biosciences	560128	Phycoerythrin (PE)	1/50	Mouse IgG3

Samples were run on a FACS Fortessa Flow Cytometry System acquiring a minimum of 10,000 events. Flow cytometry data was analysed using FlowJo (Treestar, Inc., San Carlos, CA). A general gating strategy applied to all samples is depicted below. In the unstained controls the cell population of interest was selected based on cell-size and granularity (Figure 9 A), excluding dead cells and debris, before selecting single cells based on their height (SSC-H) to area (SSC-A) ratio (Figure 9 B). Afterwards, a gate was drawn for each conjugate around the negative population to exclude false positives before applying these gates to the stained samples (Figure 9 C and D). The percentage of false positive cells was subtracted from the percentage of positive cells in the stained sample. Colour compensation was

applied to compensate for overlapping emission spectra of PE and Alexa Fluor 488. Results from three independent replicates for each cell line were pooled, expressed as the mean with standard error of the mean (SEM) and plotted.

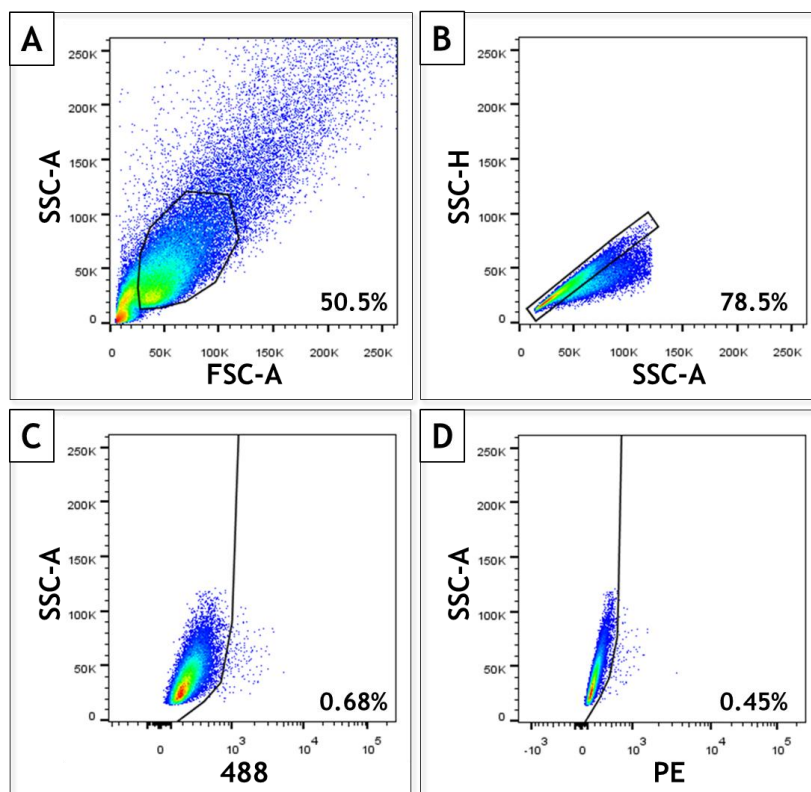


Figure 9: Representative gating strategy for flow cytometry analysis

A – cell population, **B** – single cells, **C** – Alexa Fluor 488 (SSEA-3) positive cells in unstained control, **D** – PE (SSEA-4) positive cells in unstained control

2.6.4 Reverse transcriptase polymerase chain reaction (RT-PCR)

2.6.4.1 RNA extraction and purification

RNA was extracted from cells in culture using the single-step method of RNA isolation by acid guanidinium thiocyanate-phenol-chloroform extraction developed by Chomczynski and Sacchi¹⁷⁷. Cells were lysed with TRIzol reagent (LifeTechnologies, 15596-026) containing phenol and guanidine isothiocyanate. TRIzol preserves RNA integrity while disrupting cells and denaturing proteins including RNases. Samples were either processed immediately or stored at

-20°C/-80°C. To extract RNA, samples were thawed on ice before adding 200 µL of chloroform per 1 mL TRIzol. Organic and aqueous phase were mixed by shaking vigorously and separated by centrifuging at 12000 rpm at 4°C for 15 min. In acidic conditions RNA partitions into the aqueous phase (top) while hydrophobic denatured proteins will partition into the organic phenol-chloroform phase (bottom). RNA was precipitated from the aqueous phase by transferring it to a new tube and adding an equal volume of isopropanol. After a 30 min incubation on ice RNA was pelleted by centrifuging at 12000 rpm for 15 min at 4°C, washed with 70% ethanol and pelleted again for 5 min at 4°C and 7500 rpm. After removing the supernatant the RNA pellet was air-dried without letting it dry out and resuspended in 20 µL of nuclease-free water. Dissolved RNA was stored at -20°C. Extracted RNA was purified with RQ1 RNase-Free DNase (Promega, M6101) according to the manufacturer's specifications. In summary, 1 µg of RNA was treated with 1 unit of DNase for 30-60 min at 37°C. The reaction was then stopped with Stop Solution and DNase was deactivated at 65°C for 10 min. Purified RNA was stored at -20°C.

2.6.4.2 Complementary DNA synthesis

Complementary DNA (cDNA) was synthesised by reverse transcribing 0.5-2 µg purified RNA using the High Capacity cDNA Reverse Transcription Kit (Applied Biosystems, 4368814) according to manufacturer's specifications in a final volume of 20 µL. The synthesis was performed in a Thermo Hybaid MBS 0.5G Satellite Thermal Cycler with the following programme: 25°C for 10 min, 37°C for 2 hours (reverse transcription) and 85°C for 5 min (reverse transcriptase deactivation). Synthesised cDNA was stored at -20°C or used immediately for PCR. For each cDNA synthesis a -RT control sample was prepared containing all RT-PCR reagents except the reverse transcriptase (RT). PCR amplicons of any -RT samples would result from genomic DNA contamination of isolated RNA.

2.6.4.3 Polymerase chain reaction (PCR)

Synthesized cDNA was amplified using the AmpliTaq Gold PCR Master Mix (Applied Biosystems, 4318739) according to the manufacturer's specifications with 12.5 ng cDNA per reaction and primers at 500 nM final concentration. Samples were run on a Thermo Hybaid MBS 0.5G Satellite Thermal Cycler with the program detailed below. Steps 2-4 were repeated several times while steps 1, 5 and 6 only ran once.

Step 1 (activation of Taq polymerase)	:	95°C – 5 min
Step 2 (denaturation)	:	95°C – 15 s
Step 3 (annealing)	:	T _A – 15 s
Step 4 (elongation)	:	72°C – 1.05 min
Step 5 (final prolongation)	:	72°C – 7 min
Step 6	:	4°C – hold

For analysis 20 µL of PCR product were mixed with 6x loading dye (Promega, G1881) and loaded onto a 1.5% (w/v) agarose (Sigma-Aldrich, A9539) gel prepared with 1x TBE and 1/25000 GelRed Nucleic Acid Gel Stain (Cambridge Bioscience, BT41002). The loading dye contained 0.4% orange G, 0.03% bromophenol blue, 0.03% xylene cyanol FF to track progress of migration and 15% Ficoll 400, a sucrose polymer, to increase the density of the sample to concentrate it at the bottom of the well. GelRed, intercalated in double stranded DNA, was visualised with a Gel Doc imaging system. A 1kb DNA ladder was run in order to estimate the size of the PCR products. The optimal annealing temperature (T_A) and number of cycle repeats of steps 2-4 were systematically optimised for each primer on one representative cell line (34-D6). Reactions with each primer pair were run with 30 cycles at different T_A employing a temperature gradient covering 54°C, 56°C, 58°C and 60°C (Figure 10 A). The temperature resulting in the strongest band was chosen for each primer pair and used in reactions changing the number of cycles to either 32 or 35 (Figure 10 B). Each reaction was run with cDNA as well as –RT controls and the conditions resulting in the strongest bands for cDNA reactions while showing no genomic DNA contamination in the –RT controls were chosen for each primer pair (Table 10).

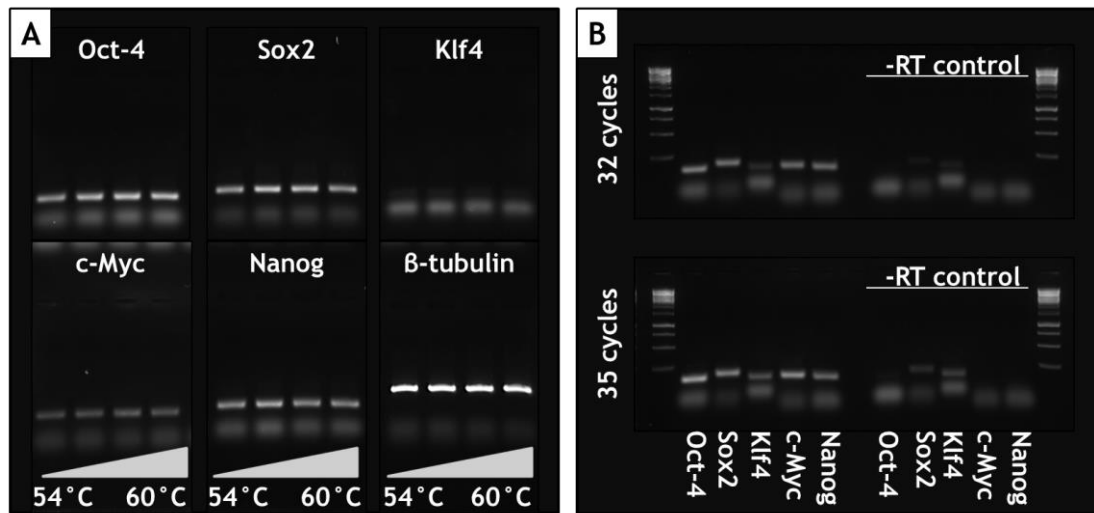


Figure 10: PCR optimisation of primers for pluripotency markers

Annealing temperature (T_A) and number of amplification cycles were systematically optimised for each primer pair on one representative cell line (34-D6). PCR products were run out on a 1.5% agarose gel. **A** – Reactions with primers for Oct-4, Sox2, Klf4, c-Myc, Nanog and β -tubulin were run with 30 amplification cycles and a T_A gradient (54°C, 56°C, 58°C and 60°C). **B** – PCR reactions for the same primer pairs were repeated with $T_A=56^\circ\text{C}$ and 32 or 35 amplification cycles. Each reaction was run with cDNA as well as –RT controls and the conditions resulting in the strongest bands for cDNA reactions while showing no genomic DNA contamination in the –RT controls were chosen for each primer pair.

Table 10: Primers used for RT-PCR with optimised conditions

Gene	Sequence forward primer (5'→3') and reverse primer (5'→3')	Product size	Number of cycles	T_A
β -tubulin	TGGCTTTGCCCTCTCACCA CGGCGGAACATGGCAGTGAA	369bp	30	56°C
c-Myc	TACCCTCTCAACGACAGCAG GTCTCCTCATGGAGCACCAGG	143bp	32	56°C
Nanog	GACAAGGTCCCGGTCAAGAA CTGAGGTCAGGATGTTGGA	140bp	32	56°C
Oct-4	CCCGCCGTATGAGTTCTGTG CATCGGAGTTGCTCTCCACC	134bp	30	56°C
Sox2	AGTCCGAGGCCAGCTCCA TAGTGCTGGGACATGTGAAGTC	160bp	30	56°C

T_A – annealing temperature

2.6.4.4 Real-time quantitative reverse transcription PCR (qPCR)

qPCR reactions were set up using the GoTaq qPCR Master Mix (Promega, A6001) kit with the following protocol. Steps 2-4 were repeated 40 times.

Master Mix	:	10 μ L
Primer mix	:	3 μ L
CXR reference dye	:	0.2 μ L
cDNA	:	3 μ L
H ₂ O	:	ad 20 μ L

Step 1 (activation of Taq polymerase)	:	95°C – 10 min
Step 2 (denaturation)	:	95°C – 10 s
Step 3 (annealing)	:	56°C – 15 s
Step 4 (elongation)	:	72°C – 20 s

The GoTaq qPCR Master Mix contains the BRYT Green dye, which fluoresces upon binding double stranded DNA. As more double stranded DNA is synthesised over the course of the PCR reaction the fluorescence signal increases. Fluorescence intensity was traced over time using a Rotor-Gene 6000 (Corbett Life Science). In addition to BRYT Green, the orange CXR signal was measured in each tube. CXR is a reference dye to which the BRYT Green signal was normalised, reducing the error between technical replicas. Finally, the melting temperature of each PCR product was investigated between 72°C-95°C, increasing temperature by 1°C per step, each step being 5 s long. Primer and cDNA concentrations were optimised before generating a standard curve for every primer pair. To that end samples were run using 1, 10, 25 and 50 ng of cDNA per reaction with a final primer concentration of 1500 nM (Figure 11 A). Next, final primer concentrations of 50, 100, 250, 500, 1000 and 1500 nM were compared using 10 ng of cDNA as template. The optimal conditions resulting in good amplification as well as no primer dimer formation were identified for each primer pair. Primer dimers were identified as secondary peaks in the melt curve analysis (Figure 11 B). Using the optimised conditions a standard curve using 1, 10, 25 and 50 ng of cDNA was generated for each primer pair to confirm $R^2 > 0.99$ (Figure 11 C).

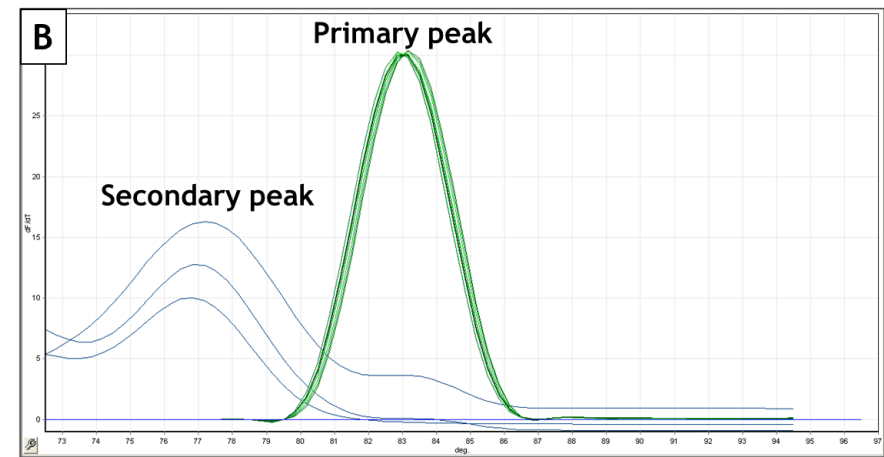
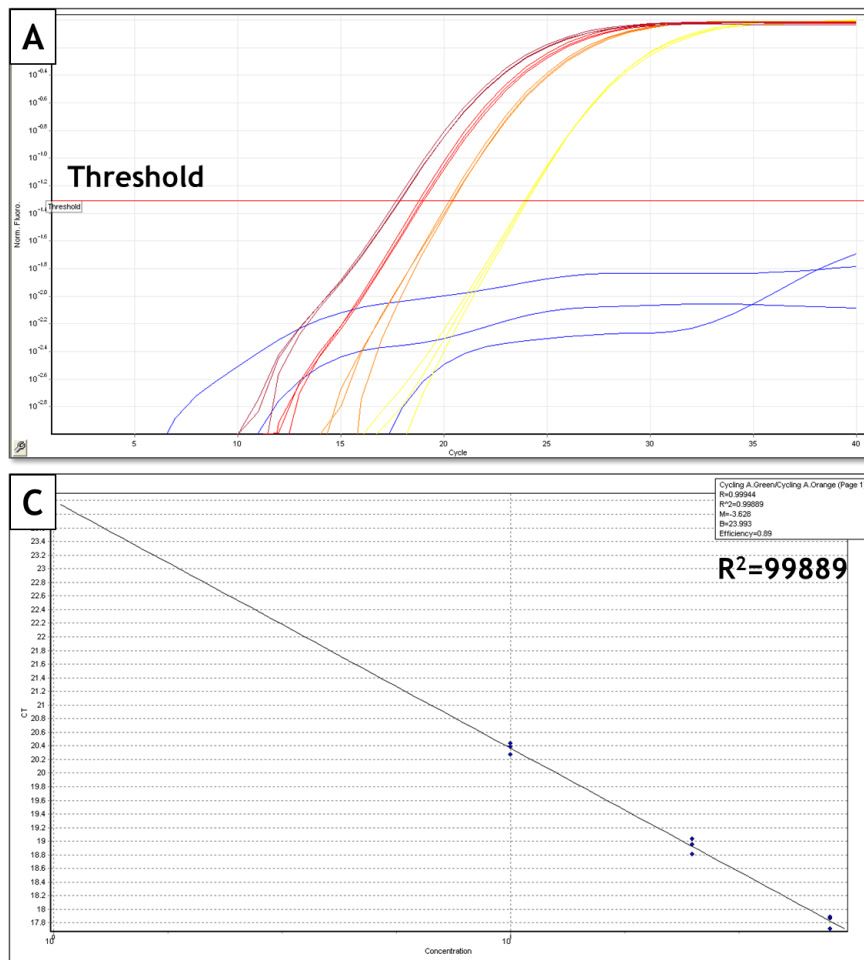


Figure 11: Optimisation of qPCR conditions

A – Primers at 1500 nM final concentration were tested with 1, 10, 25 and 50 ng of H9 cDNA to determine the detection limit of each primer pair.

B – Primers at final concentrations of 50, 100, 250, 500, 1000 and 1500 nM were compared using 10 ng of cDNA as template to identify primer concentrations resulting in good amplification as well as no primer dimer formation. Primer dimers were identified as secondary peaks in the melt curve analysis.

C – Using optimised primer concentrations a standard curve with 1, 10, 25 and 50 ng of cDNA was generated for each primer pair to confirm $R^2 > 0.99$.

In order to investigate the relative expression of pluripotency markers in each pluripotent stem cell line, each sample was run in biological triplicate using the established optimised qPCR conditions summarised in Table 11.

Table 11: Primers used for qPCR with optimised final concentration

Gene	Sequence forward primer (5'→3') and reverse primer (5'→3')	Final concentration
β-actin	CAAACATGATCTGGGTCATCTT GCTCGTCGTCGACAACGGCTC	100 nM
c-Myc	TACCCTCTCAACGACAGCAG GTCTCCTCATGGAGCACCAGG	250 nM
Nanog	GACAAGGTCCCGGTCAAGAA CTGAGGTTCAAGGATGTTGGA	250 nM
Oct-4	CCCGCCGATGAGTTCTGTG CATCGGAGTTGCTCTCCACC	50 nM
Sox2	AGTCCGAGGCCAGCTCCA TAGTGCTGGGACATGTGAAGTC	250 nM

Employing the Rotor-Gene 6000 series software 1.7 (Corbett Life Science), all BRYT Green signals were normalised to CXR signals before further analysis. Using the analysis tool a threshold was set and cycle threshold (Ct) values for each sample were exported into Microsoft Excel. Relative expression of each gene of interest (GOI) for each sample was calculated by averaging technical triplicates, relating expression of the GOI in each sample to the expression of the house-keeping gene in the same sample (ΔCt), before normalising expression to the positive control ($\Delta\Delta Ct$) and converting it to relative expression ($2^{(-\Delta\Delta Ct)}$). β -actin was used as the house-keeping gene while H9 served as positive control.

$$\Delta Ct = Ct (GOI) - Ct (House-keeping gene)$$

$$\Delta\Delta Ct = \Delta Ct(\text{sample}) - \Delta Ct(\text{positive control})$$

$$\text{Relative expression} = 2^{(-\Delta\Delta Ct)}$$

Biological triplicates were averaged, standard errors of the mean were calculated and graphs were plotted using GraphPad Prism 5.00. The relative expression of the gene of interest in different cell lines was compared using a one-way ANOVA with either the Dunnett's or Tukey post-test.

2.6.5 Transmission electron microscopy (TEM)

2.6.5.1 Sample preparation

Overnight resin: 1:1 (w/w) Araldite CY212 and Dodecenyl Succinic Anhydride (DDSA)

Final embedding resin: 11.5 g Araldite CY212, 11 g DDSA, 0.55 mLs Benzyl Dimethylamine (BDMA), 0.5 mLs Dibutylphthalate

Araldite CY212 (Agar Scientific, AGR1040)	- Epoxy resins
DDSA (Agar Scientific, AGR1051)	- Hardener for epoxy resins
BDMA (Agar Scientific, AGR1062)	- Accelerator for epoxy resins
Dibutylphthalate (Agar Scientific, R1071)	- Plasticisers

In preparation for TEM, samples underwent protein fixation, lipid fixation, dehydration and finally embedding in resin. Primary human cardiac tissue from foetal hearts, right atrial appendages and donor hearts was processed to yield pieces with a maximum diameter of 1 mm. Foetal hearts and right atrial appendages were processed within 30 min of obtaining the sample. The width of the sample was restricted by the limited penetration abilities of the fixative Glutaraldehyde (maximum penetration 0.5 mm). Proteins were fixed with 2.5% Glutaraldehyde (Sigma-Aldrich, G5882) in 4% PFA either for 1 hour at room temperature or overnight at 4°C. Samples were then either processed or stored up to 7 days at 4°C in 1% Glutaraldehyde in 0.1 M Phosphate buffer. The fixative was removed with 3 x 15 min washes in 0.1 M Phosphate buffer. Next, lipids were fixed with 1% OsO₄ in 0.1M Phosphate buffer for 1 hour at room temperature. During fixation osmium dioxide is deposited in the polar head regions of lipids resulting in staining of the plasma membrane in contrast to cytoplasm¹⁷⁸.

Lipid fixation was again followed by 3 x 15 min washes in 0.1 M Phosphate buffer and osmium tetroxide waste was deactivated with corn oil. Next, the tissue was dehydrated through a series of washes with increasing concentrations of ethanol at

50%, 70% and 90% for 3 x 5 min each. Dehydration was finalised with 2 x 10 min washes in 100% ethanol and 1 x 10 min wash in propylene oxide (Sigma-Aldrich, 82320). The tissue was transitioned to embedding resin in a 1:1 (v/v) mixture of propylene oxide and overnight resin for 1 hour at room temperature on a carousel. After propylene oxide had evaporated the tissue was transferred to overnight resin and left overnight on a carousel. The next day, the overnight resin was changed every 1.5 hours for 3.5 hours after which it was replaced with final embedding resin. Final embedding resin was changed every hour for 3 hours to ensure complete replacement of the previous resin mixture which would not harden during the final step. For the final embedding step tissues were transferred to fresh final embedding resin and left in a 60°C oven for 48 hours in order for the resin to fully harden for sectioning.

2.6.5.2 Sectioning and analysis

The final sample preparation including sectioning and staining was done by Stephen Mitchell (Manager of TEM facility) as follows. Sections (1 µm thick) were cut on a Reichert OMU4 ultramicrotome, stained with Toluidine Blue, and viewed in a light microscope to select suitable areas for investigation. Ultrathin sections (60 nm thick) were cut from selected areas, stained in Uranyl Acetate and Lead Citrate then viewed in a Philips CM120 Transmission electron microscope. Images were taken on a Gatan Orius CCD camera.

2.6.6 Intracellular Ca²⁺ handling

2.6.6.1 Sample preparation

In preparation for intracellular calcium imaging, primary tissue or beating bodies were disaggregated as described above (2.5.5 Disaggregation of beating bodies) and cells plated onto 1% gelatine coated 22 mm glass coverslips. Cells were washed 3 times with CM isolation buffer 1 with a final concentration of CaCl₂ of 1.78 mM. Intracellular Ca²⁺ was visualised using Fluo-4 (LifeTechnologies, F-14217), a dye that fluoresces when it comes in contact with Ca²⁺. Fluo-4 AM, the

non-fluorescent acetoxymethyl ester, was added to CM isolation buffer 1 (CaCl_2 1.78 mM) at a final concentration of 5 μM and cells were incubated for 30 min at room temperature in the dark during which the ester diffused into the cells and was cleaved into its active fluorescent form. The cells were washed 3 times with CM isolation buffer 1 before transferring the coverslip to a coverslip chamber and replacing the medium. Cells were incubated for a further 30 min at 37°C and 5% CO_2 before imaging. For investigation of excitation-contraction coupling a beating body was incubated for 5 min with 10 μM of the sodium channel blocker Tetrodotoxin before imaging.

2.6.6.2 Image acquisition and analysis

Spontaneously contracting cardiomyocytes were imaged at room temperature on an Olympus 1X50 microscope through a FITC filter with an optical camera (QImaging Retiga-2000R, Fast 1394) linked to the Velocity software (Version 4.2.0.). Videos were recorded in black and white at 20x or 40x magnification at a constant frame-rate of 17.8 frames per second for 20 s. Videos were analysed using the Velocity software version 6. Regions of interest (ROIs) were marked in the centre of each recorded cell and fluorescence intensity was traced over time. Data sets were exported into Microsoft Excel and fluorescence intensity plotted against time. For each cell the data set corresponding to one calcium-flash over a period of 2 s was taken, the background fluorescence subtracted, and each data point normalised to the peak value. For each cell line 14-35 cells were analysed and data for all analysed cells was pooled and each time point plotted as a mean with SEM.

2.6.7 Membrane visualisation

2.6.7.1 Sample preparation

In preparation for membrane visualisation, primary tissue or beating bodies were disaggregated as described above and cells plated onto 1% gelatine coated 22 mm glass coverslip. The outer cell membrane of single cardiomyocytes was visualised

with the membrane dye Di-8-ANEPPS (Pyridinium, 4-[2-[6-(dioctylamino)-2-naphthalenyl]ethenyl]-1-(3-sulfopropyl)-, inner salt/ 157134-53-7, LifeTechnologies, D-3167). The staining was done up to 72 hours after disaggregation of beating bodies and within 48 hours of isolation from primary tissue. This dye is less susceptible to internalisation and hence suitable to visualise outer membrane structures such as transverse tubules. Di-8-ANEPPS was added to cells in culture medium at a final concentration of 5 μ M and incubated for 10 min at 37°C. Surplus Di-8-ANEPPS was removed with 3 washes of PBS before coverslips were transferred to a coverslip chamber and medium was replaced. Cells were incubated for 30 min at 37°C before imaging to allow recovery of spontaneous contraction.

2.6.7.2 Image acquisition and analysis

Cardiomyocytes were identified through spontaneous contraction and imaged at 37°C and 5% CO₂ using the Leica TCS SP8 STED. Di-8-ANEPPS was excited at 400-500nm with the 488 nm line of the argon-ion laser, emission was measured at 550-700nm. Z-stacks were recorded using the Leica Application Suite Advanced Fluorescence Software (LAS AF 3.3.0.10134).

2.6.8 Electrophysiology

Beating bodies were disaggregated and plated onto gelatine-coated glass coverslips as described previously for immunocytochemistry. In collaboration with Prof Ramon Brugada's research group at the Universitat de Girona, in particular with Dr Fabiana Scornik and Dr Guillermo Pérez, settings for sodium current recordings in single stem cell-derived cardiomyocytes were optimised. Electrophysiological recordings were performed on single cells, identified as cardiomyocytes by their morphology and/or spontaneous contraction, usually 1-2 days after disaggregation. Short recovery time ensured limited attachment to culture plastic. While attachment of cells itself is crucial, limited contact area between the cell and the culture surface largely contributes to good voltage control. Buffers were prepared as listed in

, filter sterilised and stored at -20°C . Pipettes were pulled from glass capillaries (BF150-117-10, Sutter Instruments Co) with a PC-10 vertical Puller (Narishige). Pipette resistances ranged from 2.8 to 3.5 $\text{M}\Omega$ when filled with pipette solution. Whole cell sodium currents were measured at room temperature using the perforated patch-clamp technique in voltage clamp mode. In this set-up, one electrode is placed in the bath solution and is connected to ground, while a second electrode, inside a glass pipette filled with the mentioned solution, is electrically connected to the cytoplasm of a cell of interest.

Table 12: Buffers for electrophysiology

Component	Supplier	Catalogue number	Bath solution		
			High Na^+	Low Na^+	Pipette solution
NaCl	Sigma-Aldrich	S5886	140 mM	40 mM	10 mM
HEPES	Sigma-Aldrich	H3375	10 mM	10 mM	10 mM
KCl	Sigma-Aldrich	P5405	3 mM	3 mM	-
CaCl_2	Sigma-Aldrich	C5080	1.8 mM	1.8 mM	-
MgCl_2	Sigma-Aldrich	M8266	1.2 mM	1.2 mM	-
NMdG	Sigma-Aldrich	M2004	-	100 mM	-
L-Aspartic acid	Sigma-Aldrich	A9256	-	-	130 mM
EGTA	Sigma-Aldrich	E0396	-	-	1 mM
MgATP	Sigma-Aldrich	A9187	-	-	2 mM
pH			7.4 (NaOH)	7.4 (HCl)	7.2 (CsOH)
Glucose	Sigma-Aldrich	G0350500	~ 323 mOsm	~ 323 mOsm	~ 305 mOsm

NMdG – N-Methyl-D-glucamine

In this perforated patch-clamp setting the pipette solutions ionic composition matches that of cytoplasm and contained 240 µg/mL Amphotericin B (Sigma-Aldrich, A9528). Over time (~15-30 min) Amphotericin B permeabilises the cell membrane, thereby creating an electrical connection between the electrode in the pipette and the inside of the target cell. In voltage-clamp experiments the voltage is kept constant while changes in current are recorded. Voltage clamp experiments were controlled and analysed with an Axopatch 200B amplifier and pClamp 10.2 / Digidata 1440A acquisition system (Molecular Devices) and OriginPro 8 software (OriginLab Corporation). Data were typically filtered at 5 kHz and sampled at 20 kHz. To study the relationship of current-density to the voltage applied (I-V), currents were elicited by 50 ms depolarising steps (from -80 to +80 mV in 5 mV increments) from a holding potential of -120 mV. Current density was calculated by normalising the peak current for each applied potential to the cell's capacitance. A cell's capacitance (C_m) depends on its size and normalisation of recorded currents to C_m , termed current density, allowed comparison between different sized cells. The current density for each applied potential was plotted as the mean \pm SEM using GraphPad Prism 5.00.

Initial recordings of H9-derived cardiomyocytes in a bath solution containing 140 mM sodium showed sodium currents too large to accurately represent voltage-dependent sodium channel activation (Figure 12). As mentioned in the introduction, in normal sodium conditions, a small change in membrane potential leads to a drastic influx of sodium ions, producing large inward currents which make it difficult to accurately control the voltage in an experimental setting. In order to get a more accurate representation of voltage-dependent sodium channel activation, a low sodium bath solution was used. Sodium currents in 34-D6 and BP-derived cardiomyocytes were recorded by Dr Elisabet Selga using previously established protocols.

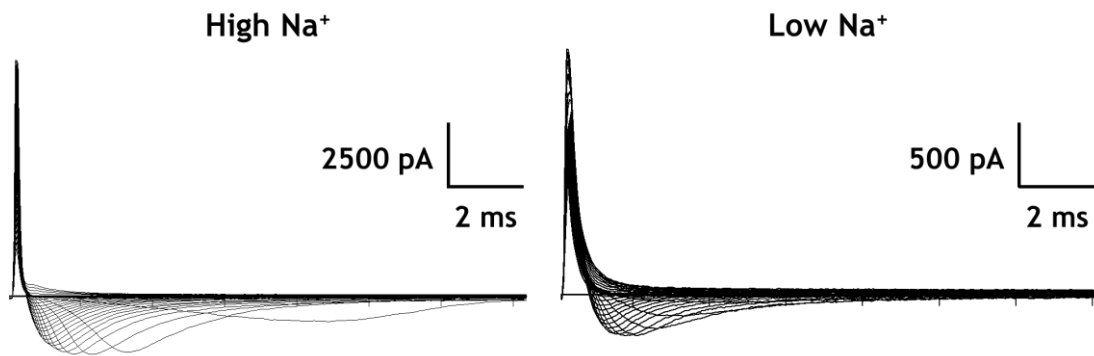


Figure 12: Sodium current recordings in High Na⁺ and Low Na⁺ bath solution

Sodium currents in a single pluripotent stem cell-derived cardiomyocyte were elicited by increasing potentials and recorded in bath solutions containing high (140 mM) or low (40 mM) concentrations of sodium. When using High Na⁺ bath solution, a sudden increase in sodium current was recorded, while in Low Na⁺ bath solution the gradual increase in potential corresponded to a gradual increase in current.

2.7 Statistical Analysis

Data was plotted as mean \pm SEM and statistically analysed in GraphPad Prism 5.00. Normal distribution was confirmed with the D'Agostino and Pearson omnibus K2 normality test. Differences between independent groups, each consisting of three or more samples, were investigated using a one-way ANOVA. To correct for multiple comparisons the Tukey post-test was employed in cases where all groups were compared to each other and the Dunnett's post-test in cases where all groups were compared to a control group. Where two independent variables were analysed a two-way ANOVA with a Bonferroni post-test was used.

CHAPTER 3

CHARACTERISATION OF PLURIPOTENT STEM CELLS AND THEIR DIFFERENTIATION TO CARDIOMYOCYTES

3.1 Abstract

Human embryonic and induced pluripotent stem cells can be differentiated towards any lineage, providing a source for otherwise difficult to obtain cell types, including cardiomyocytes. Using a set of comprehensive tests, three pluripotent stem cell lines (H9, 33-D9, 34-D6) were assessed. Under a light microscope cells showed stem cell morphology while quantitative reverse transcription PCR demonstrated expression of pluripotency markers Oct-4, Sox2, Nanog and c-Myc. Flow cytometry and immunocytochemistry additionally demonstrated presence of pluripotency cell surface markers SSEA-3, SSEA-4 and Tra-1-60. All tested pluripotent stem cell lines were able to form the three germ layers. SNP analysis identified microduplications in H9 in chromosome 7 and 14, both regions are not associated with genes, and one common microduplication in 33-D9 and 34-D6 that has been associated with long term cell culture. Subsequent differentiation towards cardiomyocytes employed a systematic comparison of a variety of protocols investigating efficiency with total numbers as well as percentages of beating bodies as the end-point. Results revealed significant inter-line variability and found that guided differentiation protocols could be used to reliably and efficiently generate beating bodies. Protocols optimised in this chapter can be used at subsequent stages to characterise newly generated patient-derived iPS cell lines and to efficiently generate beating bodies from them in order to characterise patient-specific cardiomyocytes.

3.2 Introduction

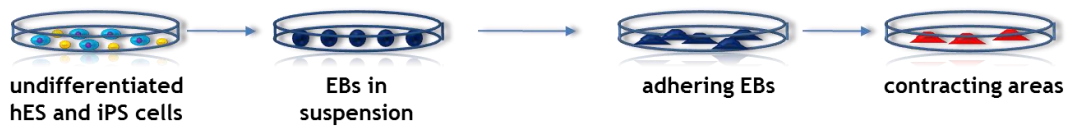
Human embryonic stem (hES) cells can be differentiated into any cell type, theoretically offering an unlimited supply of cells of interest that might otherwise be difficult to obtain from primary sources. However, in addition to their controversial nature, hES cells are less than ideal as a disease model system for numerous reasons. Access to hES cells harbouring the disease of interest is very limited and genetically manipulating hES cells has its own challenges¹⁷⁹. Furthermore, it would require knowledge of the genetic background that causes the disease, and therefore limits this approach to monogenic diseases. Yamanaka and colleagues¹⁰⁵ demonstrated that somatic cells can be reprogrammed to a pluripotent state by the introduction of a number of transcription factors involved in pluripotency and proliferation^{180, 181}, thereby providing an alternative for hES cells. The initial experiments were conducted using the transcription factors for octamer-binding transcription factor 4 (Oct-4), sex determining region Y-box 2 (Sox2), Krüppel-like factor 4 (Klf4) and c-Myc, introducing them to the host cell through retroviruses¹⁰⁵. The resulting reprogrammed cells (induced pluripotent stem (iPS) cells) were almost indistinguishable from embryonic stem cells in morphology, cell surface markers, gene expression and their ability to differentiate into cells from all three germ layers. The major advantage of this technique is that skin cells carrying a desired genetic profile can be obtained directly from the patient, reprogrammed and differentiated to cells from the specific tissue affected by the disease. Additionally, this technique allows the study of mutant proteins in their native environment, including all modifier proteins, independent of whether the genetic alteration is known or not.

A variety of differentiation protocols for deriving cardiomyocytes from pluripotent stem cells have been published (Figure 13), all of which belong to one of three categories. Protocols are based on unguided differentiation, guided differentiation or co-culture, with efficiency being the lowest for unguided and highest for guided differentiation^{141, 146, 150}. However, comparison of the different protocols is complicated by the fact that efficiency might be expressed as either total number or percentage of beating bodies. A common problem with most methods remains the inter-line variability of cardiac differentiation potential which has been attributed to

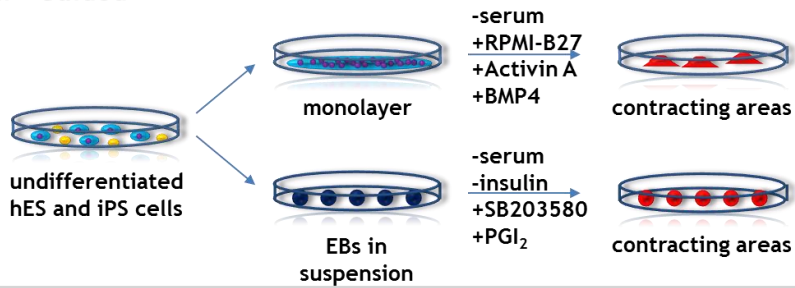
genetic as well as epigenetic differences between cell lines^{182, 183}. Furthermore, considerable heterogeneity of cardiac and non-cardiac cells exists within beating bodies. Interestingly, depending on which differentiation protocol is applied the ratio of the specific cardiac cell types within the contractile tissue changes¹⁸⁴.

Model systems utilising iPS cell technology rely on the fact that the cell lines derived are pluripotent and genetically unaltered after reprogramming. Comprehensive tests to assess pluripotency and differentiation potential of derived cell lines are therefore crucial. Because of the differences in assessment of efficiency and inter-line variability, a systematic comparison of cardiac differentiation protocols investigating numbers as well as percentages of beating bodies derived from three pluripotent stem cell lines is necessary to find a reliable protocol to be used on patient-derived iPS cell lines.

I - Unguided



II - Guided



III - END-2 co-culture

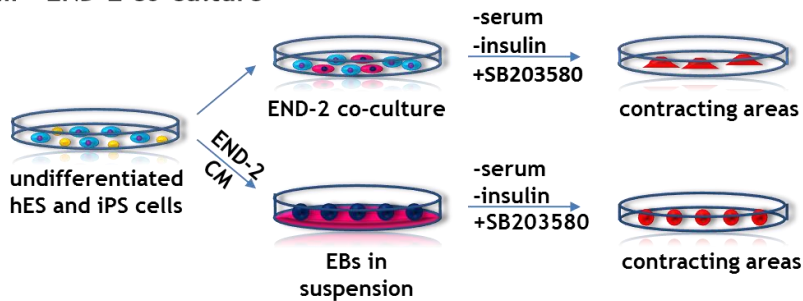


Figure 13: Overview of protocols employed to generate cardiomyocytes from iPS and hES cells

I - Unguided differentiation, EBs are formed from undifferentiated hES and iPS cells and cultured in suspension in low-attachment plates for 7 days before being plated onto coated plates¹⁸⁵. Unguided differentiation is the least efficient way to generate cardiomyocytes and shows vast inter-line variability; **II** – Guided differentiation, undifferentiated hES and iPS cells are cultured either as a feeder-free monolayer or as EBs in suspension in low-attachment plates. Alternatively, for a more standardised protocol, 3D structures are formed using the hanging drop or forced aggregate method. Monolayer and aggregates are then treated with various factors such as BMP4 and activin-A for several days^{134, 157}. EBs are plated onto coated plates after 6 days in suspension. Protocols based on guided differentiation show the highest efficiency for generating cardiomyocytes but the same inter-line variability as unguided differentiation; **III** – END-2 co-culture, undifferentiated hES or iPS cells are either co-cultured feeder-free with growth arrested END-2 cells or as EBs in END-2 conditioned medium (END-2 CM). Removal of serum and insulin, as well as supplementation with the MAPK inhibitor SB203580 and Prostaglandin I₂ (PGI₂) has been proven to enhance cardiac differentiation^{146, 148-150}.

3.3 Aims

To establish comprehensive tests to assess pluripotency and differentiation potential of pluripotent stem cells and to systematically compare and optimise cardiac differentiation protocols to establish a reliable, efficient and robust protocol.

3.4 Results

One hES (H9) and two previously generated human iPS cell lines (33-D9 and 34-D6) were fully characterised investigating their morphology, genomic integrity, expression of pluripotency markers and ability to differentiate into all three germ layers. These cell lines were subsequently used to compare efficiency and reproducibility of published guided and unguided cardiac differentiation protocols. Protocols optimised in this chapter were later used to characterise newly generated healthy volunteer and patient-derived iPS cell lines and to efficiently differentiate both to cardiomyocytes.

3.4.1 Morphology

Pluripotent stem cells were cultured either on a mouse embryonic fibroblast (MEF) feeder layer or feeder-free in TeSR-E8 medium (Figure 14). The morphology of pluripotent stem cells in culture was assessed daily with a light microscope and used as an indicator of pluripotency. H9, 33-D9 and 34-D6 grew in flat densely packed colonies, cells exhibiting the high nucleus to cytoplasm ratio typical for hES and iPS cells. Spontaneously differentiated cells were observed occasionally in the feeder-free culture system using TeSR-E8 medium and regularly when cultured on a MEF feeder-layer. In addition, colonies grown feeder-free appeared more densely packed and survived lower seeding densities after passaging. No obvious differences in morphology were observed between earlier (p40) and later (p80) passages.

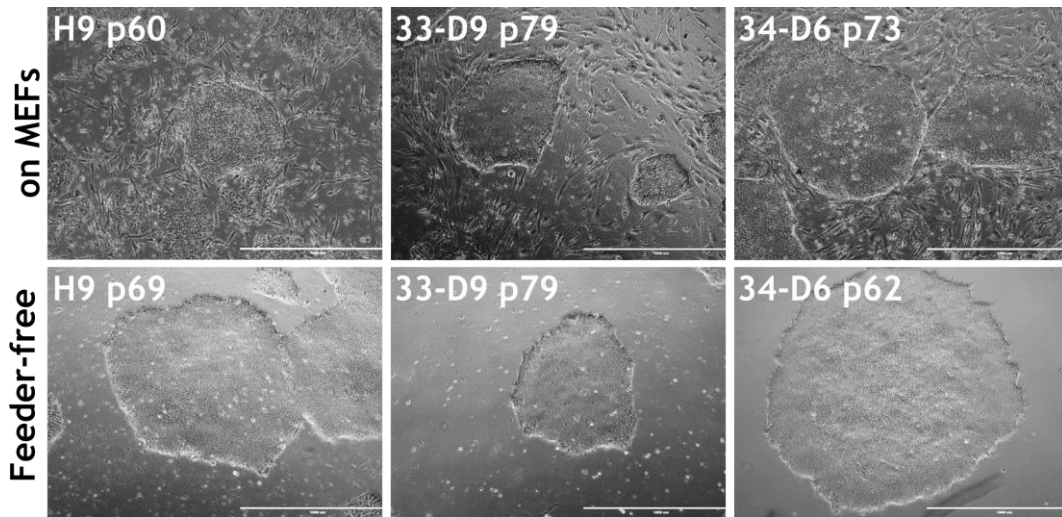


Figure 14: Morphology of hES and iPS cells in culture

Representative light microscopy images of human pluripotent stem cell lines H9, 33-D9 and 34-D6 in culture on MEFs and feeder-free. Scale bars represent 1000 μm .

3.4.2 Chromosomal integrity

Genomic DNA was extracted from each of the three pluripotent stem cell lines and analysed for genomic integrity with a single nucleotide polymorphism (SNP) array. Analysis of the LogR ratio in combination with the β -Allele frequency revealed two microduplications in H9 and one microduplication each in 33-D9 and 34-D6 (Figure 15). No microdeletions were detected. A complete list of all chromosomes is supplied in the Appendix 1.

Microduplications in H9 were found in chromosome 7 (q11.21, 62.139.338 - 62.834.662) and chromosome 14 (q23.2, 63.569.297 - 63.668.333) in regions that are not associated with known genes. Both 33-D9 and 34-D6 showed microduplications in q11.21 in chromosome 20, including *ID1*, *BCL2L1* and *HMI3*, genes expressed in hES cells. This particular microduplication has previously been described in cultured hES and iPS cells and was expected not to interfere with pluripotency or differentiation potential¹⁸⁶.

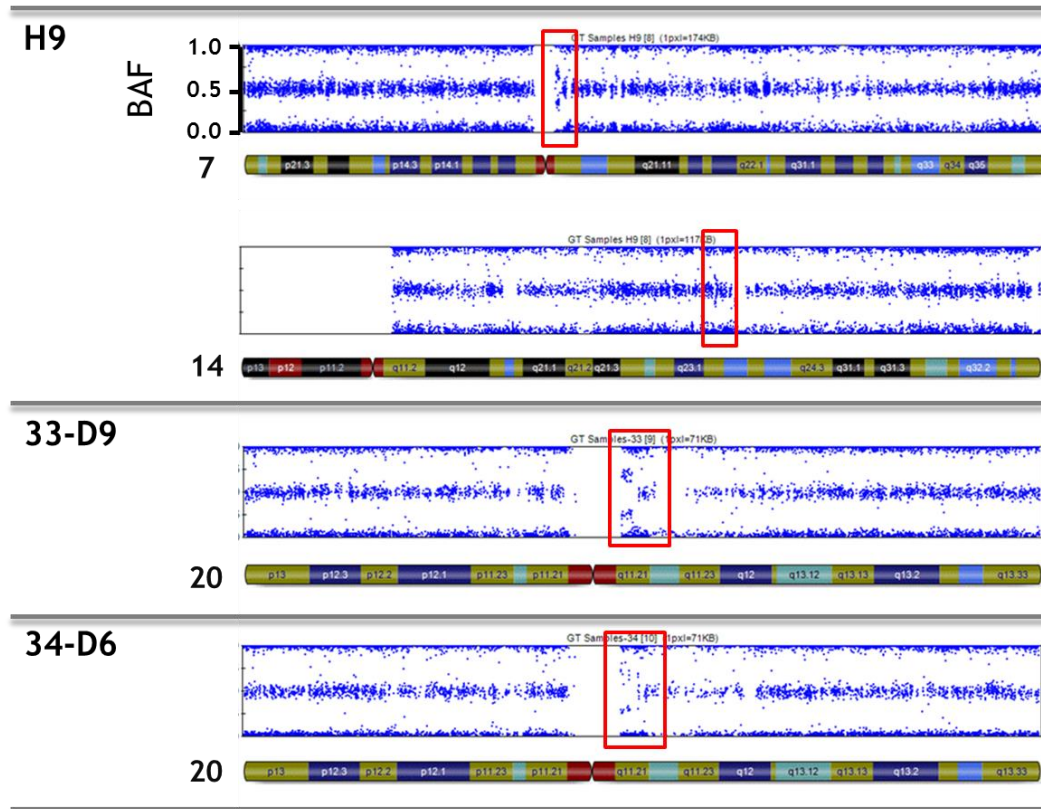


Figure 15: Microduplications identified through SNP analysis

Analysis of the β -Allele Frequency of a SNP array revealed microduplications in H9 in chromosomes 7 (q11.21, 62.139.338 - 62.834.662) and 14 (q23.2, 63.569.297 - 63.668.333), both in non-coding regions. Microduplications in chromosome 20 (q11.21) in 33-D9 and 34-D6 affected several genes, including *IDI1*, *BCL2L1* and *HMI3*, genes expressed in hES cells. Red box indicates position of microduplication. BAF – β -Allele Frequency.

3.4.3 Expression of pluripotency markers - Reverse transcription polymerase chain reaction

Expression of pluripotency markers in undifferentiated cultures was investigated using reverse transcription followed by polymerase chain reaction (RT-PCR). RNA from fibroblasts and undifferentiated cell lines H9, 33-D9 and 34-D6 was extracted, purified and reverse transcribed to complementary DNA (cDNA). Reverse transcription of messenger RNA (mRNA) to cDNA allows investigation into whether a gene of interest is being expressed. To that end, cDNA was PCR amplified using

exon spanning primers designed to prevent amplification of genomic DNA. PCR conditions for primers for pluripotency markers Oct-4, Sox2, Nanog and c-Myc, and the house-keeping gene β -tubulin were optimised with regard to annealing temperature and number of amplification cycles as described in Materials and Methods (2.6.4.3 Polymerase chain reaction). H9, 33-D9 and 34-D6 showed expression of Oct-4, Sox2, Nanog, c-Myc and β -tubulin, while fibroblasts exhibited expression of c-Myc and β -tubulin but not Oct-4, Sox2 or Nanog (Figure 16). Although the intensity of a band can be indicative of relative expression of the gene of interest in different cell lines RT-PCRs are not quantitative. A –RT control sample contains all RT-PCR reagents except the reverse transcriptase and therefore PCR amplicons of any –RT sample represent genomic DNA contamination of isolated RNA.

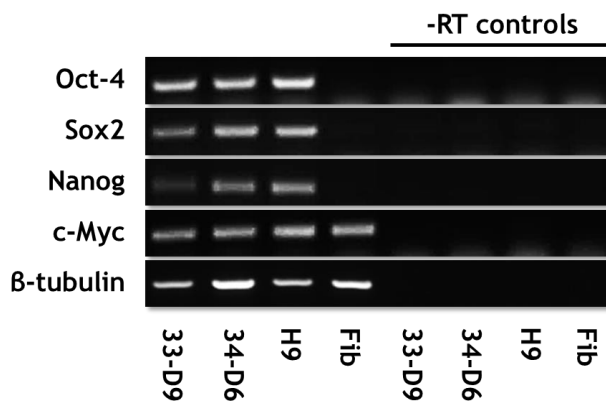


Figure 16: RT-PCR analysis of pluripotency markers

RNA from fibroblasts and undifferentiated H9, 33-D9 and 34-D6 was extracted, purified and reverse transcribed to cDNA. cDNA was PCR amplified using exon spanning primers for pluripotency markers Oct-4, Sox2, Nanog and c-Myc, and the house-keeping gene β -tubulin. PCR products were run out on a 1.5% agarose gel and visualised with GelRed Nucleic Acid Gel Stain. H9, 33-D9 and 34-D6 show expression of β -tubulin, Oct-4, Sox2, Nanog and c-Myc while fibroblasts exhibit expression of β -tubulin and c-Myc but not Oct-4, Sox2 or Nanog. Fib – fibroblasts; –RT control – test for genomic DNA contamination

3.4.4 Expression of pluripotency markers - Quantitative RT-PCR

In order to compare relative expression of pluripotency markers, quantitative RT-PCR (qPCR) was employed. RNA from undifferentiated cultures was extracted, purified and reverse transcribed as before for each sample in biological triplicate. Primer and cDNA concentrations were optimised for each primer-set as detailed in Materials and Methods (2.6.4.4 Real-time quantitative reverse transcription PCR) and samples were run in technical triplicate. H9, 33-D9, 34-D6 and fibroblasts were tested for expression of Oct-4, Sox2, c-Myc and Nanog.

For each sample the expression of the gene of interest was related to expression of the house-keeping gene β -actin in the same sample, before normalising expression to the positive control H9. Relative expression of all genes of interest, given as the mean of biological triplicates with the standard error of the mean (SEM), is shown in Figure 17. The relative expression of the gene of interest in different cell lines was compared using a one-way analysis of variance (ANOVA) with a Tukey post-test. Undifferentiated H9, 33-D9 and 34-D6 express all pluripotency transcription factors at similar levels with no significant differences. Fibroblasts, as previously observed with RT-PCR, expressed no Oct-4, Sox2 or Nanog but c-Myc at levels not significantly different from H9.

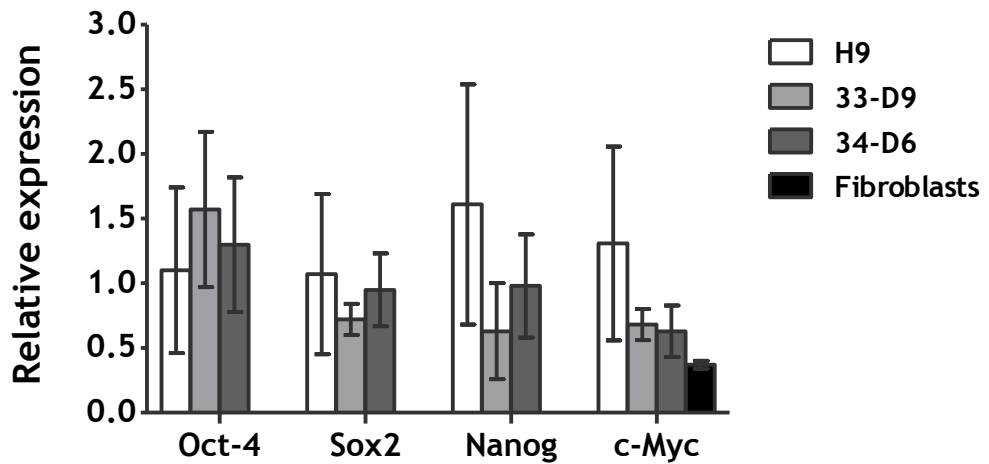


Figure 17: Pluripotency transcription factor expression

Relative expression of pluripotency transcription factors Oct-4, Sox2, c-Myc and Nanog was investigated in fibroblasts and undifferentiated H9, 33-D9 and 34-D6. Fibroblasts express no Oct-4, Sox2 or Nanog but c-Myc. H9, 33-D9 and 34-D6 express pluripotency transcription factors at similar levels with no significant differences (one-way ANOVA). Bars represent mean values of biological triplicates with error bars representing SEM.

3.4.5 Expression of pluripotency markers - Immunocytochemistry

Undifferentiated pluripotent stem cells were fixed 2 days after passaging and stained for pluripotency markers Nanog, Oct-4 and Tra-1-60. Nuclei were counterstained with DAPI. As Nanog and Oct-4 are transcription factors, the staining co-localises with the DAPI counterstain. Tra-1-60, a keratan sulfate proteoglycan, on the other hand is a cell surface antigen. All three cell lines showed Nanog and Oct-4 staining co-localising with DAPI and cell surface staining with Tra-1-60 (Figure 18). Differentiated cells surrounding the colonies did not stain for pluripotency markers but are visible as DAPI stained nuclei.

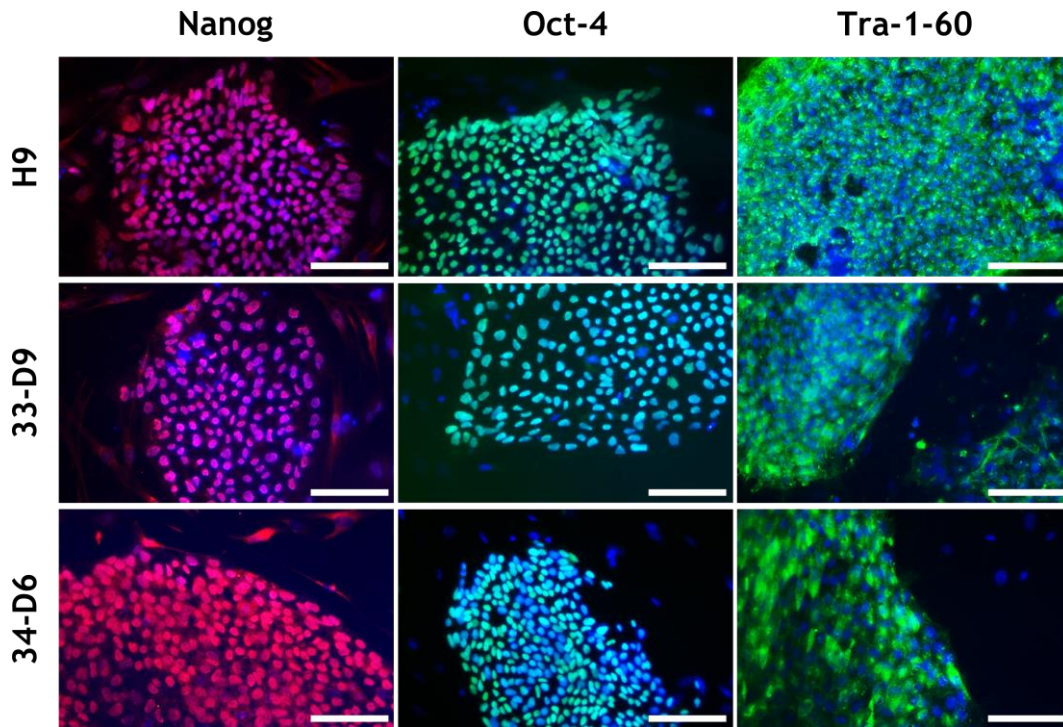


Figure 18: Immunocytochemistry for pluripotency markers Nanog, Oct-4 and Tra-1-60

H9, 33-D9 and 34-D6 stain positive for pluripotency markers Nanog, Oct-4 and Tra-1-60. Nuclei were counterstained with DAPI (blue). Scale bars represent 100 μm .

3.4.6 Expression of pluripotency markers - Flow cytometry

The percentages of stage-specific embryonic antigen 3 (SSEA-3) and SSEA-4 positive cells in the undifferentiated population of H9, 33-D9 and 34-D6 were investigated using flow cytometry. SSEA-3 and SSEA-4 are cell surface markers associated with stem cells. Each cell line was harvested, stained and analysed in biological triplicate. For each sample an unstained control was used to eliminate false positive cells. Cells were gated as described in detail in the Materials and Methods (2.6.3.5 Flow cytometry) to include single cells of the cell population of interest and exclude debris and cell aggregates. Figure 19 shows representative histograms of undifferentiated H9, 33-D9 and 34-D6 stained for cell surface markers SSEA-3 and SSEA-4.

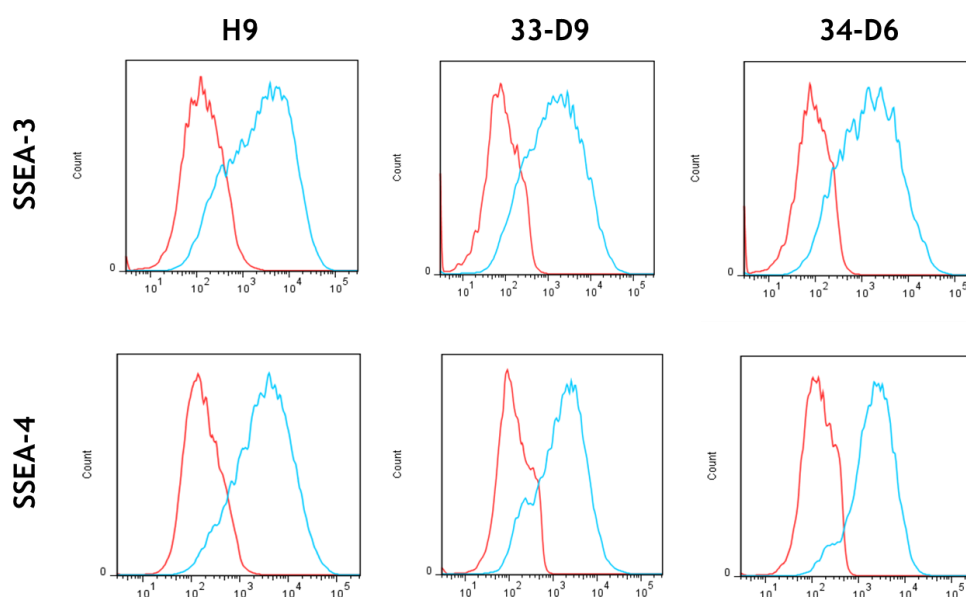


Figure 19: Flow cytometry analysis of pluripotency markers SSEA-3 and SSEA-4

Representative histograms of undifferentiated H9, 33-D9 and 34-D6 stained for cell surface markers SSEA-3 and SSEA-4. All three cell lines showed a clear shift of stained (blue) samples from unstained controls (red).

Results of biological triplicates were pooled and expressed as a mean value with the SEM. Undifferentiated cultures of all three cell lines contained a high percentage of SSEA-3 (H9 $80.1 \pm 5.7\%$, 33-D9 $74.7 \pm 7\%$, 34-D6 $81.1 \pm 2.9\%$) and SSEA-4 (H9 $88.3 \pm 2.2\%$, 33-D9 $85.1 \pm 2.4\%$, 34-D6 $92 \pm 2.7\%$) positive cells (Table 13).

Table 13: Percentage of cells expressing SSEA-3 and SSEA-4

	H9	33-D9	34-D6
SSEA-3	80.1 ± 5.7	74.7 ± 7.0	81.1 ± 2.9
SSEA-4	88.3 ± 2.2	85.1 ± 2.4	92.0 ± 2.7

3.4.7 Three germ layer formation

Embryoid bodies (EBs) formed from undifferentiated H9, 33-D9 and 34-D6 grown on a feeder layer were cultured in EB medium in suspension for 7 days before being cultured for 10 additional days on gelatine coated dishes. EBs were then fixed and stained for markers of the three germ layers endoderm (Alpha-fetoprotein, AFP), ectoderm (β -tubulin III) and mesoderm (muscle actin). All three pluripotent stem cell lines showed positive staining for markers of all three germ layers (Figure 20).

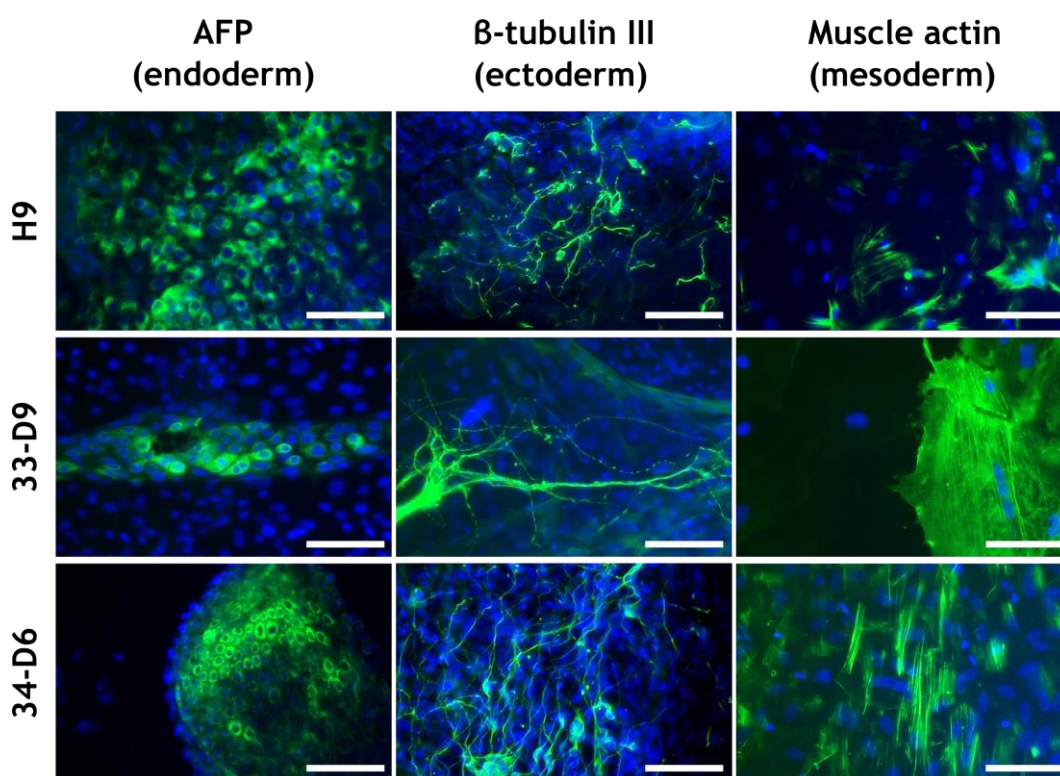


Figure 20: Immunocytochemistry for the three germ layers

EBs were formed from undifferentiated H9, 33-D9 and 34-D6 and differentiated in suspension for 7 days and for an additional 10 days adherent to plates. Fixed EBs stained positive for markers of all three germ layers endoderm (AFP), ectoderm (β -tubulin III) and mesoderm (muscle actin). Nuclei were counterstained with DAPI (blue). Scale bars represent 100 μ m.

3.4.8 Comparison of cardiac differentiation protocols

At the start of this project, several cardiac differentiation protocols had been published, all of which belonged to one of three categories: guided differentiation, unguided differentiation or co-culture with END-2 cells. To make results comparable and efficiency quickly assessable only protocols involving EB formation were selected. All differentiation protocols involved EB formation for 24 hours and subsequent culture in suspension with media changes every 3 days for 15-25 days. EBs were formed from undifferentiated cultures with and without incubation with collagenase and in different media with the aim to form EBs of equal size. Size, morphology and survival of EBs were assessed for 7 days after EB formation and the most efficient protocol (30 s collagenase treatment, media supplemented with serum) was used for the following experiments. In order to identify a protocol that would efficiently, robustly and reliably generate cardiac tissue from a number of pluripotent stem cell lines, one protocol from each category was chosen. For unguided differentiation, EBs were cultured in medium supplemented with 20% HyClone FCS. The medium for guided differentiation consisted of a serum-free base medium (bSF) supplemented with SB203580, an inhibitor of the p38-MAPK pathway, and Prostaglandin I₂ (PGI₂). Instead of direct co-culture, EBs were cultured in END-2 cell conditioned medium (END-2 CM). The initial screen, a summary of which is provided in Figure 21, solely considered if a protocol generated beating bodies. Results showed that at least one protocol from each of the three categories generated beating bodies.

Unguided differentiation: Culturing EBs in medium supplemented with 20% HyClone serum for the entire duration of differentiation was successful in generating beating bodies.

Guided differentiation: Differentiation in bSF supplemented with SB203580 and PGI₂ generated contracting cardiac tissue when EBs were formed in medium containing serum or in bSF supplemented with SB203580 and PGI₂ but not in bSF alone.

	EB formation 24 hours	Differentiation medium 15-25 days	Beating bodies
Unguided	20% HyClone	20% HyClone	Yes
	iPS medium	bSF	No
Guided	iPS medium	bSF+SB+PGI ₂	Yes
	bSF	bSF+SB+PGI ₂	No
	20% HyClone	bSF+SB+PGI ₂	Yes
	bSF+SB+PGI ₂	bSF+SB+PGI ₂	Yes
Co-culture	bSF	END-2 CM	No
	20% HyClone	END-2 CM	No
	END-2 CM	END-2 CM	No
	bSF	END-2 CM+SB	Yes
	20% HyClone	END-2 CM+SB	No
	END-2 CM+SB	END-2 CM+SB	Yes

Figure 21: Initial comparison of different EB formation media and cardiac differentiation media

All differentiation protocols tested were based on EB formation for 24 hours and subsequent culture in suspension with media changes every 3 days for 15-25 days. Different combinations of EB formation media and differentiation media were assessed for beating body formation in an initial screen using one iPS cell line. Media were chosen based on previously published work on cardiac differentiation using unguided, guided and co-culture protocols. Compositions of media are listed in section 2.1.2 Media. bSF – basic serum-free medium; CM – conditioned medium; PGI₂ – Prostaglandin I₂; SB – p38 MAPK inhibitor SB203580

Co-culture: END-2 CM by itself failed to produce beating bodies but succeeded in combination with the small molecule SB203580 when EBs were formed in bSF or SB203580 supplemented END-2 CM.

Based on data from the initial screen 3 protocols were chosen for in-depth comparison of efficiency. The first protocol, unguided differentiation, was chosen because of its simplicity. The second protocol selected was the guided differentiation protocol using bSF supplemented with SB203580 and PGI₂. Although the initial

screen showed cardiac differentiation for both guided differentiation and END-2 co-culture, the former had been developed as a chemically defined medium mimicking the cardiogenic effects of END-2 CM and was therefore considered preferable because of its xeno-free composition. Lastly, a third protocol was created by combining the first two, differentiating EBs in medium supplemented with 20% HyClone serum, SB203580 and PGI₂. Two previously published studies had reported an inhibitory effect of serum on cardiac differentiation efficiency^{150,148}. However, one study counted the total number of beating bodies, whereas the other assessed the percentage of beating bodies of all EBs. In both studies beating areas were scored on day 12 of the differentiation.

We hypothesised that the presence of serum might not inhibit cardiac formation but rather delay it and therefore counted beating bodies on days 14 and 17 after EB formation. In order to make counting beating bodies faster, the above listed differentiation protocols used for the efficiency comparison were altered to allow for attachment of EBs. To that end, EBs were maintained in suspension for the first 4 days and were subsequently plated onto tissue-culture treated plates. In addition to simplifying the assessment, attachment on day 4 after EB formation had previously been shown to enhance cardiomyocyte development¹³⁹. Each of the 3 protocols was performed for each cell line (H9, 33-D9 and 34-D6) in technical triplicate as well as biological triplicate. Technical triplicates for each experiment were averaged and results were expressed as the total number of beating bodies formed per well of a 6 well plate of undifferentiated cells as well as the percentage of EBs that formed beating bodies. The D'Agostino and Pearson omnibus K2 normality test showed normal distribution of the data. In accordance with that, means and SEM of biological triplicates, displayed in Figure 22, were analysed with tests appropriate for normally distributed data. Using GraphPad Prism, data was analysed with regard to differences between cell lines using the same protocol, differences between protocols within the same cell line and differences between days 14 and 17 after EB formation. Differences between cell lines using the same protocol were analysed using a one-way ANOVA with a Tukey post-test. Differences between protocols within the same cell line and differences between days 14 and 17 after EB formation were

analysed using a two-way ANOVA with a Bonferroni post-test. Both post-tests involved correction for multiple comparisons resulting in multiplicity adjusted p-values.

Results from the statistical analysis of total numbers of beating bodies are summarised in Table 14. The serum-free guided protocol (bSF+SB+PGI₂) generated significantly more beating bodies for 34-D6 than 33-D9 on day 14 ($p<0.05$). The unguided protocol produced significantly more beating bodies on day 17 for H9 than 33-D9 ($p<0.05$). There were no significant increases from day 14 to day 17 for any protocol using any cell line. 34-D6 showed significant differences between protocols ($p<0.05$). The Bonferroni post-test showed that for 34-D6, significantly more beating bodies were generated with the serum-free guided protocol (bSF+SB+PGI₂) on day 17 compared to using the unguided protocol ($p<0.05$). Similarly, for 33-D9 the guided protocol containing serum resulted in significantly more beating bodies on day 17 than the unguided protocol ($p<0.05$).

Results from the statistical analysis of percentages of beating bodies are summarised in Table 15. Comparing percentages of beating bodies, the unguided protocol produced significantly more beating bodies on day 17 for H9 compared to 33-D9 ($p<0.05$) and 34-D6 ($p<0.05$). Again, there were no significant increases from day 14 to day 17 for any protocol using any cell line. 34-D6 showed significant differences between protocols ($p<0.01$). The Bonferroni post-test showed that significantly more beating bodies had been generated after 17 days with guided protocols compared to using the unguided protocol (with serum $p<0.05$, serum-free $p<0.01$).

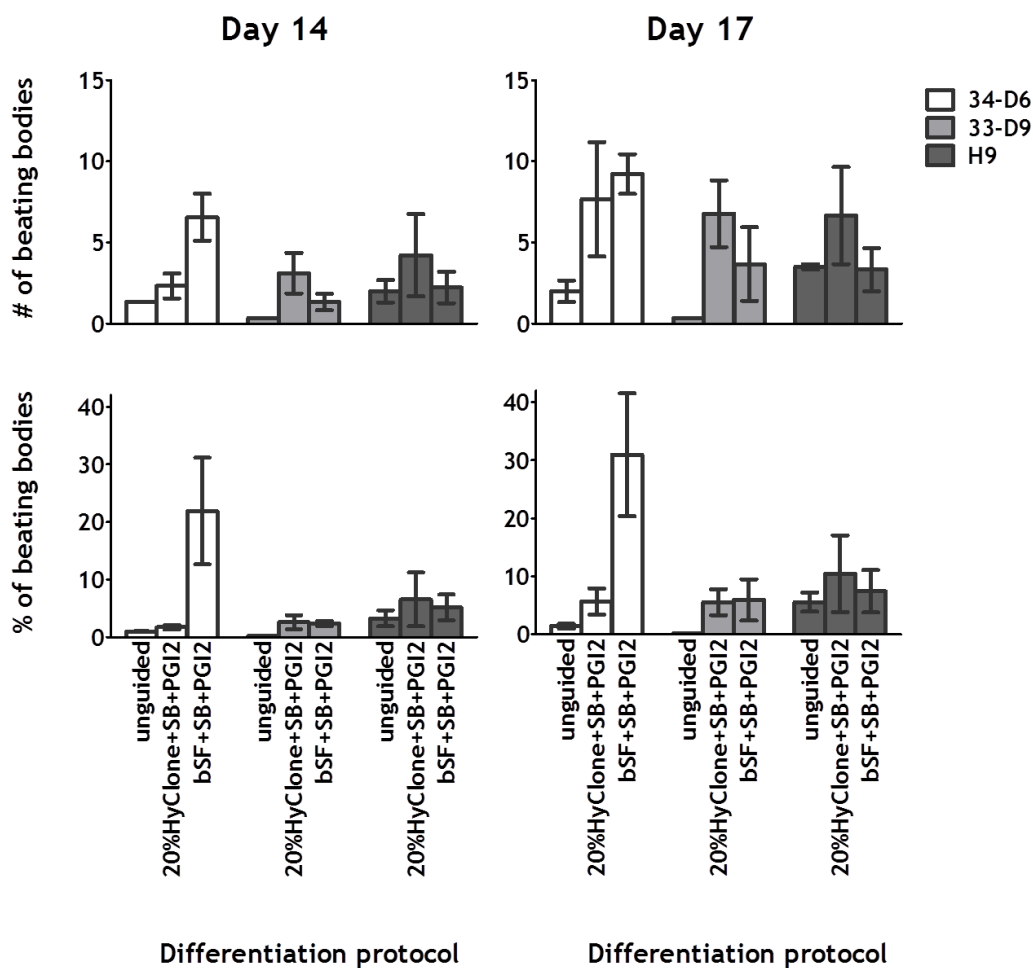


Figure 22: Comparison of unguided and guided cardiac differentiation protocols in three pluripotent stem cell lines

EBs were formed from undifferentiated 33-D9, 34-D6 and H9 and cultured in suspension in 20% HyClone (unguided), 20% HyClone supplemented with SB203580 and PGI₂ (guided) or bSF supplemented with SB203580 and PGI₂ (guided). After 4 days, EBs were plated onto 0.1% gelatine, cultured for a further 13 days and beating bodies were counted on day 14 and day 17 after EB formation. Each of the 3 protocols was performed for each cell line in technical triplicate as well as biological triplicate. Technical triplicates for each experiment were averaged and results were expressed as the total number of beating bodies formed per well of a 6 well plate of undifferentiated cells as well as the percentage of EBs that formed beating bodies. Bars represent means of biological triplicates with error bars representing SEM. Means and SEM are shown for total numbers and percentages on day 14 and day 17.

Table 14: Statistical comparison of total numbers of beating bodies generated during cardiac differentiation

Cell line	Day 14			Day 17			Two-way ANOVA	
	Unguided	20% HyClone +SB+PGI ₂	bSF +SB+PGI ₂	Unguided	20% HyClone +SB+PGI ₂	bSF +SB+PGI ₂	Protocol	Day of count
33-D9	0.33 ± 0.001	3.11 ± 1.25	1.33 ± 0.51 †	0.33 ± 0.001 #	6.78 ± 2.06 ‡	3.67 ± 2.27	0.051	0.160
34-D6	1.33 ± 0.001	2.33 ± 0.77	6.56 ± 1.44	2 ± 0.67 *	7.67 ± 3.53	9.22 ± 1.22	0.011	0.058
H9	2 ± 0.69	4.22 ± 2.54	2.22 ± 0.97	3.5 ± 0.17	6.67 ± 3	3.33 ± 1.33	0.273	0.277
One-way ANOVA	0.145	0.743	0.026	0.045	0.966	0.112		

† p<0.05 Tukey's Multiple Comparison post-test comparing cell line 33-D9 and 34-D6 for the guided protocol (bSF+SB+PGI₂)

p<0.05 Tukey's Multiple Comparison post-test comparing cell line 33-D9 and H9 for the unguided protocol

‡ p<0.05 Bonferroni Multiple Comparison post-test comparing unguided and guided protocol (20% HyClone+SB+PGI₂) for cell line 33-D9

* p<0.05 Bonferroni Multiple Comparison post-test comparing unguided and guided protocol (bSF+SB+PGI₂) for cell line 34-D6

Table 15: Statistical comparison of percentage of beating bodies generated during cardiac differentiation

Cell line	Day 14			Day 17			Two-way ANOVA	
	Unguided	20% HyClone +SB+PGI ₂	bSF +SB+PGI ₂	Unguided	20% HyClone +SB+PGI ₂	bSF +SB+PGI ₂	Protocols	Day of count
33-D9	0.22 ± 0.01	2.6 ± 1.25	2.36 ± 0.46	0.21 ± 0.001	5.59 ± 2.24	5.96 ± 3.55	0.156	0.235
34-D6	0.98 ± 0.05	1.73 ± 0.42	21.91 ± 9.27	1.44 ± 0.41 §	5.71 ± 2.25 \$	30.95 ± 10.57 **	0.002	0.363
H9	3.28 ± 1.4	6.56 ± 4.7	5.16 ± 2.23	5.6 ± 1.65 #	10.46 ± 6.59	7.45 ± 3.66	0.564	0.370
One-way ANOVA	0.149	0.478	0.09	0.027	0.590	0.107		

** p<0.01 Bonferroni post-test comparing unguided and guided protocol (bSF+SB+PGI₂) for cell line 34-D6

\$ p<0.05 Bonferroni post-test comparing guided protocols (20% HyClone +SB+PGI₂ and bSF+SB+PGI₂) for cell line 34-D6

p<0.05 Tukey's Multiple Comparison post-test comparing cell line H9 and 33-D9 for the unguided protocol

§ p<0.05 Tukey's Multiple Comparison post-test comparing cell line H9 and 34-D6 for the unguided protocol

3.5 Discussion and Conclusion

The aims of this chapter were to establish comprehensive tests to assess pluripotency and differentiation potential of pluripotent stem cells and to establish a reliable, efficient and robust cardiac differentiation protocol, both to be used at a later stage on patient-derived iPS cell lines. Analysis of one hES cell line and two iPS cell lines showed comparable morphology and expression of pluripotency markers on mRNA and protein level. All analysed pluripotent stem cell lines formed all three germ layers and successfully underwent cardiac differentiation. Comparison of three cardiac differentiation protocols for these three stem cell lines showed significant inter-line variability with regard to efficiency of cardiac formation.

Evaluating the morphology of pluripotent stem cells in culture is the easiest and quickest way to evaluate the state of the cells in question on a daily basis. Changes in morphology can be indicative of karyotypic abnormalities or cells leaving their undifferentiated state. However, morphology of stem cells can differ between cell lines as well as between culture systems making it more difficult to notice and interpret changes in morphology. For an accurate characterisation of stem cells, a more in depth analysis is required to determine karyotypic integrity, pluripotency and differentiation potential. Genomic integrity was examined with a SNP array instead of the traditional karyotyping; because of their higher resolution, SNP arrays are more accurate than regular karyotyping, detecting microdeletions and microduplications that would otherwise be missed. However, SNP arrays are unable to detect translocations and inversions because all individually detected SNPs are subsequently sorted by a computer program to generate a digital karyogram. Genomic integrity is known to decrease over time in long-term cultures¹⁸⁶ and should therefore be investigated regularly. Indeed, both iPS cell lines 33-D9 and 34-D6 carried a microduplication in chromosome 20q11.21, which has been shown to occur in >20% of stem cell lines in culture. The region includes three genes, *ID1*, *BCL2L1* and *HM13*, which are expressed in human pluripotent stem cells. With its anti-apoptotic role, *BCL2L1* is likely the reason for positive selection of this microduplication in culture¹⁸⁶. Based on this assessment, the 20q11.21 microduplication was not expected to adversely interfere with pluripotency or

differentiation in the affected cell lines. Microduplications found on chromosomes 7 and 14 in the hES cell line H9 were not associated with known genes and were therefore not expected to have an effect on pluripotency or differentiation potential. Pluripotency was assessed and confirmed for all three stem cell lines on an mRNA as well as protein level. RT-PCR offers a fast if not quantitative screening method for expression of genes of interest. Beside the difference in band intensity, all pluripotent stem cell lines showed a profile distinctly different from fibroblasts. Although often associated with pluripotency or cancer cells, c-Myc plays an integral role in proliferating cells¹⁸⁷, expression in fibroblasts was therefore expected. The difference in band intensity of the house-keeping gene β -tubulin between different samples suggests that an unequal amount of cDNA was used as template for PCR amplification. The β -tubulin band was the weakest for 33-D9 suggesting the least amount of cDNA was used. Less cDNA as a template for the PCR reaction in 33-D9 compared to the other samples could explain the weaker bands observed for Nanog and Sox2. Quantitative RT-PCR confirmed that in spite of different band intensities in the RT-PCR there are in fact no significant differences in expression levels of the pluripotency markers in 33-D9 compared to H9. Since the data is presented as the mean of three biological replicas with varying passage numbers, the relatively large error bars could be indicative of changes in pluripotency marker expression over time. The error could also result from a varying number of differentiated cells in the culture.

On a protein level, flow cytometry analysis showed that pluripotency markers were expressed on a high percentage of pluripotent stem cells. The small number of cells negative for SSEA3 and SSEA4 might be explained by the gating strategy based on forward and side scatter not entirely excluding differentiated or differentiating cells. Prior to these experiments, both antibodies had been titrated to find the optimal working concentration; insufficient amounts of antibody could therefore be excluded as an issue. Expression of pluripotency markers was also confirmed visually with immunocytochemistry. Colonies showed nuclear staining for transcription factors Oct-4 and Nanog and cell surface staining for Tra-1-60 indicating a pluripotent phenotype.

Besides differentiating to all three germ layers, all tested stem cell lines formed spontaneously beating cardiac tissue using a variety of protocols. Guided protocols generated significantly more beating bodies than the unguided protocol for both iPS cell lines but not the hES cell line. Due to the small sample size there is no reason to assume that this is due to inherent differences between iPS and hES cell lines rather than inter-line variability. Variability of cardiac differentiation potential can be attributed to genetic as well as epigenetic differences between cell lines^{182, 183}. Overall, the comparison showed that different protocols work significantly better than others across the different cell lines. Inter-line variability for the same protocol as well as differences between protocols investigating the same cell line had been expected based on previous publications^{188, 189}. Contrary to expectations, serum did not have an inhibitory effect on the total number or percentage of beating bodies for two of the three pluripotent stem cell lines (H9 and 33-D9). The third cell line (34-D6) showed little difference in terms of total numbers but a significantly higher percentage of beating bodies under serum-free conditions. These results emphasised the importance of keeping the assessment of efficiency consistent in order to make direct comparisons between published protocols possible.

Employing three pluripotent stem cell lines, a set of comprehensive tests to assess pluripotency and differentiation potential was established. Comparison of cardiac differentiation protocols using the same stem cell lines found that guided differentiation protocols could be used to reliably and efficiently generate beating bodies. Protocols optimised in this chapter can be used at subsequent stages to characterise newly generated patient-derived iPS cell lines and to efficiently generate beating bodies from them.

CHAPTER 4

CHARACTERISATION OF HUMAN CARDIAC TISSUE AND PLURIPOTENT STEM CELL-DERIVED CARDIOMYOCYTES

4.1 Abstract

During development of the heart, cardiomyocytes undergo changes in physiology and electrophysiological properties and detailed characterisation of adult and foetal cardiomyocytes will enable assessment of the maturity and function of stem cell-derived cardiomyocytes. Cardiomyocytes were successfully isolated from foetal and adult cardiac tissue. Morphological and structural comparison using light microscopy, immunocytochemistry, immunohistochemistry, and transmission electron microscopy demonstrated the expected classical adult and foetal phenotypes with great differences in morphology and organisation and ultrastructure of their contractile apparatus. Adult cardiomyocytes displayed rod-shaped morphology and parallel aligned myofibrils with fully formed sarcomeres. In contrast, foetal cardiac cells were not rod-shaped, had fewer myofibrils that lacked parallel alignment and showed immature sarcomeres lacking I-bands, A-bands, H-zones and M-lines. Cardiomyocytes derived from hES cells (H9) and healthy control iPS cells (34-D6) using guided differentiation more closely resembled foetal than adult cardiomyocytes but altogether showed an intermediary phenotype. While most cells had immature contractile apparatus comparable with foetal cardiomyocytes, a few cells showed greater numbers of myofibrils with increased alignment and sarcomeres with I-bands and A-bands in addition to Z-lines. Membrane staining revealed that like foetal cardiomyocytes they exhibited no t-tubules, however, compared to foetal controls, stem cell-derived cardiomyocytes displayed faster calcium removal from sarcoplasm. Finally, sodium currents were recorded from individual pluripotent stem cell-derived cardiomyocytes. Protocols optimised in this chapter will subsequently be used to characterise derived patient-specific cardiomyocytes.

4.2 Introduction

The heart is the first functional organ to be formed in the human embryo and starts to spontaneously contract at the beginning of the fourth week¹⁹⁰. During cardiac morphogenesis, cell clusters containing cardiac progenitor cells form a tube that later loops and divides into the four chambers of the adult heart.

During gastrulation cells migrate through the primitive streak to form the three germ layers ectoderm, endoderm, and mesoderm¹⁹¹. The mesoderm, the layer between ectoderm and endoderm, spreads laterally and cranially within the embryonic disc and ultimately gives rise to the lateral plate mesoderm. Approximately, on day 18 blood islands are formed from these lateral plate mesoderm cells which migrate and form a crescent shape at the cranial border, the prospective head of the embryo¹⁹². Blood islands contain haemangioblasts and cardiac progenitors. While endothelial cells differentiated from haemangioblasts form an endocardial tube on either side of the midline, cardiac progenitor cells differentiate to myoblasts and then cardiomyocytes that will form the myocardium surrounding the endocardial tubes. At the beginning of the fourth week the two endocardial tubes migrate towards the midline where they fuse into the primitive heart tube and start to spontaneously contract. Cells of the endocardial tubes will line the inside of the heart chambers and valves, while the surrounding myocardium forms the cardiac muscle of the ventricles and the atria. As the brain develops during the fourth week, the primitive heart tube is moved in a ventral direction, away from the head, forcing it to fold in on itself, resulting in the formation of the first primitive atrium and ventricle.

Cardiac morphogenesis is driven by spatially and temporally regulated inhibition and activation of signalling proteins and transcription factors. Proteins secreted by the anterior endoderm induce cardiac specification of the lateral mesoderm. While neural differentiation of these cells is prevented through Wnt inhibitors, Bone morphogenetic protein 2 (BMP-2) and Fibroblast growth factor 8 (FGF-8) activate expression of Nkx2.5 leading to the formation of cardiac myoblasts¹⁹³. Nkx2.5 is a cardiac specific transcription factor that induces expression of the transcription factors Myocyte-specific enhancer factor 2C (MEF-2c) and GATA-4 that in turn

activate the expression of cardiac muscle specific proteins¹⁹⁴. This activation causes the differentiation from cardiac myoblasts to cardiomyocytes. Laterality of each cell, meaning whether they will contribute to the left or right side of the heart, is mainly determined by transcription factors Heart- and neural crest derivatives-expressed protein 1 (HAND1) and HAND2. This decision is made even before fusion of the endocardial tubes.

While little is known about the mechanisms that subsequently drive maturation of foetal to adult cardiomyocytes, the changes in gene expression, morphology and functionality that accompany this transition have been well documented. Prior to tube formation smooth muscle actin is the only isoform present before up-regulation of cardiac sarcomeric actin marks the onset of spontaneous contraction^{195, 196}. For a short period of time contractions are isotropic, uniform in all directions, before they become directionally dependent, i.e. anisotropic.

Regulation of myofibrillogenesis is not well understood but different steps involved have been described¹⁹⁷. Initially, myofibrils are disorganised but become aligned in response to mechanical load throughout development. The number of myofibrils increases at the same rate as the number of mitochondria supplying ATP essential for contractions. As the cardiomyocytes become more mature, mitochondria increase in size and gain cristae, folds of a mitochondrion's inner membrane^{198, 199}. Formation of the sarcoplasmic reticulum (SR) coincides with the development of transverse tubules (t-tubules), invaginations in the cell membrane closely associated with the SR network and crucial for excitation-contraction coupling, at a relatively late stage of structural morphogenesis of the heart^{200, 201}.

Maturation also sees changes in electrophysiological properties largely due to increased expression of ion channels. The resting potential increases, i.e. becomes more negative²⁰⁰, the peak calcium current and density increase²⁰² and while in foetal cells calcium release from SR is triggered by Na^+ - Ca^{2+} exchange, in adult cardiomyocytes it is triggered by calcium entry through T-type calcium channels²⁰³.

Being able to evaluate the level of maturity of iPS cell-derived cardiomyocytes will be helpful in interpreting the results from patient-specific cardiomyocytes and to determine their use and limitations for modelling disease. However, while it might be essential to have cardiomyocytes with an adult phenotype in case of modelling cardiac diseases that are acquired or affect channels that are expressed only at a relatively late stage of myogenesis (e.g. Phospholamban) that does not apply to modelling cases of Brugada Syndrome caused by a mutation in *SCN5A*. The gene encoding for the alpha subunit of cardiac sodium channel $Na_v1.5$ is expressed at high levels in immature cardiomyocytes and Brugada Syndrome affects children as well as adults.

4.3 Aims

To assess the maturity and functionality of pluripotent stem cell-derived cardiomyocytes by comparing them to isolated primary human adult and foetal cardiomyocytes.

4.4 Results

Considering the extent of cardiomyocyte characterisation and the fact that no differences between 34-D6 and 33-D9 had been observed in Chapter 3, analysis of stem cell-derived cardiomyocytes was limited to one hES and one iPS cell line.

Beating bodies were generated from human ES (H9) and iPS (34-D6) cell lines characterised in Chapter 3 using guided cardiac differentiation established to be the most efficient protocol for these lines in the same chapter. Protocols to assess cardiomyocytes for cardiac markers, ultrastructure and functionality were first tested and optimised on primary human tissue. These validated protocols were subsequently used to characterise the cardiomyocytes derived from H9 and 34-D6. Finally, the results obtained were compared to primary human cardiomyocytes isolated from adult and foetal tissue.

4.4.1 Morphology

4.4.1.1 *Primary cardiac tissue*

Previously published protocols for the isolation of viable human cardiomyocytes^{173, 174} were tested and modified as required for adult and foetal cardiac tissue.

Adult cardiac tissue was obtained with consent from two sources, atrial and ventricular donor tissue from the Scottish National Blood Transfusion Service (SNBTS) and right atrial appendages (RAA) from patients undergoing cardiac surgery. All samples were processed within 30 min of collection.

At 24-48 hours post isolation, adult cardiomyocytes had typical rod-shaped morphology with visible striations (Figure 23 A, B) but showed very limited attachment and survival in both 10% DMEM and M199 medium. SNBTS, particularly ventricular, tissue yielded considerably more cells than RAA due to vast differences in available tissue size. Foetal cardiomyocytes, more spindle than

rod-shaped without visible striations, attached quickly and spontaneously contracted after 24 hours (Figure 23 C, D) with no apparent differences between culture in 10% DMEM and M199 medium. A video of spontaneously contracting foetal cardiomyocytes in culture is supplied in Appendix 2.

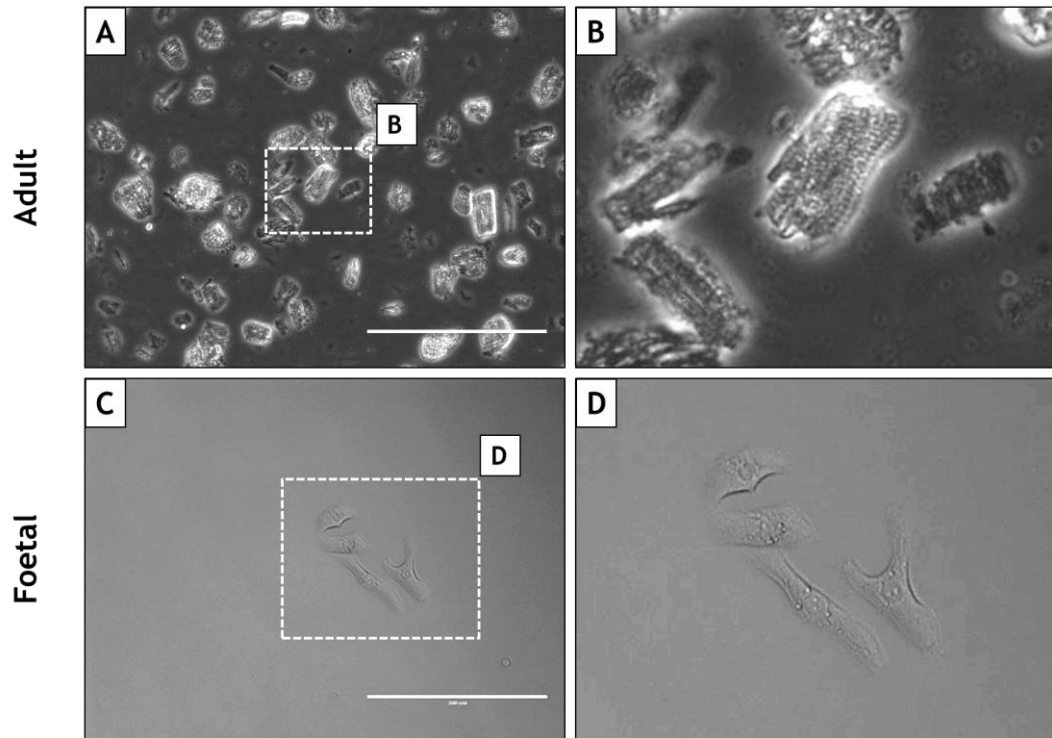


Figure 23: Morphology of adult and foetal cardiomyocytes

Cardiomyocytes were isolated from primary human adult and foetal tissues through enzymatic digestion. Morphology was assessed 24-48 hours after isolation. **A and B** – Adult cardiomyocytes, isolated from atrial and ventricular donor tissue and right atrial appendages, had typical rod-shaped morphology with visible striations but showed very limited attachment and survival. **C and D** – Foetal cardiomyocytes, isolated from 11-16 week old foetuses, were more spindle shaped, showed no visible striations, attached quickly and contracted spontaneously. Representative images of 3 biological replicates for each sample are shown. B and D are magnified areas in A and C respectively. Scale bars represent 200 μm .

4.4.1.2 *Pluripotent stem cell-derived beating bodies and cardiomyocytes*

Beating bodies were generated from human ES (H9) and iPS (34-D6) cell lines using the guided cardiac differentiation protocols established in Chapter 3 (Figure 24 A and C). Beating bodies varied in size and rate at which they contracted even when derived from the same stem cell line using the same differentiation protocol. The percentage of cardiomyocytes within a beating body, estimated by the size of the contracting area, also differed. With regular dissections to remove surrounding proliferating non-cardiac tissue, beating bodies could be maintained in culture for several months.

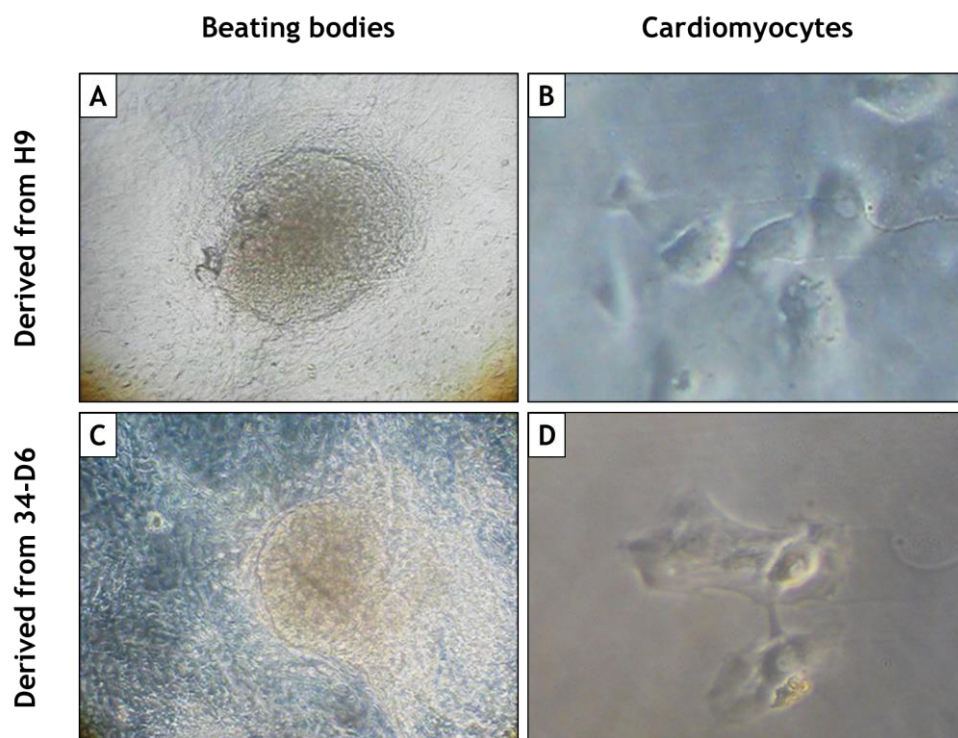


Figure 24: hES and iPS cell-derived beating bodies and single cardiomyocytes

A and C (10x magnification) – H9 (hES) and 34-D6 (iPS) were differentiated using guided cardiac differentiation protocols. Size, contraction rate and percentage of contractile tissue within a beating body differed between beating bodies. Beating bodies were cultured for 3-4 weeks before enzymatic and mechanical disaggregation. **B and D** (40x magnification) – Disaggregation resulted in single as well as clusters of beating cardiomyocytes, with groups of connected cardiomyocytes exhibiting synchronised contraction. Spontaneously contracting stem cell-derived cardiomyocytes showed morphologies similar to foetal cardiomyocytes. Representative images of 5 biological replicates for each sample are shown.

Cardiomyocytes characterised in this chapter were isolated from beating bodies cultured for 3-4 weeks. To investigate the morphological and functional properties of pluripotent stem cell-derived cardiomyocytes on a single cell level, beating bodies were enzymatically and mechanically disaggregated and plated onto 1% gelatine. Disaggregation resulted in single as well as clusters of beating cardiomyocytes, with groups of connected cardiomyocytes exhibiting synchronised contraction. Stem cell-derived cardiomyocytes started contracting as early as 24 hours post disaggregation and showed morphologies similar to foetal cardiomyocytes (Figure 24 B and D). Videos of spontaneously contracting stem cell-derived beating bodies and cardiomyocytes in culture are supplied in Appendix 2. Beating bodies do not contain a pure population of cardiomyocytes but rather a mixture of cell types. Therefore, to allow for attachment but prevent overgrowth by proliferating non-cardiac cells, cardiomyocytes were analysed 3-4 days after disaggregation.

4.4.2 Expression of cardiac markers

4.4.2.1 Primary human cardiac tissue

Staining protocols for cardiac markers were optimised on primary human cardiac tissue varying conditions for permeabilisation, blocking of unspecific antibody binding and antibody concentrations. Adult cardiac tissue from SNBTS donors and RAA were dissociated and plated onto 1% gelatine or laminin. Cells were fixed 24 or 72 hours post isolation and stained for alpha actinin, a protein of the cardiac contractile apparatus that is localised at the Z-lines. Staining of cells fixed 24 hours after isolation for alpha actinin resulted in the characteristic striation pattern of intact and parallel aligned myofibrils (Figure 25 A, B). Cardiomyocytes isolated from both tissues showed limited attachment and survival. Cells fixed 72 hours post isolation exhibited a loss of rod-shaped morphology, loss of parallel alignment of myofibrils as well as a lack of myofibril organisation with some striation patterns remaining (Figure 25 C, D).

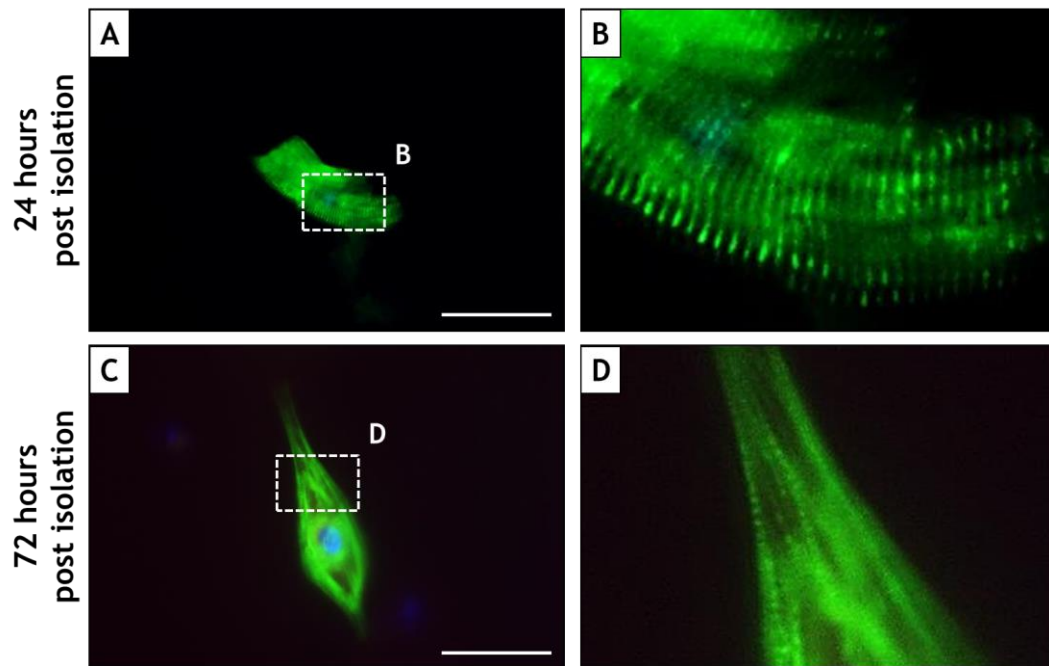


Figure 25: Immunocytochemistry for cardiac marker alpha actinin in adult cardiomyocytes in culture

A and B – Adult cardiomyocytes plated onto 1% gelatine, fixed after 24 hours and stained for alpha actinin showed rod-shaped morphology with striated parallel myofibrils. **C and D** – Adult cardiomyocytes plated onto 1% gelatine, fixed after 72 hours and stained for alpha actinin showed loss of rod-shaped morphology and myofibril organisation. Nuclei were counterstained with DAPI (blue). Figure shows merged images. Representative images of 2 biological replicates are shown. B and D are magnified areas in A and C respectively. Scale bars represent 50 μm .

Hearts from 14-15 week old fetuses were dissociated and plated onto 1% gelatine coated glass coverslips. Well attached and spontaneously contracting cells were fixed 48-72 hours after dissociation and stained for alpha actinin, cardiac troponin I (cTnI) and cardiac troponin T (cTnT). Single cTnT staining exhibited the striated pattern of thin filaments while double stainings for cTnI and alpha actinin resulted in alternating striations, staining thin filaments and Z-lines respectively (Figure 26). Both cTnI and cTnT are proteins of the contractile apparatus and are localised at the thin filaments. As observed with light microscopy, foetal cardiomyocytes had no distinct rod-shaped morphology. Stainings showed myofibrils throughout the cells that lacked the parallel alignment detected in mature cardiomyocytes (Figure 26 B,

D).

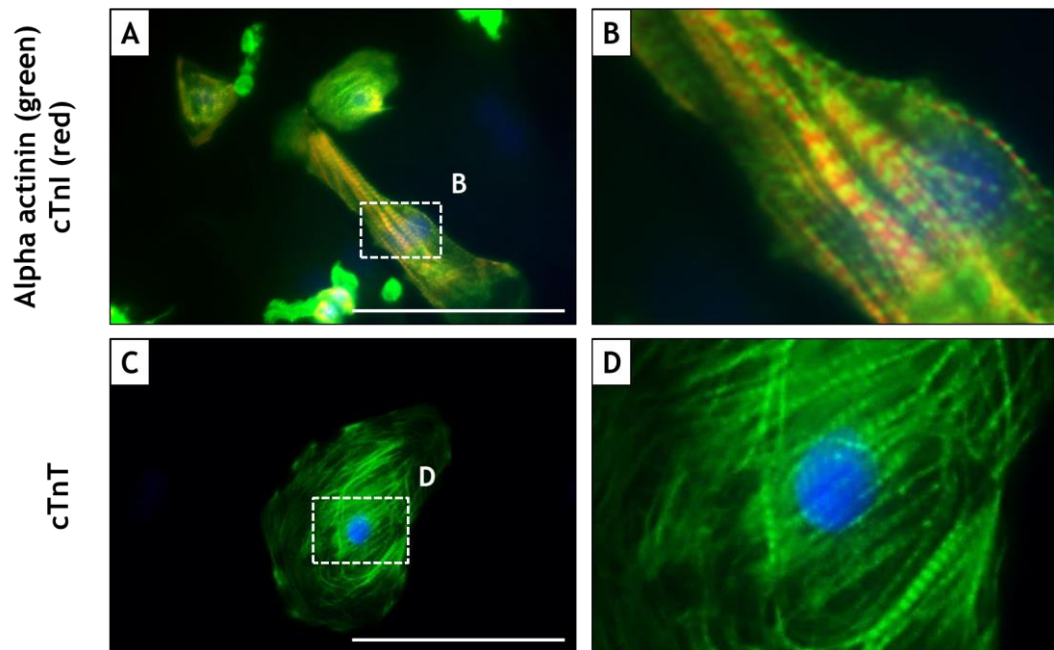


Figure 26: Immunocytochemistry for cardiac markers in foetal cardiomyocytes in culture

Cardiomyocytes isolated from 14-15 week old foetal hearts were plated onto 1% gelatine coated glass coverslips and fixed after 48-72 hours once cells had attached and resumed to spontaneously contract. **A and C** – Cells stained positive for alpha actinin (green), cTnI (red) and cTnT (green) and showed no rod-shaped morphology. **B and D** – Striated myofibrils were not aligned in parallel. Nuclei were counterstained with DAPI (blue). Figure shows merged images. Representative images of 3 biological replicates are shown. B and D are magnified areas in A and C respectively. Scale bars represent 100 μm .

To investigate the effects of dissociation and culture on the morphology and structural organisation of myofibrils, part of the intact cardiac tissue obtained was immediately cryopreserved for sectioning and staining. Samples were dissected into pieces $<1 \text{ cm}^3$ before cryopreservation in an isopentane bath in liquid nitrogen. Frozen tissue pieces were sectioned on a Vibratome Cryostat into 6 μm thick sections and stained for cardiac markers alpha actinin, cTnI and cTnT.

Adult cardiac tissue sections stained positive for all three markers showing the characteristic striation pattern (Figure 27 A, C). Single cTnT staining exhibited the

striated pattern of thin filaments while double stainings for cTnI and alpha actinin resulted in alternating striations, staining thin filaments and Z-lines respectively. Myofibrils were aligned in parallel, with Z-lines lined-up across the width of cells (Figure 27 B, D).

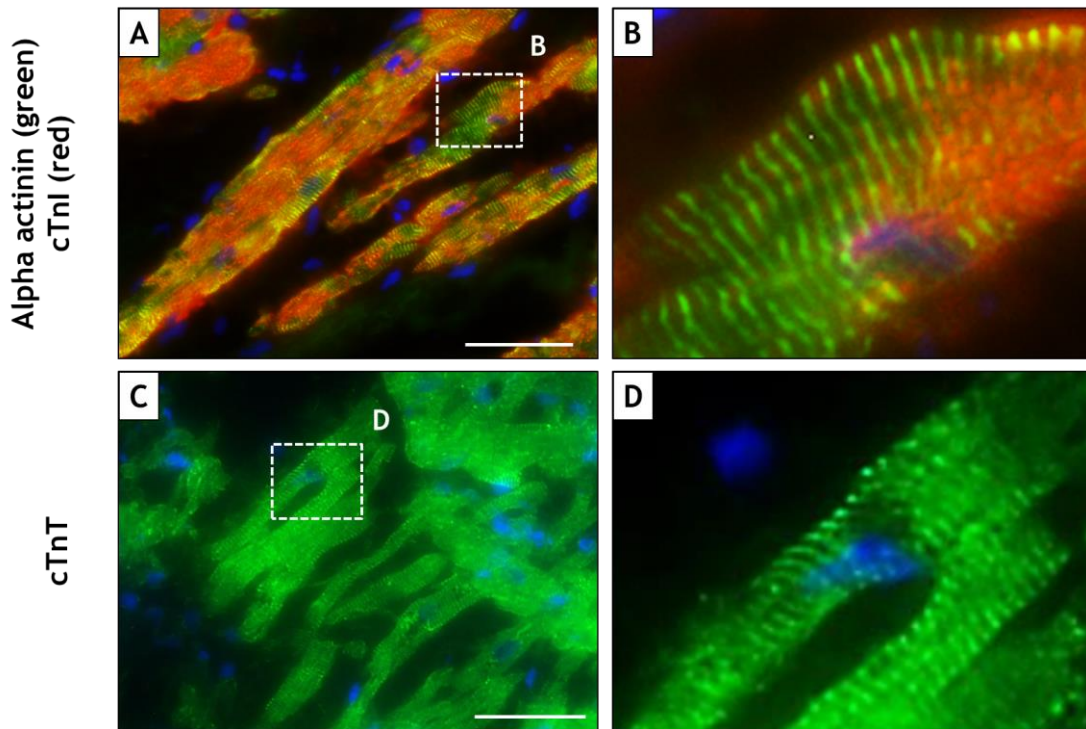


Figure 27: Immunohistochemistry for cardiac markers in sections of adult cardiac tissue

Adult cardiac tissue pieces of $<1 \text{ cm}^3$ were cryopreserved in liquid nitrogen cooled isopentane and sectioned. $6 \mu\text{m}$ thick sections were stained for alpha actinin, cTnI and cTnT. **A and B** – Sections double stained with alpha actinin (green) and cTnI (red) showed highlighted Z-lines and thin filaments in an alternating striation pattern. **C and D** – Sections stained with cTnT (green) showed striation patterns consistent with stained thin filaments. Myofibrils running along the length of a cell were aligned parallel with Z-lines of neighbouring myofibrils. Nuclei were counterstained with DAPI (blue). Figure shows merged images. Representative images of 2 biological replicates are shown. B and D are magnified areas in A and C respectively. Scale bars represent $50 \mu\text{m}$.

In 14-15 week old foetal hearts double staining for alpha actinin and cTnI showed the characteristic striations of myofibrils (Figure 28). Myofibrils in foetal sections were observed throughout the cells but showed no alignment of Z-lines across the width of cells (Figure 28 B).

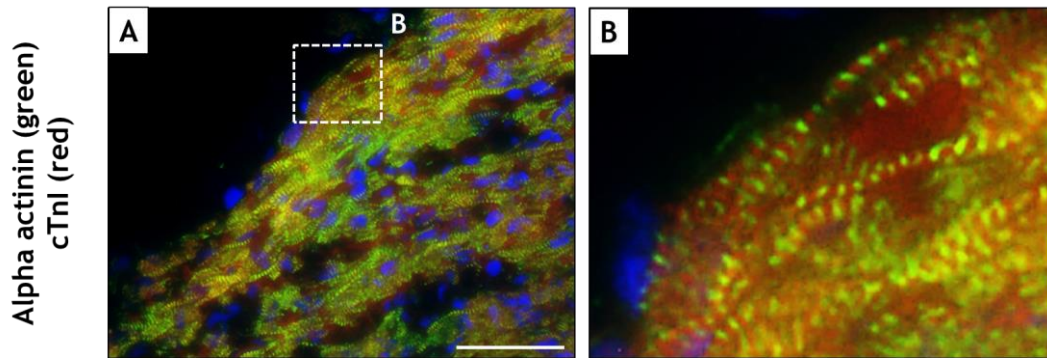


Figure 28: Immunohistochemistry for cardiac markers in sections of foetal cardiac tissue

Pieces of 14-15 week old foetal hearts with $<1\text{ cm}^3$ were cryopreserved in liquid nitrogen cooled isopentane and sectioned. $6\ \mu\text{m}$ thick sections were stained for alpha actinin and cTnI. **A** – Sections double stained with alpha actinin (green) and cTnI (red) showed highlighted Z-lines and thin filaments in an alternating striation pattern. **B** – Myofibrils running along the length of cells displayed no parallel alignment of Z-lines across the width of cells. Nuclei were counterstained with DAPI (blue). Figure shows merged images. Representative images of 2 biological replicates are shown. B shows a magnified area in A. Scale bar represents $50\ \mu\text{m}$.

4.4.2.2 Pluripotent stem cell-derived cardiomyocytes

Staining protocols optimised on primary human cardiac tissue were used to stain pluripotent stem cell-derived cardiomyocytes. H9 and 34-D6 beating bodies were enzymatically and mechanically disaggregated and plated onto 1% gelatine coated glass coverslips. After 3-5 days of recovery, cells were fixed and stained for markers of the cardiac contractile apparatus. Cells isolated from beating bodies stained positive for alpha actinin (green), cTnI (red) and cTnT (green) showing intact myofibrils (Figure 29). Single cTnT staining exhibited the striated pattern of thin filaments while double stainings for cTnI and alpha actinin resulted in alternating striations, staining thin filaments and Z-lines respectively. Stainings showed myofibrils throughout the cells that lacked the parallel alignment of Z-lines detected in mature cardiomyocytes (Figure 29 B, E). As observed with light microscopy, pluripotent stem cell-derived cardiomyocytes had no distinct rod-shaped morphology.

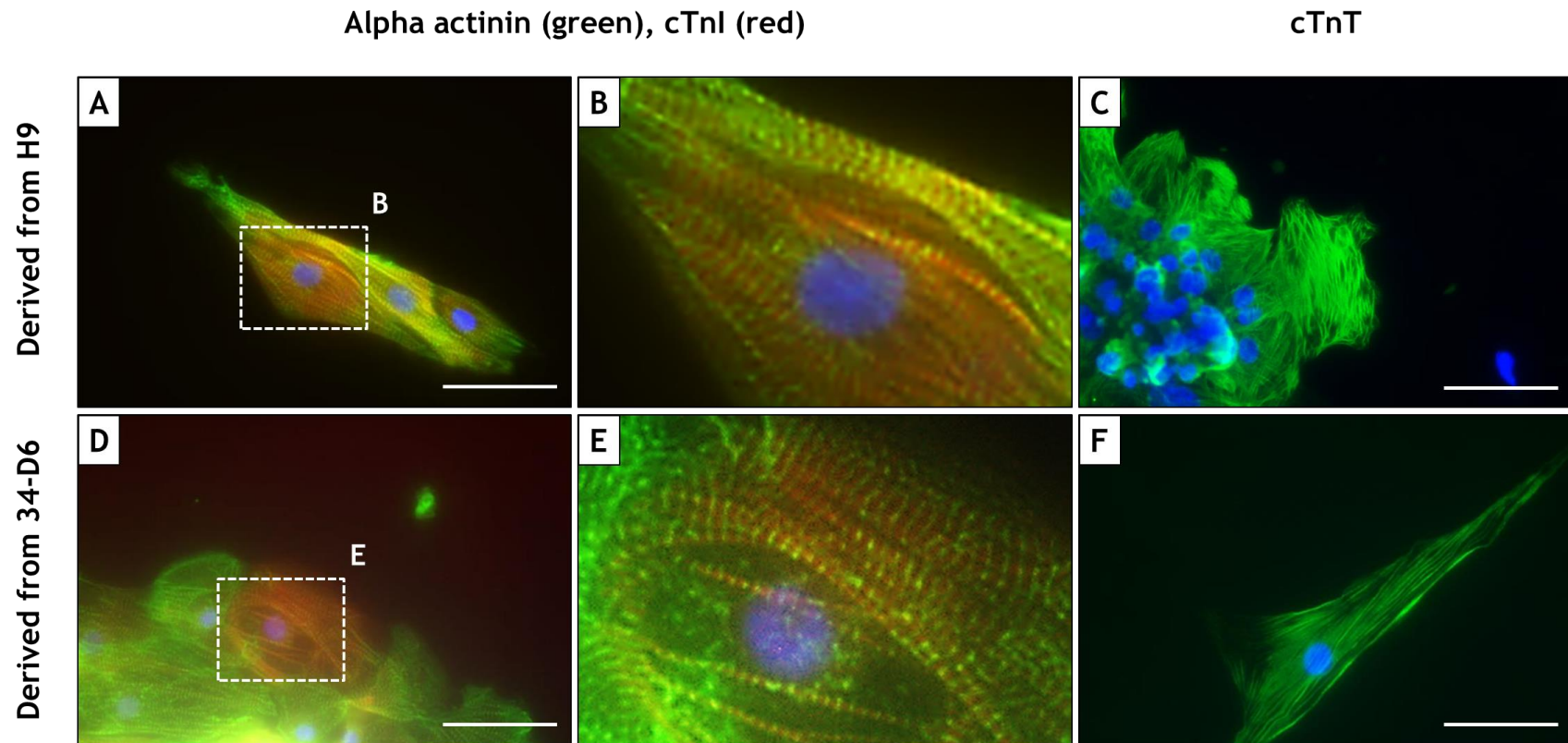


Figure 29: Immunocytochemistry for cardiac markers in pluripotent stem cell-derived cardiomyocytes

3-4 week old beating bodies were disaggregated, plated onto 1% gelatine coated glass coverslips, fixed after 3-5 days and stained for proteins of the cardiac contractile apparatus. Cells stained positive for alpha actinin (green), cTnI (red) and cTnT (green) showing intact myofibrils but displayed no rod-shaped morphology. Nuclei were counterstained with DAPI (blue). Figure shows merged images. Representative images of 20-30 cells from 5 beating bodies are shown for each sample. B and E are magnified areas in A and D respectively. Scale bars represent 50 μm .

4.4.3 Ultrastructure

4.4.3.1 Primary tissue

The ultrastructure of primary cardiomyocytes was investigated using transmission electron microscopy (TEM). Primary human cardiac tissue from foetal hearts, adult RAA and SNBTS donor ventricles was processed within 30 min of obtaining the sample. In preparation for TEM, samples underwent protein fixation, lipid fixation and serial dehydration. Samples embedded in resin were stained and ultrathin sections were imaged. Figure 30 shows representative images of 3 biological replicates of adult and foetal cardiomyocytes.

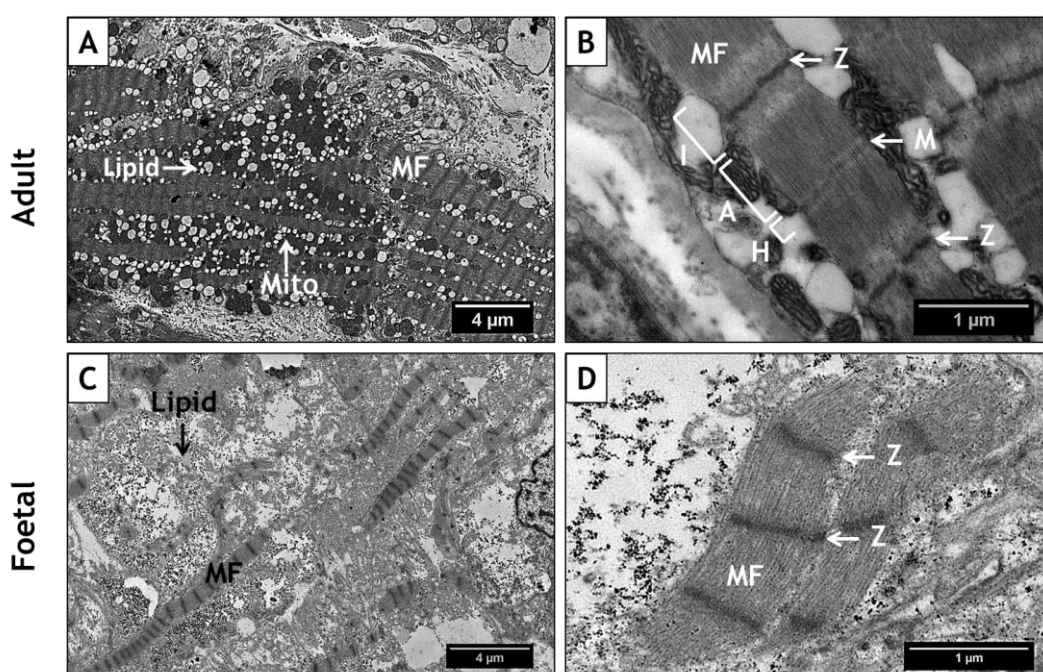


Figure 30: TEM images of primary human cardiomyocytes

Primary human adult and foetal cardiac tissue was prepared for TEM through protein fixation, lipid fixation and dehydration. Samples embedded in resin were stained and ultrathin sections were imaged. **A** – Adult ventricular cardiomyocytes isolated from SNBTS donor tissue showed parallel aligned myofibrils (MF) with Z-lines (Z) of neighbouring myofibrils aligned across the width of a cell. **B** – Higher magnification of sarcomeres showed I-bands (I), A-bands (A), H-zones (H), M-lines (M) and Z-lines. **C** – Cardiomyocytes of 14.5-16.5 week old foetal hearts had fewer and shorter myofibrils. Z-lines of neighbouring myofibrils were not aligned. **D** – At higher magnification foetal sarcomeres showed Z-lines. Representative images of 2 and 4 biological replicates for adult (one RAA, one SNBTS) and foetal samples respectively are shown. Mito – mitochondrion

Adult cardiomyocytes exhibited characteristic striation patterns of intact and parallel aligned myofibrils with Z-lines of neighbouring myofibrils aligned across the width of a cell. All cardiomyocytes of 14.5-16.5 week old foetal hearts had fewer and shorter myofibrils, some only a few sarcomeres long, that lacked the alignment observed in adult cardiomyocytes. At high magnification, sarcomeres in adult cardiomyocytes showed I-bands, A-bands, H-zones, M-lines and Z-lines. In foetal cardiomyocytes, only Z-lines were observed. Adult cardiomyocytes contained a large number of mitochondria and lipid deposits (Figure 31 A, C). Although present in SNBTS tissue as well as RAA, cardiomyocytes of the latter contained more glycogen granules in between myofibril filaments (Figure 31 B, D). Foetal cardiomyocytes also contained mitochondria and lipid deposits, albeit less than the adult cells, as well as glycogen granules in between myofibril filaments (Figure 30 C, Figure 31 E, F).

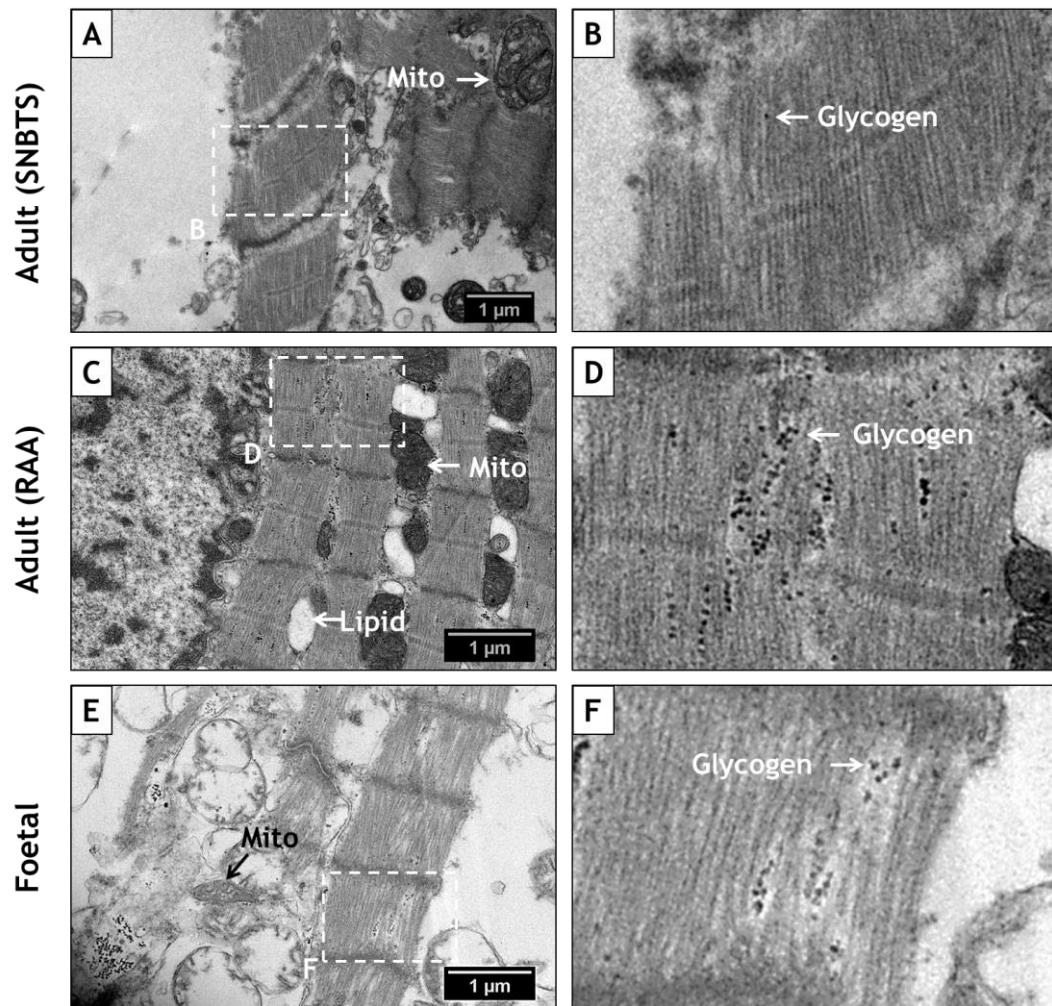


Figure 31: TEM images of primary human cardiomyocytes

A and C – Adult cardiomyocytes contained a large number of mitochondria and lipid deposits. **B and D** – Cardiomyocytes in RAA contained more glycogen granules in between myofibril filaments compared to cardiomyocytes in atrial SNBTS donor tissue. **E** – Cardiomyocytes from 14.5-16.5 week old foetuses contained fewer mitochondria and lipid deposits than those in adult tissue. **F** – Glycogen granules were found in between myofibril filaments of foetal cardiomyocytes. B, D and F are magnified areas in A, C and E respectively. Mito – mitochondrion.

4.4.3.2 Pluripotent stem cell-derived cardiomyocytes

Beating bodies derived from a hES (H9) and an iPS (34-D6) cell line were cultured for 3-4 weeks before being processed for TEM as described above for primary cardiac tissue. TEM images from different layers of beating bodies confirmed the presence of cardiac and non-cardiac cells. Images of cardiomyocytes found in hES

and iPS cell-derived beating bodies shown in Figure 32 are representative of 3 biological replicates.

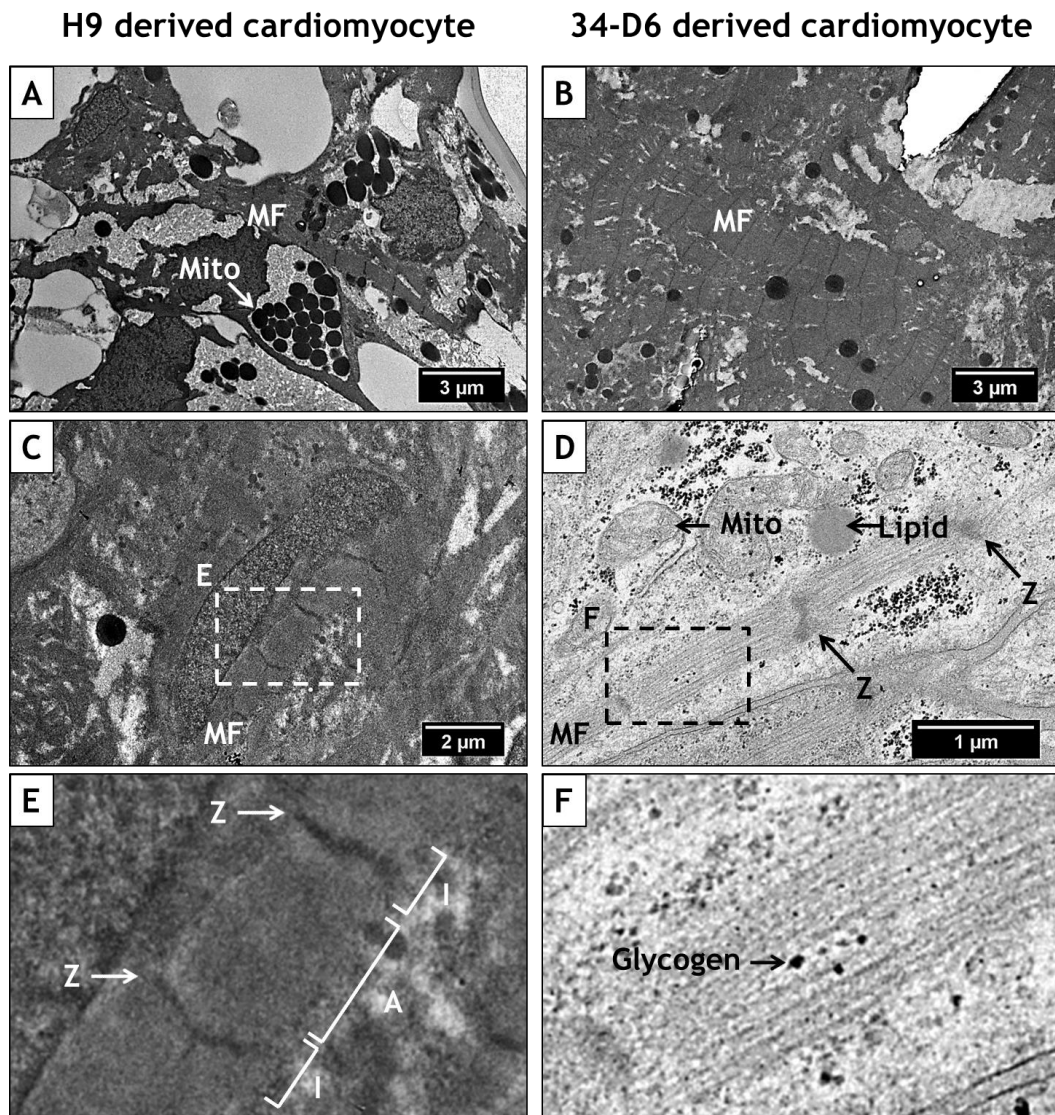


Figure 32: TEM images of pluripotent stem cell-derived cardiomyocytes

A – Most stem cell-derived cardiomyocytes of 3-4 week old beating bodies showed myofibrils (MF) comparable to foetal cells in number, size and sarcomere structure. **B** – Some cells contained a greater number of myofibrils with increased organisation and alignment of Z-lines (Z). **C and E** – A few cells contained sarcomeres with I-bands (I) and A-bands (A) in addition to Z-lines. **D and F** – Stem cell-derived cardiomyocytes contained mitochondria and lipid deposits as well as glycogen granules in between myofibril filaments. Representative images of 3 biological replicates for each sample are shown. E and F are magnified areas in C and D respectively. Mito – mitochondrion.

Most stem cell-derived cardiomyocytes showed great resemblance with 14.5-16.5 week old foetal cardiomyocytes. Myofibrils varied in size with some consisting of a single sarcomere. Myofibrils were generally sparser than in adult cardiomyocyte and lacked the alignment of Z-lines (Figure 32 A). However, some cells contained a greater number of myofibrils with increased organisation, exhibiting some alignment of Z-lines between neighbouring myofibrils (Figure 32 B). Stem cell-derived cardiomyocytes contained mitochondria and lipid deposits (Figure 32 D) as well as glycogen granules in between myofibril filaments (Figure 32 F) as seen in both adult and foetal samples. At high magnification, all sarcomeres showed Z-lines but a small number of cells contained sarcomeres with I-bands and A-bands in addition to Z-lines (Figure 32 E). Overall there were no obvious differences observed between cardiomyocytes derived from hES and iPS cells.

4.4.4 Membrane visualisation

The cell membrane of foetal and stem cell-derived cardiomyocytes was visualised using a membrane dye in order to determine if t-tubules were present.

Beating bodies cultured for 3-4 weeks post differentiation and 14.5-16.5 week old foetal hearts were disaggregated and plated onto glass coverslips as detailed above for immunocytochemistry. After disaggregated cells resumed to spontaneously contract (48-72 hours), cell membranes of disaggregated single cells were stained with the membrane dye Di-8-ANEPPS. This dye is not susceptible to internalisation and hence suitable to visualise outer membrane structures such as t-tubules.

Spontaneously contracting cells, regarded to be cardiomyocytes, were imaged in Z-stacks on a confocal microscope at 37°C. No t-tubule structures were visible in stained cell membranes of foetal or stem cell-derived cardiomyocytes; representative images are shown in Figure 33. Staining membranes of adult cardiomyocytes was unsuccessful due to technical difficulties.

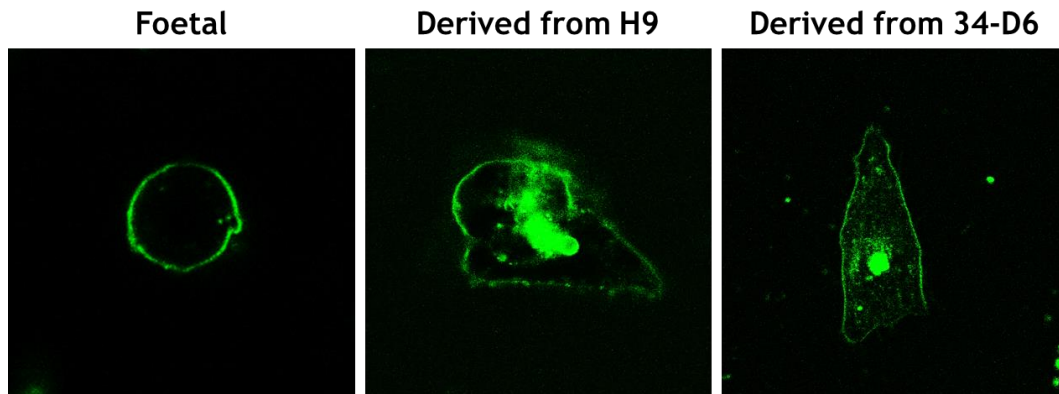


Figure 33: Visualisation of cell membrane

Single cells from disaggregated 14.5-16.5 week old foetal hearts and 3-4 week old beating bodies were stained with the membrane dye Di-8-ANEPPS. Z-stacks of spontaneously contracting cells were recorded on a confocal microscope. Visualised cell membranes of foetal and stem cell-derived cardiomyocytes showed no t-tubules. Representative images of 10 cells from 2 biological replicates for each sample are shown.

4.4.5 Intracellular calcium imaging

An essential characteristic of functional cardiomyocytes is excitation-contraction coupling in which an action potential triggers calcium-induced calcium release (CICR) leading to muscle contraction. Calcium-induced calcium release refers to a mechanism by which extracellular calcium entering a cell induces the release of calcium from intracellular calcium storages like the sarcoplasmic reticulum. This vast increase in cytosolic calcium concentration results in cardiac muscle contraction that ends when calcium is pumped back into the sarcoplasmic reticulum. This release of calcium into the cytosol can be detected as spatiotemporally restricted calcium transients in cells loaded with Fluo-4, a dye that fluoresces upon binding calcium.

To investigate if spontaneous contraction of stem cell-derived cardiomyocytes was due to excitation-contraction coupling, one stem cell-derived beating body was treated with Tetrodotoxin (TTX). TTX selectively inhibits voltage gated sodium channels preventing action potentials. In cells with functional excitation-contraction coupling, the absence of action potentials will hinder the activation of voltage-gated calcium channels, thus impeding CICR.

Cytoplasmic calcium in a beating body derived from H9 was visualised with 5 μM Fluo-4 and continuously imaged at room temperature. A video of the Fluo-4 loaded beating body is supplied in Appendix 2. Intensity of fluorescence was displayed through an intensity map (Figure 34 A). Peaks in fluorescence coincided with contractions, and fluorescence peaks in different regions of interest throughout the beating body were in-sync. For investigation of excitation-contraction coupling, the same beating body was incubated with 10 μM Tetrodotoxin. Fluorescence intensity in a region of interest traced over time before and after TTX treatment is shown in Figure 34 B.

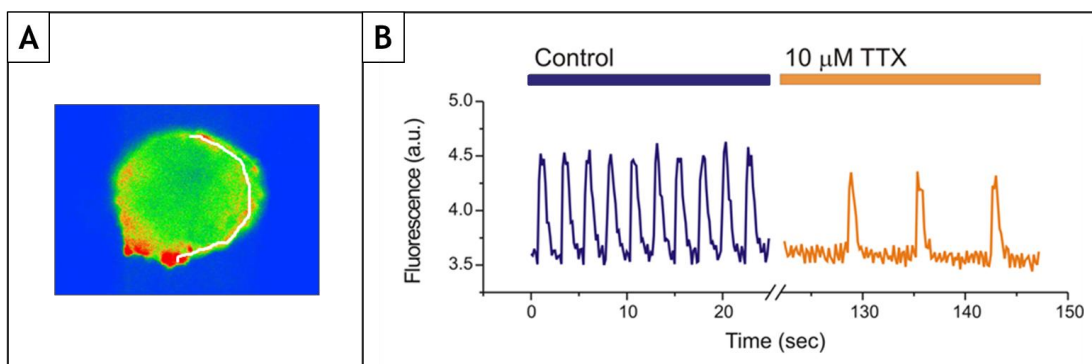


Figure 34: Effect of Tetrodotoxin on calcium-induced calcium release in a beating body

Cytoplasmic calcium in a beating body derived from H9 was visualised with Fluo-4, a green-fluorescent calcium indicator. Peaks in fluorescence, i.e. calcium transients, coincided with contractions. **A** – Fluorescence intensities were displayed through an intensity map, green indicating low and red indicating high intensity. **B** – Fluorescence intensity in a region of interest (indicated by white line in A) was recorded over time. Incubation with the competitive sodium channel inhibitor TTX suppressed calcium transients, suggesting functional excitation-contraction coupling. Fluorescence intensity is shown in arbitrary units (a.u.). TTX – Tetrodotoxin.

Prior to TTX treatment, the beating body showed regular calcium transients. After adding sodium channel inhibitor TTX, the number of calcium transients, which were still coinciding with contractions, decreased and time intervals between flashes became irregular and increased over time.

For visualisation of calcium transients in single cells, a 16 week old foetal heart and beating bodies derived from pluripotent stem cell lines H9 and 34-D6 were disaggregated and plated onto glass coverslips as described for immunocytochemistry. Beating bodies from both cell lines had been cultured for 5 weeks after differentiation before disaggregation. After disaggregated cells resumed to spontaneously contract, cytoplasmic calcium was visualised as above with Fluo-4. Spontaneously contracting cells, regarded to be cardiomyocytes, were imaged for 20 s at room temperature using an optical camera connected to a fluorescence microscope. Representative videos are supplied in Appendix 2. Fluorescence intensities were traced over time and representative traces of calcium transients in single foetal, hES and iPS cell-derived cardiomyocytes are shown in Figure 35. The width and height of fluorescence peaks differed between foetal and stem cell-derived cardiomyocytes and peak heights decreased in all of them over time.

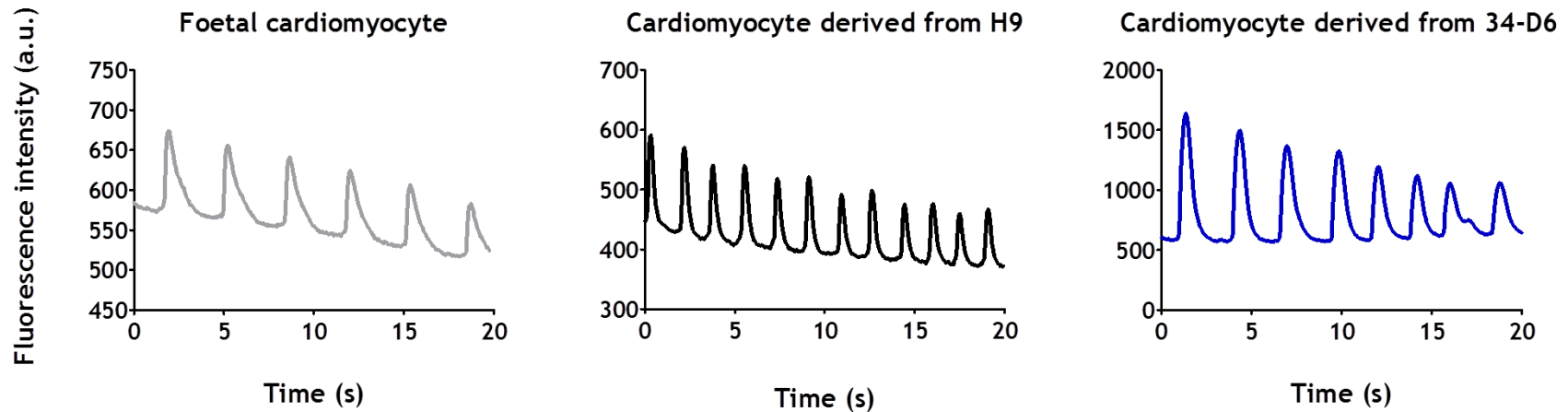


Figure 35: Calcium transients in foetal and stem cell-derived cardiomyocytes

A heart from a 16 week old foetus and beating bodies generated from H9 and 34-D6 were disaggregated and plated as single cells. Beating bodies had been cultured for 5 weeks prior to disaggregation. After spontaneous contractions resumed, intracellular calcium was visualised with Fluo-4 and fluorescence intensities were recorded. Images show representative traces of fluorescence intensity in one cell over 20 s. The width and height of fluorescence peaks differed in foetal and stem cell-derived cardiomyocytes and peak heights decreased in both over time. Fluorescence intensity is shown in arbitrary units (a.u.). Representative traces of 14-16 cells from one foetal heart and 2 beating bodies generated from each H9 and 34-D6 are shown.

In order to compare the kinetics of calcium transients in foetal and pluripotent stem cell-derived cardiomyocytes, data from a representative calcium transient from each of 14-16 cells was analysed and pooled for each cell line. For each calcium transient, the background fluorescence was subtracted, and each data point normalised to the peak value. Pooled data for each time point was plotted as a mean \pm SEM and is shown in Figure 36.

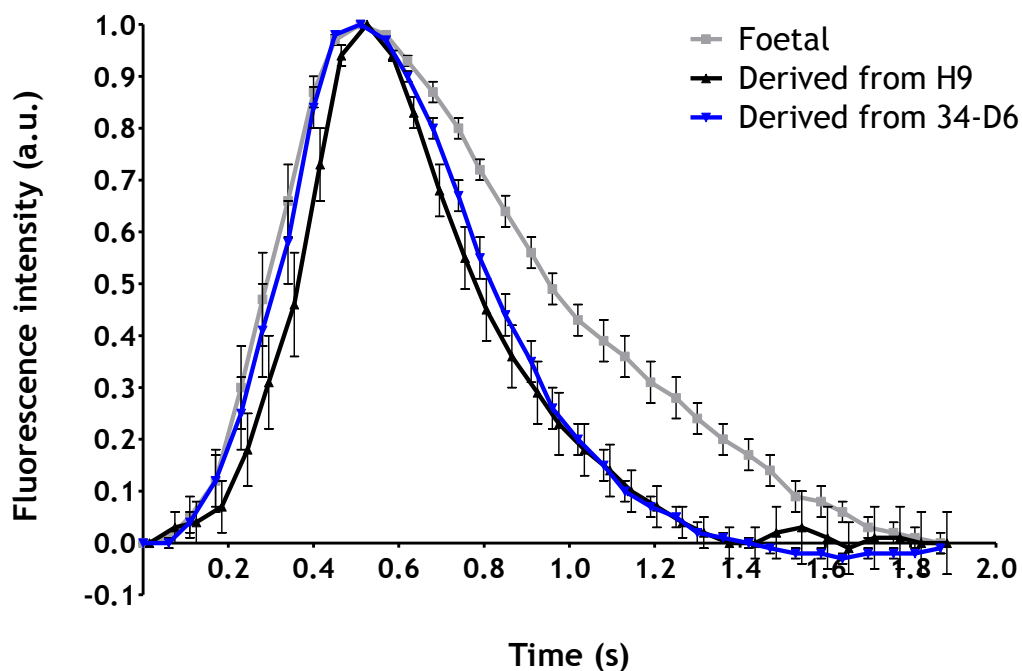


Figure 36: Single calcium transient in spontaneously contracting cardiomyocytes

Calcium transients in foetal and pluripotent stem cell-derived cardiomyocytes were analysed in 14-16 cells for each group. One representative calcium transient from each cell was analysed and data from all cells from each cell line were pooled. For each calcium transient the background fluorescence was subtracted and each data point normalised to the peak value. Fluorescence intensity is shown in arbitrary units (a.u.) as the mean value of 14-16 data points with error bars representing SEM.

Cardiomyocytes derived from 34-D6 generally showed less variability, i.e. smaller SEM, between cells compared to H9 and were hence chosen for comparison with foetal cells. Because data had been normalised, amplitude (F/F_0) was the same for all cells and could not be compared between foetal and stem cell-derived

cardiomyocytes. However, differences were detected between their decay kinetics (t_{50} , t_{75} , t_{90}) shown in Figure 37. The decay kinetics are related to the speed at which calcium is pumped back into the sarcoplasmic reticulum and t_{50} , t_{75} and t_{90} refer to the times correlating to 50%, 75% and 90% decay of calcium transients. Decay of calcium transients was considerably slower in foetal cardiomyocytes compared to stem cell-derived cardiomyocytes ($t_{50}=0.96$ s *vs* 0.81 s, $\Delta t_{50}=0.15$ s). The difference further increased at t_{75} (1.28 s *vs* 0.96 s, $\Delta t_{75}=0.32$ s) and t_{90} (1.53 s *vs* 1.13 s, $\Delta t_{90}=0.4$ s).

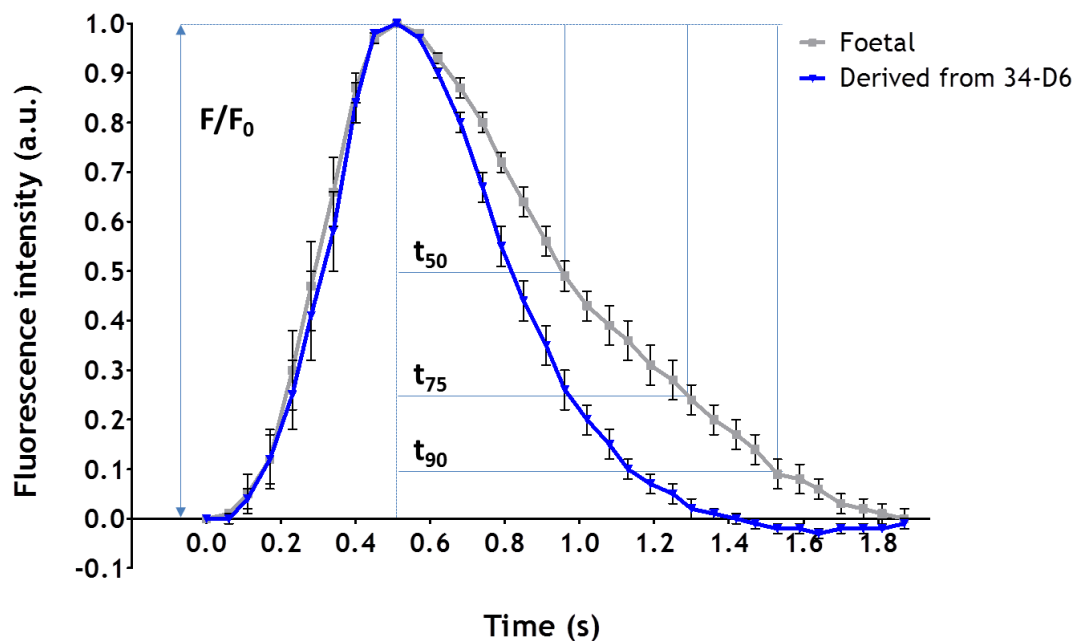


Figure 37: Decay kinetics of calcium transients in foetal and stem cell-derived cardiomyocytes

Decay kinetics differed considerably between foetal and stem cell-derived cardiomyocytes at times correlating to 50%, 75% and 90% decay of calcium transients (t_{50} , t_{75} and t_{90} respectively). Decay of calcium transients was markedly slower in foetal compared to stem cell-derived cardiomyocytes ($t_{50}=0.96$ s *vs* 0.81 s, $t_{75}= 1.28$ s *vs* 0.96 s and $t_{90}=1.53$ s *vs* 1.13 s). The difference between foetal and stem cell-derived cells increased over time ($\Delta t_{50}=0.15$ s, $\Delta t_{75}=0.32$ s, $\Delta t_{90}=0.4$ s). Fluorescence intensity is shown in arbitrary units (a.u.) as the mean value of 14-15 data points with error bars representing SEM. F/F_0 – amplitude

4.4.6 Electrophysiology

Sodium currents were recorded in cardiomyocytes derived from human ES cells (H9) to identify appropriate buffer compositions, equipment settings, and patch-clamp technique. Perforated patch-clamping using Amphotericin B and a low sodium bath solution was identified as the suitable technique. In preparation for sodium current recordings beating bodies were generated from undifferentiated H9, disaggregated and plated onto gelatine-coated glass coverslips as described previously for immunocytochemistry. Electrophysiological recordings were performed on single cells, identified as cardiomyocytes by their morphology and/or spontaneous contraction, 2-3 days after disaggregation.

Sodium currents were elicited by applying gradually increasing potentials and current-potential relationships were plotted as an I-V curve. The I-V curve shown in Figure 38 was plotted from recordings of one H9-derived cardiomyocyte. It displays a gradual increase in measured current corresponding to a gradual increase in applied potential and a large sodium current even in a low-sodium bath solution.

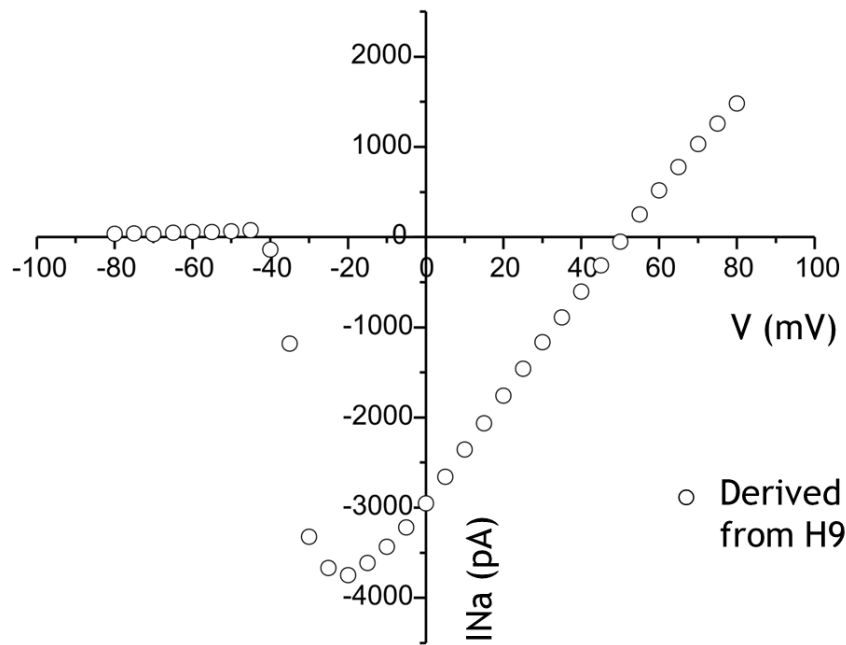


Figure 38: I-V curve of H9-derived cardiomyocytes

Using perforated patch clamping sodium currents were elicited from single H9-derived cardiomyocytes by applying gradually increasing potentials. The representative current-potential (I-V) curve of one cell shows an increase of current in a voltage-dependent manner.

4.5 Discussion and Conclusion

The aims of this chapter were to I) isolate and characterise viable and functional cardiomyocytes from human foetal and adult primary tissue, II) isolate and characterise pluripotent stem cell-derived cardiomyocytes from beating bodies and III) compare them to human adult and foetal cardiomyocytes to evaluate their maturity. Adult and foetal cardiomyocytes showed great differences with regard to morphology, survival in culture, and organisation and ultrastructure of their contractile apparatus. Analysis of one hES cell line (H9) and one previously derived healthy control iPS cell line (34-D6) showed stem cell-derived cardiomyocytes more closely resembled foetal than adult cardiomyocytes but overall showed an intermediary phenotype.

Successful isolation of viable cardiomyocytes from adult and foetal cardiac tissue was crucial for optimisation of protocols for structural and functional characterisation and as a control to compare stem cell-derived cardiomyocytes against. Dissociation of right atrial appendages (RAA) yielded far fewer cells than that of SNBTS donor tissue due to the vast difference in tissue size and even though donor tissue would have had the advantage of allowing access to atrial as well as ventricular cells, these cells showed drastically reduced survival in culture. This was most likely due to the fact that up to 24 hours could pass post-mortem before samples were available for collection and despite storage on ice during that period. Dissociation of foetal hearts, available within 30 min post-mortem, produced much greater numbers of viable cells that quickly attached and spontaneously contracted. Spontaneous contraction was also observed in cardiomyocytes isolated from beating bodies, but not adult cardiomyocytes, indicating stem cell-derived cardiomyocytes have a more foetal than adult phenotype. The different rates at which beating bodies contracted could be caused by the presence of different cells with varying inherent rhythmicity. All cardiomyocytes have an inherent rhythmicity but the rate at which they spontaneously depolarise and contract differs depending on the cell type. The cells with the fastest depolarisation dictate the contraction rate of the heart, therefore different contraction rates observed in beating bodies possibly mirror different populations of cardiomyocyte subtypes present. External factors like stress,

restriction of movement due to surrounding tissue and matrix could also play a role and influence contraction rate.

Investigation of structural and functional characteristics of stem cell-derived cardiomyocytes required single cells rather than beating clusters. Disaggregation of beating clusters was carried out with the fragile nature of cardiomyocytes in mind, prioritising survival of the cells over complete disaggregation. This resulted in a mixed population of single cells and groups of cells with varying sizes. In clusters of connected cells, contractions appeared to be initiated at one end and spread to the other, showing functional electrophysiological coupling of neighbouring cardiomyocytes.

All adult cardiomyocytes that survived isolation showed rapid de-differentiation, observed as de-organisation of myofibrils compared to freshly isolated cells. Myofibrils were visualised by immunocytochemistry using antibodies against alpha actinin, cardiac troponin I (cTnI) and cardiac troponin T (cTnT), three proteins of the contractile apparatus, and while alpha actinin is localised to Z-lines, both cTnI and cTnT are localised at the thin filaments. Stainings of tissue sections instead of cultured cells circumvented the issue of culture-induced dedifferentiation and accurately represented the characteristic adult phenotype with striated myofibrils aligned in parallel across the entire width of a rod-shaped cell^{173, 204}. Foetal cardiomyocytes on the other hand showed no differences in myofibril organisation between cultured cells and tissue sections. Both contained myofibrils that stained for alpha actinin, cTnI and cTnT but lacked alignment and the organisation seen in adult cardiomyocytes, confirming that unaligned myofibrils are a feature of immaturity rather than culture-induced dedifferentiation in foetal cardiomyocytes²⁰⁵. Pluripotent stem cell (H9 and 34-D6) derived cardiomyocytes showed myofibril organisation and alignment similar to foetal cardiomyocytes. Some however had a greater number of myofibrils with increased alignment possibly suggesting that some hES and iPS cell-derived cardiomyocytes possessed a more mature phenotype than cardiomyocytes isolated from 14-16 week old foetal hearts.

All fluorescent images were acquired using standard fluorescent rather than confocal microscopy. The resulting lower quality of pictures limited the possibilities of more detailed analysis such as the length of sarcomeres in individual cells. This parameter can be used as an indicator for an adult vs foetal or healthy vs diseased phenotype and could have been used as another characteristic for comparison of stem cell-derived with primary cardiomyocytes. Adult sarcomeres measure approximately 2 μm in their resting state, while foetal sarcomeres measure approximately 1.5-1.6 μm ²⁰⁶.

Investigation of the ultrastructure of myofibrils in hES and iPS cell-derived cardiomyocytes with transmission electron microscopy (TEM) confirmed their predominantly immature phenotype and similarity to 16 week old foetal cardiomyocytes. However, as observed with immunocytochemistry, a few stem cell-derived cardiomyocytes exhibited a more organised alignment of myofibrils, as well as more complex sarcomeres, indicative of a mixture of maturities with more and less mature cardiomyocytes in the same beating body. Although slightly more developed than foetal cells, stem cell-derived cardiomyocytes were considerably different from adult cells with regard to myofibril organisation, ultrastructure of sarcomeres and number of mitochondria. Myofibrils of varying lengths observed in foetal samples as well as beating bodies were not an artefact of fixation or sample preparation but have indeed previously been shown to represent myofibril formation throughout different stages¹⁹⁷.

Another feature shared by foetal and stem cell-derived cardiomyocytes was the anticipated absence of transverse tubules (t-tubules) in their cell membrane. Absence of t-tubules in stem cell-derived cardiomyocytes, expected and in accordance with observations made in mouse and human embryonic stem cell-derived cardiomyocytes²⁰⁷, further underlined their immature phenotype. Cell membrane visualisation of rat cardiomyocytes throughout development showed that t-tubules only started being formed postnatally²⁰⁸. Staining membranes of adult cardiomyocytes was unsuccessful since only a small number of cells survived isolation and those that were viable, had de-differentiated by the time they

successfully attached. Attachment however was crucial, since imaging of t-tubules required Z-stack imaging using a confocal microscope.

Investigation of calcium transients proved similarly difficult in adult cardiomyocytes not only because of issues with viability but also because they require electrical stimulation to trigger calcium-induced calcium release (CICR) and the necessary equipment was not available. Foetal and stem cell-derived cardiomyocytes, spontaneously contracting and thus not requiring electrical stimulation, showed calcium transients that were almost indistinguishable from each other in their upstroke but differed noticeably with regard to decay kinetics. The shape of calcium transients measured in foetal cells paralleled previously published observations and was distinctly different from transients seen in adult cells in the same study²⁰⁸. Compared to foetal cardiomyocytes, adult calcium transients are marked by a faster upstroke (calcium release into the sarcoplasm) and faster decay (calcium removal from sarcoplasm). Faster calcium decay measured in stem cell-derived compared to foetal cardiomyocytes could be interpreted as another indication that they have a slightly more mature phenotype. Results from a recent publication indicating that calcium handling properties of cardiomyocytes derived from iPS cells are relatively immature compared to those derived from hES cells could not be confirmed²⁰⁹.

Calcium transient signals were recorded using time-lapse recordings because a continuous recording was not possible with the equipment available. Data reconstruction from signals sampled over time can lead to distortion of the original continuous signal referred to as temporal aliasing. In addition, the frame rate at which the calcium signals were recorded was limited by the equipment and at 17 fps relatively low. Faster acquisition would of course allow for a more detailed and accurate representation of calcium transients but considering how well the recorded results of foetal cardiomyocytes compared to previously published data the loss of information caused by the experimental set-up was of minor concern.

Due to variability in fluorescence intensity, partly due to photobleaching, the

fluorescence for each of the calcium transients was normalised to their respective amplitude (F/F_0). Therefore, F/F_0 is the same for all cells and could not be used to estimate and compare intracellular calcium concentrations.

Calcium imaging on a beating body treated with the sodium channel inhibitor Tetrodotoxin (TTX) proved functional excitation-contraction coupling in stem cell-derived cardiomyocytes. Tetrodotoxin competes with sodium ions, binds to the pore region and blocks the sodium channel until it slowly diffuses off. By blocking flow of sodium ions through the channel, it prevents the development of action potentials and thereby CICR. The cardiac sodium channel $Na_v1.5$ is classed as TTX resistant in contrast to TTX sensitive sodium channels. The TTX concentration chosen would have blocked all sensitive channels but recordings showed some peaks indicating the presence of resistant channels, therefore indicating the presence of resistant cardiac sodium channels. Contractions and calcium transients slowed over time as TTX diffused throughout the buffer. As the recording was made at room temperature it would have been difficult to prove that an eventual complete halt of calcium transients would have been caused by TTX rather than by low temperature.

Finally, the most important functional test of Brugada Syndrome patient-derived cardiomyocytes will be the recording of sodium currents as it will reveal if they accurately recapitulate the expected disease phenotype and are therefore a suitable model system. In a proof of principle experiment, sodium currents were recorded from H9-derived cardiomyocytes. Despite their relative immaturity, pluripotent stem cell-derived cardiomyocytes expressed functional voltage-dependent cardiac sodium channels at levels high enough that the resulting sodium current necessitated a switch to Low Na^+ bath solution. The absence of potassium in the bath solution ensured, that only sodium currents were recorded. In the heart most of the sodium current is conducted by $Na_v1.5$, the channel implicated in the majority of Brugada Syndrome cases with identified genetic alterations. Recording sodium currents in single cells will be the crucial functional assessment of Brugada Syndrome patient-derived cardiomyocytes in the subsequent chapter. It is expected that although structurally

indistinguishable from healthy controls, patient-specific cardiomyocytes will show reduced maximum sodium current density.

In conclusion, cardiomyocytes were successfully isolated from foetal cardiac tissue while isolation of viable cells from adult tissue proved challenging. Morphological and structural comparisons demonstrated the expected classical foetal and adult phenotypes. Structural and functional characterisation of cardiomyocytes derived from healthy hES and iPS cell lines showed varying degrees of maturity but overall a more foetal-like phenotype. Protocols optimised in this chapter can subsequently be used to characterise newly derived patient-specific cardiomyocytes while the data gathered will provide a platform for comparison against healthy control pluripotent stem cell-derived cardiomyocytes as well as adult and foetal controls.

CHAPTER 5

GENERATION AND CHARACTERISATION OF BRUGADA SYNDROME IPS CELL-DERIVED CARDIOMYOCYTES

5.1 Abstract

Brugada Syndrome is an autosomal dominant congenital cardiac disorder that is responsible for 20% of sudden deaths of patients with structurally normal hearts. The majority of mutations are found in *SCN5A*, the gene encoding for the alpha subunit of cardiac sodium channel $Na_v1.5$. Fibroblasts from a patient with Brugada Syndrome (male, 69) and classical ST segment elevation in his ECG due to a mutation (c.1100G>A) in *SCN5A* and a healthy age- and sex-matched volunteer were reprogrammed using episomal vectors carrying Oct-4, shp53, Sox2, Klf4, L-Myc and Lin28. Newly derived patient (BP) and control iPS cell lines (HV3) did not differ significantly from hES cells (H9) in terms of morphology and expression of pluripotency markers as detected by immunocytochemistry and quantitative RT-PCR, however flow cytometry revealed three clones (BP-C5, BP-C6, HV3-C28) had a significantly lower percentage of SSEA3 positive cells. Patient-specific cardiomyocytes, derived from 2 patient iPS cell lines, were similar to foetal cardiomyocytes and indistinguishable from cardiomyocytes derived from hES (H9) and other iPS cell lines (34-D6) in terms of morphology, myofibril organisation, sarcomere structure, t-tubule structures and kinetics of intracellular calcium transients. However, electrophysiological analysis showed a 48.4% reduction of sodium current in patient-derived compared to healthy control-derived cardiomyocytes. This finding is consistent with previous observations in HEK293 cells and *Xenopus* oocytes, but for the first time demonstrates that classical Brugada Syndrome can successfully be modelled in cardiomyocytes using patient-specific iPS cells.

5.2 Introduction

Brugada Syndrome is an autosomal dominant congenital disease that is responsible for 20% of sudden cardiac deaths of patients with structurally normal hearts¹. First described by the Brugada brothers in 1992², it is characterised by an abnormal electrocardiogram (ECG) with ST segment elevation in the right precordial leads V1 to V3 and right bundle-branch block frequently leading to ventricular fibrillation (VF). Patients often present with symptoms of ventricular tachycardia (VT), bradycardia, and atrial ventricular (AV) node conduction disorder, and more males than females are diagnosed with Brugada Syndrome. To date, the implantation of a cardioverter defibrillator is the only proven effective treatment of the disease^{4,5}.

Even though Brugada Syndrome has been associated with mutations in 17 genes¹⁵, its main identified genetic cause is a mutation in *SCN5A*¹⁶. This gene encodes for the alpha-subunit of the cardiac sodium channel $Na_v1.5$, the channel responsible for sodium inward current (I_{Na}). In order to understand the underlying mechanisms of the Brugada phenotype, a variety of model systems have been utilised. These models include transgenic mice¹⁷, canine heart preparations¹⁸ and expression of mutant *SCN5A* in different cellular expression systems¹⁶. These three model systems have provided some insight into the molecular basis of Brugada Syndrome. The main limitation for all model systems thus far remains that they are only able to model cases in which the underlying genetic alteration has been identified. However, a potentially pathogenic mutation is identified in only one third of Brugada Syndrome patients¹⁰².

A new model system, based on the generation of iPS cells, could for the first time allow us to study the molecular basis of this disorder in patients without an identified mutation. Reprogramming fibroblasts from patients with Brugada Syndrome to generate iPS cells could generate new insight into the effects of mutations in their natural genetic environment. Not only will patient-specific iPS cells allow for the generation of the cell type directly affected by the disease, they also carry the patient's exact genetic background. To date, several other cardiac disorders including LQT1¹²⁶, LQT2¹²⁷ and Timothy syndrome¹²⁸ have been modelled using the iPS cell

approach. Although there are no studies looking at pure Brugada phenotypes, Davis et al. recently derived cardiomyocytes from patients carrying the *SCN5A*-1795insD mutation¹²⁹. *SCN5A*-1795insD causes Brugada Syndrome/LQT3 overlap symptoms and has previously been studied in both mouse model and expression systems. The patient-specific iPS cell-derived cardiomyocytes recapitulated the decreased I_{Na} peak and persistent I_{Na} associated with Brugada Syndrome and LQT3 respectively. To validate this system's viability as a model system for classical Brugada Syndrome, a patient with classical Brugada Syndrome ECG and an identified mutation in *SCN5A* was chosen. The missense mutation that this patient carried (c.1100G>A, leading to p.R367H) had previously been studied in cellular expression systems, allowing direct comparison of electrophysiological findings across model systems.

Expression of the sodium channel carrying the missense mutation c.1100G>A in *SCN5A* in HEK293 cells and *Xenopus* oocytes showed no sodium current, while normal currents were recorded from cells expressing wild type channels^{74, 210}. Should iPS cell-derived cardiomyocytes prove to be a feasible model system for Brugada Syndrome, they would offer the possibility to investigate Brugada Syndrome patients without known genetic cause and mutation carriers that show no symptoms. This is an advantage that none of the other model systems possess. It would also deliver the most accurate and relevant setting for drug toxicity screenings of all the model systems which could help exclude possible drugs, based on their toxic effects on cardiomyocytes, before they go into expensive trials.

5.3 Aims

To generate iPS cells lines from a Brugada Syndrome patient and a matched healthy control, to assess their pluripotency and differentiation potential and finally to derive, characterise and compare patient and healthy control-derived cardiomyocytes.

5.4 Results

A male Caucasian aged 69 with Brugada Syndrome, with a classical ST segment elevation in the ECG and a missense mutation in *SCN5A* (c.1100G>A – p.R367H), was identified through the Familial Arrhythmia Network for Scotland (FANS). Skin biopsies from this patient with Brugada Syndrome (BP) and one age- and sex-matched healthy volunteer (HV3) were obtained and processed within an hour of collection. The dermal tissue was dissected into 1 mm³ pieces and cultured under a sterile glass coverslip for 2 weeks in fibroblast growth medium before harvesting emerging fibroblasts. After further expansion, 0.5 x 10⁶ fibroblasts were transfected with Addgene Y4 combination episomes and cultured in fibroblast growth medium for 7 days. After transferring transformed fibroblasts onto 0.1% gelatine, the medium was changed to hES cell selection medium TeSR-E8. Possible iPS cell colonies, assessed based on morphology, appeared between 20-25 days after electroporation and were manually picked into separate Matrigel coated wells. Colonies were treated as individual clones and expanded to give rise to independent cell lines. The name of each cell line was derived from the donor, BP or HV3, the abbreviation 'C' for clone and number of the clone at the time of picking. Since episomal vectors do not integrate into the host genome and are not co-replicated during cell proliferation, they are lost over time and therefore, clones that failed to express pluripotency genes endogenously would not give rise to stable pluripotent stem cell lines. Based on previous experience, cell lines exhibiting pluripotent stem cell morphology after 8 passages were considered stable. Five patient (BP-C5, C6, C11, C15 and C26) and three healthy control (HV3-C23, C24 and C28) cell lines were fully characterised investigating morphology, chromosomal integrity, expression of pluripotency markers and the ability to differentiate into all three germ layers. Once fully validated, cardiomyocytes generated from BP iPS cell lines were investigated and compared to those generated from a healthy control stem cell line.

5.4.1 Generation and characterisation of iPS cells

The patient recruited for this study had been diagnosed 30 years ago based on the classical ST segment elevation in his ECG (Figure 39 A). Genetic screening identified a mutation in *SCN5A* as the likely cause of his disorder which has since been studied in cellular expression systems. He has experienced syncope but neither VT nor VF and does hence not carry a cardioverter defibrillator or receive ajmaline or flecainide treatment. After his diagnosis other family members were identified who carried the same mutation and were either symptomatic or asymptomatic (Figure 39 B).

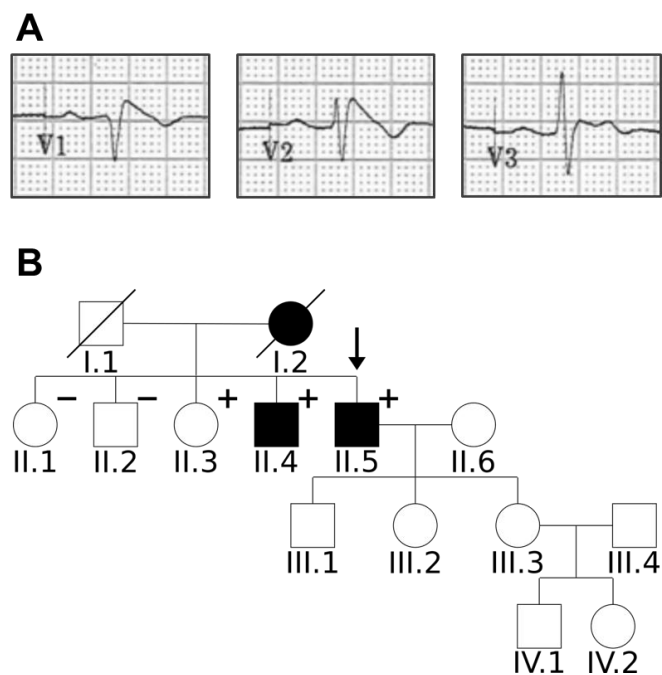


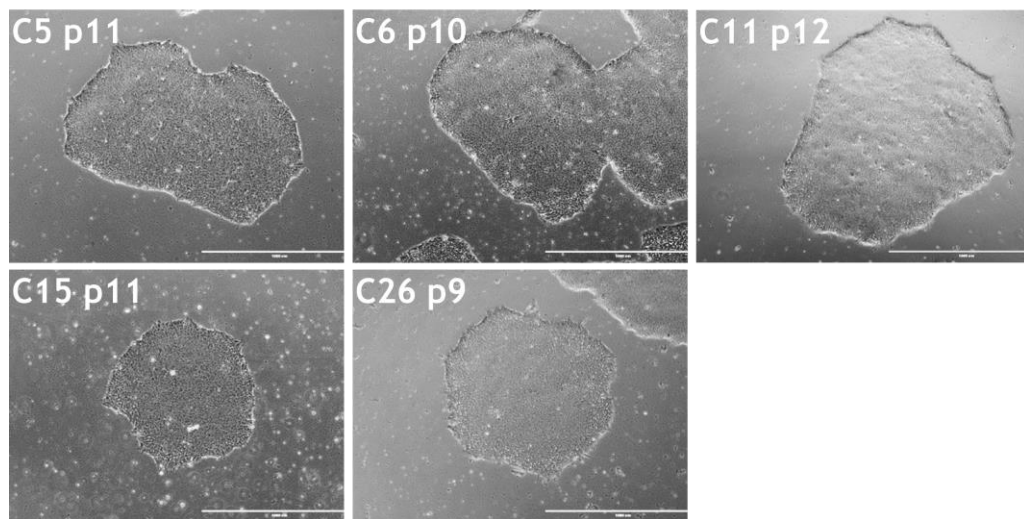
Figure 39: Clinical and genetic characterization of the patient and his family.

A – V₁-V₃ of a 12-lead ECG of the patient showing the ST segment elevation characteristic of Brugada Syndrome. **B** – Family pedigree of the patient with Brugada Syndrome. Squares indicate males, circles females, solid symbols individuals with Brugada Syndrome, and open symbols unaffected family members. Plus signs indicate the carriers of the mutation c.1100G>A in *SCN5A* and minus signs, non-carriers. Family members for whom genetic information was not available are unmarked. The patient is indicated by an arrow.

5.4.1.1 Morphology

All 5 Brugada Syndrome patient (BP) and three healthy control (HV3) derived iPS cell lines grew in flat densely packed colonies with cells exhibiting the high nucleus to cytoplasm ratio typical for hES cells (Figure 40). For routine culture, cells were maintained on matrigel in feeder-free conditions in TeSR-E8 medium with very few spontaneously differentiated cells surrounding colonies. There were no obvious morphological differences observed between BP and HV3 clones compared to control cell lines H9, 33-D9 and 34-D6. No obvious differences in morphology were observed between earlier (p10) and later (p40) passages (data not shown).

BP



HV3

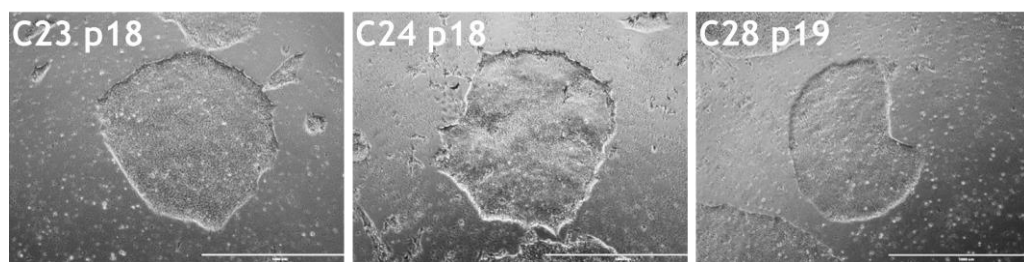


Figure 40: Morphology of BP and HV3 iPS cell lines in culture

Representative light microscopy images of induced pluripotent stem cell lines derived from a patient with Brugada Syndrome (BP) and a healthy volunteer (HV3) in feeder-free culture. Scale bars represent 1000 μm , p indicates passage number.

5.4.1.2 Mutation in SCN5A

Patient BP carries the missense mutation c.1100G>A in *SCN5A* resulting in an Arginine to Histidine substitution at position 367 (p.R367H) in the alpha subunit of cardiac sodium channel Na_v1.5. To assess if this mutation was still present after reprogramming in patient and absent in healthy control iPS cells, genomic DNA was isolated from each iPS cell line. Sequencing of exon 9 of *SCN5A* in all genomic DNA samples confirmed the presence of c.1100G>A in BP-C5, C6, C11, C15 and C26 but not in HV3-C23, C24 or C28 (Figure 41).

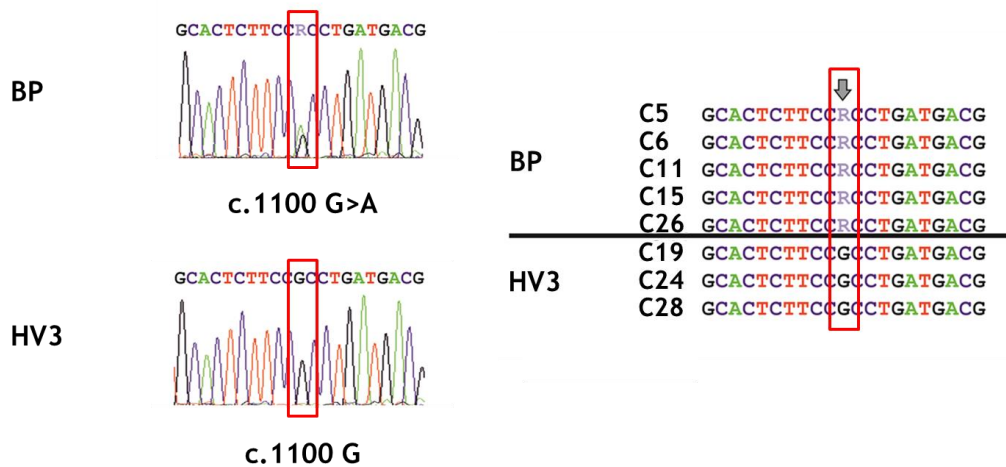


Figure 41: Sequencing analysis of SCN5A in BP and HV3 cell lines

The missense mutation c.1100G>A was identified in genomic DNA isolated from BP-C5, C6, C11, C15 and C26 but not in HV3-C23, C24 or C28. Sequencing was carried out by Dr Elisabet Selga.

5.4.1.3 Expression of pluripotency markers - Quantitative RT-PCR

RNA from undifferentiated cultures was extracted, purified and reverse transcribed as before for each sample in biological triplicate. BP clones, HV3 clones and H9 were assessed for relative expression of Oct-4, Sox2, c-Myc and Nanog using previously optimised quantitative RT-PCR conditions. For each sample the expression of the gene of interest was related to expression of the house-keeping gene β -actin in the same sample, before normalising expression to the positive control H9. Relative expression of all genes of interest is shown in Figure 42.

One-way ANOVA with a Dunnett's post-test for multiple comparison showed no significant difference in expression of the tested pluripotency transcription factors between any of the newly derived iPS cell lines and H9 but significantly ($p < 0.05$) lower expression of Nanog in BP-C11, C15, C26 and HV3-C28 compared to 34-D6.

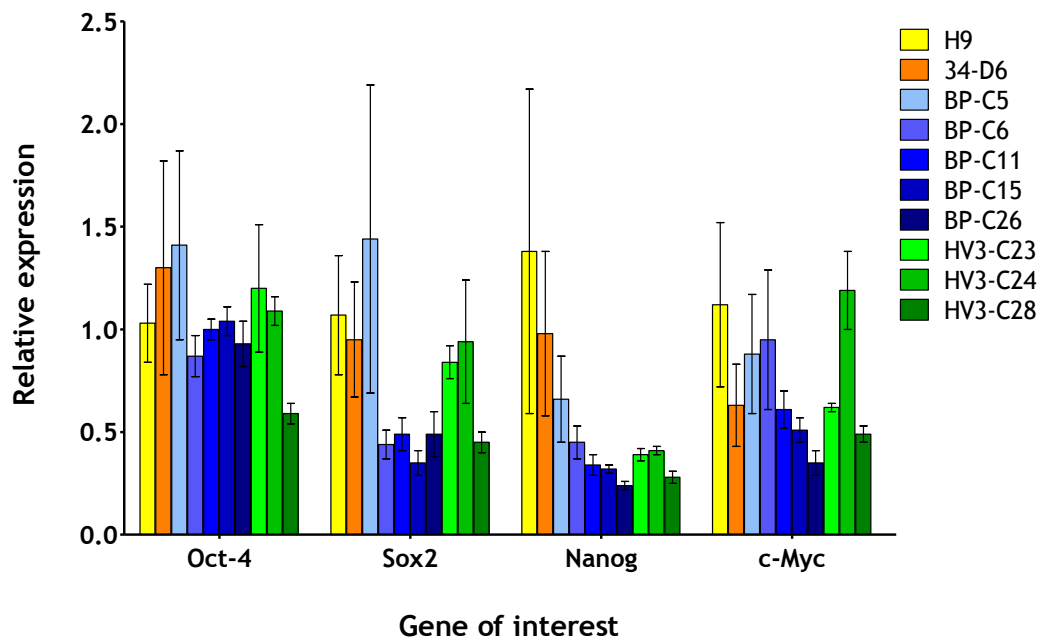


Figure 42: Pluripotency transcription factor expression

Relative expression of pluripotency transcription factors Oct-4, Sox2, Nanog and c-Myc was investigated in undifferentiated H9, BP iPS cell clones and HV3 iPS cell clones. A one-way ANOVA with a Dunnett's post-test for multiple comparison showed no significant difference in pluripotency transcription factor expression in any of the newly derived iPS cell lines and H9 but significantly lower expression of Nanog in BP-C11, C15, C26 and HV3-C28 compared to 34-D6 ($p < 0.05$). Bars represent mean values of biological triplicates with error bars representing SEM.

5.4.1.4 Expression of pluripotency markers - Immunocytochemistry

To assess pluripotency on a protein level, undifferentiated pluripotent stem cells were fixed 2 days after passaging or upon reaching 30% confluency and stained for pluripotency markers Nanog, Oct-4 and Tra-1-60. Nuclei were counterstained with DAPI. All cell lines showed nuclear Nanog and Oct-4 staining and cell surface

staining for Tra-1-60 (Figure 43 and Figure 44). Differentiated cells surrounding the colonies did not stain for pluripotency markers but are visible as DAPI stained nuclei. These stainings were indistinguishable from those of undifferentiated H9 and 34-D6 (Chapter 3, page 91).

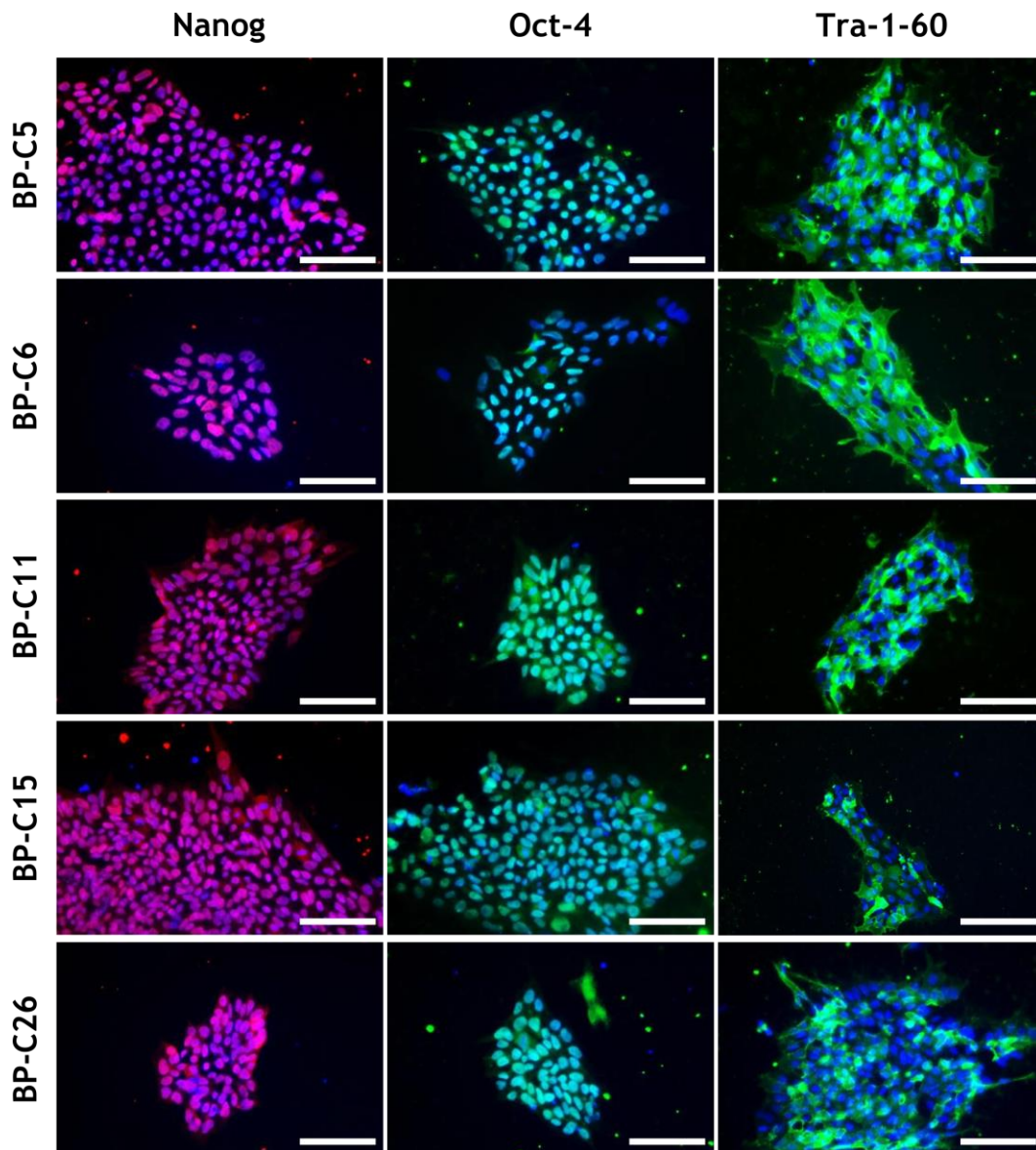


Figure 43: Immunocytochemistry for pluripotency markers Nanog, Oct-4 and Tra-1-60 in BP iPS cell clones

BP-C5, C6, C11, C15 and C26 stained positive for pluripotency markers Nanog, Oct-4 and Tra-1-60. Nuclei were counterstained with DAPI (blue). Representative merged images of 10 colonies per clone are shown. Scale bars represent 100 μ m.

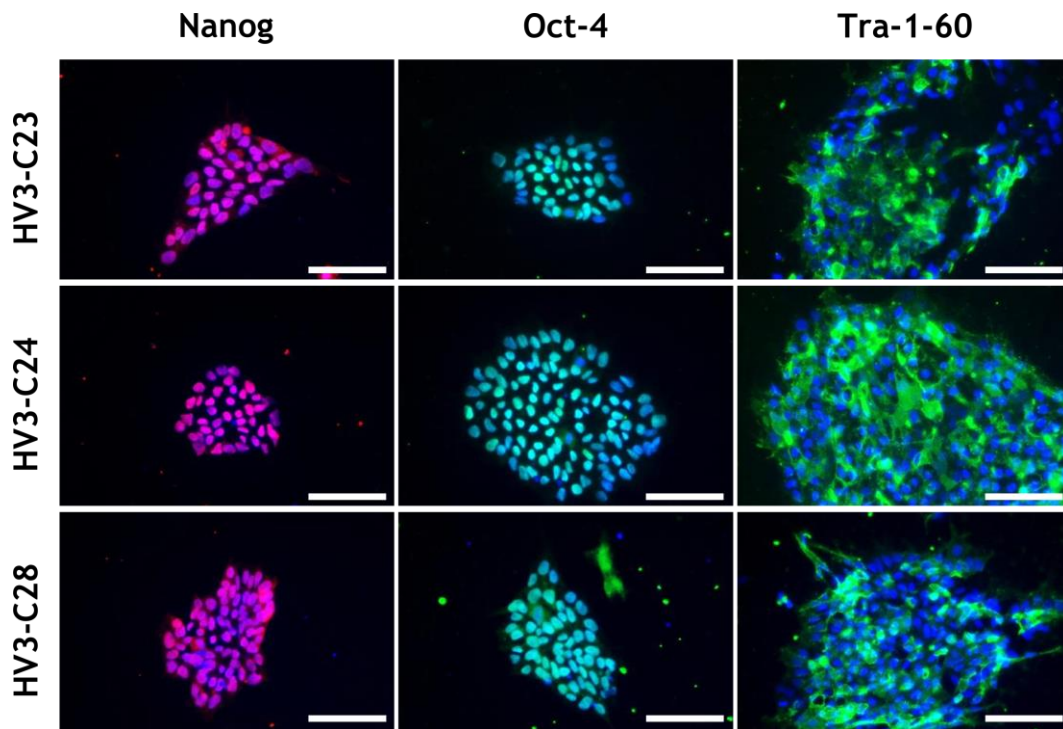


Figure 44: Immunocytochemistry for pluripotency markers Nanog, Oct-4 and Tra-1-60 in HV3 iPS cell clones

HV3-C23, C24 and C28 stained positive for pluripotency markers Nanog, Oct-4 and Tra-1-60. Nuclei were counterstained with DAPI (blue). Representative merged images of 10 colonies per clone are shown. Scale bars represent 100 μm .

5.4.1.5 Expression of pluripotency markers - Flow cytometry

The percentage of cells expressing cell surface markers SSEA-3 and SSEA-4 in undifferentiated populations of BP and HV3 iPS cell clones was investigated using flow cytometry and compared to undifferentiated H9 and 34-D6. Each cell line was harvested, stained and analysed in biological triplicate using the protocols optimised in Chapter 3. The percentages of SSEA-3 and SSEA-4 positive cells in each undifferentiated culture, expressed as the mean value of biological triplicates with the standard error of the mean (SEM), are summarised in Table 16.

Table 16: Percentage of cells expressing SSEA-3 and SSEA-4

	H9	34-D6	BP					HV3		
			C5	C6	C11	C15	C26	C23	C24	C28
SSEA-3	80.1	81.1	82.2	49.9	72.1	63.4	46.0	74.3	73.1	56.0
	± 5.7	± 2.9	± 1.1	± 2.6	± 3.8	± 4.2	± 4.1	± 6.9	± 2.1	± 3.3
SSEA-4	88.3	92.0	96.0	89.5	96.1	96.8	97.1	97.6	90.1	95.2
	± 2.2	± 2.7	± 1.9	± 0.7	± 0.2	± 0.3	± 0.4	± 0.9	± 1.1	± 0.1

Undifferentiated cultures of all BP- and HV3-derived iPS cell lines contained a high percentage of SSEA-4 positive cells at levels similar to undifferentiated H9 and 34-D6. One-way ANOVA with a Dunnett's post-test for multiple comparison showed percentages of SSEA-3 positive cells in those same cultures were significantly lower in BP-C6, BP-C15, BP-C26 and HV3-C28 ($p < 0.05$) compared to H9 and 34-D6.

5.4.1.6 Three germ layer formation

Before embryoid body (EB) formation, all clones were transitioned from a feeder-free culture system onto a feeder layer and cultured for three passages. EBs were then formed from undifferentiated cultures of BP and HV3 iPS cell clones and cultured in EB media in suspension for 7 days. Subsequently, EBs were plated onto gelatine-coated dishes, cultured for 10 additional days and finally fixed and stained for markers of the three germ layers endoderm (Alpha-fetoprotein, AFP), ectoderm (β -tubulin III) and mesoderm (muscle actin). EBs from all BP and HV3 iPS cell clones showed positive staining for markers of all three germ layers (Figure 45 and Figure 46). Unlike H9 and 34-D6, EBs from newly derived BP and HV3 iPS cell lines did not spontaneously differentiate to cells that stain for AFP. Guided hepatic differentiation of these cell lines however gave rise to AFP positive cells of the endodermal germ layer.

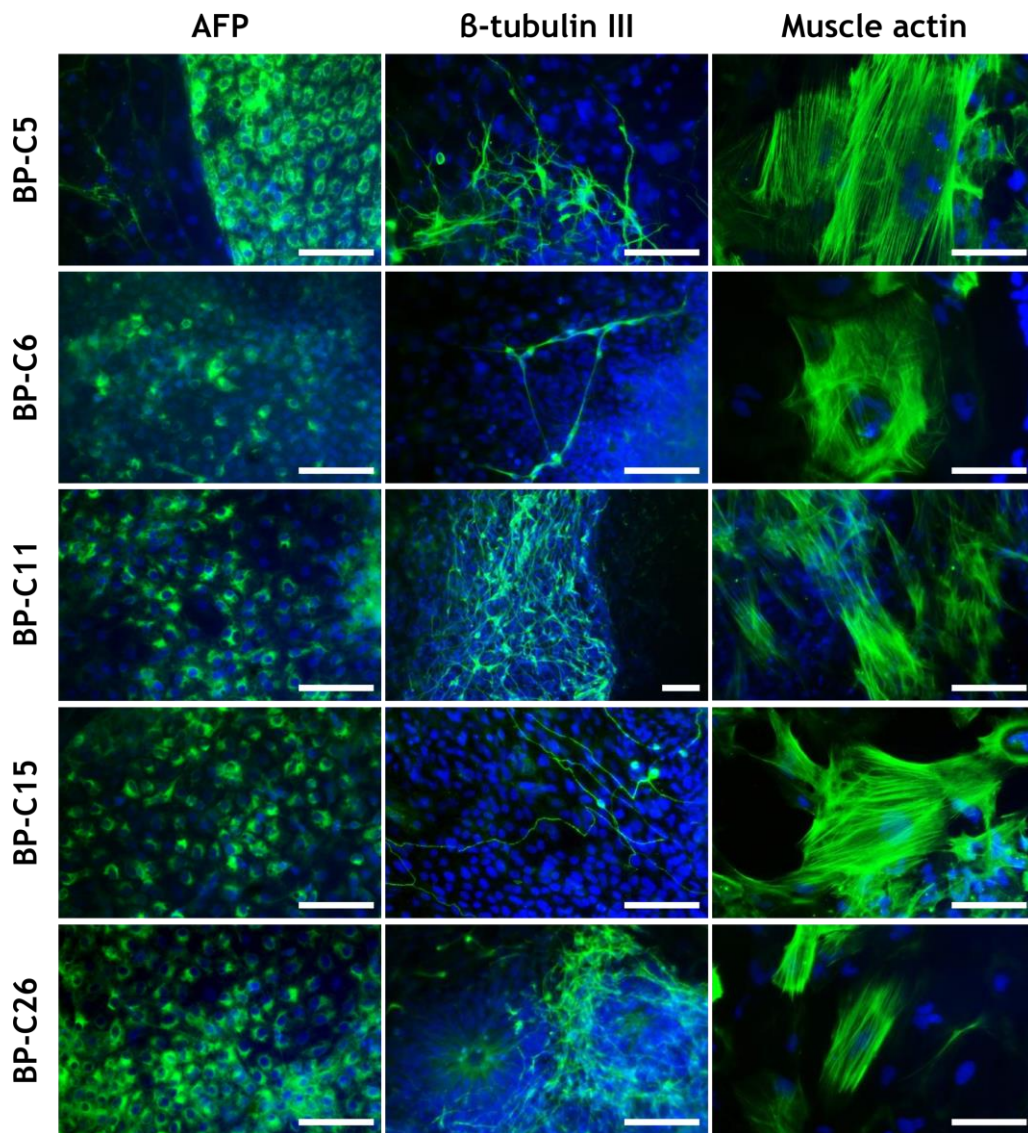


Figure 45: Immunocytochemistry for the three germ layers formed by BP iPS cell clones

EBs were formed from undifferentiated BP iPS cell clones and differentiated in suspension for 7 days and for an additional 10 days adherent to plates. EBs from all clones showed formation of all three germ layers endoderm (AFP), ectoderm (β -tubulin III) and mesoderm (muscle actin). Nuclei were counterstained with DAPI (blue). Scale bars represent 100 μ m.

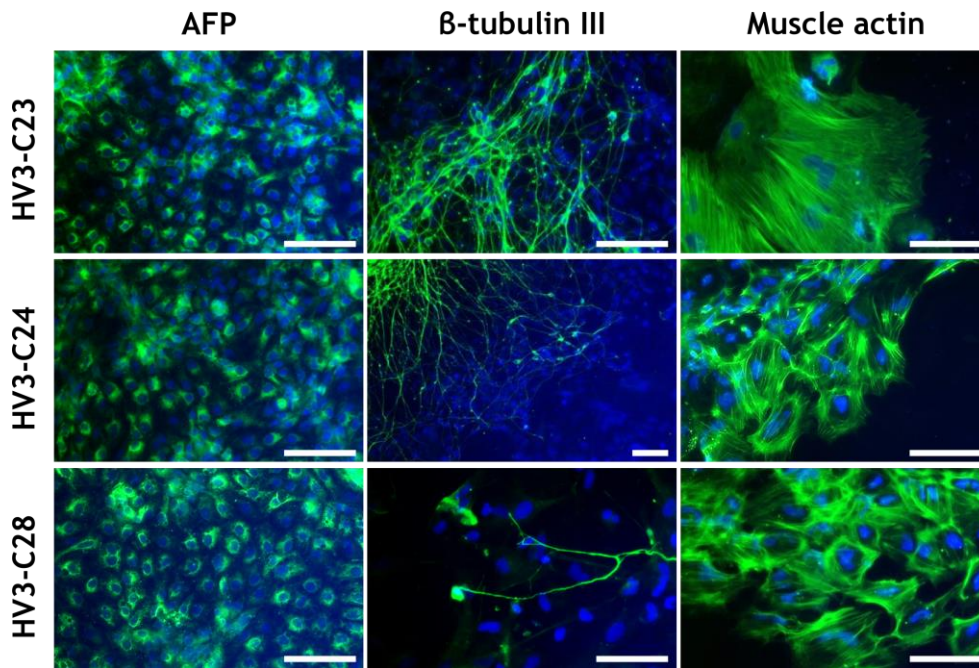


Figure 46: Immunocytochemistry for the three germ layers formed by HV3 iPS cell clones

EBs were formed from undifferentiated HV3 iPS cell clones and differentiated in suspension for 7 days and for an additional 10 days adherent to plates. EBs from all clones showed formation of all three germ layers endoderm (AFP), ectoderm (β -tubulin III) and mesoderm (muscle actin). Nuclei were counterstained with DAPI (blue). Scale bars represent 100 μ m.

5.4.1.7 Chromosomal integrity

Genomic DNA from each iPS cell line was analysed for chromosomal integrity as before with a single nucleotide polymorphism (SNP) array. Analysis of the LogR ratio in combination with the β -Allele Frequency revealed no microduplications in BP-C5, C15, C26 or any of the HV3 clones. A complete overview of all chromosomes is supplied in Appendix 1. Microduplications, shown in Figure 47, were detected in BP-C6 in chromosome 5 (q33.2, 155.453.475 - 155.967.030) and BP-C11 in chromosome 2 (q31.1, 171.032.090 - 171.435.002), chromosome 3 (p13, 71.688.564 - 74.289.885), chromosome 4 (q32.1, 155.654.421 - 155.938.012), chromosome 12 (p13.1, 13.394.582 - 13.446.880) and chromosome 17 (q12, 36.821.619 - 37.024.319). No microdeletions were detected in any of the samples. A list of the genes affected by microduplications in BP-C6 and C11 is provided in Table 17. Based on the SNP analysis, BP-C6 and C11 were excluded from subsequent experiments.

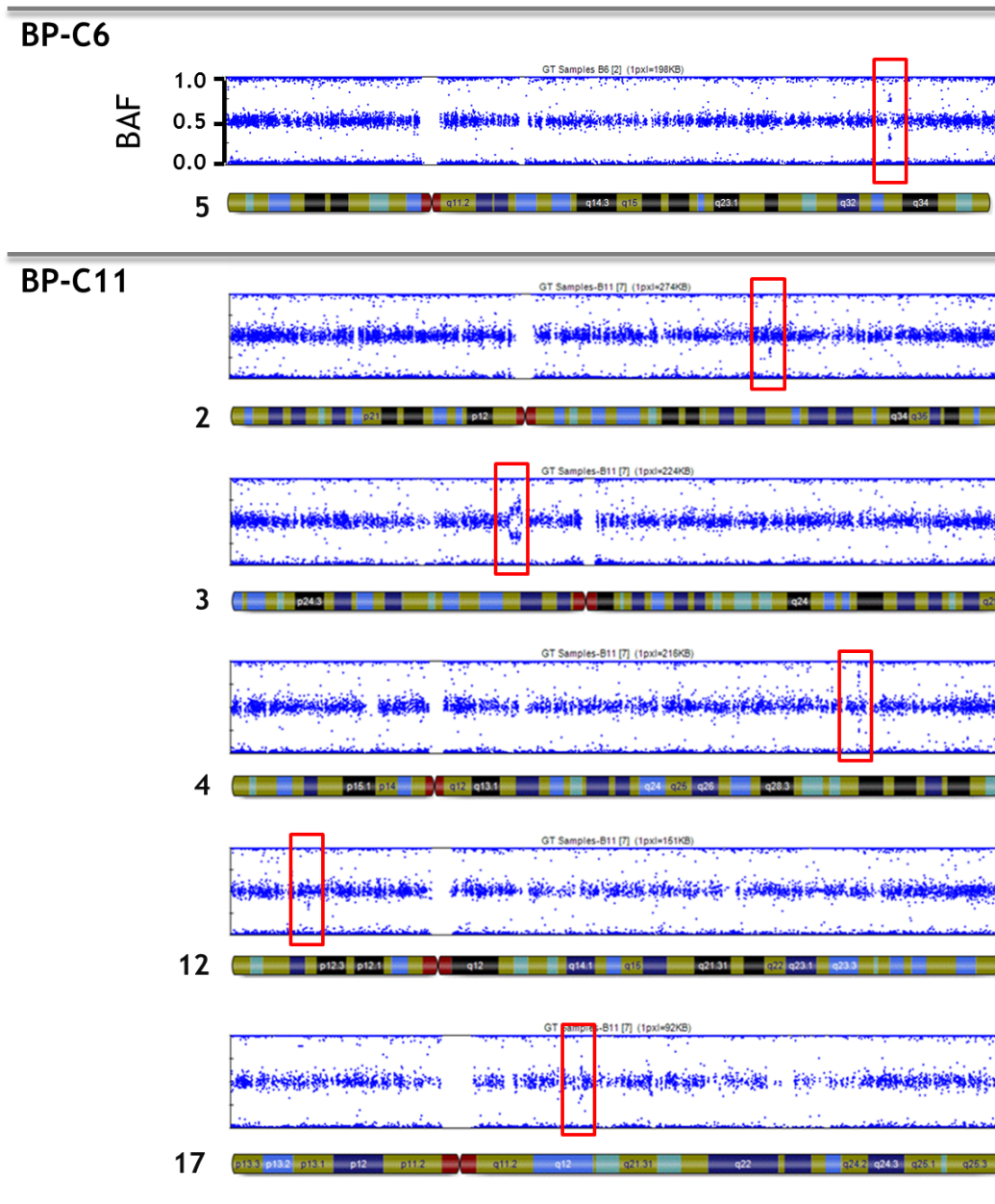


Figure 47: Microduplications identified through SNP analysis

Analysis of the β -Allele Frequency of a SNP array revealed microduplications in BP-C6 in chromosome 5 (q33.2, 155.453.475 - 155.967.030) and BP-C11 in chromosome 2 (q31.1, 171.032.090 - 171.435.002), chromosome 3 (p13, 71.688.564 – 74.289.885), chromosome 4 (q32.1, 155.654.421 - 155.938.012), chromosome 12 (p13.1, 13.394.582 - 13.446.880) and chromosome 17 (q12, 36.821.619 - 37.024.319). No microdeletions were detected in any of the samples. Red box indicates position of microduplication. BAF – β -Allele Frequency

Table 17: Microduplications identified through SNP analysis and the genes affected

Cell line	Region of microduplication	Genes affected
BP-C6	Chromosome 5 (q33.2, 155.453.475 - 155.967.030)	SGCG (delta-sarcoglycan)
	Chromosome 2 (q31.1, 171.032.090 - 171.435.002)	MYO3B (myosin IIIB)
BP-C11	Chromosome 3 (p13, 71.688.564 - 74.289.885)	PROK2 (prokineticin 2 isoform a precursor)
		GPR27 (G protein-coupled receptor 27)
		EIF4E3 (eukaryotic translation initiation factor 4E)
		RYBP (RING1 and YY1 binding protein)
		SHQ1 (SHQ1 homolog)
		GLT8D4 (glycosyltransferase 8 domain containing 4)
		PPP4R2 (protein phosphatase 4, regulatory subunit 2)
		FLJ10213 (hypothetical protein LOC55096)
		PDZRN3 (PDZ domain containing ring finger 3)
		Chromosome 4 (q32.1, 155.654.421 - 155.938.012)
BP-C11	Chromosome 12 (p13.1, 13.394.582 - 13.446.880)	no gene associated
		C17orf96 (hypothetical protein LOC100170841)
		MLLT6 (myeloid/lymphoid or mixed-lineage leukemia)
		CISD3 (CDGSH iron sulfur domain 3 precursor)
		PCGF2 (ring finger protein 110)
		PSMB3 (proteasome beta 3 subunit)
		PIP4K2B (phosphatidylinositol-5-phosphate 4-kinase, type)
		CCDC49 (coiled-coil domain containing 49)
		C17orf96 (hypothetical protein LOC388381)
		RPL23 (ribosomal protein L23)
SNORA21 (Homo sapiens small nucleolar RNA, H/ACA box 21 (SNORA21), non-coding RNA.)		

5.4.2 Generation and characterisation of cardiomyocytes

Previous experiments (3.2.8 Comparison of cardiac differentiation protocols) showed that, despite inter-line variability, guided differentiation protocols could be used to reliably and efficiently generate beating bodies. Due to technical difficulties discussed later on, no beating bodies were generated from HV3 iPS cell lines. No such issues were encountered with BP-derived iPS cell lines and beating bodies were generated from two patient-specific lines, BP-C5 and C26.

5.4.2.1 BP-derived cardiomyocytes - Morphology

Beating bodies generated from Brugada Syndrome patient iPS cell lines BP-C5 and BP-C26 (Figure 48 A, C) varied in size and rate at which they contracted even when derived from the same iPS cell line using the same differentiation protocol. The percentage of cardiomyocytes within a beating body, observed as the size of the contracting area, also differed. With regular dissections to remove surrounding proliferating non-cardiac tissue, beating bodies were maintained in culture for 3-4 weeks before disaggregation and analysis of single cardiomyocytes.

To investigate the properties of single BP iPS cell line derived cardiomyocytes, beating bodies were enzymatically and mechanically disaggregated and plated onto 1% gelatine. Disaggregation resulted in single as well as clusters of beating cardiomyocytes, with groups of connected cardiomyocytes exhibiting synchronised contraction. Cardiomyocytes derived from BP iPS cell lines resumed to contract 24-48 hours post disaggregation and showed morphologies similar to foetal cardiomyocytes (Figure 48 B, D). To allow for attachment but prevent overgrowth by proliferating non-cardiac cells, cardiomyocytes were analysed 3-4 days after disaggregation. Videos of spontaneously contracting beating bodies and single cardiomyocytes in culture derived from BP-C5 and BP-C26 are supplied in Appendix 2.

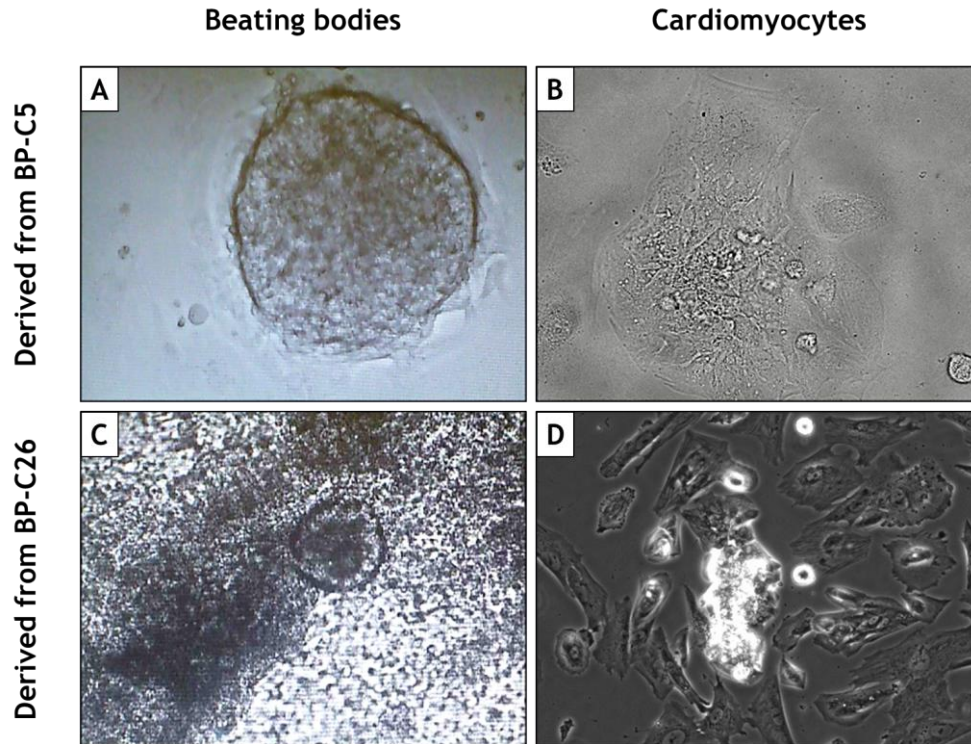


Figure 48: Beating bodies and single cardiomyocytes derived from BP-C5 and BP-C26

A and C (10x magnification) – BP-C5 and BP-C26 were differentiated using guided cardiac differentiation protocols. Size, contraction rate and percentage of contractile tissue differed between beating bodies. Beating bodies were cultured for 3-4 weeks before enzymatic and mechanical disaggregation. **B and D** (40x magnification) – Disaggregation resulted in single as well as clusters of beating cardiomyocytes, with groups of connected cardiomyocytes exhibiting synchronised contraction. Spontaneously contracting stem cell-derived cardiomyocytes showed morphologies similar to foetal cardiomyocytes.

5.4.2.2 BP-derived cardiomyocytes - Cardiac markers

Staining protocols optimised on primary human cardiac tissue were used to stain cardiomyocytes derived from BP-C5 and BP-C26. After 3-4 weeks of culture, beating bodies were enzymatically and mechanically disaggregated and plated onto 1% gelatine-coated glass coverslips. After 3-5 days of recovery, cells were fixed and stained for markers of the cardiac contractile apparatus. Cells isolated from beating bodies stained positive for alpha actinin, cardiac troponin I (cTnI) and cardiac troponin T (cTnT) (Figure 49 and Figure 50). Single cTnT staining exhibited the

striated pattern of thin filaments while double stainings for cTnI and alpha actinin resulted in alternating striations, staining thin filaments and Z-lines respectively. In most BP iPS cell-derived cardiomyocytes stainings showed myofibrils throughout the cells that lacked the complete parallel alignment of Z-lines detected in mature cardiomyocytes (Figure 49 B and Figure 50 F). Some cells, however, showed a greater number of myofibrils that exhibited a higher level of organisation (Figure 49 D and Figure 50 B). As observed with light microscopy, pluripotent stem cell-derived cardiomyocytes had no distinct rod shaped morphology.

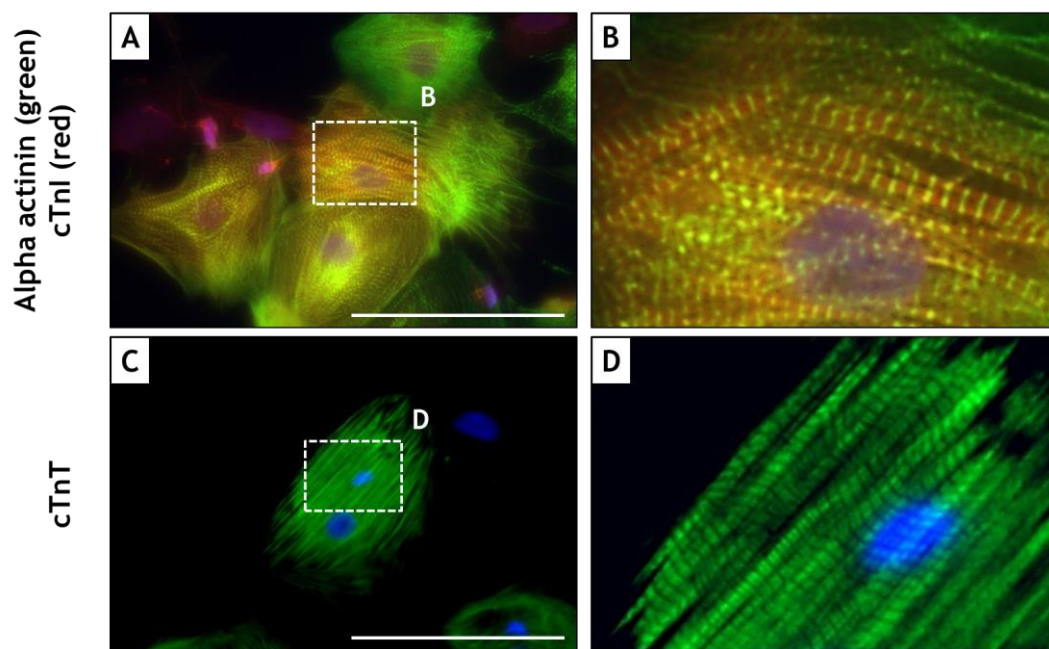


Figure 49: Immunocytochemistry for cardiac markers in cardiomyocytes derived from BP-C26
 3-4 week old beating bodies were disaggregated, plated onto 1% gelatine-coated glass coverslips, fixed after 3-5 days and stained for proteins of the cardiac contractile apparatus. Cells stained positive for **(A and B)** alpha actinin (green) and cTnI (red) and **(C and D)** cTnT, showing intact myofibrils but they displayed no rod shaped morphology. Nuclei were counterstained with DAPI (blue). Figure shows merged images. B and D are magnified areas in A and C respectively. Scale bars represent 100 μ m. Representative images of 20-30 cells from 3 beating bodies are shown.

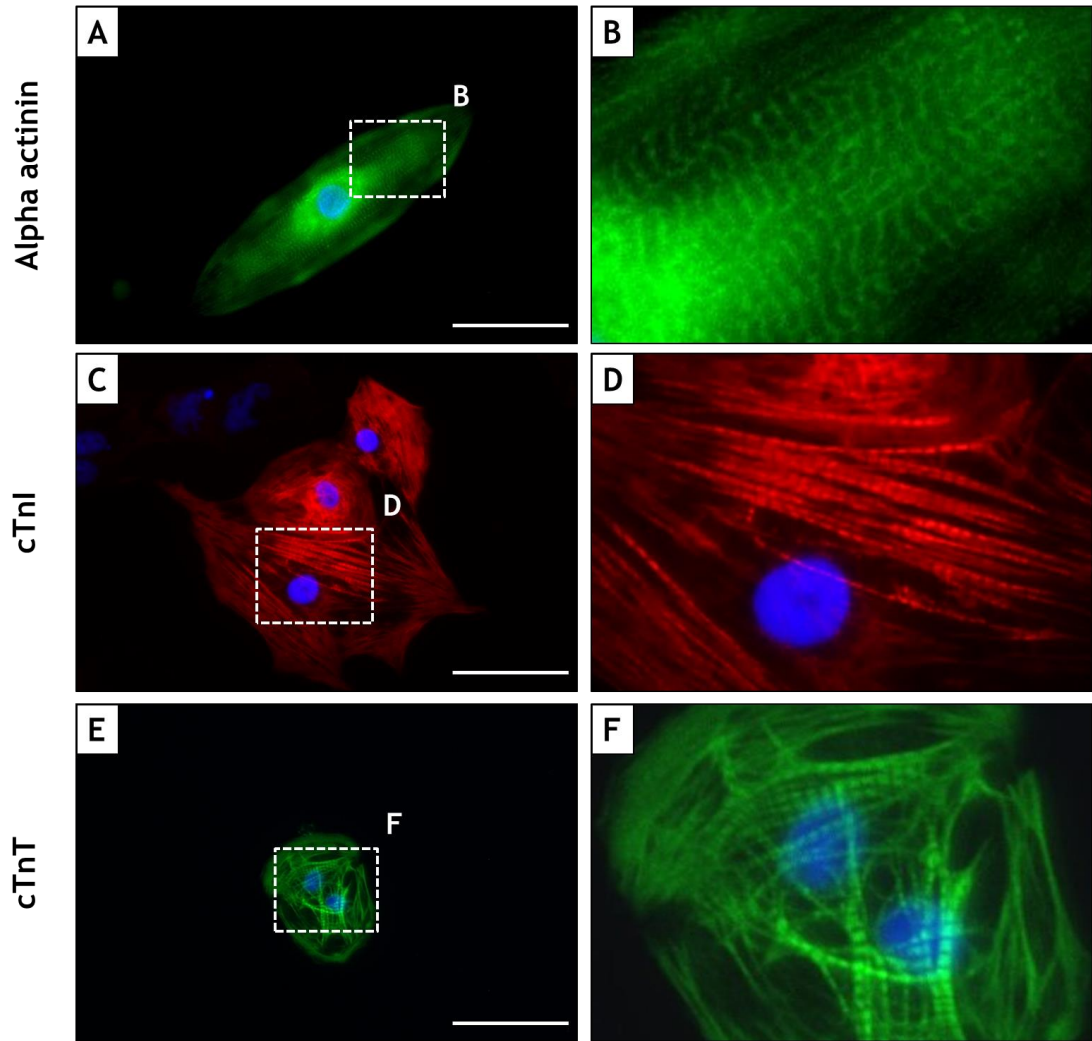


Figure 50: Immunocytochemistry for cardiac markers in cardiomyocytes derived from BP-C5

3-4 week old beating bodies were disaggregated, plated onto 1% gelatine-coated glass coverslips, fixed after 3-5 days and stained for proteins of the cardiac contractile apparatus. Cells stained positive for alpha actinin (**A and D**), cTnI (**B and E**) and cTnT (**C and F**) showing intact myofibrils but displayed no rod shaped morphology. Nuclei were counterstained with DAPI (blue). Figure shows merged images. D, E and F are magnified areas in A, B and C respectively. Scale bars represent 50 μm . Representative images of 20-30 cells from 3 beating bodies are shown.

5.4.2.3 BP-derived cardiomyocytes - Ultrastructure

Beating bodies derived from BP-C5 and BP-C26 were cultured for 3-4 weeks before being processed for transmission electron microscopy (TEM). In preparation for TEM, samples underwent protein fixation, lipid fixation and serial dehydration. Samples embedded in resin were stained and ultrathin sections were imaged. TEM images from different layers of beating bodies showed the presence of cardiac and non-cardiac cells. Images of cardiomyocytes are shown in Figure 51 and are representative of cells found in beating bodies derived from BP-C5 and BP-C26.

The ultrastructure of cardiomyocytes found in these beating bodies resembled that of those generated from healthy control hES and iPS cells (Chapter 4, page 120). Myofibrils varied in size with some consisting of a single sarcomere. Myofibrils were generally sparser than in adult cardiomyocytes and lacked the alignment of Z-lines (Figure 51 A). However, some cells contained a greater number of myofibrils with increased organisation, exhibiting some alignment of Z-lines between adjacent myofibrils (Figure 51 B). Patient-specific iPS cell-derived cardiomyocytes contained mitochondria and lipid deposits (Figure 51 C) as observed in adult and foetal cardiomyocytes. At high magnification, all sarcomeres showed Z-lines but a small number of cells contained sarcomeres with I-bands and A-bands in addition to Z-lines (Figure 51 D).

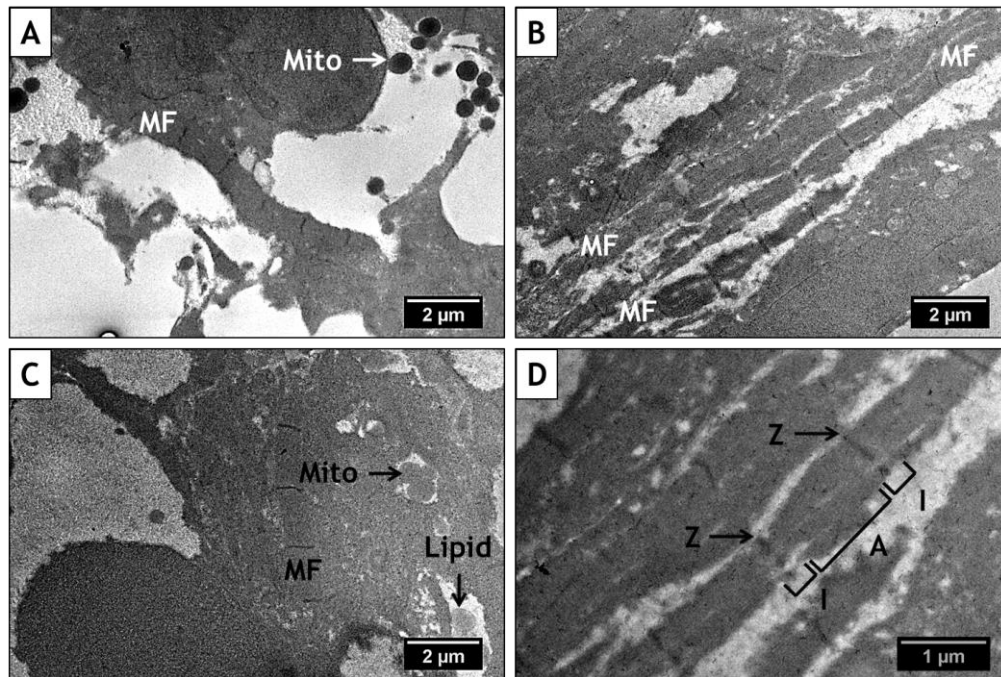


Figure 51: TEM of BP iPS cell-derived cardiomyocytes

A – After 3-4 weeks in culture most BP iPS cell-derived cardiomyocytes showed myofibrils (MF) comparable to foetal cells in number, size and sarcomere structure. **B** – Some cells contained a greater number of myofibrils with increased organisation and alignment of Z-lines (Z) of adjacent myofibrils. **C** – Mitochondria and lipid deposits were present. **D** – A few cells contained sarcomeres with I-bands (I) and A-bands (A) in addition to Z-lines. Representative images of cardiomyocytes derived from BP-C5 and BP-C26 from 3 beating bodies each are shown. Mito – mitochondrion

5.4.2.4 BP-derived cardiomyocytes - Membrane visualisation

The cell membrane of cardiomyocytes derived from BP-C5 and BP-C26 was visualised using a membrane dye in order to determine if transverse tubules (t-tubules) were present. Beating bodies that had been cultured for 3-4 weeks were disaggregated and seeded onto glass coverslips as described above for immunocytochemistry. After disaggregated cells resumed to spontaneously contract, their cell membrane was stained with the membrane dye Di-8-ANEPPS. Spontaneously contracting cells, regarded to be cardiomyocytes, were imaged in Z-stacks on a confocal microscope at 37°C. As observed in cardiomyocytes derived from H9 and 34-D6, no t-tubule structures were visible in stained cell membranes of cardiomyocytes derived from BP-C5 or BP-C26, representative images of which are shown in Figure 52.

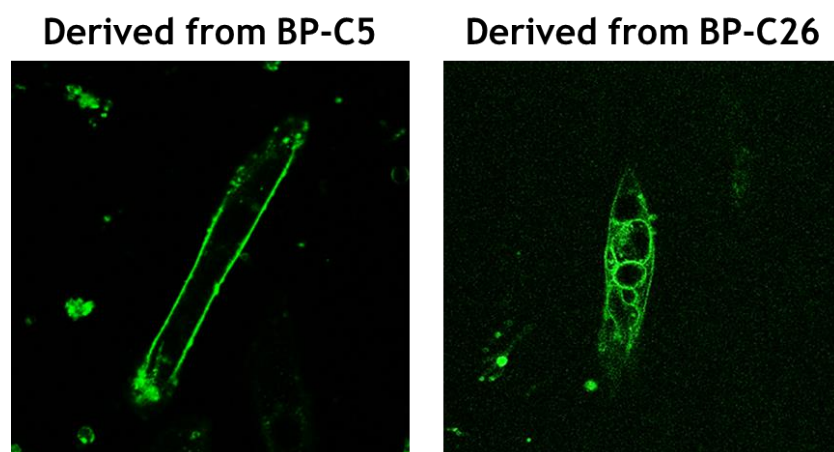


Figure 52: Visualisation of cell membrane of BP iPS cell-derived cardiomyocytes

Single cells from disaggregated 3-4 week old beating bodies were stained with the membrane dye Di-8-ANEPPS. Z-stacks of spontaneously contracting cells were imaged on a confocal microscope at 37°C. Visualised cell membranes of cardiomyocytes derived from BP-C5 or BP-C26 showed no t-tubules. Representative images of 5 cells for both BP-C5 and BP-C26 are shown.

5.4.2.5 BP-derived cardiomyocytes - Intracellular calcium imaging

For visualisation of calcium transients in patient-specific single cardiomyocytes, beating bodies derived from BP-C5 and BP-C26, which had been cultured for 2-3 weeks, were disaggregated and seeded onto glass coverslips as described for immunocytochemistry. After disaggregated cells resumed to spontaneously contract, cytoplasmic calcium was visualised with Fluo-4 as described in Chapter 4 (4.3.5 Intracellular calcium imaging). Spontaneously contracting cells were imaged for 20 s at room temperature using an optical camera connected to a fluorescence microscope. Representative videos of calcium transients are supplied in Appendix 2. Fluorescence intensities were traced over time and representative traces of calcium transients in BP-C5 and BP-C26 iPS cell-derived cardiomyocyte are shown in Figure 53. Peak heights decreased in both over time.

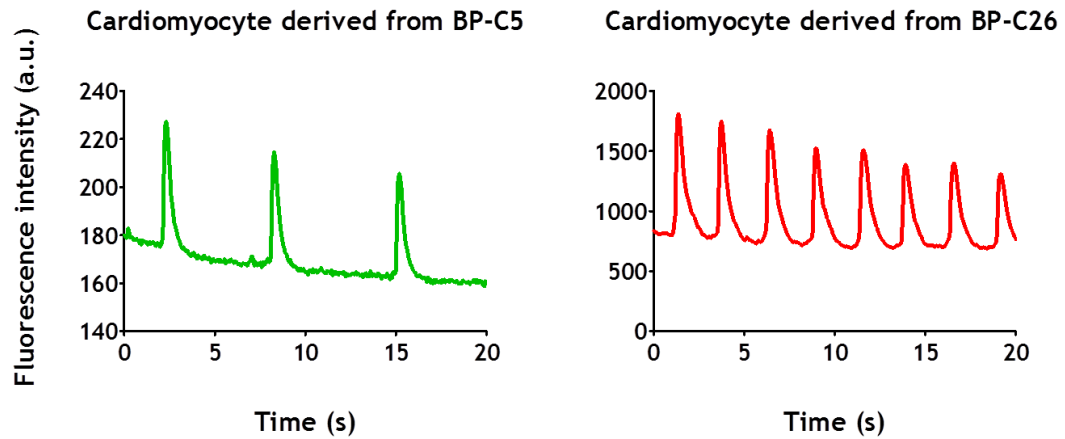


Figure 53: Calcium transients in BP iPS cell-derived cardiomyocytes

Beating bodies generated from BP-C5 and BP-C26 that had been cultured for 2-3 weeks were disaggregated and plated as single cells. After spontaneous contractions resumed, intracellular calcium was visualised with Fluo-4 and fluorescence intensities were recorded. Images show traces of fluorescence intensity in one cell over 20 s for both cell lines. Images are representative of 32 cells and 20 cells derived from three BP-C5 and three BP-C26 beating bodies respectively. Peak heights decreased in both over time. Fluorescence intensity is shown in arbitrary units (a.u.).

In order to compare the kinetics of calcium transients in patient-derived cardiomyocytes to previously analysed foetal and healthy control iPS cell-derived cardiomyocytes, data from one representative calcium transient from each of 52 cells (BP-C5 and C26 derived) was analysed and pooled. For each calcium transient, the background fluorescence was subtracted, and each data point normalised to the peak value. Pooled data for each time point was plotted as a mean \pm SEM (Figure 54).

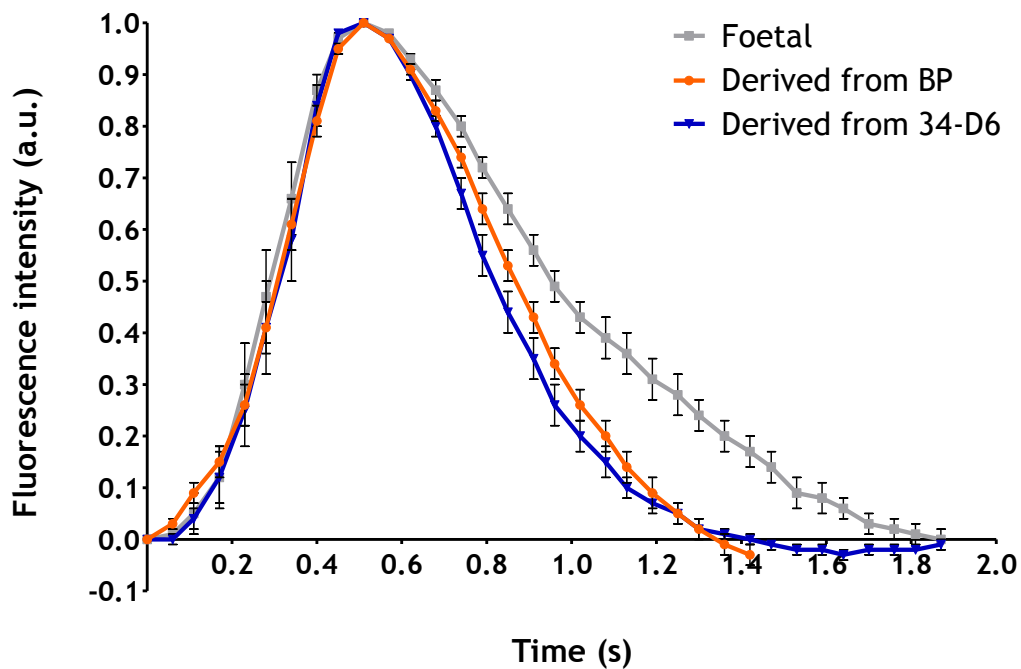


Figure 54: Single calcium transient in spontaneously contracting cardiomyocytes

One representative calcium transient from each of 52 BP iPS cell-derived cardiomyocytes was analysed as previously described in Chapter 4. Calcium transients of patient-specific derived cardiomyocytes resemble healthy control iPS cell-derived cardiomyocytes with faster decay kinetics than foetal cardiomyocytes. Fluorescence intensity is shown in arbitrary units (a.u.) as mean values with error bars representing SEM.

Because data had been normalised, amplitude (F/F_0) was the same for all cells and could not be compared between different cell lines. However, considerable differences were detected between their decay kinetics (t_{50} , t_{75} , t_{90}) (Figure 55). The decay kinetics are related to the speed at which calcium is pumped back into the sarcoplasmic reticulum and t_{50} , t_{75} and t_{90} refer to the times correlating to 50%, 75% and 90% decay of calcium transients. Decay of calcium transients was considerably slower in foetal cardiomyocytes compared to BP iPS cell-derived cardiomyocytes ($t_{50}=0.96$ s vs 0.86 s, $\Delta t_{50}=0.1$ s). The difference further increased at t_{75} (1.28 s vs 1.02 s, $\Delta t_{75}=0.26$ s) and t_{90} (1.53 s vs 1.19 s, $\Delta t_{90}=0.34$ s). Two-way ANOVA with a Bonferroni post-test showed no significant difference in calcium transients between 34-D6 and BP iPS cell-derived cardiomyocytes.

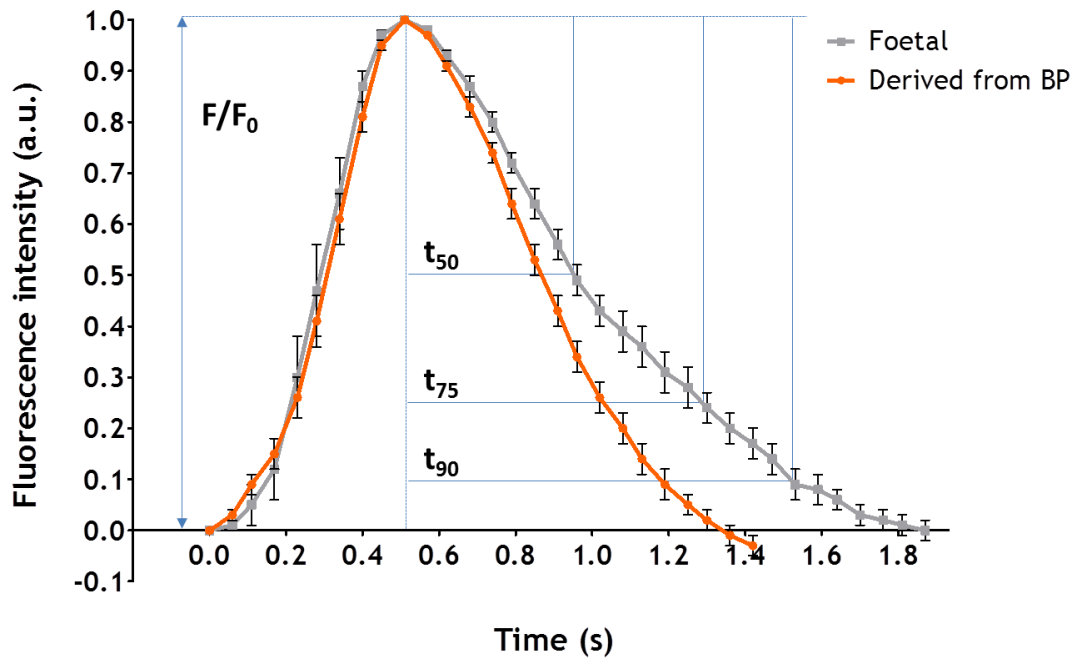


Figure 55: Decay kinetics of calcium transients in foetal and BP iPS cell-derived cardiomyocytes
 Decay kinetics differed between foetal and BP iPS cell-derived cardiomyocytes at times correlating to 50%, 75% and 90% decay of calcium transients (t_{50} , t_{75} and t_{90} respectively). Decay of calcium transients was markedly slower in foetal cells ($t_{50}=0.96$ s vs 0.86 s, $t_{75}= 1.28$ s vs 1.02 s and $t_{90}=1.53$ s vs 1.19 s). The difference between foetal and BP iPS cell-derived cells increased over time ($\Delta t_{50}=0.1$ s, $\Delta t_{75}=0.26$ s, $\Delta t_{90}=0.34$ s). Fluorescence intensity is shown in arbitrary units (a.u.) as the mean value of 14 (foetal) and 52 (BP) data points with error bars representing SEM.

5.4.2.6 Electrophysiology

Sodium currents in patient (BP-C5, BP-C26) and healthy (34-D6) control-derived cardiomyocytes were studied using the perforated patch-clamp technique previously optimised on hES cell-derived cardiomyocytes. Beating bodies were derived from undifferentiated BP-C5, BP-C26 and 34-D6 at the same time and cultured for similar lengths of time before shipment to Spain. In preparation for sodium current recordings of single cells beating bodies were disaggregated and plated onto gelatine as described previously for immunocytochemistry. Electrophysiological recordings were performed on single cells, identified as cardiomyocytes by their morphology and/or spontaneous contraction, 2-3 days after disaggregation. Sodium currents in

patient (n=10) and healthy control (n=4) iPS cell-derived cardiomyocytes at varying potentials were recorded and are shown in Figure 56 as mean \pm SEM. Recordings from BP-C5 (n=7) and BP-C26 (n=3) derived cardiomyocytes were pooled. Average sodium current density, calculated as the measured current normalised to the cells capacitance, was significantly reduced in patient-derived compared to healthy control-derived cardiomyocytes ($p=0.0027$) when analysing peak current densities with an unpaired student t-test. Maximum sodium current density was reduced by 48.38% in patient-specific cardiomyocytes.

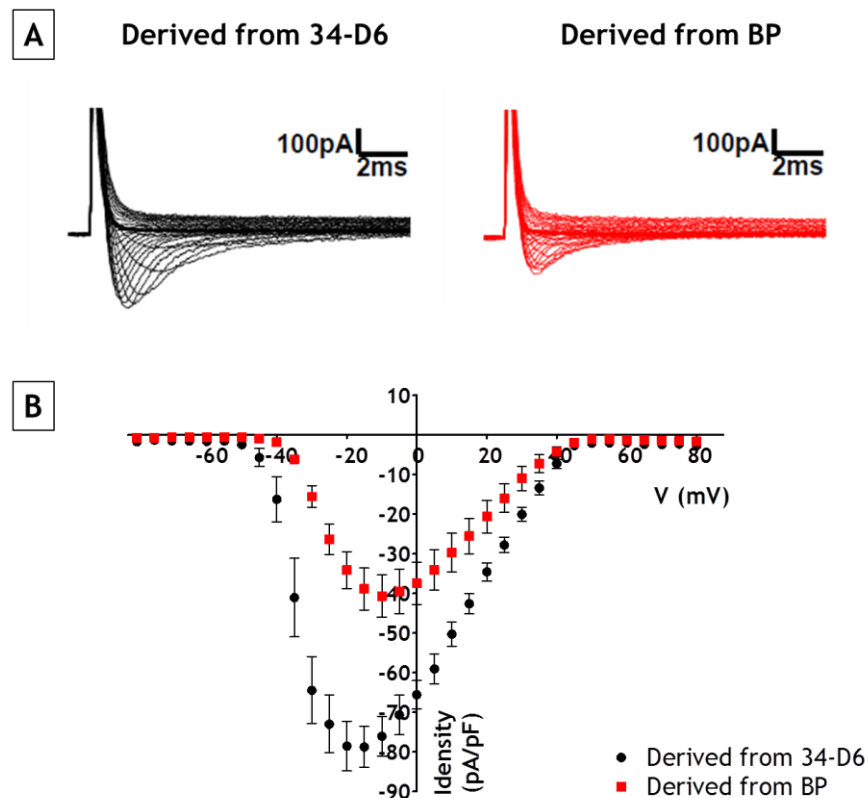


Figure 56: Sodium current densities of cardiomyocytes derived from Brugada Syndrome patient and healthy control iPS cells

A – Representative sodium current traces recorded from cardiomyocytes derived from Brugada Syndrome patient BP (C5 and C26) and healthy control 34-D6 iPS cells using perforated patch clamping. **B** – Current-voltage relationships for patient (n=10) and control-derived (n=4) cardiomyocytes are shown as mean \pm SEM. Maximum sodium current density of patient-derived cells was reduced to 51.62% of the healthy control-derived cardiomyocytes. Sodium currents were recorded by Dr Elisabet Selga.

5.5 Discussion and Conclusion

The aims of this chapter were to I) generate and fully characterise iPS cells from one Brugada Syndrome patient and one age- and sex-matched healthy volunteer and II) characterise cardiomyocytes derived from these iPS cell lines. Using techniques optimised in Chapter 3, newly generated iPS cell lines showed morphology and pluripotency marker expression on mRNA and protein level comparable to control lines H9, 33-D9 and 34-D6 and formed all three germ layers upon differentiation. Investigation of structural and functional characteristics of Brugada Syndrome patient-specific cardiomyocytes, using protocols optimised in Chapter 4, showed they more closely resembled foetal rather than adult cardiomyocytes and were indistinguishable from healthy control iPS cell line (34-D6) derived cardiomyocytes. Electrophysiological analysis of sodium current density however revealed a 48.38% reduction in patient-derived compared to healthy control cardiomyocytes.

Our patient with Brugada Syndrome was chosen for a number of reasons. Brugada Syndrome is a relatively rare disorder and only a handful of families in Scotland are known to be affected, not all of whom carry a known mutation. The recruited patient carried the missense mutation c.1100G>A in *SCN5A* resulting in a substitution of Arginine for Histidine at position 367 (p.R367H) in the alpha subunit of the cardiac sodium channel Na_v1.5. His classical Brugada Syndrome ECG with ST segment elevation and a mutation in *SCN5A*, the main identified genetic cause in Brugada Syndrome patients, made him an ideal candidate for this study. In addition, this particular mutation, in the first P segment of a pore-lining region, had previously been studied in expression systems allowing a comparison of results across different model systems. Since this was the first time classical Brugada Syndrome was modelled using iPS cell-derived cardiomyocytes a direct comparison with an analogous conventional expression system looking at the same mutation was deemed beneficial as a control before investigating novel mutations. Furthermore, studying the same mutation in its natural environment could reveal other alterations in the properties of the Na_v1.5 channel undetected by conventional expression systems. Genetic screening of the immediate family had identified siblings of the patient with and without the mutation with and without an abnormal ECG allowing for future

studies of symptomatic and asymptomatic patients that not only carry the same mutation but also have a very similar genetic background.

Reprogrammed fibroblasts from patient BP and age- and sex-matched healthy volunteer HV3 gave rise to 5 and 3 stable iPS cell lines respectively. The newly derived iPS cell lines did not differ from the hES control line H9 characterised in Chapter 3 in terms of morphology or expression of pluripotency markers as detected by immunocytochemistry and quantitative RT-PCR. Despite a trend towards lower expression of pluripotency markers Nanog, Sox-2 and c-Myc in most newly derived lines, none of the differences to H9 were significant, likely due to the large variability between biological repeats of H9. It is possible H9 samples showed greater variability because samples had been collected over a longer period of time whereas samples from BP and HV3 iPS cell clones usually differed by 2-3 passages. Analysed by flow cytometry, undifferentiated cultures of BP-C5, BP-C26 and HV3-C28 had a significantly lower percentage of SSEA3 positive cells. The differences observed might be attributed to genetic abnormalities or natural variability between pluripotent stem cell lines. To exclude genomic instability, all newly derived iPS cell lines were analysed with a SNP array. Microduplications found in BP-C6 and C11 were specific to those cell lines and were therefore acquired during reprogramming or subsequent culture. The multitude of microduplications found in BP-C11 made it difficult to predict the specific effects they would have on cardiac differentiation or on cardiomyocytes function. Based on the SNP analysis BP clones 6 and 11 were deemed unsuitable for disease modelling and excluded from further experiments. Detection of these microduplications again underlined the importance of SNP analysis instead of or at least in addition to regular karyotyping. Since lower expression levels of pluripotency markers did not appear to correlate with genomic instability, with the exception of BP-C6, it seems likely that different expression levels represented normal variability. None of these slight variations appeared to have an effect on the cell line's potential to differentiate into cells from all three germ layers and were therefore no reason for exclusion from further experiments. For subsequent experiments BP-C5 and BP-C26 were chosen, two cell lines at opposite ends of the pluripotency spectrum.

Due to reoccurring issues with mycoplasma exclusively in healthy volunteer HV3-derived iPS cell cultures, no characterisation of cardiomyocytes derived from these cell lines was possible. Mycoplasma contamination is one of the main problems associated with cell culture²¹¹ effecting cell morphology as well as metabolism²¹². Contaminated HV3 iPS cells were treated repeatedly for reoccurring mycoplasma contamination that likely affected their cardiac differentiation potential negatively. Mycoplasma treatment has been shown to significantly reduce cardiac differentiation in hES cells²¹³ and could explain why HV3-derived iPS cell clones failed to generate beating bodies. Nonetheless, the two guided cardiac differentiation protocols optimised in Chapter 3 efficiently and reliably generated beating bodies from undifferentiated BP clones 5 and 26. Patient-specific derived cardiomyocytes shared all the characteristics of previously investigated cardiomyocytes derived from healthy control hES (H9) and iPS cell lines (34-D6). Spontaneous contractions, unaligned myofibrils, immature sarcomeres and a lack of t-tubule structures in the cell membrane are all evidence of an immature foetal-like phenotype. However, as observed in healthy stem cell (H9 and 34-D6) derived cardiomyocytes in Chapter 4, some cardiomyocytes showed a slightly more mature phenotype with greater myofibril density, alignment of Z-lines of neighbouring myofibrils as well as presence of I- and A-bands in sarcomeres. Greater myofibril density and alignment of Z-lines of neighbouring myofibrils was observed with immunocytochemistry as well as TEM while the ultrastructure of more developed sarcomeres were observed in few cells with TEM.

Assessment of kinetics of intracellular calcium transients showed faster decay in BP iPS cell-derived cardiomyocytes compared to primary foetal cardiomyocytes. The minimally slower calcium decay compared to 34-D6 (healthy control iPS cell) derived cardiomyocytes was not significantly different and might be explained with differences in length of culture of the beating bodies prior to assessment. While calcium transients were measured in BP-derived beating bodies after 2 weeks in culture, beating bodies derived from 34-D6 were assessed after 5 weeks. This reduction of culture time by 3 weeks would have given the BP-derived beating

bodies less time to mature and could explain the slight shift of decay dynamics towards the foetal phenotype, as a 4 week difference in culture time has been shown to result in ultrastructural maturation. Overall, comparison of structure and intracellular calcium handling revealed no significant differences between cardiomyocytes derived from healthy control (H9, 34-D6) and patient-specific (BP) pluripotent stem cells. However, analysis of electrophysiological recordings revealed a 48.38% reduction of sodium current density in patient-derived compared to healthy control cardiomyocytes suggesting that the patient's heterozygous mutation in *SCN5A* resulted in a complete loss of function in mutated channels. This was in accordance with electrophysiological studies carried out in HEK293 cells and *Xenopus* oocytes where expression of channels carrying the patient's mutation (c.1100G>A) produced no measurable current^{74, 210}. These results illustrate the ability of patient-specific iPS cell technology to model the abnormal functional phenotype of an inherited channelopathy that is independent of structural abnormalities and that the relative immaturity of iPS cell-derived cardiomyocytes does not prevent their use as an accurate model system for channelopathies affecting the cardiac sodium channel Na_v1.5. This successful generation of a patient-specific iPS cell based model system for classical Brugada Syndrome allows for the first time to study a mutation in their native environment and holds the promise for further studies to investigate disease mechanisms of known and unknown mutations and to develop new therapies.

In conclusion, fibroblasts from one patient with classical Brugada Syndrome and one healthy volunteer were successfully reprogrammed. Using techniques optimised in Chapter 3, the morphological and functional characteristics of newly generated iPS cell lines were shown to be comparable to control lines H9, 33-D9 and 34-D6 in all regards. Examination of structural and functional characteristics of Brugada Syndrome patient-specific cardiomyocytes, derived using guided differentiation protocols optimised in Chapter 4, showed they were indistinguishable from healthy control iPS cell line (34-D6) derived cardiomyocytes in every aspect except sodium current density which was reduced by almost 50% in patient-derived cardiomyocytes.

CHAPTER 6

GENERAL DISCUSSION

Brugada Syndrome is a heterogeneous condition with an unpredictable clinical course. Understanding the cellular mechanisms that lead to the disease will help to provide clarity about differences in clinical outcome between patients and the role of modifier genes. However, with more than 400 genetic alterations known to cause Brugada Syndrome, this poses an enormous challenge. Complimentary *in vitro* and *in vivo* models have improved our understanding, however, some show contradictory results investigating the same mutation and they are all restricted to modelling cases in which the underlying genetic alteration is identified. Patient-specific iPS cells will help us to understand the consequences of different mutations that influence the clinical outcome for individual patients as well as help us to validate previous model systems and to overcome some of their limitations. The functional characterisation of cardiomyocytes derived from iPS cells bearing specific mutations have the potential to provide novel insight into the mechanisms and pathophysiology of this condition and may offer opportunities to improve the diagnosis and treatment of patients with Brugada Syndrome.

The overall aim of this study was to develop such a model system for Brugada Syndrome by generating iPS cell-derived cardiomyocytes from a patient with classical symptoms and a mutation that had previously been studied in other model systems. This was to be achieved step by step by developing and optimising protocols for reprogramming, cardiac differentiation and characterisation of *de novo* patient and healthy control cell lines.

In Chapter 3, comprehensive tests to assess pluripotency and differentiation potential of control pluripotent stem cells were established in order to subsequently validate patient-derived iPS cell lines. Additionally, cardiac differentiation protocols were systematically compared and optimised to establish a reliable, efficient and robust protocol to be adopted for patient-derived iPS cell lines. Cells from hES (H9) and iPS cell lines (33-D9 and 34-D6) exhibited typical stem cell morphology and expression of pluripotency markers Oct-4, Sox2, Nanog, c-Myc, SSEA-3, SSEA-4 and Tra-1-60 which was shown at the RNA or protein level. All tested pluripotent stem cell lines were capable of forming the three germ layers confirming their

pluripotency. SNP analysis identified two microduplications in H9 in regions not associated with genes, and one microduplication in 33-D9 and 34-D6 each that has been associated with long-term cell culture. Subsequent systematic comparison of a variety of cardiac differentiation protocols revealed significant inter-line variability in terms of efficiency and found that guided differentiation protocols could be used to reliably and efficiently generate beating bodies.

Healthy control hES and iPS cell lines fully validated in this chapter were used in subsequent chapters to generate healthy control cardiomyocytes for characterisation. Additionally, protocols optimised in this chapter were used at later stages to validate pluripotency of newly generated Brugada Syndrome patient-derived iPS cell lines and to efficiently generate beating bodies from them in order to characterise patient-specific cardiomyocytes.

In Chapter 4, pluripotent stem cell-derived cardiomyocytes generated from previously validated control pluripotent stem cell lines were compared to isolated primary human adult and foetal cardiomyocytes to evaluate their maturity and functionality. Improving our knowledge about the maturity of stem cell-derived cardiomyocytes will be critical if these are to be employed for the assessment of cellular function in cardiac disease modelling.

Cardiomyocytes were successfully isolated from foetal cardiac tissue while isolation of viable cells from adult tissue proved challenging. Morphological and structural comparisons demonstrated the respective classical phenotypes with adult cardiomyocytes displaying rod-shaped morphology and parallel aligned myofibrils with fully formed sarcomeres, while foetal cardiac cells exhibited less defined morphology, had fewer myofibrils that lacked parallel alignment and showed immature sarcomeres. Structural and functional characterisation of cardiomyocytes derived from a healthy hES (H9) and a healthy control iPS (34-D6) cell line showed varying degrees of maturity but overall more closely resembled foetal rather than adult cardiomyocytes. Spontaneous contraction was observed in stem cell-derived cardiomyocytes and immature human foetal but not adult cardiomyocytes. Stem

cell-derived cardiomyocytes also displayed organisation of myofibrils, ultrastructure, lack of t-tubules and intracellular calcium handling more similar to foetal than adult cardiomyocytes. In addition, they expressed functional voltage-activated sodium channels and exhibited action potential triggered CICR.

The maturity of healthy pluripotent stem cell-derived cardiomyocytes was comparable to a foetal phenotype but functional cardiac sodium channels were detected. Their functionality was confirmed and protocols optimised in this chapter were subsequently used to characterise newly derived patient-specific cardiomyocytes while the data gathered provides a platform for comparison against healthy control pluripotent stem cell-derived cardiomyocytes as well as adult and foetal controls.

Protocols established in Chapter 3 were then employed to generate and validate iPS cell lines from a Brugada Syndrome patient and a sex and age matched healthy volunteer. Next, patient-specific cardiomyocytes were generated and characterised employing protocols optimised in Chapter 4.

Fibroblasts from a Brugada Syndrome patient (BP) with classical symptoms and a mutation (c.1100G>A) in *SCN5A* and a healthy age- and sex-matched volunteer (HV3) were reprogrammed using episomal vectors carrying Oct-4, shp53, Sox2, Klf4, L-Myc and Lin28. Newly derived patient (n=5) and control iPS cell lines (n=3), did not differ significantly from the hES control line H9 characterised in Chapter 3 in terms of morphology and expression of pluripotency markers, with the exception of three clones (BP-C5, BP-C6, HV3-C28) that showed a significantly lower percentage of SSEA3 positive cells. Examination of structural and functional characteristics of Brugada Syndrome patient-specific cardiomyocytes, derived from two clones using guided differentiation, showed they were indistinguishable from healthy control iPS cell line (34-D6) derived cardiomyocytes in every aspect (morphology, myofibril organisation, sarcomere structure, t-tubule structures and kinetics of intracellular calcium transients). Importantly, sodium current density was reduced by 48.38% in Brugada Syndrome patient-derived cardiomyocytes. This

reduction in current density not only matches previous observations made in HEK293 cells and *Xenopus* oocytes, but for the first time demonstrates that classic Brugada Syndrome can successfully be modelled using patient-specific iPS cells. These results illustrate the ability of patient-specific iPS cell technology to model the abnormal functional phenotype of an inherited channelopathy that is independent of structural abnormalities and that the relative immaturity of iPS cell-derived cardiomyocytes does not prevent their use as an accurate model system for channelopathies affecting the cardiac sodium channel Na_v1.5. This iPS cell based model system for classical Brugada Syndrome allows for the first time to study the mutation in its native environment and holds the promise for further studies to investigate disease mechanisms of known and unknown mutations and to develop new therapies.

6.1 Limitations of this study

Although this study was ultimately successful in achieving our aims and provides promising future opportunities, it has its limitations with regard to both iPS cell technology in general and the experimental set-up of this particular project.

The iPS cell based model system has great strengths, but also limitations and should be considered to complement rather than replace other model systems. A major advantage of iPS cell technology is the generation of patient-specific iPS cells that not only carry the patient's exact genetic background but also permit the generation of the specific cell type directly affected by the disease, i.e. cardiomyocytes in the case of Brugada Syndrome. However, generating relevant iPS cells requires ethical approval, patient consent and a tissue sample. In comparison to expression systems it is also very expensive and time consuming. As with other *in vitro* systems cardiomyocytes generated from iPS cells also lack the complexity of an organ, specifically the 3D *in vivo* structure and the presence of other cell types providing complex signalling networks. Although *in vitro* differentiation techniques yield beating clusters or sheets composed of ventricular, atrial and pacemaker cells²¹⁴, they are not organised in layers of endo- and epicardium and are usually not pure

populations of ventricular or atrial cells. However, methods have been developed to direct differentiation towards a specific cardiac subtype by manipulating retinoid signals²¹⁵. Identification of the cell surface marker VCAM1²¹⁶ also made it possible to purify and reassemble iPS cell-derived cardiac cells in cardiac tissue sheets²¹⁷. This might prove particularly challenging for modelling VT/VF in cases of Brugada Syndrome, since arrhythmias have been linked to transmural gradients across the ventricular wall involving cells of the endo- and ectoderm and abnormalities in the RVOT.

A particular challenge remains the relative immaturity of the derived cardiomyocytes as evidenced by spontaneous contractions, immature ultra-structure and a lack of t-tubules. Further functional characteristics of pluripotent stem cell-derived cardiomyocytes have been reviewed in depth by Hoekstra et al²¹⁸. Although no cells resembling adult cardiomyocytes have been derived from pluripotent stem cells yet, recent studies have shown that stem cell-derived cardiomyocytes slowly mature structurally and functionally when kept in long term *in vitro* culture^{219, 220} and when exposed to mechanical loading²²¹.

In addition to the general limitations of iPS cell based model systems, some technical difficulties and limitations specific to this project such as low efficiency or suboptimal controls have to be considered and leave room for improvement. Although systematic comparison of cardiac differentiation protocols identified a reliable protocol, the efficiency was comparatively low. The main contributor to low efficiency was the selection of protocols for the comparison study, which was influenced by a variety of criteria. Protocols were chosen based on the fact that they were technically comparatively simple, cost-effective, allowed for investigation into the effect of serum and made efficiency easily assessable. The last condition in particular was the determining factor to use protocols involving EB formation. At the same time, to simplify comparison of a multitude of factors at the same time, protocols with identical or similar timings for addition of supplements and medium changes were preferred. Without these restrictions for a comparison study efforts can be focused on a chemically defined, growth factor-free monolayer protocol²²² that

was recently published and has proven reliable and efficient in our laboratory.

A major limitation was the occasional lack of adult cardiomyocyte controls. This was partly due to the absence of suitable equipment, e.g. field-stimulator to induce contraction for calcium imaging, and partly a result of the fact that mature adult cardiomyocytes quickly de-differentiate in culture, making experiments such as membrane staining, calcium imaging and electrophysiology, which require cells to be attached to a culture surface, particularly challenging. However, based on the fact that results from foetal cardiomyocytes in this study were in accordance with previously published results and vastly different from the expected adult phenotype, comparison with data on adult cardiomyocytes available in literature was considered sufficient for this aspect of our study.

Although age- and sex-matched control iPS cell lines were derived they did not give rise to beating bodies due to technical difficulties, i.e. persistent mycoplasma contamination, and could hence not be used as the appropriate control for patient-derived cardiomyocytes. Instead an iPS cell line previously derived from a healthy 35-year-old female was used as a control. Although Brugada Syndrome manifests differently in male and female patients carrying the same mutation this is thought to be caused by inherent differences in transient outward potassium current density and should hence have no effect on sodium current recordings⁶⁶. It is also more likely to become evident when considering the whole heart rather than a single cell. The age of the tissue donor on the other hand was not expected to have any significant influence on functionality of derived cardiomyocytes not only because Brugada Syndrome is not a disease that manifests later in life but also because cardiomyocytes generated from different iPS cell lines are all equally immature, independent of donor age.

6.2 Future directions

Having shown that classical Brugada Syndrome can successfully be modelled *in vitro* using patient-specific iPS cell-derived cardiomyocytes has both scientific as well as clinical implications and opens up exciting new opportunities.

The immediate focus is on ongoing efforts to not only increase the number of electrophysiologically characterised control and patient-derived cells to decrease the error and to include cardiomyocytes from age- and sex-matched controls, but also to broaden the spectrum of parameters analysed. In addition to total sodium current, kinetics of activation and inactivation can be investigated. However, mutations that lead to a complete loss of function, observed as a reduction of sodium current to 50% of wild type current, are unlikely to alter channel kinetics⁸³. Examining the mutated channel in its appropriate environment will allow us to determine the mechanism (e.g. disrupted cell-surface localisation, production of truncated proteins) by which it causes a complete loss of function. Identification of a mechanism that has thus far not been described may provide clues as to how better treat the patient. Additionally, patient-specific cardiomyocytes can provide a platform for screening of *de novo* drugs or those that are already in use to personalise treatment.

Generally, investigating mutant $\text{Na}_v1.5$ in their appropriate environment will help determine whether HEK293 cells or *Xenopus* oocytes more accurately represent the biophysical properties of mutant channels in cases where results are contradictory. In addition to being able to record action potentials, researchers can also investigate the effects of possible modulator proteins. This is particularly interesting in patients with clear Brugada Syndrome symptoms but no known mutation and symptom free individuals carrying the same mutation as their symptomatic siblings. The possibility to investigate Brugada Syndrome patients without known genetic cause and mutation carriers that show no symptoms is an advantage none of the other model systems have. On a larger scale it might even be conceivable to screen affected families in an attempt to understand the mechanisms of sudden cardiac disease. The iPS cell based model system also offers the most accurate and relevant setting for drug toxicity screening of all the model systems, which could help exclude potential drugs, based

on their toxic effects on cardiomyocytes, before they go into expensive trials. Lastly, since iPS cell lines are immortal and compared to other expression systems do not transiently express the mutant channel, they can be shared between groups, allowing for new collaborations and more in-depth characterisation.

Although cardiomyocytes derived from iPS cells represent a mixture of immature and more mature cells, they all exhibit typical cardiac markers and have functional cardiac sodium channels. This model system may be utilised to investigate patients with and without known genetic mutations to provide a better understanding of the pathophysiology of inherited cardiac channelopathies and has great potential to further scientific understanding and ultimately improve patient care.

REFERENCES

1. Antzelevitch C, Brugada P, Borggrefe M, Brugada J, Brugada R, Corrado D, Gussak I, LeMarec H, Nademanee K, Perez Riera AR, Shimizu W, Schulze-Bahr E, Tan H, Wilde A. Brugada syndrome: Report of the second consensus conference. *Heart Rhythm*. 2005;2:429-440
2. Brugada P, Brugada J. Right bundle branch block, persistent st segment elevation and sudden cardiac death: A distinct clinical and electrocardiographic syndrome. A multicenter report. *J Am Coll Cardiol*. 1992;20:1391-1396
3. Cerrato N, Giustetto C, Gribaudo E, Richiardi E, Barbonaglia L, Scrocco C, Zema D, Gaita F. Prevalence of type 1 brugada electrocardiographic pattern evaluated by twelve-lead twenty-four-hour holter monitoring. *Am J Cardiol*. 2015;115:52-56
4. Brugada P, Brugada R, Brugada J, Geelen P. Use of the prophylactic implantable cardioverter defibrillator for patients with normal hearts. *Am J Cardiol*. 1999;83:98D-100D
5. Brugada J, Brugada R, Brugada P. Pharmacological and device approach to therapy of inherited cardiac diseases associated with cardiac arrhythmias and sudden death. *J Electrocardiol*. 2000;33 Suppl:41-47
6. Probst V, Denjoy I, Meregalli PG, Amirault JC, Sacher F, Mansourati J, Babuty D, Villain E, Victor J, Schott JJ, Lupoglazoff JM, Mabo P, Veltmann C, Jesel L, Chevalier P, Clur SA, Haissaguerre M, Wolpert C, Le Marec H, Wilde AA. Clinical aspects and prognosis of brugada syndrome in children. *Circulation*. 2007;115:2042-2048
7. Priori SG, Napolitano C, Giordano U, Collisani G, Memmi M. Brugada syndrome and sudden cardiac death in children. *Lancet*. England; 2000:808-809.
8. Mizusawa Y, Wilde AA. Brugada syndrome. *Circ Arrhythm Electrophysiol*. 2012;5:606-616
9. Oe H, Takagi M, Tanaka A, Namba M, Nishibori Y, Nishida Y, Kawarabayashi T, Yoshiyama M, Nishimoto M, Tanaka K, Yoshikawa J. Prevalence and clinical course of the juveniles with brugada-type ecg in japanese population. *Pacing Clin Electrophysiol*. 2005;28:549-554
10. Chockalingam P, Rammeloo LA, Postema PG, Hruda J, Clur SA, Blom NA, Wilde AA. Fever-induced life-threatening arrhythmias in children harboring an scn5a mutation. *Pediatrics*. 2011;127:e239-244
11. Takigawa M, Noda T, Shimizu W, Miyamoto K, Okamura H, Satomi K, Suyama K, Aihara N, Kamakura S, Kurita T. Seasonal and circadian distributions of ventricular fibrillation in patients with brugada syndrome. *Heart Rhythm*. 2008;5:1523-1527
12. Kasanuki H, Ohnishi S, Ohtuka M, Matsuda N, Nirei T, Isogai R, Shoda M, Toyoshima Y, Hosoda S. Idiopathic ventricular fibrillation induced with vagal activity in patients without obvious heart disease. *Circulation*. 1997;95:2277-2285
13. Agostini D, Scanu P, Loiselet P, Babatasi G, Darlas Y, Grollier G, Potier JC,

- Bouvard G. Iodine-123-metaiodobenzylguanidine spect of regional cardiac adrenergic denervation in brugada syndrome. *J Nucl Med.* 1998;39:1129-1132
14. Kusano KF, Taniyama M, Nakamura K, Miura D, Banba K, Nagase S, Morita H, Nishii N, Watanabe A, Tada T, Murakami M, Miyaji K, Hiramatsu S, Nakagawa K, Tanaka M, Miura A, Kimura H, Fuke S, Sumita W, Sakuragi S, Urakawa S, Iwasaki J, Ohe T. Atrial fibrillation in patients with brugada syndrome relationships of gene mutation, electrophysiology, and clinical backgrounds. *J Am Coll Cardiol.* 2008;51:1169-1175
 15. Nielsen MW, Holst AG, Olesen SP, Olesen MS. The genetic component of brugada syndrome. *Front Physiol.* 2013;4:179
 16. Chen Q, Kirsch G, Zhang D, Brugada R, Brugada J, Brugada P, Potenza D, Moya A, Borggreffe M, Breithardt G, Ortiz-Lopez R, Wang Z, Antzelevitch C, O'Brien R, Schulze-Bahr E, Keating M, Towbin J, Wang Q. Genetic basis and molecular mechanism for idiopathic ventricular fibrillation. *Nature.* 1998;392:293-296
 17. Papadatos G, Wallerstein P, Head C, Ratcliff R, Brady P, Benndorf K, Saumarez R, Trezise A, Huang C, Vandenberg J, Colledge W, Grace A. Slowed conduction and ventricular tachycardia after targeted disruption of the cardiac sodium channel gene *scn5a*. *Proc Natl Acad Sci U S A.* 2002;99:6210-6215
 18. Yan G, Antzelevitch C. Cellular basis for the electrocardiographic j wave. *Circulation.* 1996;93:372-379
 19. Nademanee K, Veerakul G, Chandanamattha P, Chaothawee L, Ariyachaipanich A, Jirasirojanakorn K, Likittanasombat K, Bhuripanyo K, Ngarmukos T. Prevention of ventricular fibrillation episodes in brugada syndrome by catheter ablation over the anterior right ventricular outflow tract epicardium. *Circulation.* United States; 2011:1270-1279.
 20. Tukkie R, Sogaard P, Vleugels J, de Groot IK, Wilde AA, Tan HL. Delay in right ventricular activation contributes to brugada syndrome. *Circulation.* United States; 2004:1272-1277.
 21. Coronel R, Casini S, Koopmann TT, Wilms-Schopman FJ, Verkerk AO, de Groot JR, Bhuiyan Z, Bezzina CR, Veldkamp MW, Linnenbank AC, van der Wal AC, Tan HL, Brugada P, Wilde AA, de Bakker JM. Right ventricular fibrosis and conduction delay in a patient with clinical signs of brugada syndrome: A combined electrophysiological, genetic, histopathologic, and computational study. *Circulation.* United States; 2005:2769-2777.
 22. Meregalli PG, Wilde AA, Tan HL. Pathophysiological mechanisms of brugada syndrome: Depolarization disorder, repolarization disorder, or more? *Cardiovasc res.* Netherlands; 2005:367-378.
 23. Wilde AA, Postema PG, Di Diego JM, Viskin S, Morita H, Fish JM, Antzelevitch C. The pathophysiological mechanism underlying brugada syndrome: Depolarization versus repolarization. *J Mol Cell Cardiol.* 2010;49:543-553
 24. Rook MB, Evers MM, Vos MA, Bierhuizen MF. Biology of cardiac sodium channel *nav1.5* expression. *Cardiovasc Res.* 2012;93:12-23
 25. Herfst LJ, Rook MB, Jongsma HJ. Trafficking and functional expression of cardiac na^+ channels. *J Mol Cell Cardiol.* 2004;36:185-193

26. Ruan Y, Liu N, Priori SG. Sodium channel mutations and arrhythmias. *Nat Rev Cardiol.* 2009;6:337-348
27. Abriel H. Cardiac sodium channel nav1.5 and its associated proteins. *Arch Mal Coeur Vaiss.* 2007;100:787-793
28. Willis BC, Ponce-Balbuena D, Jalife J. Protein assemblies of sodium and inward rectifier potassium channels control cardiac excitability and arrhythmogenesis. *Am j physiol heart circ physiol.* Copyright (c) 2015 the American Physiological Society.; 2015:H1463-h1473.
29. Lemaillet G, Walker B, Lambert S. Identification of a conserved ankyrin-binding motif in the family of sodium channel alpha subunits. *J Biol Chem.* 2003;278:27333-27339
30. Cronk LB, Ye B, Kaku T, Tester DJ, Vatta M, Makielski JC, Ackerman MJ. Novel mechanism for sudden infant death syndrome: Persistent late sodium current secondary to mutations in caveolin-3. *Heart Rhythm.* 2007;4:161-166
31. Rizzo S, Lodder EM, Verkerk AO, Wolswinkel R, Beekman L, Pilichou K, Basso C, Remme CA, Thiene G, Bezzina CR. Intercalated disc abnormalities, reduced na(+) current density, and conduction slowing in desmoglein-2 mutant mice prior to cardiomyopathic changes. *Cardiovasc Res.* 2012;95:409-418
32. Gavillet B, Rougier JS, Domenighetti AA, Behar R, Boixel C, Ruchat P, Lehr HA, Pedrazzini T, Abriel H. Cardiac sodium channel nav1.5 is regulated by a multiprotein complex composed of syntrophins and dystrophin. *Circ Res.* 2006;99:407-414
33. Hennessey JA, Marcou CA, Wang C, Wei EQ, Tester DJ, Torchio M, Dagradi F, Crotti L, Schwartz PJ, Ackerman MJ, Pitt GS. Fgf12 is a candidate brugada syndrome locus. *Heart Rhythm.* 2013;10:1886-1894
34. London B, Michalec M, Mehdi H, Zhu X, Kerchner L, Sanyal S, Viswanathan PC, Pfahnl AE, Shang LL, Madhusudanan M, Baty CJ, Lagana S, Aleong R, Gutmann R, Ackerman MJ, McNamara DM, Weiss R, Dudley SC, Jr. Mutation in glycerol-3-phosphate dehydrogenase 1 like gene (gpd1-1) decreases cardiac na+ current and causes inherited arrhythmias. *Circulation.* 2007;116:2260-2268
35. Kattynarath D, Maugenre S, Neyroud N, Balse E, Ichai C, Denjoy I, Dilanian G, Martins RP, Fressart V, Berthet M, Schott JJ, Leenhardt A, Probst V, Le Marec H, Hainque B, Coulombe A, Hatem SN, Guicheney P. Mog1: A new susceptibility gene for brugada syndrome. *Circ Cardiovasc Genet.* 2011;4:261-268
36. Sato PY, Musa H, Coombs W, Guerrero-Serna G, Patino GA, Taffet SM, Isom LL, Delmar M. Loss of plakophilin-2 expression leads to decreased sodium current and slower conduction velocity in cultured cardiac myocytes. *Circ Res.* 2009;105:523-526
37. Shy D, Gillet L, Ogrodnik J, Albesa M, Verkerk AO, Wolswinkel R, Rougier JS, Barc J, Essers MC, Syam N, Marsman RF, van Mil AM, Rotman S, Redon R, Bezzina CR, Remme CA, Abriel H. Pdz domain-binding motif regulates cardiomyocyte compartment-specific nav1.5 channel expression and function. *Circulation.* 2014;130:147-160
38. Petitprez S, Zmoos AF, Ogrodnik J, Balse E, Raad N, El-Haou S, Albesa M, Bittihn P, Luther S, Lehnart SE, Hatem SN, Coulombe A, Abriel H. Sap97

- and dystrophin macromolecular complexes determine two pools of cardiac sodium channels nav1.5 in cardiomyocytes. *Circ Res.* 2011;108:294-304
39. Liu M, Yang KC, Dudley SC, Jr. Cardiac sodium channel mutations: Why so many phenotypes? *Nat Rev Cardiol.* 2014;11:607-615
 40. Leoni A, Gavillet B, Rougier J, Marionneau C, Probst V, Le Scouarnec S, Schott J, Demolombe S, Bruneval P, Huang C, Colledge W, Grace A, Le Marec H, Wilde A, Mohler P, Escande D, Abriel H, Charpentier F. Variable nav1.5 protein expression from the wild-type allele correlates with the penetrance of cardiac conduction disease in the scn5a(+/-) mouse model. *PLoS One.* 2010;5:e9298
 41. Royer A, van Veen TA, Le Bouter S, Marionneau C, Griol-Charhbili V, Léoni AL, Steenman M, van Rijen HV, Demolombe S, Goddard CA, Richer C, Escoubet B, Jarry-Guichard T, Colledge WH, Gros D, de Bakker JM, Grace AA, Escande D, Charpentier F. Mouse model of scn5a-linked hereditary long QT syndrome: Age-related conduction slowing and myocardial fibrosis. *Circulation.* 2005;111:1738-1746
 42. van Veen TA, Stein M, Royer A, Le Quang K, Charpentier F, Colledge WH, Huang CL, Wilders R, Grace AA, Escande D, de Bakker JM, van Rijen HV. Impaired impulse propagation in scn5a-knockout mice: Combined contribution of excitability, connexin expression, and tissue architecture in relation to aging. *Circulation.* 2005;112:1927-1935
 43. Jeevaratnam K, Zhang Y, Guzadhur L, Duehmke R, Lei M, Grace A, Huang C. Differences in sino-atrial and atrio-ventricular function with age and sex attributable to the scn5a+/- mutation in a murine cardiac model. *Acta Physiol (Oxf).* 2010;200:23-33
 44. Stokoe K, Balasubramaniam R, Goddard C, Colledge W, Grace A, Huang C. Effects of flecainide and quinidine on arrhythmogenic properties of scn5a+/- murine hearts modelling the brugada syndrome. *J Physiol.* 2007;581:255-275
 45. Martin C, Zhang Y, Grace A, Huang C. In vivo studies of scn5a+/- mice modeling brugada syndrome demonstrate both conduction and repolarization abnormalities. *J Electrocardiol.* 2010;43:433-439
 46. Dautova Y, Zhang Y, Grace A, Huang C. Atrial arrhythmogenic properties in wild-type and scn5a+/- murine hearts. *Exp Physiol.* 2010;95:994-1007
 47. Martin C, Zhang Y, Grace A, Huang C. Increased right ventricular repolarization gradients promote arrhythmogenesis in a murine model of brugada syndrome. *J Cardiovasc Electrophysiol.* 2010
 48. Matthews G, Martin C, Grace A, Zhang Y, Huang C. Regional variations in action potential alternans in isolated murine scn5a(+/-) hearts during dynamic pacing. *Acta Physiol (Oxf).* 2010
 49. Postema P, Van den Berg M, Van Tintelen J, Van den Heuvel F, Grundeken M, Hofman N, Van der Roest W, Nannenbergh E, Krapels I, Bezzina C, Wilde A. Founder mutations in the netherlands: Scn5a 1795insd, the first described arrhythmia overlap syndrome and one of the largest and best characterised families worldwide. *Neth Heart J.* 2009;17:422-428
 50. Remme CA, Verkerk AO, Nuyens D, van Ginneken AC, van Brunschot S, Belterman CN, Wilders R, van Roon MA, Tan HL, Wilde AA, Carmeliet P, de Bakker JM, Veldkamp MW, Bezzina CR. Overlap syndrome of cardiac sodium channel disease in mice carrying the equivalent mutation of human

- scn5a-1795insd. *Circulation*. 2006;114:2584-2594
51. Lopez-Santiago LF, Meadows LS, Ernst SJ, Chen C, Malhotra JD, McEwen DP, Speelman A, Noebels JL, Maier SK, Lopatin AN, Isom LL. Sodium channel *scn1b* null mice exhibit prolonged qt and rr intervals. *J Mol Cell Cardiol*. 2007;43:636-647
 52. Kapplinger JD, Tester DJ, Alders M, Benito B, Berthet M, Brugada J, Brugada P, Fressart V, Guerschicoff A, Harris-Kerr C, Kamakura S, Kyndt F, Koopmann TT, Miyamoto Y, Pfeiffer R, Pollevick GD, Probst V, Zumhagen S, Vatta M, Towbin JA, Shimizu W, Schulze-Bahr E, Antzelevitch C, Salisbury BA, Guicheney P, Wilde AA, Brugada R, Schott JJ, Ackerman MJ. An international compendium of mutations in the *scn5a*-encoded cardiac sodium channel in patients referred for brugada syndrome genetic testing. *Heart Rhythm*. 2010;7:33-46
 53. Park DS, Cerrone M, Morley G, Vasquez C, Fowler S, Liu N, Bernstein SA, Liu FY, Zhang J, Rogers CS, Priori SG, Chinitz LA, Fishman GI. Genetically engineered *scn5a* mutant pig hearts exhibit conduction defects and arrhythmias. *J Clin Invest*. 2014
 54. Kimura M, Kobayashi T, Owada S, Ashikaga K, Higuma T, Sasaki S, Iwasa A, Motomura S, Okumura K. Mechanism of st elevation and ventricular arrhythmias in an experimental brugada syndrome model. *Circulation*. 2004;109:125-131
 55. Szél T, Koncz I, Antzelevitch C. Cellular mechanisms underlying the effects of milrinone and cilostazol to suppress arrhythmogenesis associated with brugada syndrome. *Heart Rhythm*. 2013;10:1720-1727
 56. Take Y, Morita H, Wu J, Nagase S, Morita S, Toh N, Nishii N, Nakamura K, Kusano KF, Ohe T, Ito H, Zipes DP. Spontaneous electrocardiogram alterations predict ventricular fibrillation in brugada syndrome. *Heart Rhythm*. 2011;8:1014-1021
 57. Nishida K, Fujiki A, Mizumaki K, Sakabe M, Sugao M, Tsuneda T, Inoue H. Canine model of brugada syndrome using regional epicardial cooling of the right ventricular outflow tract. *J Cardiovasc Electrophysiol*. 2004;15:936-941
 58. Yan G, Antzelevitch C. Cellular basis for the brugada syndrome and other mechanisms of arrhythmogenesis associated with st-segment elevation. *Circulation*. 1999;100:1660-1666
 59. Morita H, Fukushima-Kusano K, Nagase S, Takenaka-Morita S, Nishii N, Kakishita M, Nakamura K, Emori T, Matsubara H, Ohe T. Site-specific arrhythmogenesis in patients with brugada syndrome. *J Cardiovasc Electrophysiol*. 2003;14:373-379
 60. Morita H, Zipes D, Fukushima-Kusano K, Nagase S, Nakamura K, Morita S, Ohe T, Wu J. Repolarization heterogeneity in the right ventricular outflow tract: Correlation with ventricular arrhythmias in brugada patients and in an in vitro canine brugada model. *Heart Rhythm*. 2008;5:725-733
 61. Morita H, Zipes D, Lopshire J, Morita S, Wu J. T wave alternans in an in vitro canine tissue model of brugada syndrome. *Am J Physiol Heart Circ Physiol*. 2006;291:H421-428
 62. Fish J, Antzelevitch C. Cellular mechanism and arrhythmogenic potential of t-wave alternans in the brugada syndrome. *J Cardiovasc Electrophysiol*. 2008;19:301-308

63. Morita H, Zipes D, Morita S, Wu J. Genotype-phenotype correlation in tissue models of brugada syndrome simulating patients with sodium and calcium channelopathies. *Heart Rhythm*. 2010;7:820-827
64. Morita H, Zipes D, Morita S, Wu J. Temperature modulation of ventricular arrhythmogenicity in a canine tissue model of brugada syndrome. *Heart Rhythm*. 2007;4:188-197
65. Hong K, Brugada J, Oliva A, Berruezo-Sanchez A, Potenza D, Pollevick GD, Guerchicoff A, Matsuo K, Burashnikov E, Dumaine R, Towbin JA, Nesterenko V, Brugada P, Antzelevitch C, Brugada R. Value of electrocardiographic parameters and ajmaline test in the diagnosis of brugada syndrome caused by scn5a mutations. *Circulation*. 2004;110:3023-3027
66. Fish J, Antzelevitch C. Cellular and ionic basis for the sex-related difference in the manifestation of the brugada syndrome and progressive conduction disease phenotypes. *J Electrocardiol*. 2003;36 Suppl:173-179
67. Barajas-Martinez H, Haufe V, Chamberland C, Roy M, Fecteau M, Cordeiro J, Dumaine R. Larger dispersion of ina in female dog ventricle as a mechanism for gender-specific incidence of cardiac arrhythmias. *Cardiovasc Res*. 2009;81:82-89
68. Morita H, Kusano K, Miura D, Nagase S, Nakamura K, Morita S, Ohe T, Zipes D, Wu J. Fragmented qrs as a marker of conduction abnormality and a predictor of prognosis of brugada syndrome. *Circulation*. 2008;118:1697-1704
69. Morita H, Zipes D, Morita S, Lopshire J, Wu J. Epicardial ablation eliminates ventricular arrhythmias in an experimental model of brugada syndrome. *Heart Rhythm*. 2009;6:665-671
70. Surber R, Hensellek S, Prochnau D, Werner GS, Benndorf K, Figulla HR, Zimmer T. Combination of cardiac conduction disease and long qt syndrome caused by mutation t1620k in the cardiac sodium channel. *Cardiovasc Res*. 2008;77:740-748
71. Bezzina C, Veldkamp M, van Den Berg M, Postma A, Rook M, Viersma J, van Langen I, Tan-Sindhunata G, Bink-Boelkens M, van Der Hout A, Mannens M, Wilde A. A single na(+) channel mutation causing both long-qt and brugada syndromes. *Circ Res*. 1999;85:1206-1213
72. Baroudi G, Chahine M. Biophysical phenotypes of scn5a mutations causing long qt and brugada syndromes. *FEBS Lett*. 2000;487:224-228
73. Huang H, Zhao J, Barrane FZ, Champagne J, Chahine M. Nav1.5/r1193q polymorphism is associated with both long qt and brugada syndromes. *Can J Cardiol*. 2006;22:309-313
74. Vatta M, Dumaine R, Varghese G, Richard T, Shimizu W, Aihara N, Nademanee K, Brugada R, Brugada J, Veerakul G, Li H, Bowles N, Brugada P, Antzelevitch C, Towbin J. Genetic and biophysical basis of sudden unexplained nocturnal death syndrome (sunds), a disease allelic to brugada syndrome. *Hum Mol Genet*. 2002;11:337-345
75. Veldkamp MW, Viswanathan PC, Bezzina C, Baartscheer A, Wilde AA, Balsler JR. Two distinct congenital arrhythmias evoked by a multidysfunctional na(+) channel. *Circ Res*. 2000;86:E91-97
76. Rook M, Bezzina Alshinawi C, Groenewegen W, van Gelder I, van Ginneken A, Jongsma H, Mannens M, Wilde A. Human scn5a gene mutations alter

- cardiac sodium channel kinetics and are associated with the brugada syndrome. *Cardiovasc Res.* 1999;44:507-517
77. Makita N, Shirai N, Wang D, Sasaki K, George AJ, Kanno M, Kitabatake A. Cardiac na(+) channel dysfunction in brugada syndrome is aggravated by beta(1)-subunit. *Circulation.* 2000;101:54-60
 78. Keller DI, Rougier JS, Kucera JP, Benammar N, Fressart V, Guicheney P, Madle A, Fromer M, Schläpfer J, Abriel H. Brugada syndrome and fever: Genetic and molecular characterization of patients carrying scn5a mutations. *Cardiovasc Res.* 2005;67:510-519
 79. Wan X, Chen S, Sadeghpour A, Wang Q, Kirsch GE. Accelerated inactivation in a mutant na(+) channel associated with idiopathic ventricular fibrillation. *Am J Physiol Heart Circ Physiol.* 2001;280:H354-360
 80. Vatta M, Dumaine R, Antzelevitch C, Brugada R, Li H, Bowles NE, Nademanee K, Brugada J, Brugada P, Towbin JA. Novel mutations in domain i of scn5a cause brugada syndrome. *Mol Genet Metab.* 2002;75:317-324
 81. Baroudi G, Pouliot V, Denjoy I, Guicheney P, Shrier A, Chahine M. Novel mechanism for brugada syndrome: Defective surface localization of an scn5a mutant (r1432g). *Circ Res.* 2001;88:E78-83
 82. Baroudi G, Napolitano C, Priori SG, Del Bufalo A, Chahine M. Loss of function associated with novel mutations of the scn5a gene in patients with brugada syndrome. *Can J Cardiol.* 2004;20:425-430
 83. Shin DJ, Kim E, Park SB, Jang WC, Bae Y, Han J, Jang Y, Joung B, Lee MH, Kim SS, Huang H, Chahine M, Yoon SK. A novel mutation in the scn5a gene is associated with brugada syndrome. *Life Sci.* 2007;80:716-724
 84. Barajas-Martínez HM, Hu D, Cordeiro JM, Wu Y, Kovacs RJ, Meltser H, Kui H, Elena B, Brugada R, Antzelevitch C, Dumaine R. Lidocaine-induced brugada syndrome phenotype linked to a novel double mutation in the cardiac sodium channel. *Circ Res.* 2008;103:396-404
 85. Cordeiro JM, Marieb M, Pfeiffer R, Calloe K, Burashnikov E, Antzelevitch C. Accelerated inactivation of the l-type calcium current due to a mutation in cacnb2b underlies brugada syndrome. *J Mol Cell Cardiol.* 2009;46:695-703
 86. Antzelevitch C, Pollevick GD, Cordeiro JM, Casis O, Sanguinetti MC, Aizawa Y, Guerchicoff A, Pfeiffer R, Oliva A, Wollnik B, Gelber P, Bonaros EP, Burashnikov E, Wu Y, Sargent JD, Schickel S, Oberheiden R, Bhatia A, Hsu LF, Haïssaguerre M, Schimpf R, Borggreffe M, Wolpert C. Loss-of-function mutations in the cardiac calcium channel underlie a new clinical entity characterized by st-segment elevation, short qt intervals, and sudden cardiac death. *Circulation.* 2007;115:442-449
 87. London B, Michalec M, Mehdi H, Zhu X, Kerchner L, Sanyal S, Viswanathan PC, Pfahnl AE, Shang LL, Madhusudanan M, Baty CJ, Lagana S, Aleong R, Gutmann R, Ackerman MJ, McNamara DM, Weiss R, Dudley SC. Mutation in glycerol-3-phosphate dehydrogenase 1 like gene (gpd1-l) decreases cardiac na+ current and causes inherited arrhythmias. *Circulation.* 2007;116:2260-2268
 88. Watanabe H, Koopmann TT, Le Scouarnec S, Yang T, Ingram CR, Schott JJ, Demolombe S, Probst V, Anselme F, Escande D, Wiesfeld AC, Pfeufer A, Kääh S, Wichmann HE, Hasdemir C, Aizawa Y, Wilde AA, Roden DM, Bezzina CR. Sodium channel beta1 subunit mutations associated with

- brugada syndrome and cardiac conduction disease in humans. *J Clin Invest.* 2008;118:2260-2268
89. Riuró H, Beltran-Alvarez P, Tarradas A, Selga E, Campuzano O, Vergés M, Pagans S, Iglesias A, Brugada J, Brugada P, Vázquez FM, Pérez GJ, Scornik FS, Brugada R. A missense mutation in the sodium channel $\beta 2$ subunit reveals *scn2b* as a new candidate gene for brugada syndrome. *Hum Mutat.* 2013;34:961-966
 90. Hu D, Barajas-Martinez H, Burashnikov E, Springer M, Wu Y, Varro A, Pfeiffer R, Koopmann TT, Cordeiro JM, Guerchicoff A, Pollevick GD, Antzelevitch C. A mutation in the beta 3 subunit of the cardiac sodium channel associated with brugada ecg phenotype. *Circ Cardiovasc Genet.* 2009;2:270-278
 91. Delpón E, Cordeiro JM, Núñez L, Thomsen PE, Guerchicoff A, Pollevick GD, Wu Y, Kanters JK, Larsen CT, Hofman-Bang J, Burashnikov E, Christiansen M, Antzelevitch C. Functional effects of *kcne3* mutation and its role in the development of brugada syndrome. *Circ Arrhythm Electrophysiol.* 2008;1:209-218
 92. Hu D, Barajas-Martinez H, Burashnikov E, Springer M, Wu Y, Varro A, Pfeiffer R, Koopmann TT, Cordeiro JM, Guerchicoff A, Pollevick GD, Antzelevitch C. A mutation in the beta 3 subunit of the cardiac sodium channel associated with brugada ecg phenotype. *Circ Cardiovasc Genet.* 2009;2:270-278
 93. Itoh H, Sakaguchi T, Ashihara T, Ding WG, Nagaoka I, Oka Y, Nakazawa Y, Yao T, Jo H, Ito M, Nakamura K, Ohe T, Matsuura H, Horie M. A novel *kcnh2* mutation as a modifier for short qt interval. *Int j cardiol.* Netherlands; 2009:83-85.
 94. Medeiros-Domingo A, Tan BH, Crotti L, Tester DJ, Eckhardt L, Cuoretti A, Kroboth SL, Song C, Zhou Q, Kopp D, Schwartz PJ, Makielski JC, Ackerman MJ. Gain-of-function mutation s422l in the *kcnj8*-encoded cardiac k(atp) channel *kir6.1* as a pathogenic substrate for j-wave syndromes. *Heart Rhythm.* 2010;7:1466-1471
 95. Burashnikov E, Pfeiffer R, Barajas-Martinez H, Delpon E, Hu D, Desai M, Borggrefe M, Haissaguerre M, Kanter R, Pollevick GD, Guerchicoff A, Laino R, Marieb M, Nademanee K, Nam GB, Robles R, Schimpf R, Stapleton DD, Viskin S, Winters S, Wolpert C, Zimmern S, Veltmann C, Antzelevitch C. Mutations in the cardiac l-type calcium channel associated with inherited j-wave syndromes and sudden cardiac death. *Heart Rhythm.* 2010;7:1872-1882
 96. Ohno S, Zankov DP, Ding WG, Itoh H, Makiyama T, Doi T, Shizuta S, Hattori T, Miyamoto A, Naiki N, Hancox JC, Matsuura H, Horie M. *Kcne5* (*kcne11*) variants are novel modulators of brugada syndrome and idiopathic ventricular fibrillation. *Circ Arrhythm Electrophysiol.* 2011;4:352-361
 97. .
 98. Crotti L, Marcou CA, Tester DJ, Castelletti S, Giudicessi JR, Torchio M, Medeiros-Domingo A, Simone S, Will ML, Dagradi F, Schwartz PJ, Ackerman MJ. Spectrum and prevalence of mutations involving *brs1*-through *brs12*-susceptibility genes in a cohort of unrelated patients referred for brugada syndrome genetic testing: Implications for genetic testing. *J Am Coll Cardiol.* 2012;60:1410-1418

99. Ishikawa T, Sato A, Marcou CA, Tester DJ, Ackerman MJ, Crotti L, Schwartz PJ, On YK, Park JE, Nakamura K, Hiraoka M, Nakazawa K, Sakurada H, Arimura T, Makita N, Kimura A. A novel disease gene for brugada syndrome: Sarcolemmal membrane-associated protein gene mutations impair intracellular trafficking of hnav1.5. *Circ Arrhythm Electrophysiol.* 2012;5:1098-1107
100. Liu H, Chatel S, Simard C, Syam N, Salle L, Probst V, Morel J, Millat G, Lopez M, Abriel H, Schott JJ, Guinamard R, Bouvagnet P. Molecular genetics and functional anomalies in a series of 248 brugada cases with 11 mutations in the trpm4 channel. *PLoS One.* 2013;8:e54131
101. Riuro H, Beltran-Alvarez P, Tarradas A, Selga E, Campuzano O, Verges M, Pagans S, Iglesias A, Brugada J, Brugada P, Vazquez FM, Perez GJ, Scornik FS, Brugada R. A missense mutation in the sodium channel beta2 subunit reveals scn2b as a new candidate gene for brugada syndrome. *Hum Mutat.* 2013;34:961-966
102. Hedley PL, Jørgensen P, Schlamowitz S, Moolman-Smook J, Kanters JK, Corfield VA, Christiansen M. The genetic basis of brugada syndrome: A mutation update. *Hum Mutat.* 2009;30:1256-1266
103. Gurdon JB, Elsdale TR, Fischberg M. Sexually mature individuals of xenopus laevis from the transplantation of single somatic nuclei. *Nature.* 1958;182:64-65
104. Campbell KH, McWhir J, Ritchie WA, Wilmut I. Sheep cloned by nuclear transfer from a cultured cell line. *Nature.* 1996;380:64-66
105. Takahashi K, Yamanaka S. Induction of pluripotent stem cells from mouse embryonic and adult fibroblast cultures by defined factors. *Cell.* 2006;126:663-676
106. Yu J, Vodyanik MA, Smuga-Otto K, Antosiewicz-Bourget J, Frane JL, Tian S, Nie J, Jonsdottir GA, Ruotti V, Stewart R, Slukvin, II, Thomson JA. Induced pluripotent stem cell lines derived from human somatic cells. *Science.* 2007;318:1917-1920
107. Okita K, Ichisaka T, Yamanaka S. Generation of germline-competent induced pluripotent stem cells. *Nature.* 2007;448:313-317
108. Takahashi K, Tanabe K, Ohnuki M, Narita M, Ichisaka T, Tomoda K, Yamanaka S. Induction of pluripotent stem cells from adult human fibroblasts by defined factors. *Cell.* 2007;131:861-872
109. Park IH, Zhao R, West JA, Yabuuchi A, Huo H, Ince TA, Lerou PH, Lensch MW, Daley GQ. Reprogramming of human somatic cells to pluripotency with defined factors. *Nature.* 2008;451:141-146
110. Nakagawa M, Koyanagi M, Tanabe K, Takahashi K, Ichisaka T, Aoi T, Okita K, Mochiduki Y, Takizawa N, Yamanaka S. Generation of induced pluripotent stem cells without myc from mouse and human fibroblasts. *Nat Biotechnol.* 2008;26:101-106
111. Park IH, Lerou PH, Zhao R, Huo H, Daley GQ. Generation of human-induced pluripotent stem cells. *Nat Protoc.* 2008;3:1180-1186
112. Zhao Y, Yin X, Qin H, Zhu F, Liu H, Yang W, Zhang Q, Xiang C, Hou P, Song Z, Liu Y, Yong J, Zhang P, Cai J, Liu M, Li H, Li Y, Qu X, Cui K, Zhang W, Xiang T, Wu Y, Liu C, Yu C, Yuan K, Lou J, Ding M, Deng H. Two supporting factors greatly improve the efficiency of human ipsc generation.

- Cell stem cell*. United States; 2008:475-479.
113. Feng B, Ng JH, Heng JC, Ng HH. Molecules that promote or enhance reprogramming of somatic cells to induced pluripotent stem cells. *Cell Stem Cell*. 2009;4:301-312
 114. Hou P, Li Y, Zhang X, Liu C, Guan J, Li H, Zhao T, Ye J, Yang W, Liu K, Ge J, Xu J, Zhang Q, Zhao Y, Deng H. Pluripotent stem cells induced from mouse somatic cells by small-molecule compounds. *Science*. 2013;341:651-654
 115. Masuda S, Wu J, Hishida T, Pandian GN, Sugiyama H, Izpisua Belmonte JC. Chemically induced pluripotent stem cells (cipscs): A transgene-free approach. *J Mol Cell Biol*. 2013;5:354-355
 116. Huangfu D, Maehr R, Guo W, Eijkelenboom A, Snitow M, Chen AE, Melton DA. Induction of pluripotent stem cells by defined factors is greatly improved by small-molecule compounds. *Nat Biotechnol*. 2008;26:795-797
 117. Stadtfeld M, Nagaya M, Utikal J, Weir G, Hochedlinger K. Induced pluripotent stem cells generated without viral integration. *Science*. 2008;322:945-949
 118. Zhou W, Freed CR. Adenoviral gene delivery can reprogram human fibroblasts to induced pluripotent stem cells. *Stem Cells*. 2009;27:2667-2674
 119. Okita K, Nakagawa M, Hyenjong H, Ichisaka T, Yamanaka S. Generation of mouse induced pluripotent stem cells without viral vectors. *Science*. 2008;322:949-953
 120. Yu J, Hu K, Smuga-Otto K, Tian S, Stewart R, Slukvin II, Thomson JA. Human induced pluripotent stem cells free of vector and transgene sequences. *Science*. 2009;324:797-801
 121. Kaji K, Norrby K, Paca A, Mileikovsky M, Mohseni P, Woltjen K. Virus-free induction of pluripotency and subsequent excision of reprogramming factors. *Nature*. 2009;458:771-775
 122. Woltjen K, Michael IP, Mohseni P, Desai R, Mileikovsky M, Hamalainen R, Cowling R, Wang W, Liu P, Gertsenstein M, Kaji K, Sung HK, Nagy A. Piggybac transposition reprograms fibroblasts to induced pluripotent stem cells. *Nature*. 2009;458:766-770
 123. Kim D, Kim CH, Moon JI, Chung YG, Chang MY, Han BS, Ko S, Yang E, Cha KY, Lanza R, Kim KS. Generation of human induced pluripotent stem cells by direct delivery of reprogramming proteins. *Cell Stem Cell*. 2009;4:472-476
 124. Warren L, Manos PD, Ahfeldt T, Loh YH, Li H, Lau F, Ebina W, Mandal PK, Smith ZD, Meissner A, Daley GQ, Brack AS, Collins JJ, Cowan C, Schlaeger TM, Rossi DJ. Highly efficient reprogramming to pluripotency and directed differentiation of human cells with synthetic modified mrna. *Cell Stem Cell*. 2010;7:618-630
 125. Park IH, Arora N, Huo H, Maherali N, Ahfeldt T, Shimamura A, Lensch MW, Cowan C, Hochedlinger K, Daley GQ. Disease-specific induced pluripotent stem cells. *Cell*. 2008;134:877-886
 126. Moretti A, Bellin M, Welling A, Jung CB, Lam JT, Bott-Flügel L, Dorn T, Goedel A, Höhnke C, Hofmann F, Seyfarth M, Sinnecker D, Schömig A, Laugwitz KL. Patient-specific induced pluripotent stem-cell models for long-qt syndrome. *N Engl J Med*. 2010;363:1397-1409

127. Matsa E, Rajamohan D, Dick E, Young L, Mellor I, Staniforth A, Denning C. Drug evaluation in cardiomyocytes derived from human induced pluripotent stem cells carrying a long qt syndrome type 2 mutation. *Eur Heart J.* 2011;32:952-962
128. Yazawa M, Hsueh B, Jia X, Pasca AM, Bernstein JA, Hallmayer J, Dolmetsch RE. Using induced pluripotent stem cells to investigate cardiac phenotypes in timothy syndrome. *Nature.* 2011
129. Davis RP, Casini S, van den Berg CW, Hoekstra M, Remme CA, Dambrot C, Salvatori D, Oostwaard DW, Wilde AA, Bezzina CR, Verkerk AO, Freund C, Mummery CL. Cardiomyocytes derived from pluripotent stem cells recapitulate electrophysiological characteristics of an overlap syndrome of cardiac sodium channel disease. *Circulation.* 2012;125:3079-3091
130. Nussbaum J, Minami E, Laflamme MA, Virag JA, Ware CB, Masino A, Muskheli V, Pabon L, Reinecke H, Murry CE. Transplantation of undifferentiated murine embryonic stem cells in the heart: Teratoma formation and immune response. *Faseb j.* 2007;21:1345-1357
131. Itskovitz-Eldor J, Schuldiner M, Karsenti D, Eden A, Yanuka O, Amit M, Soreq H, Benvenisty N. Differentiation of human embryonic stem cells into embryoid bodies compromising the three embryonic germ layers. *Mol Med.* 2000;6:88-95
132. Zhang J, Wilson GF, Soerens AG, Koonce CH, Yu J, Palecek SP, Thomson JA, Kamp TJ. Functional cardiomyocytes derived from human induced pluripotent stem cells. *Circ Res.* 2009;104:e30-41
133. Kehat I, Kenyagin-Karsenti D, Snir M, Segev H, Amit M, Gepstein A, Livne E, Binah O, Itskovitz-Eldor J, Gepstein L. Human embryonic stem cells can differentiate into myocytes with structural and functional properties of cardiomyocytes. *J Clin Invest.* 2001;108:407-414
134. Tran T, Wang X, Browne C, Zhang Y, Schinke M, Izumo S, Burcin M. Wnt3a-induced mesoderm formation and cardiomyogenesis in human embryonic stem cells. *Stem Cells.* 2009;27:1869-1878
135. Yoon BS, Yoo SJ, Lee JE, You S, Lee HT, Yoon HS. Enhanced differentiation of human embryonic stem cells into cardiomyocytes by combining hanging drop culture and 5-azacytidine treatment. *Differentiation.* 2006;74:149-159
136. Ng ES, Davis RP, Azzola L, Stanley EG, Elefanty AG. Forced aggregation of defined numbers of human embryonic stem cells into embryoid bodies fosters robust, reproducible hematopoietic differentiation. *Blood.* 2005;106:1601-1603
137. Burridge PW, Anderson D, Priddle H, Barbadillo Munoz MD, Chamberlain S, Allegrucci C, Young LE, Denning C. Improved human embryonic stem cell embryoid body homogeneity and cardiomyocyte differentiation from a novel v-96 plate aggregation system highlights interline variability. *Stem Cells.* 2007;25:929-938
138. Niebruegge S, Bauwens CL, Peerani R, Thavandiran N, Masse S, Sevaptisidis E, Nanthakumar K, Woodhouse K, Husain M, Kumacheva E, Zandstra PW. Generation of human embryonic stem cell-derived mesoderm and cardiac cells using size-specified aggregates in an oxygen-controlled bioreactor. *Biotechnol Bioeng.* 2009;102:493-507
139. Burridge PW, Thompson S, Millrod MA, Weinberg S, Yuan X, Peters A,

- Mahairaki V, Koliatsos VE, Tung L, Zambidis ET. A universal system for highly efficient cardiac differentiation of human induced pluripotent stem cells that eliminates interline variability. *PLoS One*. 2011;6:e18293
140. Fukuda K. Development of regenerative cardiomyocytes from mesenchymal stem cells for cardiovascular tissue engineering. *Artif Organs*. 2001;25:187-193
 141. Xu C, Police S, Rao N, Carpenter MK. Characterization and enrichment of cardiomyocytes derived from human embryonic stem cells. *Circ Res*. 2002;91:501-508
 142. Serena E, Figallo E, Tandon N, Cannizzaro C, Gerecht S, Elvassore N, Vunjak-Novakovic G. Electrical stimulation of human embryonic stem cells: Cardiac differentiation and the generation of reactive oxygen species. *Exp Cell Res*. 2009;315:3611-3619
 143. Sugi Y, Lough J. Anterior endoderm is a specific effector of terminal cardiac myocyte differentiation of cells from the embryonic heart forming region. *Dev Dyn*. 1994;200:155-162
 144. Nijmeijer RM, Leeuwis JW, DeLisio A, Mummery CL, Chuva de Sousa Lopes SM. Visceral endoderm induces specification of cardiomyocytes in mice. *Stem Cell Res*. 2009;3:170-178
 145. Mummery CL, van Achterberg TA, van den Eijnden-van Raaij AJ, van Haaster L, Willemsse A, de Laat SW, Piersma AH. Visceral-endoderm-like cell lines induce differentiation of murine p19 embryonal carcinoma cells. *Differentiation*. 1991;46:51-60
 146. Mummery C, Ward-van Oostwaard D, Doevendans P, Spijker R, van den Brink S, Hassink R, van der Heyden M, Opthof T, Pera M, de la Riviere A, Passier R, Tertoolen L. Differentiation of human embryonic stem cells to cardiomyocytes: Role of coculture with visceral endoderm-like cells. *Circulation*. 2003;107:2733-2740
 147. Freund C, Davis RP, Gkatzis K, Ward-van Oostwaard D, Mummery CL. The first reported generation of human induced pluripotent stem cells (ips cells) and ips cell-derived cardiomyocytes in the netherlands. *Neth Heart J*. 2010;18:51-54
 148. Passier R, Oostwaard D, Snapper J, Kloots J, Hassink R, Kuijk E, Roelen B, de la Riviere A, Mummery C. Increased cardiomyocyte differentiation from human embryonic stem cells in serum-free cultures. *Stem Cells*. 2005;23:772-780
 149. Graichen R, Xu X, Braam S, Balakrishnan T, Norfiza S, Sieh S, Soo S, Tham S, Mummery C, Colman A, Zweigerdt R, Davidson B. Enhanced cardiomyogenesis of human embryonic stem cells by a small molecular inhibitor of p38 mapk. *Differentiation*. 2008;76:357-370
 150. Xu X, Graichen R, Soo S, Balakrishnan T, Rahmat S, Sieh S, Tham S, Freund C, Moore J, Mummery C, Colman A, Zweigerdt R, Davidson B. Chemically defined medium supporting cardiomyocyte differentiation of human embryonic stem cells. *Differentiation*. 2008;76:958-970
 151. Voorhamme D, Yandell CA. Long r3igf-i as a more potent alternative to insulin in serum-free culture of hek293 cells. *Mol Biotechnol*. 2006;34:201-204
 152. Otsuji TG, Minami I, Kurose Y, Yamauchi K, Tada M, Nakatsuji N.

- Progressive maturation in contracting cardiomyocytes derived from human embryonic stem cells: Qualitative effects on electrophysiological responses to drugs. *Stem Cell Res.* 2010;4:201-213
153. Filipczyk AA, Passier R, Rochat A, Mummery CL. Regulation of cardiomyocyte differentiation of embryonic stem cells by extracellular signalling. *Cell Mol Life Sci.* 2007;64:704-718
 154. Smith JC, Price BM, Van Nimmen K, Huylebroeck D. Identification of a potent xenopus mesoderm-inducing factor as a homologue of activin a. *Nature.* 1990;345:729-731
 155. Ladd AN, Yatskievych TA, Antin PB. Regulation of avian cardiac myogenesis by activin/tgfbeta and bone morphogenetic proteins. *Dev Biol.* 1998;204:407-419
 156. Winnier G, Blessing M, Labosky PA, Hogan BL. Bone morphogenetic protein-4 is required for mesoderm formation and patterning in the mouse. *Genes Dev.* 1995;9:2105-2116
 157. Laflamme M, Chen K, Naumova A, Muskheli V, Fugate J, Dupras S, Reinecke H, Xu C, Hassanipour M, Police S, O'Sullivan C, Collins L, Chen Y, Minami E, Gill E, Ueno S, Yuan C, Gold J, Murry C. Cardiomyocytes derived from human embryonic stem cells in pro-survival factors enhance function of infarcted rat hearts. *Nat Biotechnol.* 2007;25:1015-1024
 158. Xu C, Police S, Hassanipour M, Li Y, Chen Y, Priest C, O'Sullivan C, Laflamme MA, Zhu WZ, Van Biber B, Hegerova L, Yang J, Delavan-Boorsma K, Davies A, Lebkowski J, Gold JD. Efficient generation and cryopreservation of cardiomyocytes derived from human embryonic stem cells. *Regen Med.* 2011;6:53-66
 159. Yang L, Soonpaa MH, Adler ED, Roepke TK, Kattman SJ, Kennedy M, Henckaerts E, Bonham K, Abbott GW, Linden RM, Field LJ, Keller GM. Human cardiovascular progenitor cells develop from a kdr+ embryonic-stem-cell-derived population. *Nature.* 2008;453:524-528
 160. Marvin MJ, Di Rocco G, Gardiner A, Bush SM, Lassar AB. Inhibition of wnt activity induces heart formation from posterior mesoderm. *Genes Dev.* 2001;15:316-327
 161. Schneider VA, Mercola M. Wnt antagonism initiates cardiogenesis in xenopus laevis. *Genes Dev.* 2001;15:304-315
 162. Ueno S, Weidinger G, Osugi T, Kohn AD, Golob JL, Pabon L, Reinecke H, Moon RT, Murry CE. Biphasic role for wnt/beta-catenin signaling in cardiac specification in zebrafish and embryonic stem cells. *Proc Natl Acad Sci U S A.* 2007;104:9685-9690
 163. Paige SL, Osugi T, Afanasiev OK, Pabon L, Reinecke H, Murry CE. Endogenous wnt/beta-catenin signaling is required for cardiac differentiation in human embryonic stem cells. *PLoS One.* 2010;5:e11134
 164. Kattman SJ, Witty AD, Gagliardi M, Dubois NC, Niapour M, Hotta A, Ellis J, Keller G. Stage-specific optimization of activin/nodal and bmp signaling promotes cardiac differentiation of mouse and human pluripotent stem cell lines. *Cell Stem Cell.* 2011;8:228-240
 165. Dinsmore J, Ratliff J, Deacon T, Pakzaban P, Jacoby D, Galpern W, Isacson O. Embryonic stem cells differentiated in vitro as a novel source of cells for transplantation. *Cell Transplant.* 1996;5:131-143

166. Takahashi T, Lord B, Schulze PC, Fryer RM, Sarang SS, Gullans SR, Lee RT. Ascorbic acid enhances differentiation of embryonic stem cells into cardiac myocytes. *Circulation*. 2003;107:1912-1916
167. Wu X, Ding S, Ding Q, Gray NS, Schultz PG. Small molecules that induce cardiomyogenesis in embryonic stem cells. *J Am Chem Soc*. 2004;126:1590-1591
168. Sadek H, Hannack B, Choe E, Wang J, Latif S, Garry MG, Garry DJ, Longgood J, Frantz DE, Olson EN, Hsieh J, Schneider JW. Cardiogenic small molecules that enhance myocardial repair by stem cells. *Proc Natl Acad Sci U S A*. 2008;105:6063-6068
169. Lian X, Hsiao C, Wilson G, Zhu K, Hazeltine LB, Azarin SM, Raval KK, Zhang J, Kamp TJ, Palecek SP. Robust cardiomyocyte differentiation from human pluripotent stem cells via temporal modulation of canonical wnt signaling. *Proc Natl Acad Sci U S A*. 2012;109:E1848-1857
170. Koeppen BM, Stanton BA. *Berne & levy physiology*. Mosby; 2009.
171. Perriard JC, Hirschy A, Ehler E. Dilated cardiomyopathy: A disease of the intercalated disc? *Trends Cardiovasc Med*. 2003;13:30-38
172. Sullivan GJ, Hay DC, Park IH, Fletcher J, Hannoun Z, Payne CM, Dalgetty D, Black JR, Ross JA, Samuel K, Wang G, Daley GQ, Lee JH, Church GM, Forbes SJ, Iredale JP, Wilmut I. Generation of functional human hepatic endoderm from human induced pluripotent stem cells. *Hepatology*. 2010;51:329-335
173. Bird SD, Doevendans PA, van Rooijen MA, Brutel de la Riviere A, Hassink RJ, Passier R, Mummery CL. The human adult cardiomyocyte phenotype. *Cardiovasc Res*. 2003;58:423-434
174. Smits AM, van Vliet P, Metz CH, Korfage T, Sluijter JP, Doevendans PA, Goumans MJ. Human cardiomyocyte progenitor cells differentiate into functional mature cardiomyocytes: An in vitro model for studying human cardiac physiology and pathophysiology. *Nat Protoc*. 2009;4:232-243
175. Maltsev VA, Wobus AM, Rohwedel J, Bader M, Hescheler J. Cardiomyocytes differentiated in vitro from embryonic stem cells developmentally express cardiac-specific genes and ionic currents. *Circ Res*. 1994;75:233-244
176. Mummery CL, Ward D, Passier R. Differentiation of human embryonic stem cells to cardiomyocytes by coculture with endoderm in serum-free medium. *Curr Protoc Stem Cell Biol*. 2007;Chapter 1:Unit 1F.2
177. Chomczynski P, Sacchi N. Single-step method of rna isolation by acid guanidinium thiocyanate-phenol-chloroform extraction. *Anal Biochem*. 1987;162:156-159
178. Riemersma JC. Osmium tetroxide fixation of lipids for electron microscopy. A possible reaction mechanism. *Biochim Biophys Acta*. 1968;152:718-727
179. Braam SR, Denning C, van den Brink S, Kats P, Hochstenbach R, Passier R, Mummery CL. Improved genetic manipulation of human embryonic stem cells. *Nat Methods*. 2008;5:389-392
180. Yu J, Vodyanik MA, Smuga-Otto K, Antosiewicz-Bourget J, Frane JL, Tian S, Nie J, Jonsdottir GA, Ruotti V, Stewart R, Slukvin II, Thomson JA. Induced pluripotent stem cell lines derived from human somatic cells. *Science*. 2007;318:1917-1920
181. Park IH, Zhao R, West JA, Yabuuchi A, Huo H, Ince TA, Lerou PH, Lensch

- MW, Daley GQ. Reprogramming of human somatic cells to pluripotency with defined factors. *Nature*. 2008;451:141-146
182. Kim K, Doi A, Wen B, Ng K, Zhao R, Cahan P, Kim J, Aryee MJ, Ji H, Ehrlich LI, Yabuuchi A, Takeuchi A, Cunniff KC, Hongguang H, McKinney-Freeman S, Naveiras O, Yoon TJ, Irizarry RA, Jung N, Seita J, Hanna J, Murakami P, Jaenisch R, Weissleder R, Orkin SH, Weissman IL, Feinberg AP, Daley GQ. Epigenetic memory in induced pluripotent stem cells. *Nature*. 2010;467:285-290
 183. Skottman H, Mikkola M, Lundin K, Olsson C, Stromberg AM, Tuuri T, Otonkoski T, Hovatta O, Lahesmaa R. Gene expression signatures of seven individual human embryonic stem cell lines. *Stem Cells*. 2005;23:1343-1356
 184. Efe JA, Hilcove S, Kim J, Zhou H, Ouyang K, Wang G, Chen J, Ding S. Conversion of mouse fibroblasts into cardiomyocytes using a direct reprogramming strategy. *Nat Cell Biol*. 2011;13:215-222
 185. Moretti A, Bellin M, Welling A, Jung CB, Lam JT, Bott-Flügel L, Dorn T, Goedel A, Höhnke C, Hofmann F, Seyfarth M, Sinnecker D, Schömig A, Laugwitz KL. Patient-specific induced pluripotent stem-cell models for long-qt syndrome. *N Engl J Med*. 2010;363:1397-1409
 186. Amps K, Andrews PW, Anyfantis G, Armstrong L, Avery S, Baharvand H, Baker J, Baker D, Munoz MB, Beil S, Benvenisty N, Ben-Yosef D, Biancotti JC, Bosman A, Brena RM, Brison D, Caisander G, Camarasa MV, Chen J, Chiao E, Choi YM, Choo AB, Collins D, Colman A, Crook JM, Daley GQ, Dalton A, De Sousa PA, Denning C, Downie J, Dvorak P, Montgomery KD, Feki A, Ford A, Fox V, Fraga AM, Frumkin T, Ge L, Gokhale PJ, Golan-Lev T, Gourabi H, Gropp M, Lu G, Hampl A, Harron K, Healy L, Herath W, Holm F, Hovatta O, Hyllner J, Inamdar MS, Irwanto AK, Ishii T, Jaconi M, Jin Y, Kimber S, Kiselev S, Knowles BB, Kopper O, Kukharensko V, Kuliev A, Lagarkova MA, Laird PW, Lako M, Laslett AL, Lavon N, Lee DR, Lee JE, Li C, Lim LS, Ludwig TE, Ma Y, Maltby E, Mateizel I, Mayshar Y, Mileikovsky M, Minger SL, Miyazaki T, Moon SY, Moore H, Mummery C, Nagy A, Nakatsuji N, Narwani K, Oh SK, Olson C, Otonkoski T, Pan F, Park IH, Pells S, Pera MF, Pereira LV, Qi O, Raj GS, Reubinoff B, Robins A, Robson P, Rossant J, Salekdeh GH, Schulz TC, Sermon K, Sheik Mohamed J, Shen H, Sherrer E, Sidhu K, Sivarajah S, Skottman H, Spits C, Stacey GN, Strehl R, Strelchenko N, Suemori H, Sun B, Suuronen R, Takahashi K, Tuuri T, Venu P, Verlinsky Y, Ward-van Oostwaard D, Weisenberger DJ, Wu Y, Yamanaka S, Young L, Zhou Q, Initiative ISC. Screening ethnically diverse human embryonic stem cells identifies a chromosome 20 minimal amplicon conferring growth advantage. *Nat Biotechnol*. 2011;29:1132-1144
 187. Waters CM, Littlewood TD, Hancock DC, Moore JP, Evan GI. C-myc protein expression in untransformed fibroblasts. *Oncogene*. 1991;6:797-805
 188. Pekkanen-Mattila M, Kerkelä E, Tanskanen JM, Pietilä M, Pelto-Huikko M, Hyttinen J, Skottman H, Suuronen R, Aalto-Setälä K. Substantial variation in the cardiac differentiation of human embryonic stem cell lines derived and propagated under the same conditions--a comparison of multiple cell lines. *Ann Med*. 2009;41:360-370
 189. Osafune K, Caron L, Borowiak M, Martinez RJ, Fitz-Gerald CS, Sato Y, Cowan CA, Chien KR, Melton DA. Marked differences in differentiation

- propensity among human embryonic stem cell lines. *Nat Biotechnol.* 2008;26:313-315
190. Moorman A, Webb S, Brown NA, Lamers W, Anderson RH. Development of the heart: (1) formation of the cardiac chambers and arterial trunks. *Heart.* 2003;89:806-814
 191. .
 192. Fuster V, O'Rourke R, Walsh R, Poole-Wilson P. *Hurst's the heart.* 2007.
 193. Schwartz RJ, Olson EN. Building the heart piece by piece: Modularity of cis-elements regulating nkx2-5 transcription. *Development.* 1999;126:4187-4192
 194. Sachinidis A, Fleischmann BK, Kolossov E, Wartenberg M, Sauer H, Hescheler J. Cardiac specific differentiation of mouse embryonic stem cells. *Cardiovasc Res.* 2003;58:278-291
 195. Ruzicka DL, Schwartz RJ. Sequential activation of alpha-actin genes during avian cardiogenesis: Vascular smooth muscle alpha-actin gene transcripts mark the onset of cardiomyocyte differentiation. *J Cell Biol.* 1988;107:2575-2586
 196. Sugi Y, Lough J. Onset of expression and regional deposition of alpha-smooth and sarcomeric actin during avian heart development. *Dev Dyn.* 1992;193:116-124
 197. Fischman DA. An electron microscope study of myofibril formation in embryonic chick skeletal muscle. *J Cell Biol.* 1967;32:557-575
 198. Sordahl LA, Crow CA, Kraft GH, Schwartz A. Some ultrastructural and biochemical aspects of heart mitochondria associated with development: Fetal and cardiomyopathic tissue. *J Mol Cell Cardiol.* 1972;4:1-10
 199. Barth E, Stammler G, Speiser B, Schaper J. Ultrastructural quantitation of mitochondria and myofilaments in cardiac muscle from 10 different animal species including man. *J Mol Cell Cardiol.* 1992;24:669-681
 200. Artman M, Henry G, Coetzee WA. Cellular basis for age-related differences in cardiac excitation-contraction coupling. *Prog Pediatr Cardiol.* 2000;11:185-194
 201. Takeshima H. Intracellular ca²⁺ store in embryonic cardiac myocytes. *Front Biosci.* 2002;7:d1642-1652
 202. Wetzel GT, Chen F, Klitzner TS. Ca²⁺ channel kinetics in acutely isolated fetal, neonatal, and adult rabbit cardiac myocytes. *Circ Res.* 1993;72:1065-1074
 203. Brette F, Orchard C. T-tubule function in mammalian cardiac myocytes. *Circ Res.* 2003;92:1182-1192
 204. Peeters GA, Sanguinetti MC, Eki Y, Konarzewska H, Renlund DG, Karwande SV, Barry WH. Method for isolation of human ventricular myocytes from single endocardial and epicardial biopsies. *Am J Physiol.* 1995;268:H1757-1764
 205. Cao N, Liao J, Liu Z, Zhu W, Wang J, Liu L, Yu L, Xu P, Cui C, Xiao L, Yang HT. In vitro differentiation of rat embryonic stem cells into functional cardiomyocytes. *Cell Res.* 2011;21:1316-1331
 206. Sanger JM, Mittal B, Pochapin MB, Sanger JW. Myofibrillogenesis in living cells microinjected with fluorescently labeled alpha-actinin. *J Cell Biol.* 1986;102:2053-2066
 207. Lieu DK, Liu J, Siu CW, McNerney GP, Tse HF, Abu-Khalil A, Huser T, Li

- RA. Absence of transverse tubules contributes to non-uniform Ca^{2+} wavefronts in mouse and human embryonic stem cell-derived cardiomyocytes. *Stem Cells Dev.* 2009;18:1493-1500
208. Seki S, Nagashima M, Yamada Y, Tsutsuura M, Kobayashi T, Namiki A, Tohse N. Fetal and postnatal development of Ca^{2+} transients and Ca^{2+} sparks in rat cardiomyocytes. *Cardiovasc Res.* 2003;58:535-548
209. Lee YK, Ng KM, Lai WH, Chan YC, Lau YM, Lian Q, Tse HF, Siu CW. Calcium homeostasis in human induced pluripotent stem cell-derived cardiomyocytes. *Stem Cell Rev.* 2011;7:976-986
210. Hong K, Berruezo-Sanchez A, Pongvarin N, Oliva A, Vatta M, Brugada J, Brugada P, Towbin JA, Dumaine R, Pinero-Galvez C, Antzelevitch C, Brugada R. Phenotypic characterization of a large European family with Brugada syndrome displaying a sudden unexpected death syndrome mutation in *scn5a*. *J Cardiovasc Electrophysiol.* 2004;15:64-69
211. Armstrong SE, Mariano JA, Lundin DJ. The scope of mycoplasma contamination within the biopharmaceutical industry. *Biologicals.* 2010;38:211-213
212. Nikfarjam L, Farzaneh P. Prevention and detection of mycoplasma contamination in cell culture. *Cell J.* 2012;13:203-212
213. P136. Effects of mycoplasma elimination agent on cardiac differentiation of human embryonic stem cells. 2010;80:S63
214. Ma J, Guo L, Fiene SJ, Anson BD, Thomson JA, Kamp TJ, Kolaja KL, Swanson BJ, January CT. High purity human-induced pluripotent stem cell-derived cardiomyocytes: Electrophysiological properties of action potentials and ionic currents. *Am J Physiol Heart Circ Physiol.* 2011;301:H2006-2017
215. Zhang Q, Jiang J, Han P, Yuan Q, Zhang J, Zhang X, Xu Y, Cao H, Meng Q, Chen L, Tian T, Wang X, Li P, Hescheler J, Ji G, Ma Y. Direct differentiation of atrial and ventricular myocytes from human embryonic stem cells by alternating retinoid signals. *Cell Res.* 2011;21:579-587
216. Uosaki H, Fukushima H, Takeuchi A, Matsuoka S, Nakatsuji N, Yamanaka S, Yamashita JK. Efficient and scalable purification of cardiomyocytes from human embryonic and induced pluripotent stem cells by *vcam1* surface expression. *PLoS One.* 2011;6:e23657
217. Masumoto H, Matsuo T, Yamamizu K, Uosaki H, Narazaki G, Katayama S, Marui A, Shimizu T, Ikeda T, Okano T, Sakata R, Yamashita JK. Pluripotent stem cell-engineered cell sheets reassembled with defined cardiovascular populations ameliorate reduction in infarct heart function through cardiomyocyte-mediated neovascularization. *Stem Cells.* 2012;30:1196-1205
218. Hoekstra M, Mummery CL, Wilde AA, Bezzina CR, Verkerk AO. Induced pluripotent stem cell derived cardiomyocytes as models for cardiac arrhythmias. *Front Physiol.* 2012;3:346
219. Lundy SD, Zhu WZ, Regnier M, Laflamme MA. Structural and functional maturation of cardiomyocytes derived from human pluripotent stem cells. *Stem Cells Dev.* 2013;22:1991-2002
220. Kamakura T, Makiyama T, Sasaki K, Yoshida Y, Wuriyanghai Y, Chen J, Hattori T, Ohno S, Kita T, Horie M, Yamanaka S, Kimura T. Ultrastructural maturation of human-induced pluripotent stem cell-derived cardiomyocytes in a long-term culture. *Circ J.* 2013;77:1307-1314

221. Ye F, Yuan F, Li X, Cooper N, Tinney JP, Keller BB. Gene expression profiles in engineered cardiac tissues respond to mechanical loading and inhibition of tyrosine kinases. *Physiol Rep*. 2013;1:e00078
222. Bhattacharya S, Burridge PW, Kropp EM, Chuppa SL, Kwok WM, Wu JC, Boheler KR, Gundry RL. High efficiency differentiation of human pluripotent stem cells to cardiomyocytes and characterization by flow cytometry. *J Vis Exp*. 2014